UNIVERSITY OF TRENTO

Doctoral School in Civil, Environmental and
Mechanical Engineering

Curriculum B. Mechanics, Materials, Chemistry and Energy

Luca Cacciali

Extended Momentum Model for Single and Multiple Hydrokinetic Turbines in Subcritical Flows

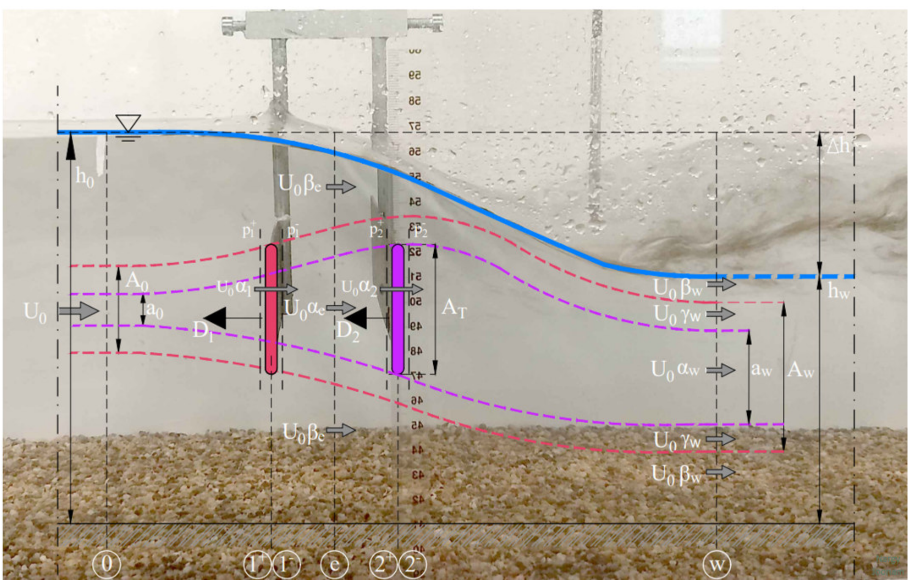

2021 - Doctoral Thesis

Department of Civil, Environmental and Mechanical Engineering

University of Trento

Ph.D candidate

Luca Cacciali

Doctoral Thesis

EXTENDED MOMENTUM MODEL FOR SINGLE AND MULTIPLE HYDROKINETIC TURBINES IN SUBCRITICAL FLOWS

Supervisor

Prof. Lorenzo Battisti

To my Mother

ACKNOWLEDGEMENTS

I want to acknowledge all the people who constantly encouraged me to pursue the goal of the Ph.D. Thanks to Prof. Lorenzo Battisti, whose professional and human esteem is unconditioned. Special thanks to Prof. Toffolon for the insights into Fluid Mechanics and the technical help with our tests at the Hydraulics facility in our department. Thanks to Prof. Ataollahi for the support in revising the articles published for this Ph.D. and for all the valuable advice. Endless thanks to Gabriella Ferri for her patience in the execution of all drawings featured in this work. Special thanks to Sergio Dell'Anna and Filippo Degasperi for their consistent and professional technical support. Thanks again to my Prof. and Sergio for the intellectual exchange that allowed my continuous improvement over these years. Without all of you, this work would not have been feasible.

JOURNAL PUBLICATIONS

The following publications were produced by the Author during his years of doctoral studies.

[1] Cacciali L., Battisti L., Dell'Anna S., Soraperra G. Case Study of a Cross-Flow Hydrokinetic Turbine in a Narrow Prismatic Canal. Ocean Engineering **2021**, 234, 109281.

DOI: https://doi.org/10.1016/j.oceaneng.2021.109281

[2] Cacciali L., Battisti L., Dell'Anna S. Free Surface Double Actuator Disc Theory and Double Multiple Streamtube Model for In-Stream Darrieus Hydrokinetic Turbines. Ocean Engineering **2022**, 260, 112017.

DOI: https://doi.org/10.1016/j.oceaneng.2022.112017

[3] Cacciali L., Battisti L., Dell'Anna S. Backwater Assessment for the Energy Conversion through Hydrokinetic Turbines in Subcritical Prismatic Canals, Ocean Engineering **2023**, 267, 113246.

DOI: https://doi.org/10.1016/j.oceaneng.2022.113246

[4] Cacciali L., Battisti L., Dell'Anna S. Multi-Array Design for Hydrokinetic Turbines in Hydropower Canals. Energies **2023**, 16(5), 2279.

DOI: https://doi.org/10.3390/en16052279

ABSTRACT

This thesis proposes equations extending the Free Surface Actuator Disc Theory to yield drag forces and interference factors from a series of two porous discs in open channel flows. The new model includes blockage ratio and Froude number as independent variables, which are inferred in advance to yield a single solution in the prescribed domain. The theoretical extension is integrated with the Blade Element Theory in a Double Multiple Streamtube model (DMS) to predict axial loads and the performance of confined Darrieus turbines. The turbine thrust force influences the flow approaching the rotor. Hence, a momentum method is applied to solve the hydraulic transition in the channel, achieving the unknown inflow factor from the undisturbed flow imposed downstream. The upstream blockage ratio and Froude number are thus updated iteratively to adapt the DMS to subcritical applications. The DMS is corrected further to account for the energy losses due to mechanical struts and turbine shaft, flow curvature, turbine depth, and streamtube expansion. Sub-models from the literature are partly corrected to comply with the extended actuator disc model. The turbine model is validated with experimental data of a high-solidity cross-flow hydrokinetic turbine that was previously tested at increasing rotor speeds. Turbine arrays are investigated by integrating the previous turbine model with wake sub-models to predict the plant layout maximizing the array power. An assessment of multi-row plants shows that the array power improves with closely spaced turbines. In addition, highly spaced arrays allow a partial recovery of the available power to be exploited upstream by a new turbine array. The highest array power is predicted by simulations on different array layouts considering constant array blockage ratio and rotor solidity. Finally, assuming a long ideal channel, the deviation in the inflow depth is speculated to become asymptotic after many arrays, implying almost identical power conversion upstream.

TABLE OF CONTENTS

INTRODUCTION

Based on the articles:

Cacciali L., Battisti L., Dell'Anna S., Soraperra G. Case Study of a Cross-Flow Hydrokinetic Turbine in a Narrow Prismatic Canal. Ocean Engineering 2021, 234, 109281. DOI: https://doi.org/10.1016/j.oceaneng.2021.109281.

Cacciali L., Battisti L., Dell'Anna S. Free Surface Double Actuator Disc Theory and Double Multiple Streamtube Model for In-Stream Darrieus Hydrokinetic Turbines. Ocean Engineering 2022, 260, 112017. DOI: https://doi.org/10.1016/j.oceaneng.2022.112017.

Cacciali L., Battisti L., Dell'Anna S. Backwater Assessment for the Energy Conversion through Hydrokinetic Turbines in Subcritical Prismatic Canals, Ocean Engineering 2023, 267, 113246. DOI: https://doi.org/10.1016/j.oceaneng.2022.113246.

OVERVIEW

The consumption of fossil fuels for electricity generation due to the global rise in energy demand negatively impacts the environment in terms of CO_2 emissions, the greenhouse effect, and global warming. According to Behrouzi et al. [1], fossil fuels are less reliable in the long term because of limited reserves and population growth. Therefore, most developed countries are attempting to exploit renewable sources to diminish the dependency on fossil fuels, ensuring sustainable development with clean, reliable, and cost-effective electricity production.

For more than a century, hydropower has been the most consistent source of renewable energy on the planet, being a continuous resource, with high density, predictable, and independent of random weather conditions, in contrast to solar and wind power options [1]. Although the scale of hydroelectric power generation varies significantly worldwide, it accounts for the highest share of global renewable energy conversion, as confirmed by the statistics of the International Renewable Energy Agency [2].

The total amount of electricity generated from renewables in 2020 was 7.468 TWh, with percentages illustrated in Fig. 1. 59% of the total (4.356 TWh) is hydroelectric energy, 21% is wind energy (1.589 TWh), 11% of solar energy (844 TWh), 8 % of bioenergy (584 TWh), 1% of geothermal energy (95 TWh), and marine energy (1 TWh). The marine capacity installed in 2020 amounts to 527 MW, and despite its growth, it is exploited only in countries with access to the coasts. Tab. 1 shows the annual trend of grouped renewable energy consumption in [TWh] from 2011 to 2019, with limited exploitation of marine energy. Among recent conversion technologies, much of the scientific community's interest is addressed to hydrokinetic turbines, i.e., low-environmentally invasive devices installed in tidal estuaries, rivers, and artificial waterways. The power conversion from tidal currents is an attractive solution, even though the requirement of a stable high-speed current is a key-element in achieving high-capacity factors. Some enthusiasm is also spreading around In-Stream River Hydrokinetics, whereby extensive research persists.

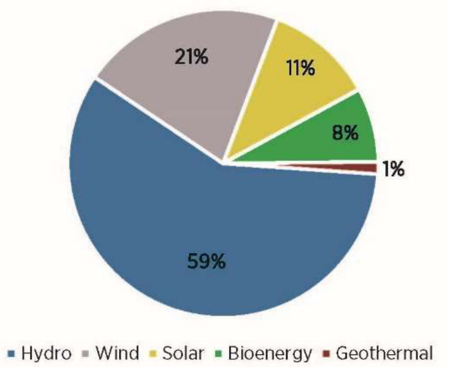

Fig. 1. Electricity generated from renewables, by energy source [1].

Tab. 1 World renewable electricity generation [TWh] [2].

Year	2011	2012	2013	2014	2015	2016	2017	2018	2019
Hydropower	3586,42	3772,39	3873,67	3992,50	3988,95	4160,14	4184,13	4280,51	4321,62
Marine	0,56	0,96	0,93	1,00	1,01	1,02	1,03	1,00	0,98
Wind	433,74	525,53	636,17	712,06	828,05	952,83	113,15	125,81	141,24
Solar	65,63	101,77	137,62	192,76	252,35	326,14	438,18	564,71	693,06
Bioenergy	335,89	371,00	404,16	436,17	459,11	485,11	503,10	526,56	557,85
Geothermal	69,86	70,84	72,36	77,29	81,21	83,27	86,02	89,52	92,05
Total	4401,68	4753,45	5035,77	5319,30	5516,43	5893,85	6222,60	6602,44	6963,45

According to Flambard et al. [3], unlike the electricity generated by wind and photovoltaic systems, hydrokinetic energy has the advantage of predictions over longer time scales. Indeed, the energy harnessed near the coasts is periodic, while the energy extraction from the rivers, with or without dams, presents seasonal variations.

The map from [4] in Fig. 2 shows the most relevant regions of tidal dissipation, i.e., the north of Australia, New Guinea, Indonesia, the east coast of China, the east coast of Alaska, Hudson's Bay in Canada, the area between the UK, Ireland and France, and southern Argentina. However, this map omits the potential of rivers or estuarine current power, which does not exclusively concern the countries bordered by the sea. Diversely, the European map in Fig. 3 from [5] distinguishes between tidal and run-of-water sources. As clearly identifiable, an abundant run-of-river operation is feasible in Scandinavia and South-Eastern Europe.

Apart from the tidal energy distribution, the available energy in rivers was mapped according to different models. One of the most valuable works determining the theoretical global riverine resource to 58.400 TWh/year ± 109 TWh/year, related to a capacity of 6.660 ± 0,012 TW, was developed by Ridgill et al. [6].

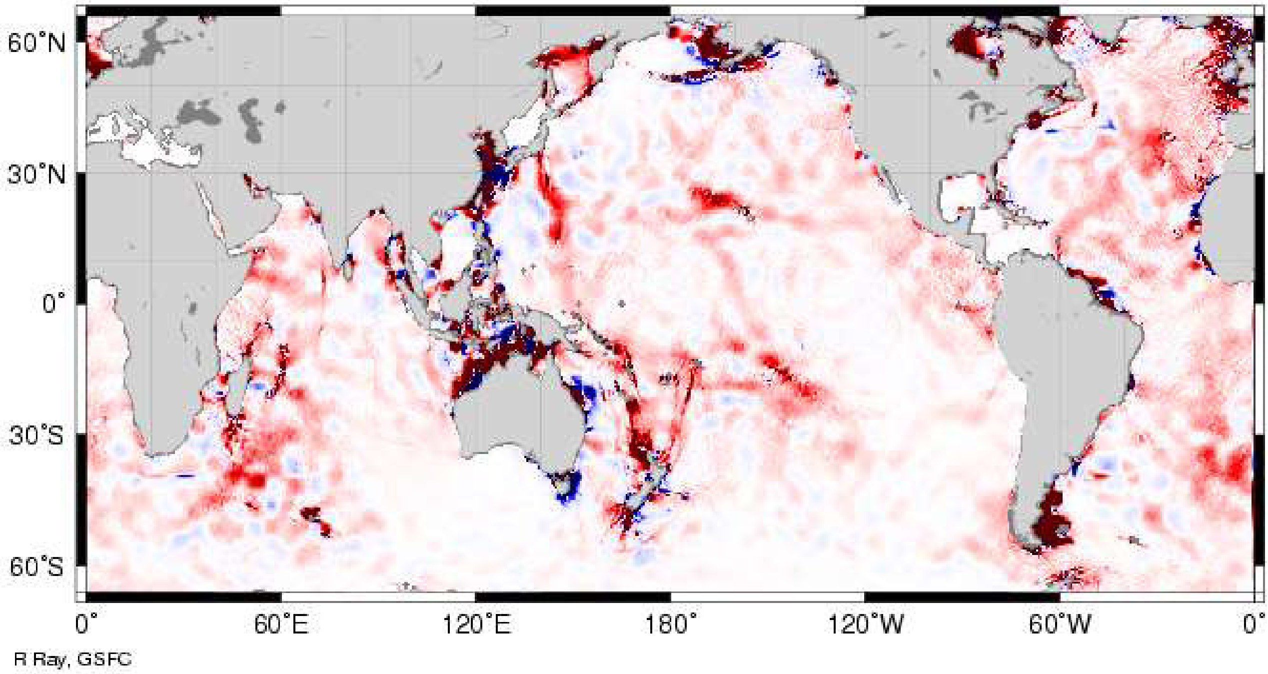

Fig. 2. Tidal energy dissipation world map [4]. The highest energy regions are marked in red.

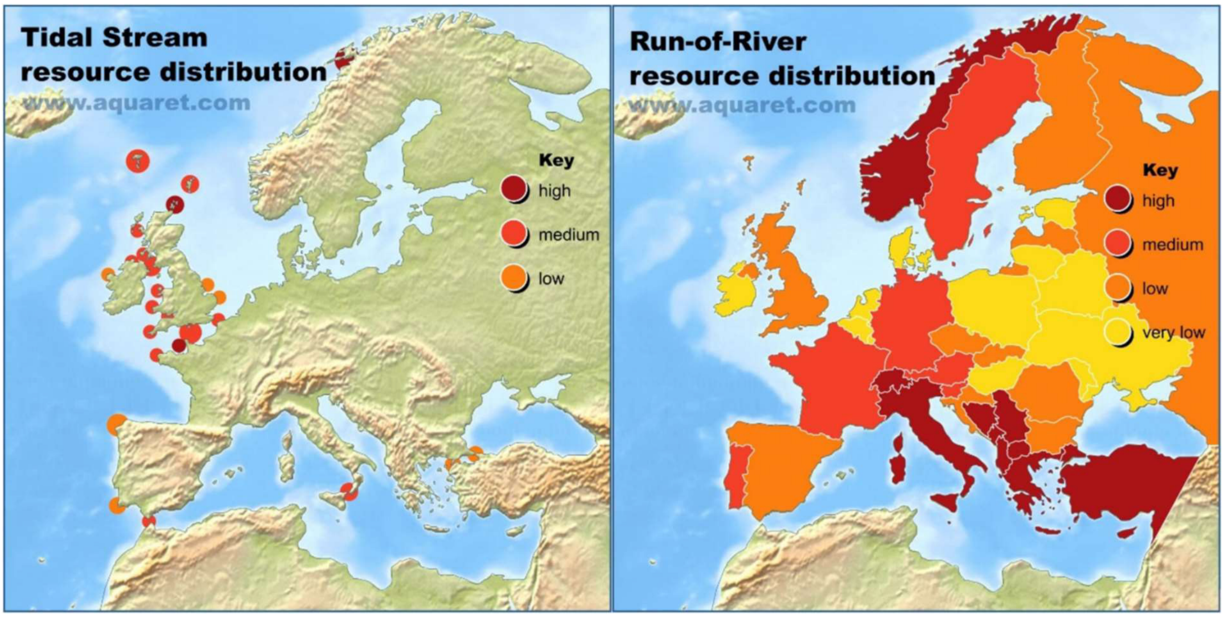

Fig. 3. Distribution maps of tidal stream and run-of-river resources [5].

Although the high uncertainty of discharge and head due to limitations in remote sensing, this result provided a first-order approximation of the overall potential for hydrokinetic energy conversion as a step toward mapping the global riverine resource. Since limited information is available at a continental scale [7], estimates were achieved by using a data set of sufficient temporal and spatial resolution for daily discharge [8], i.e., a 35-year discharge record from 1979 to 2013.

The theoretical riverine resource prediction allowed a qualitative spatial distribution in Fig. 4, identifying the regions at a high concentration. These areas comprehend the Himalayas, Tibetan Plateau, and surroundings, the islands of Borneo, Indonesia, New Guinea, New Zealand, the Andes, the Pacific Northwest, Scandinavia, the Congo Basin, Equatorial Africa, and Madagascar. This tool includes major rivers and rivers characterized by a significant elevation change.

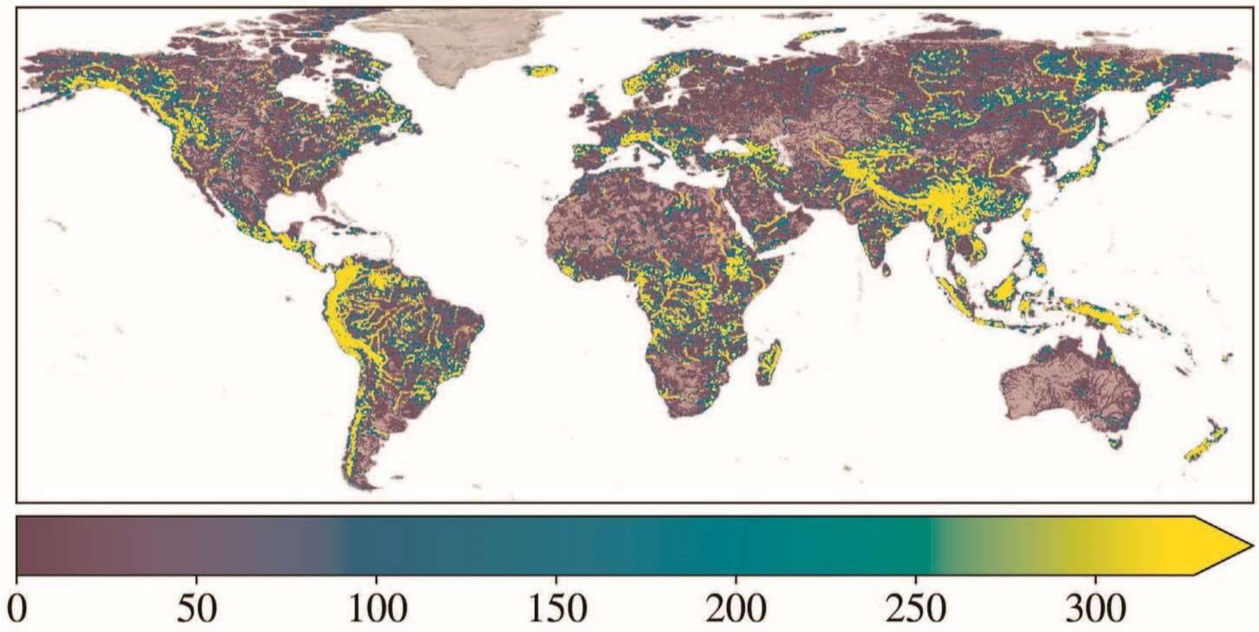

Fig. 4. Global distribution of theoretical riverine hydrokinetic resource [6] in [GWh/year].

The Electric Power Research Institute (EPRI) 2012 published a technical report [9] based on the riverine hydrokinetic resource in the 48 continental United States with Alaska and excluding tidal waters, providing estimates of the theoretically available energy and the technically recoverable resource.

A Geographic information system database, containing data of riverbed slope (S) and flow rate (Q_c), was used with the standard hydrological equation calculating hydraulic power $P = \gamma{*}Q_c{*}\Delta H$ [W] with γ the specific weight of water and ΔH the variation in hydraulic head between the beginning and end of a river segment. Only river stretches of a mean annual flow higher than 1.000 cfs were considered. The technically recoverable resource was determined by applying a recovery factor to each river segment, considering backwater effects. The recovery factor was achieved from a hydraulic model in HEC-RAS, including the turbines through a corrected Manning's roughness coefficient, relying on the models of Kartezhnikova and Ravens [10] and Garrett and Cummins [11]. However, the former is not valid for all waterways and only considers the case of a uniform distribution of turbines. The latter makes a very large approximation by assuming zero hydrostatic variation. Therefore, their model is considered outdated.

A detailed procedure capturing more closely the physics of the hydrokinetic problem was illustrated in 2017 by the U.S. Department of Energy [12] intended for planning, design, and operation of hydrokinetic plants, highlighting the main concerns, such as interruptions of water supply, flood risks, seasonal water variability, and unfavorable morphological changes. Based on the case study of an irrigation canal, the report introduces the properties to be measured, describes power and drag measurements, and illustrates bathymetric mapping recommendations and water level monitoring. Many of these properties are discussed later.

In northwest Italy, Botto et al. [13] developed a large-scale mapping of the potential from irrigation canals in Piemonte, finding 9.376 channels in an irrigable area higher than 450.000. These were identified and recorded into the Drainage and Irrigation informative system, i.e., a database for water management containing data and geographic information on irrigation canals. However, For completeness of discharge, cross-section area, and bulk flow speed data, only 1.350 channels were chosen, giving a total available power of 8 MW. For simplicity, only concession discharges were considered instead of actual values. The geometric height allowed computing the cross-section area instead of the water level because when canals are in service, the water level equals approximately that height. Differences in the flow rate from the considered inlet to the outlet were averaged. Moreover, for each canal stretch, a cross-section was investigated. Since no specific turbine geometry was assumed, the whole canal cross-section was considered for estimating the potential, even though not technically feasible because neglecting the fluid-dynamic losses.

D'Alessio [14] investigated the hydrokinetic potential in some sections of the most important rivers of the region Lombardia, starting from a hydrologic database and investigating the rotors to estimate the annual energy production. The average flow speed at the center of the river was determined with its seasonal characterization, identifying periods of higher potential and periods of hypothetical reduced operation.

Type of Hydrokinetic Turbines

The most widespread small-scale rotors are axial-flow turbines [15], more suitable for marine and tidal applications. Since operating at high rotor speed, no gearbox is present if the turbine is ducted [16]. The implementation of pitch control on axial-flow turbines improves flexibility and efficient operation. However, their high cost is due to the coupling with the generator, which must be submerged.

For river hydrokinetics and operation in narrow channels, the advantage of vertical-axis turbines is their ergonomics for placement in streams with limited flow rates and shallow waters [14]. The costs for the generators are low if installed above the water [15], [16],[17]. Moreover, they are suitable for different flow directions in marine applications. Although less efficient than axial-flow turbines [15], their cylindrical shape allows the addition of ducts [15]. Considering their low starting torque, a mechanism for their self-start can be necessary [15]. In addition, vertical-axis rotors are subject to torque ripple [15], [18]. Vermaak [19] illustrated different types of cross-flow rotors (Fig. 5), including lift and drag-driven devices, clarifying that Darrieus and Squirrel Cage types are the most common in river energy applications.

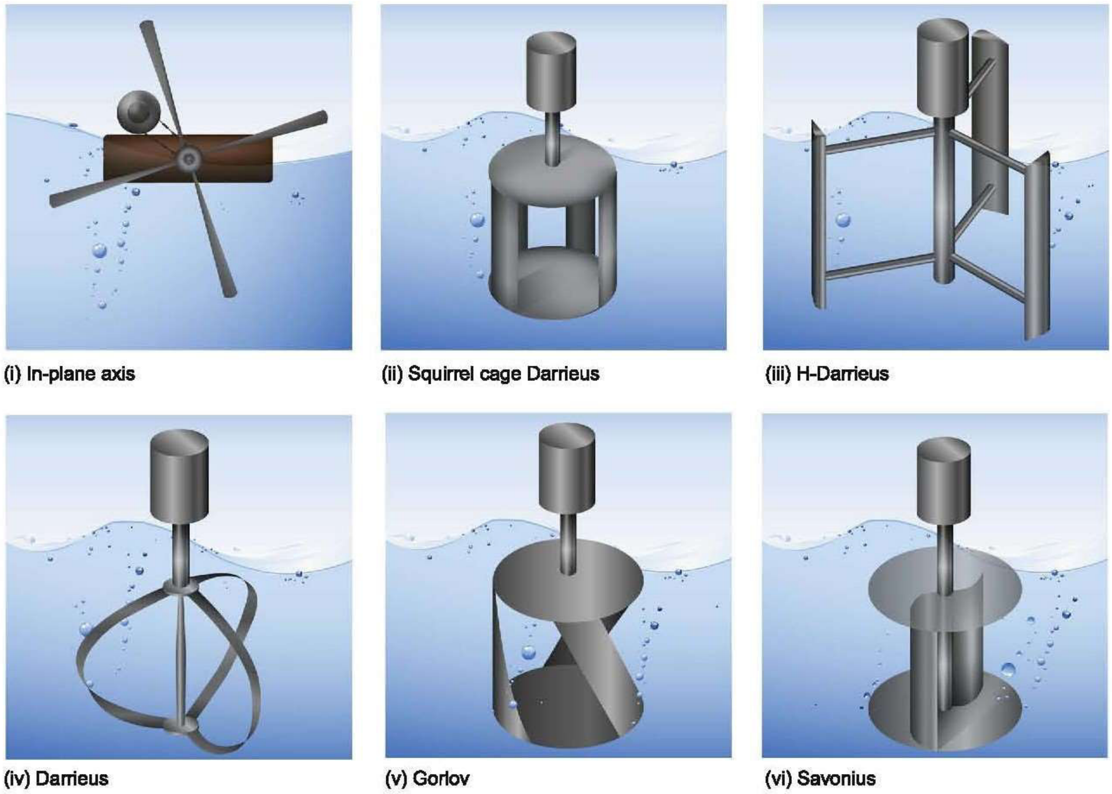

Fig. 5. Cross-flow HK turbine: a) In-plane, b) H-Darrieus, c) Darrieus, d) Savonius, e) Gorlov. Image from [18].

The decommissioned prototypes recalled by Lago et al. [20] in Fig. 6 represented a breakthrough for marine energy conversion research. The SeaGen 1.2 MW rotor was built with twin rotors mounted on a monopile support structure, and for years it represented the largest turbine ever manufactured. The Kobold 150 kW cross-flow turbine was the first H-Darrieus rotor installed offshore worldwide, deployed in the strait of Messina.

Fig. 6. SeaGen Tidal Generator, Strangford Lough (North Ireland), and Kobold H-Darrieus Turbine, Messina Strait (Italy), both decommissioned.

Different rotors are currently being engineered and developed for the marine environment, but In-Stream River Hydrokinetics is a suitable alternative to be investigated. Since the total energy released from the flow due to mechanical power conversion and wake dissipation corresponds to a limited head variation, HK turbines can be defined as "ultra-low head turbines" according to [21] and [22].

State of the art of micro-hydropower employs basin plants or run-off plants in locations where a static head exists. In rivers, traditional solutions imply large, flooded areas per unit of power output. Civil works require high investments with a noticeable environmental impact. In addition, the interruption of the natural dynamics of the streams may heavily alter the ecosystem. On the contrary, a hydrokinetic plant ensures the minimum environmental impact, as civil infrastructures like those in the classic basin and run-off plants (dams, flooded areas, etc.) are not required. The structural support can be realized with anchorages on the canal bank or floating platforms, reducing the investment cost and enhancing their reuse in case of relocation elsewhere.

The multi-turbine transversal fence can be mounted on a single supporting structure allowing a consistent rise in the power promoted by the increase of the blockage ratio, a phenomenon well-known in wind tunnel tests. Ideally, a confined turbine extracts more mechanical power than an unconfined rotor at an equal flow speed due to an enhanced pressure gradient generated through the rotor. According to [18], the increment in power conversion represents main advantage of energy exploitation in rivers and existing canals devoted to hydropower, irrigation, and navigation, even though axial loads rise. Thrust force and turbine power are affected by the confinement parametrized by the blockage ratio B, defined as the turbine swept area A_T to the channel cross-sectional area A (or flow passage) ratio. If calculated relative to the undisturbed cross-section, the blockage is termed B_∞, and if defined relative to the inflow cross-section, it is termed B.

$$B = \frac{A_T}{A}$$

Kirke [23] indicated that the turbine purchase and the execution of the civil works could generate a high cost per kWh. However, additional studies are desirable to demonstrate the feasibility due to cost and technical limitations, with extensive analysis of the profitability over the long term, accounting for transport, installation, and maintenance expenses. The canal selection is a complex task, as requirements of sufficient flow rate, velocity, and depth must be satisfied during the year. Canals with a sufficiently regular flow to generate electricity at a high-capacity factor and flow speeds higher than 1.5 m/s are uncommon. Depth must be sufficient to host a single turbine or more turbines. Clearance between the turbines' height and the free surface should exist. Therefore, only a few canals used for irrigation purposes are suitable. The candidates are typically devoted to water adduction/discharge to existing conventional hydropower plants of great size, as they ensure higher resource availability during the year, according to Liu and Packey [24]. The authors explored the attractive combination of hydrokinetic power production and conventional hydropower facilities to generate additional power cost-effectively.

Loads and Performance

The total axial load a turbine must withstand is represented by the thrust force, denoted by T, that occurs due to the pressure difference across the rotor created to balance the loss of momentum. If a torque Q is imparted to the blades, mechanical power P is collected at the blade shaft for conversion to electricity. However, in a cross-flow rotor, this occurs impulsively and results in mechanical stress, as later described in Chapter 1. Thrust, torque, and power are normalized henceforth for general treatment. The parameter identifying the axial load to the total dynamic pressure force of the current is the thrust coefficient C_T. The torque coefficient C_Q investigates the effects of the periodic behavior of the forces acting on the blades, and power coefficient C_P represents the turbine power to the kinetic power ratio. At the denominator, ρ and R_T represent water density and rotor radius, respectively.

$$C_T = \frac{T}{\frac{1}{2}\rho A_T U^2} \qquad C_Q = \frac{Q}{\frac{1}{2}\rho A_T R_T U^2} \qquad C_P = \frac{P}{\frac{1}{2}\rho A_T U^3}$$

These coefficients are expressed as a function of the tip speed ratio, i.e., the tangential speed ($\omega * R_T$) to the actual water speed U, with ω denoting the radian speed measured at blade tips. However, the flow speed, normalizing C_T, C_Q, C_P, and λ, will be specified later to understand whether the parameter refers to a station upstream or downstream of the rotor.

CONTROL OF CROSS-FLOW HK TURBINES

Horizontal wind and water turbines are controlled by a pitch strategy above the optimum power coefficient to smooth the power curve and reduce mechanical loads through a pitching blade mechanism [26]. Diversely, the stall control reduces the tip speed ratio by an increase in the angle of attack inducing stall. If present, a pitch mechanism mounted on vertical-axis rotors should modify the angle of attack over the entire revolution, making its installation expensive [27],[28]. With no active pitch mechanism, the rotor speed is the parameter to control by a regulation loop aiming to maximize the power output, control power over the rated speed, and minimize the effect of cavitation on blades.

To mitigate cavitation, Ginter and Pieper [29] indicated that the reduction in the relative flow speed W (with a drop in the rotor speed) is more effective than increasing the turbine speed for reducing the maximum angle of attack, even though the angle of attack is higher at low tip speed ratio. The torque applied to the rotor by the flowing current is decreased through a gearbox and transmitted to the high-speed shaft to a synchronous permanent magnet generator (PMG) supplying the reaction torque. For grid connection, a variable speed generator [30],[31],[32] with an AC/DC converter is generally used. Asynchronous generators (SCIG or DFIG) are alternatives to the PMG.

The hydrodynamic power output of the flow rate crossing the rotor of a swept area A_T is achieved from equation (1). For a given turbine geometry, the turbine power coefficient depends on the pitch angle and the tip speed ratio (2), yielding $C_P = C_P(\vartheta_P, \lambda)$, as illustrated in Fig. 7. Removing the pitch angle variable ϑ_P for a fixed-pitch turbine, the dependency of the C_P relies on a 2-D plane so that the hydrodynamic power is determined analytically. In power optimization, the controller operates by chasing the optimal tip speed ratio, i.e., $\lambda = \lambda_{opt}$. In this condition, the water flow speed U (3) that belongs to the optimal tip speed ratio (2) is replaced in equation (1), achieving the maximum hydrodynamic power P_{max} (4), which, in turn, dependent on the cube of the rotor speed.

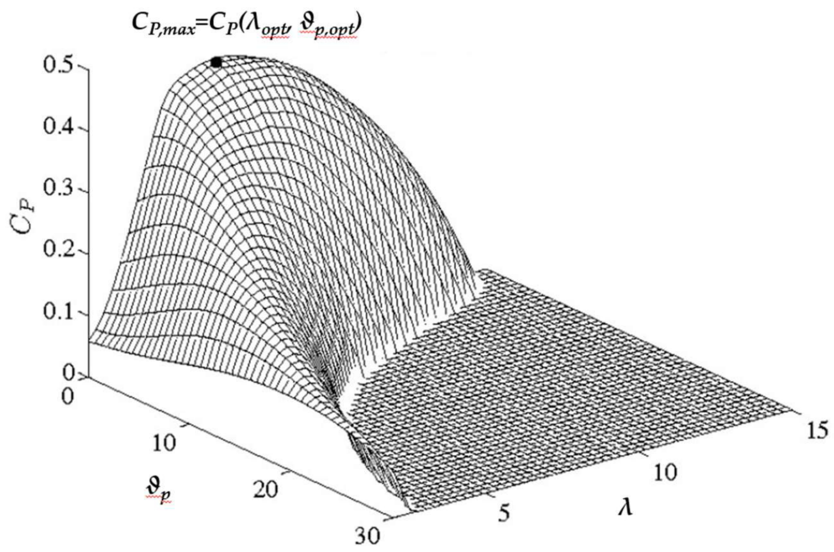

Fig. 7. Power coefficient C_P as function of the tip speed ratio λ and pitch angle ϑ_p. Image from [33].

$$P = \frac{1}{2}\rho A_T U^3 C_P(\lambda) \tag{1}$$

$$\lambda = \frac{\omega R_T}{U} \tag{2}$$

$$U = \frac{\omega R_T}{\lambda_{opt}} \tag{3}$$

$$P_{max} = \frac{1}{2}\rho A_T \left(\frac{R_T}{\lambda_{opt}}\right)^3 C_{P,max}\omega^3 \tag{4}$$

For the control strategy of a non-pitching cross-flow hydrokinetic turbine, Ginter and Pieper [29] remarked that the main challenge is to overcome the instabilities due to the cyclic pulsating torque varying based on turbine geometry and operative point. Nonlinearities occur due to the quadratic dependency of the hydrodynamic torque on the flow speed and the shape of the torque coefficient versus the tip speed ratio.

Based on [33], the power electronics act on the resistant generator torque characteristic towards variations in the rotor speed. Thus, the hydrokinetic turbine tracks the optimum speed considering the fluctuations of the channel flow rate. The maximum power, located on the mechanical torque - rotor speed plane, is achieved from equation (4), i.e., by replacing P_{max} with ($Q_{gen}*\omega_{gen}$), yielding the quadratic equation (5) representing the parabola in the Q-ω plane.

$$Q_{gen} = \frac{1}{2}\rho A_T \left(\frac{R_T}{\lambda_{opt}}\right)^3 C_{P,max}\omega^2 = c\omega_{gen}{}^2 \tag{5}$$

The strategies in Fig. 8 outline the control regions. On the left, the turbine is in shutdown as the operation is not economically convenient, assuming the low power output and wear of components up to cut-in speed. In the region (A-E), the turbine tracks the optimum tip speed ratio λ_{opt} to point E. After point E, the real power separates from the ideal power curve, leading to some power losses.

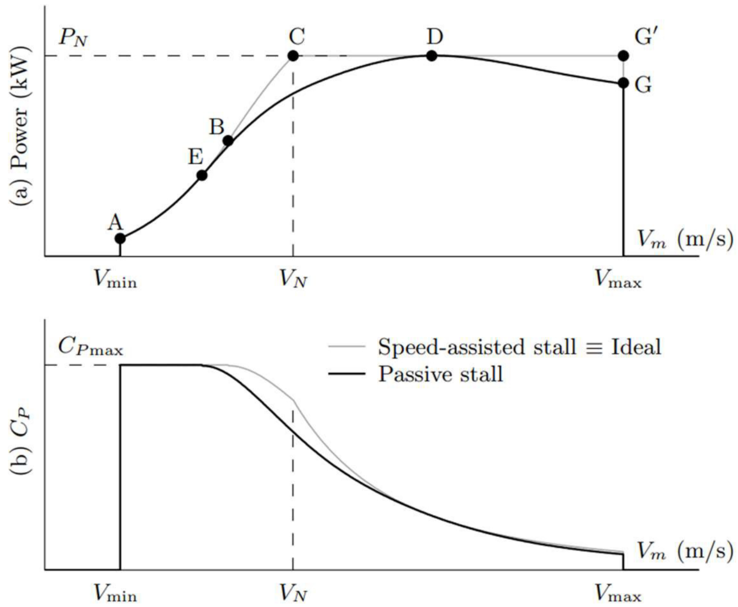

Fig. 8. Variable-speed fixed-pitch control strategies with passive stall regulation (AEDG) and speed-assisted stall regulation (ABCDG): (a) captured power and (b) power efficiency vs. wind speed. Image from [33].

At low water speeds, the tracking of the $C_{P,max}$ is feasible with the variable speed-passive stall technique, adopted for almost most vertical axis turbines, according to Battisti [34]. Fig. 9 shows the control strategy on the mechanical torque-rotor speed plane. In the low water speed region (between V_{min} and V_E), the rotor operates at variable speed along the quadratic curve AE, finding $C_{P,max}$. The rotor speed must change in response to the variation in the flow velocity fixing the velocity triangles [34]. To allow this variation, the controller acts on the electrical resistant torque (Q_{gen}) according to the law (5), allowing the rotor speed to increase from the cut-in speed (V_{min}) to P_{max} at V_D.

According to [33], a passive stall regulation implies that, above V_E, the turbine operates at a fixed speed along (E-D), thus inducing stall to limit power. Various operating points are superposed in the segment (G-D), and the maximum efficiency $C_{P,max}$ is achieved at a single water speed intersecting the point E. D denotes the point where the reaction torque intersects the stall front, i.e., the upper boundary of all hydrodynamic torque characteristics, which determines the rated power. At a water speed V_D or higher, the turbine stalls and reduces the mechanical power. Real and ideal power are attached to the point E, after which the real power separates and induces power losses. Higher water speeds reduce the hydrodynamic power, and thus the operating point moves back along the generator torque, reaching the cut-out point G corresponding to V_{max}. When the angle of attack α exceeds a given value, flow separation occurs from the low-pressure side of the hydrofoil, inducing a differential pressure that reduces the lift force and increases the drag force. This phenomenon implies a substantial increment in the thrust force with a drop in the tangential force.

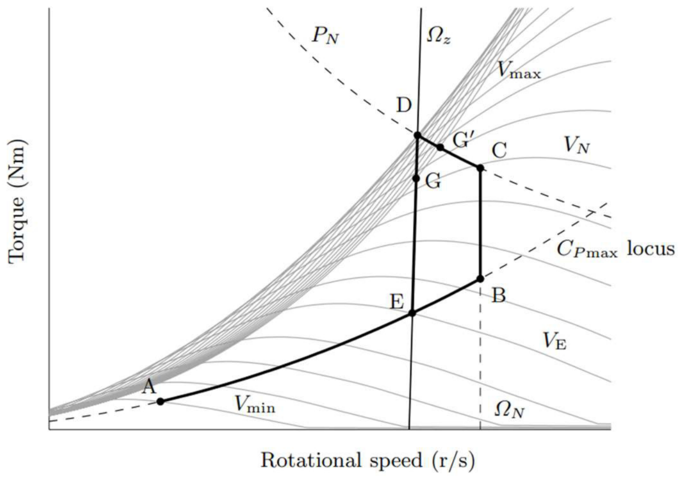

Fig. 9. Variable speed fixed-pitch control strategies with passive (AEDG) and speed-assisted (ABCDG) stall regulation. Image from [33].

With an assisted stall regulation, the turbine is regulated by chasing $C_{P,max}$ from A to B, increasing the rotor speed. Since the speed in B is maximum, the operative point moves along the segment (B-C) as water speed increases. Thus, the generator speed is kept constant at this water speed region. As water speed increases due to turbulent phenomena, the control induces stall by moving the torque characteristic toward the point shut-down point G′ along the rated power hyperbola, thus reducing rotor speed.

Hydrodynamic Properties

According to Gunawan et al. [12], the first information required for modeling the canal is the canal bathymetry. Accurate bathymetry data, including information on bed slope and cross-section geometry, is available from the canal operator. Although many irrigation canals have a bottom prone to erosion and deposition, this work aims to predict the performance of turbines deployed in waterways with a concrete bed.

The interference from tunnels, bottom sills, weirs, drains, etc., must be evaluated case-by-case. An object deployed in a canal obstructs the flow introducing a drag force. In open channel flows, this drag force causes a backwater to extend far upstream. The extreme drawback is the risk of overtopping from the canal banks. Although continuous monitoring of the water level at the sidewalls is desirable to prevent this issue, an accurate design that considers the thrust and power extracted from each turbine and a row or "array" of turbines is an aid in environmental control. According to [12], the main flow field properties and head parameters are introduced:

a) Mean flow speed (U)

Measurements of streamwise, crosswise, and vertical velocity components achieved from ADCP measurements (Acoustic Doppler Current Profiler) are required to obtain the bulk velocity in an undisturbed current, which represents the base for the calculations presented in this work. In addition, according to Gunawan et al. [12], the same procedure can be used to determine the inflow speed for assessing turbine performance and loading, evaluating the flow steadiness, checking the boundary condition in numerical models, and investigating wake velocity deficit/recovery calculations.

Moreover, velocity components u, v, and w data are required to assess the level of turbulence in each direction. The time-averaged and spatially-averaged longitudinal velocity component U yields the bulk velocity or mean flow speed. If the flow rate is almost steady, Q_c can be applied to all cross-sections of the canal stretch, while U becomes the mean value, with $U = Q_c/A$. In the incoming chapters, the flow speed at an undisturbed cross-section is termed U_∞, and the inflow speed is termed U_0.

b) Froude number (Fr)

It indicates the ratio of the flow inertia to gravity, distinguishing between subcritical ($Fr < 1$), critical ($Fr = 1$), and supercritical hydraulic regimes ($Fr > 1$). Only subcritical flows are considered in this work, and the Froude number is calculated by dividing the mean flow speed U by wave celerity c. Reminding that celerity is $(g{*}D_h)^{1/2}$, with the hydraulic depth of the channel denoted by D_h. Notice that $Dh = h$ in rectangular channels, with $D_h = A/w$, the wetter area termed with A and w denoting the free surface width.

$$Fr = \frac{U}{\sqrt{gD_h}}$$

c) Reynolds number (Re_f)

It indicates the ratio of inertia to viscous forces, distinguishing between laminar (Re_f < 2000), transient (2000 ≤ Re_f ≤ 4000), and turbulent flow (Re_f > 4000). According to Henderson [25], Re_f plays a limited role in the theory of open channel flow when the flow is on a large scale. Since it represents an inverse measure of the viscosity effect, at a high Reynolds number, the impact of viscosity on the flow is not noticeable.

The Reynolds number allows selecting canals suitable for HK applications. Indeed, fast and turbulent flows are usually characterized by $Re_f > 10^5$ [12]. Re_f is given by the product of water density ρ, to the mean flow speed U and the hydraulic radius of the canal R_h, divided by the dynamic viscosity of water μ.

$$Re_f = \frac{\rho U R_h}{\mu}$$

d) Head parameters

In open channel flows problems, the conservation of energy is stated by normalizing all terms by the unit weight of water, thus attaining bed elevation head z, the piezometric head (water depth or hydrostatic head) h, and the kinetic head k, so that the unit is in [m]. If including the elevation differences, the sum of the three components relative to a canal cross-section is the total head. Otherwise, the sum of the piezometric and kinetic components yields the specific energy denoted by E.

According to Henderson [25], the Coriolis coefficient denoted by α_c is applied to modify the kinetic head due to non-uniform velocities over the cross-section. It assumes the velocity variation over the water column by integrating the magnitude of the current at a generic point of the cross-section. The same applies to the momentum term ($\rho{*}Q_c{*}U$) with the

Boussinesq correction factor denoted by β_c. As remarked later, α_c *and* β_c are disregarded in this work. To be distinguished from the flow interference factors (Chapter 2), a subscript c is used. The head loss due to bed friction h_f is defined as the product of the friction slope S_f to the longitudinal length involved dx. The turbine head variation, denoted by ΔH_T, and the head drop due to viscous dissipation, ΔH_{diss}, cannot be distinguished in the channel flow, so the total head variation ΔH_{tot} replaces their sum in the equations of this work.

e) Turbulence parameters (u_x', u_y', u_z', TI)

The velocity fluctuates in time and diverges from the time-averaged mean flow speed. The fluctuating components u_x', u_y', and u_z' describe the turbulence level in a 3-D space. The fluctuating vorticity dominates turbulence; therefore, it can be considered as eddies of different size breaking and forming new ones. In this diffusive process, the rapid mixing of molecules leads to the conversion of kinetic energy into heat by viscous forces. According to the Reynolds decomposition, the total velocity is given by the sum of the mean value plus the fluctuating component, e.g., $u_x = u_{x,m}+u_x'$. Hence, the flow speed is calculated by averaging in space all time-averaged measurements.

As clarified by Gunawan [12], bulk velocity impacts long-time performance and converted power. In the short term, turbulence determines non-stationary loads on turbine components, including vibrations, noise, and fatigue. Turbulence intensity TI represents a measure of turbulence, and it is calculated as the standard deviation of fluctuating velocity to the mean flow speed ratio. It can be computed relative to each fluctuating component or to the mean fluctuating value, with $\sigma_x > \sigma_y > \sigma_z$, i.e., $TI_x = \sigma_x/U$, $TI_y = \sigma_y/U$, $TI_z = \sigma_z/U$. The total turbulence intensity is termed $TI = (\sigma_x^2+\sigma_y^2+\sigma_z^2)/U$. In this work, the treatment of the turbulent parameters is marginal.

AIM OF THE THESIS

This work aims to develop a tool predicting axial loads and performance of vertical-axis hydrokinetic turbines in artificial canals. The choice came down to a versatile Double Multiple Streamtube code for a single rotor to prioritize fast simulations. Blade Element Momentum codes simulate rotors in unconfined streams, while blockage corrections are available to approximate the desired performance in unbounded flows from the blocked output. Diversely, the development of a confined turbine model allowed complying with the physics of the problem, even though this choice implied a change in the core momentum equation. According to the literature, the last improvement to the Actuator Disc Theory for hydrokinetic turbines in channel flows included blockage ratio and Froude number as independent variables in a single-disc formulation. The authors attempted to solve these equations in a Blade Element Momentum model for axial-flow turbines, achieving satisfactory results. However, no Blade Element Momentum model was developed for Darrieus rotors based on an extended double-disc theory. In this perspective, a Free Surface double-disc LMADT may solve the governing equations in a Double Multiple Streamtube model, facilitating the assessment of In-Stream Darrieus hydrokinetic turbines.

Some modeling limitations have forced bold choices. First, a shear velocity was not applied. The confined actuator disc dictates the use of a bulk flow speed upstream of the turbine due to the definitions of the Froude number, implying a flow averaging. The inflow assessment adapts the turbine model to river currents. Since the sum of the energy harvested by the turbine shaft and the energy dissipated in viscous friction downstream of the rotor balances the reduction in upstream bed friction through the backwater, the rise in depth upstream of the turbine depends on the rotor operating condition. However, the turbine thrust coefficient and the inflow factor are two unknowns of the problem. Starting from the undisturbed flow downstream, the interaction between the DMS code and the inflow correction allows solving this undetermined problem for a single rotor. The model validation relies on experimental data of a high-solidity H-Darrieus turbine tested in the subcritical flow of a narrow canal. The code is extended further for assessing multi-array plants and defining the best solutions within various array layouts based on a different number of turbines, turbine aspect ratios, turbine spacing, and array spacing.

The experimental activity on the Darrieus rotor is illustrated in Chapter 1. The confined Actuator Disc Theory with the double-disc extension and the development of the Double Multiple Streamtube Model, including all sub-models, are treated in chapter 2 and 3, respectively. The inflow correction for adapting the previous code in subcritical flows is presented in Chapter 4, while the model developed for turbine arrays is illustrated in Chapter 5. Outputs and observations are presented in Chapter 6 before the conclusion of the work in Chapter 7.

References

[1] Behrouzi F., Nakisa M., Maimun A., Ahmed Yasser M. Global Renewable Energy and its Potential in Malaysia: A Review of Hydrokinetic Turbine Technology. Renewable and Sustainable Energy Reviews **2016**, 62, 270-1281.

[2] Available online: https://www.irena.org/publications/2022/Jul/Renewable-Energy-Statistics-2022 International Renewable Energy Agency (IRENA) (accessed on 01/12/2022).

[3] Flambard J., Amirat Y., Feld G., Benbouzid M., Ruiz N. River and Estuary Current Power Overview. Journal of Marine Science Engineering **2019**, 365. 7(10).

[4] Available online: https://svs.gsfc.nasa.gov/stories/topex/tides.html NASA Scientific Visualization Studio (accessed on 10 November 2022).

[5] Aqua-RET E-learning Tool: Resource Maps. Available online: https://www.aquaret.com (accessed on 10 November 2022).

[6] Ridgill M., Neill S.P., Lewis M.J., Robins P.E., Patil S.D. Global Riverine Theoretical Hydrokinetic Resource Assessment. Renewable Energy **2021**, 174, 654-665.

[7] Allen G.H., Pavelsky T.M. Patterns of River Width and Surface Area Revealed by the Satellite-Derived North American River Width Data Set, Geophysical Research Letter **2015**, 42 (2), 395-402.

[8] Lin P., Pan M., Beck H.E., Yang Y., Yamazaki D., Frasson R., David C.H., Durand M., Pavelsky T.M., Allen G. H., Gleason C.J., Wood E.F. Global Reconstruction of Naturalized River Flows at 2.94 Million Reaches. Water Resources Research **2019**, 55, 6499-6516.

[9] Jacobson J.P., Assessment and Mapping of the Riverine Hydrokinetic Resource in the Continental United States (No. 1026880), Electric Power Research Institute (EPRI), **2012**.

[10] Kartezhnikova M., Ravens T.M. Hydraulic Impacts of Hydrokinetic Devices. Renewable Energy **2014**, 66, 425-432.

[11] Garrett C., Cummins P. The Efficiency of a Turbine in a Tidal Channel. Journal of Fluid Mechanics **2007**, 588, 243-251.

[12] Gunawan B., Neary V.S., Mortensen J., Roberts J. Assessing and Testing Hydrokinetic Turbine Performance and Effects on Open Channel Hydrodynamics: An Irrigation Canal Case Study. Albuquerque, USA: U.S Department of Energy, **2017**.

[13] Botto A., Claps P., Ganora D., Laio F. Regional-Scale Assessment of Energy Potential from Hydrokinetic Turbines used in Irrigation Channels. SEEP2010 Conference Proceedings, June 29th – July 2nd, Bari, Italy, **2010**.

[14] D'Alessio G. Le Turbine Fluviali, Prospettive ed Applicazioni. La Valutazione del Potenziale Energetico in Lombardia. [MSc thesis], Politecnico di Milano, **2017**.

[15] Khan M.J., Bhuyan G., Iqbal M.T., Quaicoe J.E. Hydrokinetic Energy Conversion Systems and Assessment of Horizontal and Vertical Axis Turbines for River and Tidal Applications: A Technology Status Review. Applied Energy **2009**, 86(10), 1823–35.

[16] Zhou H. Maximum Power Point Tracking Control of Hydrokinetic Turbine and Low-Speed High-Thrust Permanent Magnet Generator Design [MSc thesis]. Missouri University of Science and Technology, **2012**.

[17] Güney M.S., Kaygusuz K. Hydrokinetic Energy Conversion Systems: a Technology Status Review. Renewable and Sustainable Energy Reviews **2010**, 14(9), 2996–3004.

[18] Cacciali L., Battisti L., Dell'Anna S., Soraperra G. Case Study of a Cross-Flow Hydrokinetic Turbine in a Narrow Prismatic Canal. Ocean Engineering **2021**, 234, 109281.

[19] Vermaak HJ., Kusakana K., Koko SP. Status of Micro-Hydrokinetic River Technology in Rural Applications: A review of Literature. Renewable and Sustainable Energy Reviews **2014**, 29, 625-633.

[20] Lago L.I., Ponta F.L., Chen L. Advances and Trends in Hydrokinetic Turbine Systems. Energy for Sustainable Development **2010**, 14, 287–296.

[21] Radkey R.L., Hibbs B.D. Definition of Cost-Effective River Turbine Designs. Technical Report AV-FR-81/595 (DE82010972). Report of US Department of Energy, Aerovironment Inc., Pasadena, California, **1981**.

[22] Khan M., Iqbal J., Quaicoe J. River Current Energy Conversion Systems: Progress, Prospects, and Challenges. Renewable & Sustainable Energy Reviews **2008**, 12, 2177-2193.

[23] Kirke B. Tests on ducted and bare helical and straight blade Darrieus hydrokinetic turbines. Renewable Energy **2011**, 36, 3013-3022.

[24] Liu Y., Packey D.J. Combined-Cycle Hydropower System - The Potential of Applying Hydrokinetic Turbines in the Tailwaters of Existing Conventional Hydropower Stations. Renewable Energy **2014**, 66, 228-231.

[25] Henderson F.M. Open Channel Flow, MacMillan Company, New York, **1966**.

[26] Goude A. Fluid Mechanics of Vertical Axis Turbines Simulations and Model Development. Thesis Dissertation, Uppsala Universitet, **2012**.

[27] B. Kirke and L. Lazauskas. Limitations of Fixed Pitch Darrieus Hydrokinetic Turbines and the Challenge of Variable Pitch. Renewable Energy **2011**, 36, 893–897.

[28] L. Lazauskas. Three Pitch Control Systems for Vertical Axis Wind Turbines Compared. Wind Engineering 1992, 16(5), 269–282.

[29] Ginter V.J., Pieper J.K. Robust Gain Scheduled Control of a Hydrokinetic Turbine Part 1: Design. Control Systems Technology, IEEE Transactions on Industry Applications **2010**, 19, 4, 805-817.

[30] Ashourianjozdani M.H., Lopes L. Pillay P. Power control strategy for fixed-pitch PMSG-based hydrokinetic turbine. Conference: IEEE International Conference on Power Electronics, Drives and Energy Systems (PEDES), **2016**.

[31] F.D. Bianchi F.D., Battista H.D., Mantz R.J. Optimal Gain-Scheduled Control of Fixed-Speed Active Stall Wind Turbines. IET Renewable Power Generation **2008**, 2, 4, 228 - 238.

[32] Hauck M., Rumeau A., Munteanu I., Bratcu A.I., Bacha S., Roye D., Hably A. A 1:1 Prototype of Power Generation System Based Upon Cross-Flow Water Turbines. Industrial Electronics (ISIE), IEEE International Symposium, **2012**.

[33] Bianchi F.D., Mantz R.J., Battista H. Wind Turbine Control Systems Principles, Modelling and Gain Scheduling Design. Advances in Industrial Control (AIC), ISBN 1846284937, 9781846284939, Springer, London, **2007**.

[34] Battisti L. Gli Impianti Motori Eolici. ISBN 978-88-907585-0-8, Lorenzo Battisti Editore, **2012**.

NOMENCLATURE

A	Cross-section or flow passage area m^2	U	Mean flow speed m/s (see subscripts)
A_T	Turbine swept area m^2	$U_{x,m}$	Mean velocity component m/s
B	Blockage ratio, (A_T/A)	u_x', u_y', u_z'	Velocity fluctuations m/s
C_P	Power coefficient, ($P/(½*ρ*A_T*U^3)$)	w	Free surface width m
$C_{P,max}$	Maximum power coefficient	ΔH_{diss}	Head drop due to dissipation m
C_Q	Torque coefficient, ($Q/(½*ρ*A_T*R_T*U^2)$)	ΔH_T	Turbine head drop m
C_T	Thrust coefficient, ($T/(½*ρ*A_T*U^2)$)	ΔH_{tot}	Total head drop m
D_h	Hydraulic depth m	α_c, β_c	Coriolis and Boussinesq coeff.
E	Specific energy, ($h+U^2/(2*g)$) m	ϑ_p	Blade pitch offset deg
Fr	Froude number, ($U/(g*D_h)^{0.5}$)	λ, λ_{opt}	Tip speed ratio, ($\omega*R_T/U$)
g	Gravity acceleration m/s^2	μ	dynamic viscosity $Pa\ s$
h	Hydrostatic head m (see subscripts)	ρ	Fluid density kg/m^3
h_f	Friction head m	σ_x^2, σ_y^2, σ_z^2	Standard deviation
P	Turbine power W	ω	Angular velocity rad/s
P_{max}	Maximum power W		
Q	Torque Nm	*Subscripts*	
Q_c	Channel flow rate m^3/s	∞	Far-field flow
R_h	Hydraulic radius m	0	Inflow
Re_f	Channel flow Reynolds number, ($ρ*U*R_h/μ$)		
S	Channel bed slope m/m	*Short forms*	
S_f	Friction slope m/m	*DMS*	Double Multiple Streamtube
T	Axial thrust N	*HK*	Hydrokinetic
TI	Turbulent intensity	*LMADT*	Linear Momentum Actuator Disc Theory

1. HYDROKINETIC TURBINE TESTS

Chapter adapted to the content of the article:

Cacciali L., Battisti L., Dell'Anna S., Soraperra G. Case Study of a Cross-Flow Hydrokinetic Turbine in a Narrow Prismatic Canal. Ocean Engineering 2021, 234, 109281. DOI: https://doi.org/10.1016/j.oceaneng.2021.109281

This chapter illustrates the experimental activity in a smooth prismatic canal where a cross-flow hydrokinetic turbine was deployed generating a highly blocked environment, as disclosed in [1]. Section 1.1 illustrates a literature review involving the testing of small-scale hydrokinetic rotors. Many of the listed references describe turbine loads and performance, often disregarding the assessment of a free surface effect such as backwater, which induces a variation in the turbine inflow. Sections 1.2 and 1.3 illustrate the features of the canal and turbine used for the experiments, including the test bench and probes. Section 4 shows the upstream free surface variation at each rotor speed and resumes the measurements of rotor thrust, mechanical torque, and power. Transients in achieving the hydraulic equilibrium in the channel were observed after the change in rotor speed, which prompted new measurements to be executed after regular time intervals. Visualization of wide torque fluctuations led to the definition of the torque ripple, a common concern in vertical-axis wind and hydrokinetic turbines. Studies from the literature about rotor solidity and aspect ratio allowed drawing information to reduce the torque ripple and renovate the rotor for future tests.

1.1. LITERATURE REVIEW ON TURBINE TESTS

River hydrokinetics is addressed as micro-hydropower due to the peak power of tens of kWs, with turbines generating electricity as long as running water is available [2] and without dams [3]. According to Riglin et al. [4], micro-hydrokinetic turbines have a limited capacity to produce a large amount of power in rivers due to limitations in wetted areas. However, turbine arrays will be essential to meet commercial power generation goals.

Several experiments investigating turbines immersed in high-blockage test flumes are available in the literature. Riglin et al. [5] tested an axial-flow turbine deployed in a water channel, finding maximum power coefficients ranging from 0.35 to 0.37 at flow speeds from 1.5 m/s to 1.7 m/s. Birjandi et al. [6] investigated a two-bladed squirrel-cage turbine at different depths and chord Reynolds number *Re*. When partially submerged, a noticeable drop in performance occurred at all *Re* investigated due to extensive cavitation caused by air drawn from the suction side of the blade. Bahaj et al. [7] studied the power coefficient and thrust coefficient of a 0.8 m diameter horizontal axis marine turbine in a cavitation tunnel for different flow conditions, showing a peak power coefficient of 0.46 at a yaw angle of 20° and flow speed of 1.7 m/s. A significant drop in performance occurred for shallow-tip immersion. McAdam et al. [8] performed extensive tests on hydrodynamic performance and structural loading of a transverse horizontal axis water turbine as a variant of a cross-flow Darrieus-type turbine. These were executed at a varying tip speed ratio and at several blockage ratios, solidities, fixed-offset pitch angles, and flow directions. Lower rotor solidity and higher blockage exhibited an increase in power conversion, channel efficiency, and structural loading. This device constantly exceeded the Lanchester-Betz limit. Ross and Polagye [9] studied a cross-flow rotor in two different test flumes at two blockage ratios. With interesting contour plots, the authors demonstrated the assumptions of higher bypass flow velocities around the rotor, reduced wake size, increased turbulence intensity, and viscous dissipation rate downstream of the turbine. Bachant and Wosnik [10] analyzed a cylindrical helical turbine for free flows and a spherical cross-flow turbine designed to operate in circular gravity-flow pipes or channels. Their power coefficients were 0.35 and 0.24, respectively. The authors justified the low performance of the spherical turbine due to its development for a higher blockage environment. Kirke [11] explored pitching systems on two cross-flow rotors, i.e., a 1 m diameter turbine with a passive eccentric mechanism tested in open water at 1.0 m/s and a 0.5 m diameter turbine with a cam-driven pitch to reduce the dynamic stall phenomenon tested in a towing tank at 0.5 m/s. Two-dimensional modeling demonstrated an overprediction of the power coefficient from 45% to 49% by ignoring parasitic drag losses and the pitch mechanism affecting low *Re* operation. Shimokawa et al. [12] analyzed a four-bladed Darrieus turbine with different chasings at a duct outlet as a dam-type rotor, showing a power coefficient higher than the Lanchester-

Betz limit at each flow condition. Finally, Myers and Bahaj [13] tested a 0.4 m diameter horizontal axis marine turbine in a water channel, investigating the upstream and downstream phenomena, i.e., an increase in water depth upstream of the rotor, a decrease in water depth downstream due to the turbine power, and a rise in depth further downstream due to the wake reaching the surface.

Different river tests were conducted, even though only some are mentioned for brevity. Kirke [14] resumed data of helical and straight-blade Darrieus turbines with and without a variable pitch system. With a diffuser, he observed the improvement of power output by a factor of three compared to the same turbine without the diffuser. Patel et al. [15] tested a Savonius turbine in different canal geometries, showing improvements in turbine power by increasing the kinetic energy upstream of the turbine by enhancing the bottom height of the canal or reducing the side wall's distance. Anyi and Kirke [16] reviewed the experiences of several teams in Australia, South America, and the UK related to different solidity axial flow turbines for 1-2 kW electrical power generation in rivers for off-grid purposes. The installation details of various rotors were described, showing how turbines can be suspended from the bank of small rivers using a pivot arm or from jetties/bridges using a long pole. According to previous literature experiences, a welded steel structure was manufactured to resist high thrust force and vibrations generated at the shaft of the cross-flow turbine illustrated in this chapter and was fixed on the canal embankments.

1.2. Characterization of the Undisturbed Flow in a Canal

Experimental tests were conducted at the smooth prismatic waterway shown in Fig. 1-1, where a cross-flow hydrokinetic turbine was deployed, which generated high blockage. Since no significant change in flow rate and depth was observed during the initial measurements, a mean flow speed allowed defining the undisturbed condition before the deployment of the turbine.

The cross-flow hydro-turbine was designed, manufactured, and assembled with its test bench for deployment in the canal. Measurements of bending moment and mechanical torque were executed at different rotor speeds. Free surface effects, such as the backwater profile upstream, including the rise in the hydrostatic pressure at the turbine proximity and the water depth drop, were visualized. All measurements were performed at a single flow condition due to the impossible regulation of flow speed and depth.

Fig. 1-1. The hydrokinetic turbine and its structural support mounted on the embankments.

The canal cross-section is trapezoidal with an additional trapezoidal bottom. The canal is in the municipality of Dro (Fig. 1-2) near Trento (Italy). It is hydraulically supplied from the river Sarca to guarantee the minimum vital flow of a neighboring trout farm.

Fig. 1-2. Satellite and transversal views of the test site.

The bottom and walls consist of cement slabs on gently sloping terrain. The mean geometric slope S of the bottom cement slabs is approximately 0.1% at the measuring station. A part of the flow rate is collected towards a micro-hydropower plant.

Turbulence parameters were investigated after measurement of the velocity components in the x, y, and z directions at 50 Hz. Turbulent fluctuations u_x', u_y', and u_z' attached in Fig. 1-3 exhibited an anisotropic behavior and a reduced oscillation on the third component. The maximum oscillation was achieved by the cumulated mean values of the axial component u_x', resolving in approximately three minutes, sufficient to characterize the flow with reliable measurements. Hence, the turbulence intensity of the canal was estimated at 6.67%.

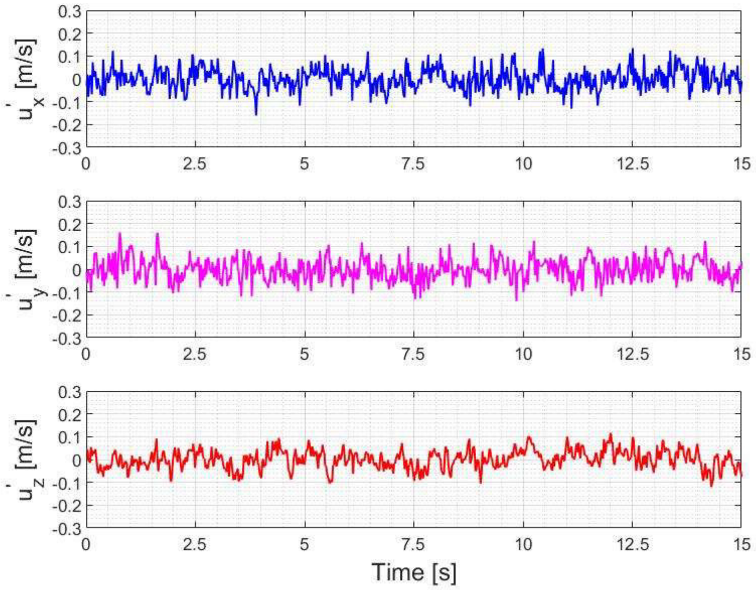

Fig. 1-3. Turbulent fluctuations u_x', u_y', u_z'.

No historical flow data series were available. Therefore, an entropy model was applied to calculate the undisturbed bulk flow speed U_∞. In the literature, entropy models were declared effective, especially for the flow near the bottom and below the free surface, where many existing measuring devices face problems [17]. Entropy models [18] are considered a reliable alternative to the most popular velocity-area approach [19] or multi-variable regression analyses [20]. According to Chiu and Tung [21], since the maximum velocity in a channel section often occurs below the water surface, the mean value of the ratio of U_∞ and maximum flow speed u_{max} at the cross-section represents a stable function invariant with time and discharge. Moreover, the problem is further simplified as the y-axis is in the middle section of prismatic channels.

$$u = \frac{u_{max}}{M} ln[1 + (e^M - 1)F(u)]$$

The probability density is obtained as a function of the velocity $f(u)$, which is the specific random variable [21]-[23]. The probability of the sampled velocity being less than or equal to the cumulative distribution function $F(u)$ of the probability density $f(u)$. It is expressed as $(\xi-\xi_0)/(\xi_{max}-\xi_0)$, with ξ, denoting the ith isovel curve, ξ_{max} denoting the maximum isovel occurring at u_{max}, and ξ_0 denoting the isovel at $u = 0$ at the channel bed, with $0 \leq u \leq u_{max}$. Assuming $\xi_0 = 0$, it yields,

$$\frac{\xi}{\xi_{max}} = \int_0^u f(u)du$$

Since the most reliable probability distribution is that with a maximum uncertainty (maximum entropy), the probability distribution of the maximum velocity in a stream is achieved by maximizing Shannon's entropy $f(u) = e^{a1+ua2}$, with $e^{a1} = M/(u_{max}(e^M-1))$ and $a_2 = M/u_{max}$. The cumulative $F(u)$ represents the fraction of the flow area in which the velocity remains lower than or equal to u_{max}, according to Farina et al. [24]. ξ is expressed as a function of the vertical coordinate y, according to [22]:

$$\xi = \frac{y}{D-h} e^{\left(1-\frac{y}{D-h}\right)}$$

In this expression, D represents water depth, and h is the vertical location of u_{max} below the free surface. According to Chiu and Tung [21], three cases are expected based on the position of u_{max}, i.e., $h > 0$, $h = 0$, and $h < 0$. In the first case, ξ_{max} occurs below the free surface at $y = (D-h)$; in the second case, ξ_{max} is at the free surface such that $y = D$, and ξ_{max} occurs on the free surface, where h loses its physical meaning but becomes a tuning parameter for the curvature of the velocity distribution, and still $y = D$.

By substituting y in the previous statement, it is achieved $\xi_{max} = 1$ for the first two cases and $D/(D-h)e^{(1-D/(D-h))}$ for the third. Therefore, the ratios ξ/ξ_{max} become, respectively:

$$\frac{\xi}{\xi_{max}} = \frac{y}{D-h} e^{\left(1-\frac{y}{D-h}\right)}$$

$$\frac{\xi}{\xi_{max}} = \frac{y}{D} e^{\left(1-\frac{y}{D}\right)}$$

$$\frac{\xi}{\xi_{max}} = \frac{y}{D} e^{\left(\frac{D-y}{D-h}\right)} \rightarrow \frac{y}{D}$$

The third equation is evaluated as $h \rightarrow -\infty$. From the probability density function $f(u)$, the ratio of the mean and maximum velocity, Chiu and Hsu [23] derived the cross-sectional average velocity $U_\infty = f(u_{max}, M)$ (1.1) as a linear function of the maximum velocity u_{max} on the vertical axis and the entropy dimensionless parameter M, which represents a constant for a given cross-section. This equation describes the velocity variation in two dimensions with the maximum velocity at or below the free surface. Hence, the function $\phi(M)$ is determined from equation (1.2).

$$U_\infty = \phi(M) u_{max} \tag{1.1}$$

$$\phi(M) = \frac{e^M}{e^M - 1} - \frac{1}{M} \tag{1.2}$$

Since no records of M were available, velocity samples were collected on the z-axis to estimate the location of u_{max} giving h_i/D_i. M was derived from the following empirical relationship with h/D [21]. Other methods are also available [24] for estimating M. This regression was assessed in the range $1.0 \leq M \leq 5.6$ and $0 \leq h_i/D_i \leq 0.61$, even though validated only for wide rivers [24].

$$\frac{h_i}{D_i} = 0.2 \ln \frac{58.3}{G(M)}$$

$$G(M) = \frac{e^M - 1}{M\, \phi(M)}$$

With a maximum velocity u_{max} of 1.44 m/s and M of 3.62, a mean bulk flow speed $U_\infty = 1.078$ m/s was achieved, generating a flow rate $Q_c = 1.189$ m^3/s, which isovels are illustrated in Fig. 1-4. From Gauckler-Manning's formula, a Manning's coefficient n of approximately 0.016 was calculated, given a hydraulic radius R_h of 0.3922 m and a bed slope S of 0.001 m/m, demonstrating a consistent result for smooth canals [25]. The hydraulic parameters referred to in the undisturbed cross-section are resumed in Tab. 1-1. Fr_∞ and the Re_f characterizing the flow yield 0.402 and 3.71e6, respectively. According to Gunawan [26], the Reynolds number is high enough to consider this canal suitable for HK applications. An absolute error of 0.0704 m/s was ascertained, calculated to the output of a multi-regression analysis, and the ADV uncertainty. It was considered as the averaging error.

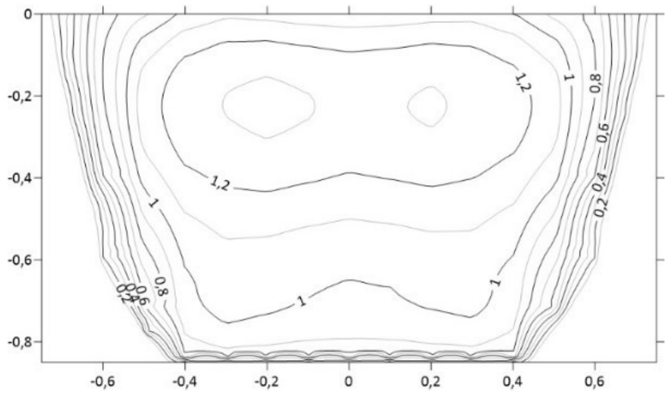

Fig. 1-4. Cross-sectional iso velocity curves distribution in the canal.

Tab. 1-1 Parameters identifying the undisturbed flow of the trapezoidal canal.

Variable	Symbol / Unit	Value
Bed slope	S [m/m]	0.001
Manning's coefficient	n [$m^{-1/3}s$]	0.016
Cross-section area	A_∞ [m^2]	1.1025
Hydraulic radius	R_h [m]	0.392
Hydrostatic depth	D [m]	0.850
Hydraulic depth	D_h [m]	0.735
Free surface width	w [m]	1.500
Mean flow speed	U_∞ [m/s]	1.078
Volumetric flow rate	Q_c [m^3/s]	1.189
Froude number	Fr_∞ [-]	0.402
Reynolds number	Re_f [-]	$3.71e^5$

1.3. THE HYDROKINETIC TURBINE

The turbine in Fig. 1-5 is a self-starting cross-flow hydrokinetic turbine based on the H-Darrieus concept, with a rotor consisting of three straight and equally-spaced blades with a zero-pitch offset angle, manufactured with a numerically controlled cutter in aluminum alloy. The fluid dynamics modeling, and the structural design of the rotor were executed by the Fluid Machinery Laboratory Staff of the University of Trento to maximize the turbine performance. The size and shape of blades confer high solidity to the rotor, determined as $\sigma = c{*}N_b/(2R_T)$ where N_b is the number of blades, c is the chord length, and R_T is the turbine radius. Its shape confers a tip loss reduction which represents a critical factor for vertical axis turbines. The blades were designed with a NACA0021 profile to reduce the rotor manufacturing cost. In Tab. 1-2, the geometrical features of the rotor are summarized. The size of the rotor was chosen to generate a significant blockage ratio B_∞, based on the maximum value foreseen for a larger-scale experiment (not described in this work). A refined measurement of the turbine swept area from the chord mid-line for the simulations illustrated in Chapter 6 yields 0.2257.

Fig. 1-5. The three-bladed cross-flow turbine.

Tab. 1-2 Hydrokinetic turbine features.

Description	Value
Diameter (D_T)	0.50 m
Height (H_T)	0.50 m
Blades (N_b)	3
Chord length (c)	0.067 m
Hydrofoil thickness (t)	0.014 m
Profile	NACA0021
Blade pitch offset (θ_P)	0°
Frontal area (A_T)	0.25 m^2
Solidity (σ)	0.402

The planimetric arrangement of the turbine and probes is shown in Fig. 1-6. Before the turbine deployment, the tests of the undisturbed flow speed were performed using an acoustic doppler velocimeter ADV in position (A) with accuracy ± 0.01 m/s. A grid of 5x7 velocity points was acquired from which cross-sectional iso velocity curves were modeled (Fig. 1-4).

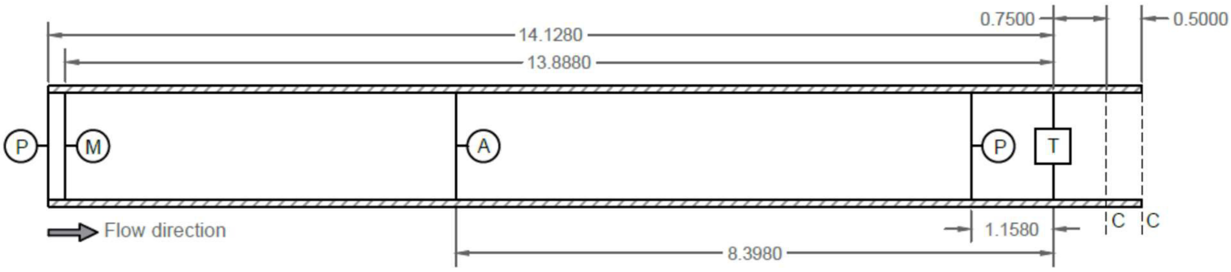

Fig. 1-6. Planimetric arrangement of pressure probes (P), propeller-type current meter (M), Acoustic doppler velocimeter (A), turbine (T), and downstream crossbars (C).

Additional measurements were performed with a propeller-type current meter (M) at the canal centerline. Data on water depth were collected from two pressure probes (P) during the turbine operation at an upstream station and the turbine proximity, aiming to check the backwater. Additional measurements were executed into the wake at 1.5 D_T and 2.5 D_T downstream of the rotor (C). The test bench for this campaign was manufactured to measure the values of torque and thrust acting on the rotor at different rotor speeds. The test bench in Fig. 1-7 was essentially provided by:

- DC motor/generator (with nominal power 0.61 kW and nominal speed 1000 rpm)
- electronic drive for the speed regulation of the DC motor (controller)
- network of probes
- data acquisition system

- structural support, i.e., a tilting frame made of welded steel pipes anchored to the canal embankments including a vertical translation system to adjust the immersion depth of the rotor.

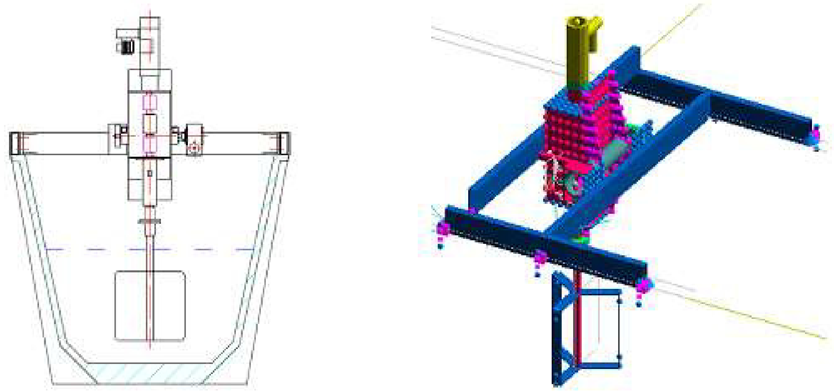

Fig. 1-7. Turbine test bench: macro components scheme (**left**) and finite element modeling (**right**).

The structural support of the test bench is a tilting frame laid on canal embankments allowing the lifting and the immersion of the turbine. The probes on the test bench, the range of signals, and the measurement accuracy are shown in Tab. 1-3. The signals from the probes were sampled at a frequency of 2 kHz with a National Instrument's Compact RIO (9082). The torque meter has an integrated encoder mod. Kistler 4503A with accuracy ± 0.1 Nm. Data were continuously displayed and stored in text files.

Tab. 1-3 Characteristics of the probes used for the test bench.

Output signal	Probe type	Range	Accuracy	Signal acquisition freq.
Axial thrust [N]	Strain gauge	± 350	±2.5 N	
Shaft torque [Nm]	Torque meter	± 200	± 0.1 Nm	
Rotor speed [rpm]	Encoder	0 ÷ 6000	± 0.2 rpm	2000 Hz
Flow velocity [m/s]	ADV	0.4 ÷1.6	± 0.01 m/s	
Water temp. [°C]	RTD	-200 ÷ 300	± 0.012 °C	

1.4. Measurements

The differences in water depth between the measurements at the stations (P) illustrated in Fig. 1-6 to the average undisturbed depth are shown in Fig. 1-8. epth measurements were executed with a running turbine at each rotor speed and with the turbine off. Notice that an undisturbed depth h_∞ of 0.85 ± 0.005 m was measured. The chart also shows the axial thrust computed from the bending moment measurements acquired with the strain gauge mounted on the test bench. Each rotor speed corresponded to different thrust and water depth. The instrumental uncertainty was considered for the computation of the average experimental data and the propagation error was evaluated for all dimensionless parameters. Temporal measurements of the axial thrust result highly concentrated within approximately ± 10 N, consistently with the low fluctuations of flow depth, thus demonstrating the high reliability of the test procedure.

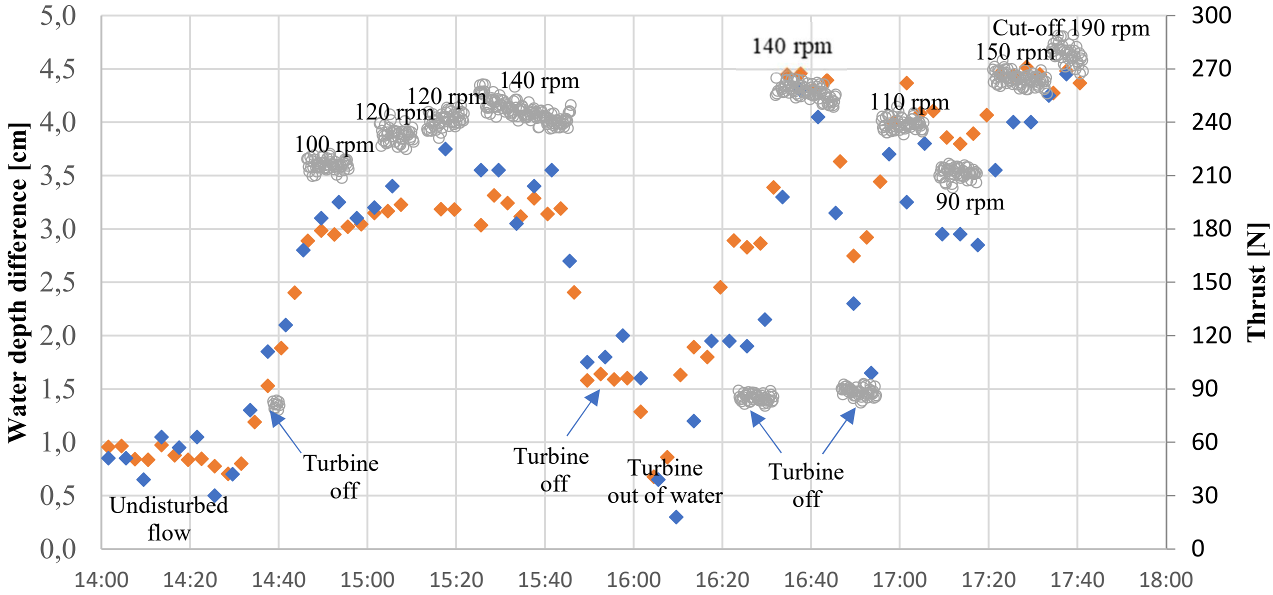

Fig. 1-8. Chart of the local water depth differences to the undisturbed depth measured at the upstream station probe (orange) and the turbine probe (blue), besides axial thrust (grey circles) on the turbine shaft calculated from bending moment data.

Data of upstream water depth shows a backwater profile propagating from the turbine upstream. At the highest rotor speed, the water depth was measured at the upstream control station, demonstrating a maximum increase of 4.5 cm to the undisturbed depth value. This test clarified that far-field velocity and depth measurements must be executed far from the turbine at an undisturbed cross-section. Indeed, the flow was still affected by backwater at twenty-eight diameters upstream of the rotor.

Additional tests were completed to verify whether a supercritical flow condition could appear at a high turbine load. The flow speed was measured with the ADV at the downstream crossbars C (Fig. 1-6), but no hydraulic jump occurred, and depth remained within the safety threshold at the highest rotor speed. Backwater was limited in this canal, despite the high geometric blockage ratio generated in the cross-sectional area. As expected, the depth upstream of the rotor increased progressively and proportionally to the axial thrust on the turbine shaft at each step in the rotor speed. Depth and velocity were measured after each rotor speed change, outlining flow transients ending with the attainment of a new flow equilibrium, which was recognized as a new quasi-steady state. The decreasing mechanical torque at each operational condition was due to flow transients lasting at least ten minutes, so measurements were discarded attentively within this time interval.

Averaged T, Q, and P were then calculated at each rotor speed for the remaining dataset, as depicted in Fig. 1-9 to Fig. 1-11. Uncertainties are specified for rotor speed and thrust in Tab. 1-3, whereas for power, the error interval varies from ± 1.16 W at 90.18 rpm to ± 2.04 W at 190.9 rpm, with a mean value of ± 1.53 W. The maximum mechanical power of 127.42 W is achieved at the optimum rotor speed of 110.22 rpm. Under the same operating condition, axial thrust and mechanical torque result in 238.29 N and 11.04 Nm, respectively.

The coefficients $C_{T,\infty}$, $C_{Q,\infty}$, and $C_{P,\infty}$ are illustrated in Fig. 1-12 to Fig. 1-14 versus the tip speed ratio λ_∞, i.e., the peripheral speed of the rotor divided by the undisturbed flow speed. The Reynolds number of the blade chord Re ranges between 1.081e5 and 2.297e5 at the optimum tip speed ratio λ_∞ of 2.68. At the optimum, a thrust coefficient of 1.64 is indicated, whereas the power coefficient surpasses the Lanchester-Betz limit at 0.81, although evidently, this limit represents a meaningless threshold in confined flows. As previously mentioned, the denominator of the power coefficient accounts for the kinetic energy of the flow, oversimplifying the mechanism of power extraction. Indeed, the hydrostatic head variation generated by the turbine is ignored in defining the power coefficient. According to Kirke [27] and McAdam [28], the energy conversion represents a variation of the total head, instead of a simple extraction of kinetic flux. Therefore, the ratio of the rotor power to the total energy removed from the flow represents the hydraulic efficiency of the system. A prediction of the hydraulic efficiency is executed in Chapter 4.

The error propagation analysis was investigated with a differential-logarithmic method. It accounts for the instrumental uncertainty of ADV, torque meter, strain gauge, and encoder and the modeling error on the far-field velocity. The mean absolute error on the dimensionless parameters is high (± 0.237 for $C_{T,\infty}$, ± 0.033 for $C_{Q,\infty}$, ± 0.141 for $C_{P,\infty}$, and ± 0.210 for λ_∞) due to the influence of the velocity estimate error on other quantities. It is evident if one observes the non-negligible uncertainty determined for the tip speed ratio.

An example of torque and axial thrust over a complete revolution is presented in Fig. 1-15 for the optimum tip speed ratio of 2.68. An evident torque ripple appeared with high shaft vibrations, phenomena that are typically related to dynamic stall issues, especially at low λ_∞. At this rotor speed, the torque ripple induced high axial thrust fluctuations. This stress level may accelerate fatigue failure [29],[30]. In addition, the torque ripple produces oscillations of the mechanical power. Therefore, rotor speed cannot be regulated adequately by the PI control.

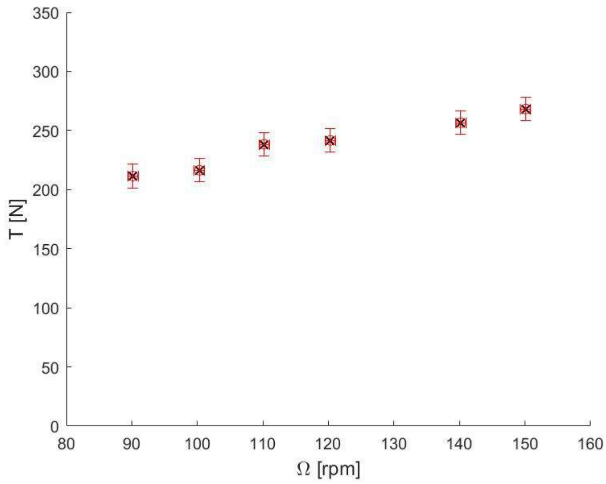

Fig. 1-9. Averaged axial thrust force $\boldsymbol{T}$ vs rotor speed $\boldsymbol{\Omega}$.

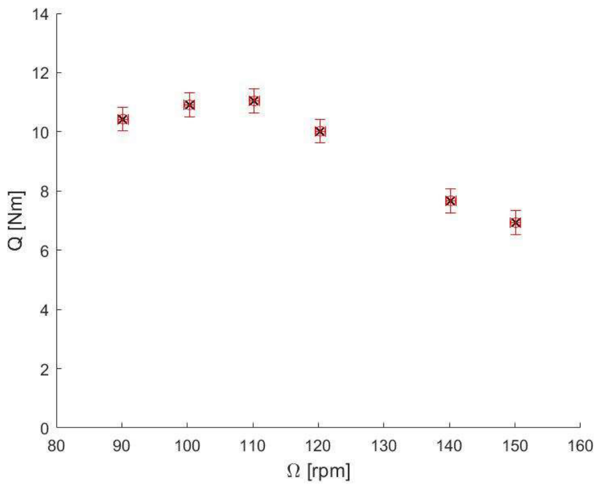

Fig. 1-10. Averaged mechanical torque $\boldsymbol{Q}$ vs rotor speed $\boldsymbol{\Omega}$.

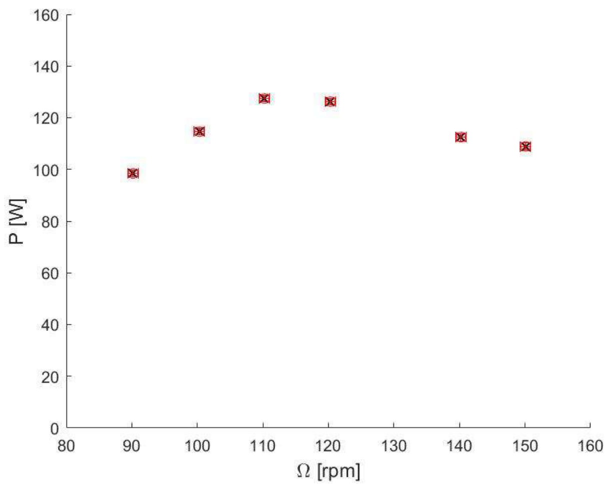

Fig. 1-11. Averaged turbine power $\boldsymbol{P}$ vs rotor speed $\boldsymbol{\Omega}$.

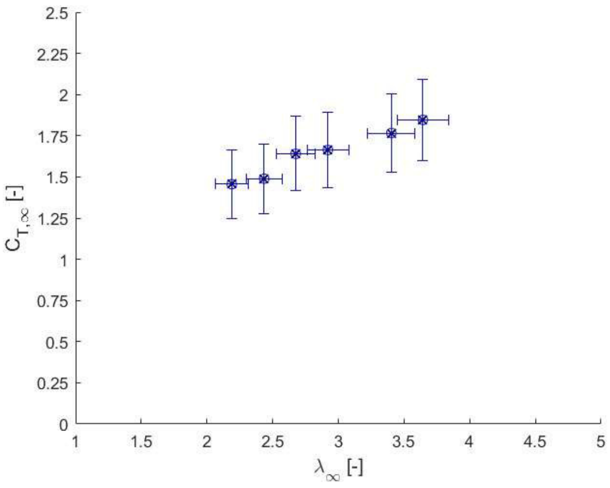

Fig. 1-12. Thrust coefficient $C_{T\infty}$ vs tip speed ratio λ_{∞}.

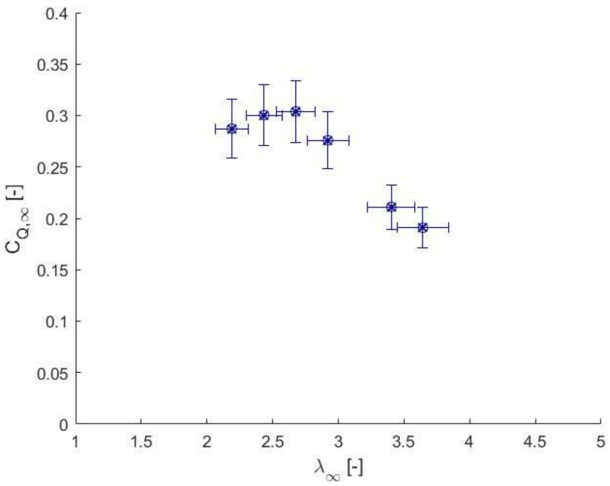

Fig. 1-13. Torque coefficient $C_{Q\infty}$ vs tip speed ratio λ_{∞}.

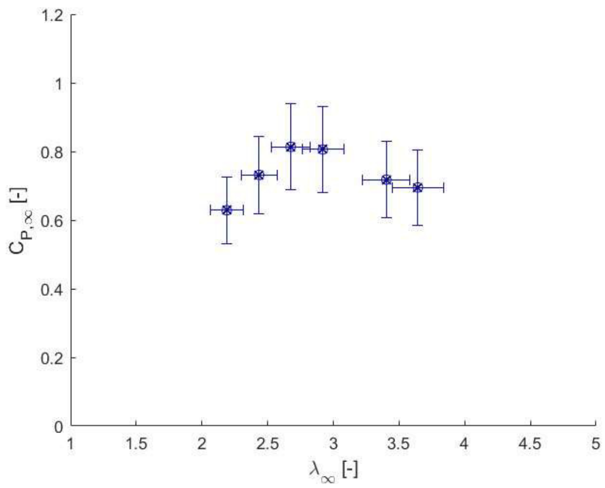

Fig. 1-14. Power coefficient $C_{P\infty}$ vs tip speed ratio λ_{∞}.

This solicitation can be eventually reduced by increasing the number of blades, according to Battisti et al. [31], but this would lead to a further increase in solidity. Another option may be the design of a Gorlov rotor, thus reducing most of the disadvantages of Darrieus rotors, i.e., self-starting issues, torque ripple, and reduced cavitation [32].

Different methods to evaluate torque fluctuations were previously published [29]. However, according to the works of Winchester and Quayle [30], Marsh et al. [33], and similarly to Shiono et al. [34], the maximum torque ripple factor *TRF* (1.3) was introduced as a parameter tracing the trend of the torque ripple phenomenon, i.e., the effect determined by pulsating lift forces on the blades, alternating from positive to negative values.

$$TRF = C_{Q,max} - C_{Q,min} \tag{1.3}$$

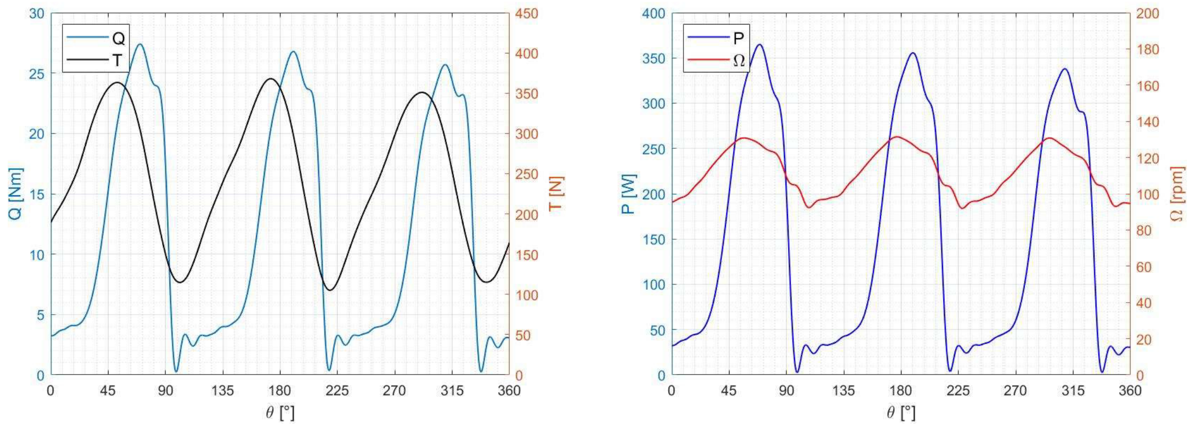

Fig. 1-15. (**Left**) Pulsating mechanical torque ***Q*** and axial thrust ***T*** data series over a revolution at a mean rotor speed ***Ω*** 110.2 rpm. (**Right**) Pulsating mechanical power ***P*** and rotor speed ***Ω*** over a complete revolution at a mean rotor speed ***Ω*** 110.2 rpm.

This experience shows that the *TRF* is maximum at the starting tip speed ratio, and a change in curvature is achieved at the optimum operating point ($\lambda_{\infty,opt}$ = 2.68), where the mean torque coefficient C_Q peaks. The *TRF* decreases as the rotor speed rises and fits well with the dynamic stall effect related to a drop in the lift force at low rotor speeds. Fig. 1-16 demonstrates that *TRF* reduces only at a high rotor speed and far from the optimality, where mechanical torque and power extracted drop significantly. The tests show excessive vibrations at the $\lambda_{\infty,opt}$, while at higher tip speed ratios, a reduction in these phenomena is demonstrated by the drop in *TRF*. Therefore, a different turbine design is justified to realize full-scale machines characterized by a lower turbine solidity, thus reducing the torque ripple phenomenon.

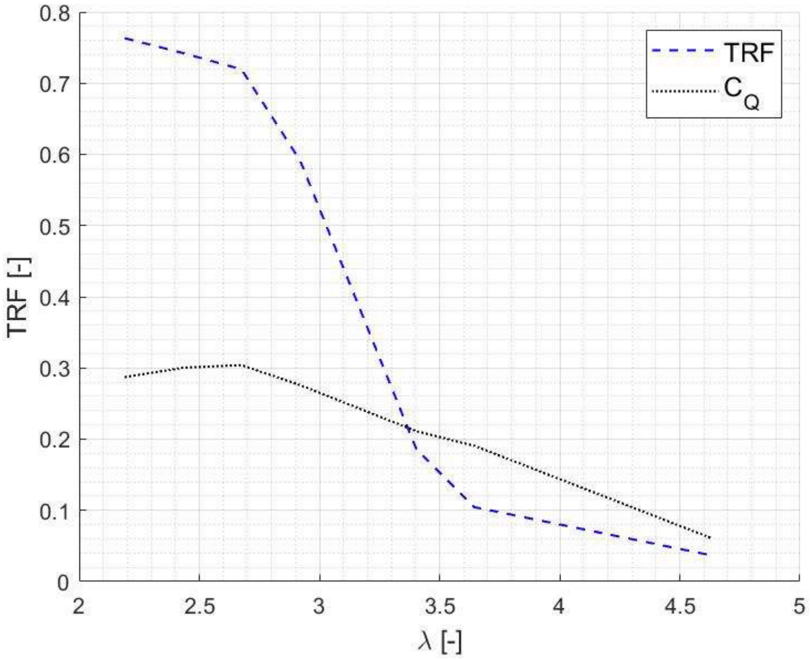

Fig. 1-16. Torque ripple factor ***TRF*** and mean value of the torque coefficient C_Q versus the tip speed ratio λ_∞.

Tips for turbine design optimization for improving this Darrieus prototype are retrieved from the literature. Investigating a straight blade rotor with a symmetrical NACA0018 hydrofoil, Brusca et al. [35] remarked that a vertical-axis rotor with a low aspect ratio has the advantage of higher power coefficient, structural advantages of a thicker blade and shorter chord, high stability from the great moment of inertia. Simulating vertical-axis rotors with aspect ratio $AR = H_T/D_T$ from $0.25 \leq AR \leq 3.0$, Zanforlin and DeLuca [36] highlighted the importance of *Re* and tip losses, highly affecting the power coefficient. The authors indicated that the effects of tip losses prevail on those of the chord *Re* for medium to large-size turbines, remarking that limiting tip losses is more convenient than increasing the chord-based Reynolds number. Therefore, longer blades with a high *AR* are desirable for large turbines. For smaller rotors and reduced flow speeds, the role played by *Re* arises, and the effects of tip losses seem to be balanced by the *Re*, showing that a change in *AR* does not determine a variation in the performance. In practice, turbines of an $AR \leq 0.8$ should be discarded to contain the effects of tip losses. Rezaeiha et al. [37] investigated the impact of rotor solidity and the number of blades on the optimal performance of VAWTs. A blade chord yielding a rotor solidity $0.09 \leq \sigma \leq 0.036$ was fixed for turbines with 2, 3, and 4 blades. An increase of σ determined a decline in the optimal tip speed ratio from high to low values in all turbines, increasing the performance due to higher *Re* and increasing the thrust coefficient asymptotically. The effect on turbine performance was absent by increasing σ at a constant *Re*. The rise in σ allowed an increased contribution of the upwind quartile to the total power production and a reduced contribution of the downwind quartile. Rezaeiha found that for a given σ, the smaller number of blades induces higher performance due to the high *Re*, thus increasing the maximum lift coefficient $C_{l,max}$ and reducing C_d. Therefore, there are various aspects to consider for the improvement of the fluid dynamics of the prototype.

An extensive assessment of this rotor, with predictions executed with a specific turbine model, is illustrated in Chapter 6. The rotor geometry is scaled for a theoretical array design in an artificial canal. The turbine aspect ratio varies between the alternatives, even though turbines are simulated with a lower rotor solidity, aiming to limit the main disadvantages. Although of great importance, the aspect of turbine design is treated in a limited manner in this work, as priority is given to the momentum model development.

References

[1] Cacciali L., Battisti L., Dell'Anna S., Soraperra G. Case Study of a Cross-Flow Hydrokinetic Turbine in a Narrow Prismatic Canal. Ocean Engineering **2021**, 234, 109281.

[2] Tanbhir Hoq Md., Nawshad U., Islam Md., Ibnea S., Syfullah K., Rahman R. Micro Hydro Power: Promising Solution for Off-grid Renewable Energy Source. International Journal of Scientific & Engineering Research **2011**, 2, 12, 1-5.

[3] Vermaak HJ., Kusakana K., Koko SP. Status of Micro-Hydrokinetic River Technology in Rural Applications: A review of Literature. Renewable and Sustainable Energy Reviews **2014**, 29, 625-633.

[4] Riglin J., Daskiran C., Jonas J., Schleicher WC., Oztekin A. Hydrokinetic Turbine Array Characteristics for River Applications and Spatially Restricted Flows. Renewable Energy **2016**, 97, 274-283.

[5] Riglin J., Carter F., Oblas N., Schleicher WC., Daskiran C., Oztekin A. Experimental and Numerical Characterization of a Full-Scale Portable Hydrokinetic Turbine Prototype for River Applications. Renewable Energy **2016**, 90, 772-783.

[6] Birjandi AH., Bibeau EL., Chatoorgoon V., Kumar A.. Power Measurement of Hydrokinetic Turbines with Free-Surface and Blockage Effect. Ocean Engineering **2013**, 69, 9-17.

[7] Bahaj AS., Molland AF., Chaplin JR., Batten WMJ. Power and Thrust Measurements of marine Current Turbines Under Various Hydrodynamic Flow Conditions in a Cavitation Tunnel and a Towing Tank. Renewable Energy **2007**, 32, 407-426.

[8] McAdam RA., Houlsby GT., Oldfield MLG. Experimental Measurements of the Hydrodynamic Performance and Structural Loading of the Transverse Horizontal Axis Water Turbine: Part 1. Renewable Energy **2013**, 59, 105-114.

[9] Ross H., Polagye B. An Experimental Evaluation of Blockage Effects on the Wake of a Cross-Flow Current Turbine. Journal of Ocean Engineering and Marine Energy **2020**, https://doi.org/10.1007/s40722-020-00172-w.

[10] Bachant P., Wosnik M. Performance Measurements of Cylindrical and Spherical-Helical Cross-Flow Marine Hydrokinetic turbines, with Estimates of Exergy Efficiency. Renewable Energy **2015**, 74, 318-325.

[11] Kirke B. Tests on Two Small Variable Pitch Cross Flow Hydrokinetic Turbines. Energy for Sustainable Development **2016**, 31, 185-193.

[12] Shimokawa K., Furukawa A., Okuma K., Matsushita D., Watanabe S. Experimental Study on Simplification of Darrieus-Type Hydro Turbine with Inlet Nozzle for Extra-Low Head Hydropower Utilization. Renewable Energy **2012**, 41, 376-382.

[13] Myers L., Bahaj AS. Wake Studies of a 1/30th Scale Horizontal Axis Marine Current Turbine. Ocean Engineering **2007**, 34, 758-762.

[14] Kirke B. Tests on Ducted and Bare Helical and Straight Blade Darrieus Hydrokinetic Turbines. Renewable Energy **2011**, 36, 3013-3022.

[15] Patel V., Eldho TI., Prabhu SV. Velocity and Performance Correction Methodology for Hydrokinetic Turbines Experimented with Different Geometry of the Channel. Renewable Energy **2019**, 131, 1300-1317.

[16] Anyi M., Kirke B. Evaluation of Small Axial Flow Hydrokinetic Turbines for Remote Communities. Energy for Sustainable Development **2010**, 14, 110–116.

[17] Mohanty L. Velocity Distribution in Trapezoidal Meandering Channel. Thesis of Master of Technology in Civil Engineering With Spec. in Water Resources Engineering, Department of Civil Engineering, National Institute of Technology **2013**, 64.

[18] Chiu C.L. Entropy and Probability Concepts in Hydraulics, Journal of Hydraulic Engineering **1987**, 113 (5), 583–59.

[19] Stosic B., Sacramento V., Filho M.C., Cantalice J.R.B., Singh V.P. Computational Approach to Improving the Efficiency of River Discharge Measurement, Journal of Hydrology **2016**, 21 (12), 212–22.

[20] Khuntia J.R., Devi K., Khatua KK. Prediction of Depth-Averaged Velocity in an Open Channel Flow. Applied Water Science **2018**, 8, 172.

[21] Chiu CL., Tung NC. Maximum Velocity and Regularities in Open-Channel Flow, Journal of Hydraulic Engineering **2002**, 128 (4), 390–39.

[22] Chiu CL., Said C.A.A. Maximum and Mean Velocities and Entropy in Open-Channel Flow, Journal of Hydraulic Engineering **1995**, 121 (1), 26–3.

[23] Chiu CL., Hsu SM. Probabilistic approach to modeling of velocity distributions in fluid flows, Journal of Hydraulic Engineering **2006**, 316 (1), 28–4.

[24] Farina G., Alvisi S., Franchini M., Moramarco T. Three Methods for Estimating the Entropy Parameter M Based on a Decreasing Number of Velocity Measurements in a River Cross-section, Entropy **2014**, 16, 2512–252.

[25] Chow VT. Open-channel Hydraulics. McGraw-Hill, New York (**1985**).

[26] Gunawan B., Neary V.S., Mortensen J., Roberts J.D. Assessing and Testing Hydrokinetic Turbine Performance and Effects on Open Channel Hydrodynamics: an Irrigation Canal Case Study. Albuquerque, USA: U.S Department of Energy (**2017**).

[27] Kirke B., Hydrokinetic and Ultra-low Head Turbines in Rivers: A Reality Check, Energy for Sustainable Development **2019**, 52, 1-10.

[28] McAdam RA., Houlsby GT., Oldfield MLG. Experimental measurements of the hydrodynamic performance and structural loading of the Transverse Horizontal Axis Water Turbine: Part 1. Renewable Energy **2013**, 59, 105-114.

[29] Reuter RC, Worstell MH. Torque Ripple in a Vertical Axis Turbine. Sandia Report SAND78-0577, Albuquerque, New Mexico (**1978**).

[30] Winchester J., Quayle S. Torque Ripple and Power in a Variable Pitch Vertical Axis Tidal Turbine. 9th European Wave and Tidal Energy Conference, Southampton, UK (**2011**).

[31] Battisti L., Persico G., Dossena V., Paradiso B., Raciti Castelli M., Brighenti A., Benini E. Experimental benchmark data for H-shaped and troposkien VAWT architectures. Renewable Energy **2018**, 125, 425-444.

[32] Espina-Valdés R., Gharib-Yosry A., Ferraiuolo R., Fernández-Jiménez A., Fernández-Pacheco V.M. Experimental Comparison between Hydrokinetic Turbines: Darrieus vs. Gorlov. Environmental Sciences Proceedings **2022**, 21, 26.

[33] Marsh P., Ranmuthugala D., Penesis I., Thomas G. Three-dimensional numerical simulations of straight-bladed vertical axis tidal turbines investigating power output, torque ripple and mounting forces. Renewable Energy **2015**, 83, 67-77.

[34] Shiono M., Katsuyuki S., Sezji K. Output Characteristics of Darrieus Water Turbine With Helical Blades For Tidal Current Generations. Proceedings of the Twelfth International Offshore and Polar Engineering Conference, Japan (**2002**).

[35] Brusca S., Lanzafame R., Messina M. Design of a Vertical-Axis Wind Turbine: How the Aspect ratio Affects the Turbine's Performance. International Journal of Energy and Environmental Engineering **2014**, 5, 333–340.

[36] Zanforlin S., DeLuca S. Effects of the Reynolds Number and the Tip Losses on the Optimal Aspect Ratio of Straight-Bladed Vertical Axis Wind Turbines. Energy **2018**, 148, 179-195.

[37] Rezaeiha A., Montazeri H., Blocken B. Towards Optimal Aerodynamic Design of Vertical Axis Wind Turbines: Impact of Solidity and Number of Blades. Energy **2018**, 165, 1129-1148.

NOMENCLATURE

A	Canal cross-section area m^2	R_h	Hydraulic radius m
A_T	Turbine swept area m^2	Re	Chord Reynolds number, $(\varrho{*}W{*}c/\mu)$
B_∞	Blockage ratio, (A_T/A_∞)	Re_f	Channel Reynolds number, $(\varrho{*}U_\infty{*}R_h/\mu)$
$C_{P,\infty}$	Power coefficient, $(P/(½{*}\varrho{*}A_T{*}U_\infty^3))$	S	Channel bed slope m/m
$C_{Q,\infty}$	Torque coefficient, $(Q/(½{*}\varrho{*}A_T{*}R_T{*}U_\infty^2))$	T	Axial thrust N
$C_{T,\infty}$	Thrust coefficient, $(T/(½{*}\varrho{*}A_T{*}U_\infty^2))$	t	Hydrofoil thickness m
C_d	Drag coefficient	U_∞	Undisturbed flow speed m/s
$C_{l,max}$	Maximum lift coefficient	u_x', u_y', u_z'	Velocity fluctuations m/s
c	Blade chord m	U_{max}	Maximum velocity of the flow m/s
D	Hydrostatic head m	W	Relative velocity m/s
D_h	Hydraulic depth m	w	Free surface width m
D_T	Turbine diameter m	y	Vertical coordinate
$F(u)$	Cumulative distribution of f(u)	$\phi(M)$	Velocity function, ref. Chiu & Hsu [23]
$f(u)$	Probability density of maximum velocity	Ω	Rotor speed rpm
Fr_∞	Froude number, $(U_\infty/(g{*}D_h)^{0.5})$	ϑ_p	Blade pitch offset deg
g	Gravity acceleration m/s^2	λ_∞	Tip speed ratio, $(\omega{*}R_T/U_\infty)$
H_T	Turbine height m	μ	Fluid dynamic viscosity
h	Water depth at u_{max} m	ξ	Isovel m/s
M	Entropy parameter, ref. Chiu & Hsu [23]	ρ	Fluid density
N_b	Blades number	σ	Rotor solidity, $(N{*}c/2R_T)$
n	Manning's coefficient $m^{-1/3}s$	ω	Angular velocity rad/s
P	Turbine power W		
Q	Rotor torque Nm	*Short forms*	
Q_c	Channel flow rate m^3/s	*HK*	Hydrokinetic
R_T	Turbine radius m	*TRF*	Torque ripple factor, $(C_{Q,max}-C_{Q,min})$

2. THE ACTUATOR DISC THEORY FOR OPEN CHANNEL FLOWS

Chapter adapted to the content of the article:

Cacciali L., Battisti L., Dell'Anna S. Free Surface Double Actuator Disc Theory and Double Multiple Streamtube Model for In-Stream Darrieus Hydrokinetic Turbines. Ocean Engineering 2022, 260, 112017. DOI: https://doi.org/10.1016/j.oceaneng.2022.112017.

The application of the Linear Momentum Actuator Disc Theory (LMADT) to propellers and turbines has a long tradition in the literature. Its classical development shows the conservation of momentum of a porous element immersed in an unbounded flow generating a wake due to boundary layer separation. A flow speed is induced through the disc due to the pressure drop from upstream to downstream, leaving the side current unaffected. Being formulated with the assumptions of inviscid and irrotational flow, it holds for ideal machines. Not surprisingly, a limit for mechanical power extraction under such conditions was found, namely the Lanchester-Betz-Joukowsky limit. Since the actuator disc extension [1] is included in a Double Multiple Streamtube model for open channel flows, the parameters influencing the loading and performance of an ideal machine are investigated, moving through the literature of wind and tidal energy converters. The use of an LMADT may seem anachronistic to the reader. Although the same idea swirled in the mind of the undersigned during the very first mathematical development, the choice of this method represents the strength of the whole work. A new feature consists of setting upstream and downstream boundaries of the control volume as unknowns. According to Cacciali et al. [1], the undisturbed cross-section is placed downstream of the viscous dissipation induced by the disruption of vorticity. This decision contrasts with what is shown by the application of actuator discs in the wind and tidal flows, whose undisturbed boundary is upstream. In subcritical flows, the backwater extending far upstream does not comply with the inviscid flow statement. Therefore, the double-disc extension interacts with the method developed for solving the hydraulic transition in Chapter 4. Moreover, by removing the dependence on the Froude number, the Rigid-Lid LMADT allows the assessment of ducted vertical-axis turbines for wind or water applications.

2.1. LMADT For Unconfined Flows

This theory was developed originally by Rankine [2] to estimate the performance of ideal propellers in adding energy to the flow. Once applied for energy extraction and after Froude's improvement [3], the axial induction factor a, i.e., the drop in the axial flow speed due to the disc-flow interaction, was introduced by Betz and Prandtl [4]. This parameter was defined by $a = (1\text{-}\alpha)$ with α the disc interference factor, i.e., the ratio of the induced velocity to the bulk flow speed at the upstream station U_∞.

Betz [5] obtained an expression for the maximum power coefficient for rotors deployed in an unconfined flow. A recent study [6] demonstrates that this theory was discovered initially by Lanchester in 1915 [6] and was also published independently by Joukowsky [8] in the same year as Betz did. The subdivision of the disc in a series of annuli was later added by Drewecki [9], introducing the chance of solving the momentum equation for a discretized rotor.

The extension of the theory accounting for the rotation was developed by Betz [10], and Glauert [11], [12] improved the Betz theory with the introduction of the tangential induction factor a', the definition of the power coefficient in terms of a, a', and the local tip speed ratio λ. Hütter [13] further improved the actuator disc theory by expressing both induction factors as a function of a single variable, the far wake velocity coefficient $\alpha_w = U_w/U$. The control volume of the flow involved in final development is shown in Fig. 2-1 from Hansen [13], with nomenclature modified according to the requirements of this work.

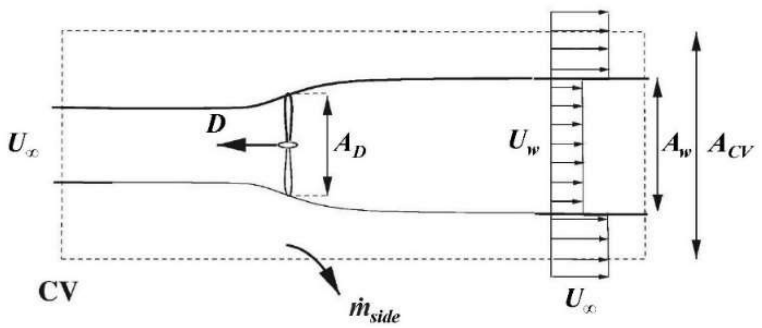

Fig. 2-1. LMADT control volume for unconfined turbine from [14].

Hence, the rotor is idealized as a drag device dissipating part of the energy of the incoming steady-state flow whose velocity is reduced as shown by streamlines diverging downstream. Since a pressure drop is applied at the disc section, a drag force is generated, and pressure recovers downstream. The wake is not rotating due to the irrotational flow assumption, even though this is corrected according to tangential induction factor a'. At low Mach numbers, the flow is incompressible and air density ρ is assumed constant. In addition, no internal energy variation is assumed from the inlet to the outlet, thus excluding mixing phenomena due to the inviscid flow assumption. Although its development is not illustrated algebraically in this work, the momentum conservation between stations {∞} and {w} allows the drag coefficient C_D to be a function of the axial induction factor a, i.e., $C_D = 4a{*}(1-a)$.

The drag coefficient in Fig. 2-2 peaks at unity and decreases for higher values of a. For $a > 0.5$, since $U_w = (1-2a){*}U_\infty$ due to mass conservation in the streamtube, the wake flow velocity becomes negative and invalidates the momentum theory. Indeed, if $a > 0.5$, a turbulent wake state occurs, according to Eggleston and Stoddard [15]. In this rotor state, an unstable shear flow occurs at the edge of the separated boundary layer due to a high jump in speed (U_∞-U_w), enclosing momentum from the outer flow into the wake [14].

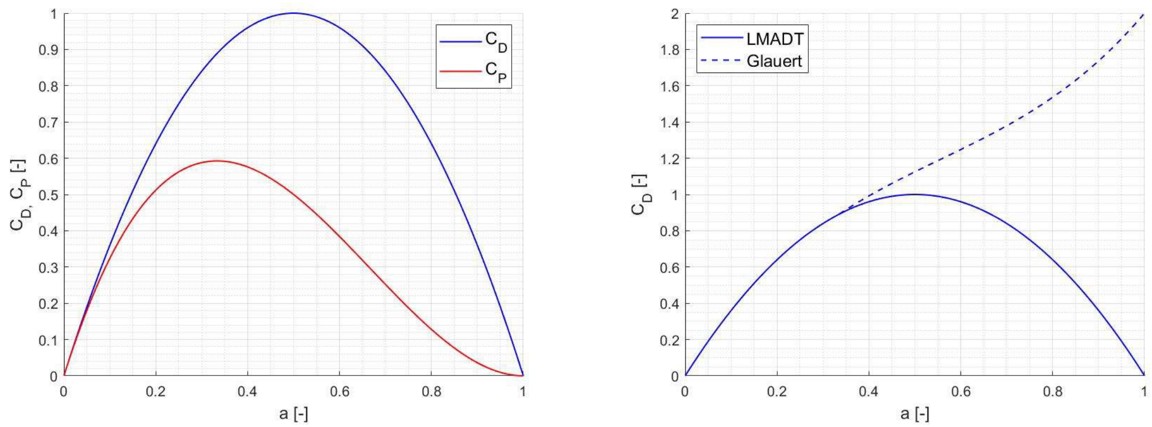

Fig. 2-2. (**Left**) LMADT solutions for drag coefficient C_D and power coefficient C_P vs the axial induction factor a. (**Right**) LMADT solutions and Glauert's correction for the drag coefficient C_D vs the axial induction factor a.

The performance is assessed with the power coefficient C_P, which is $C_P = 4a{*}(1-a)^2$. If differentiated on a, it yields the maximum ideal rotor performance of 16/27 for a = ⅓. It represents the Lanchester-Betz-Joukowky limit [6], i.e., the highest ratio of mechanical power theoretically attainable to the available kinetic power $P = ½{*}\rho{*}A_D{*}U_\infty^3$.

Experimental investigations demonstrated that the C_D equation is valid for values lower than ⅓ [14], and thus a correction is mandatory to predict the measurements at a high axial induction factor. Fig. 2-3 shows the implementation of Glauert's empirical correction for heavily loaded rotors [14], according to the following statements. F represents Prandtl's tip loss factor correcting the actuator disc assumption of an infinite number of blades. In Fig. 2-2, the curves are plotted with $F = 1$.

Lapin's representation of two unbounded porous discs [16] led to the computation of two induced velocities, approximating the interaction of the upstream and downstream blade pass into the flow during the rotation. Similar work was executed by Loth and McCoy [17], who developed a cosine-type velocity interference distribution on two semicylindrical actuators in series. Similarly, Newman [18] investigated the maximum power coefficient achieved by two discs in tandem, achieving 16/25, in contrast to the single-disc Betz limit of 16/27 [19].

By performing tests with two porous plates, Newman's smoke tunnel tests [19] in Fig. 2-3 demonstrated an agreement of the drag coefficient for disc spacings higher than 0.5 diameters. With lower spacings, the model becomes inaccurate due to the curvature of streamlines at the disc and lack of flow uniformity.

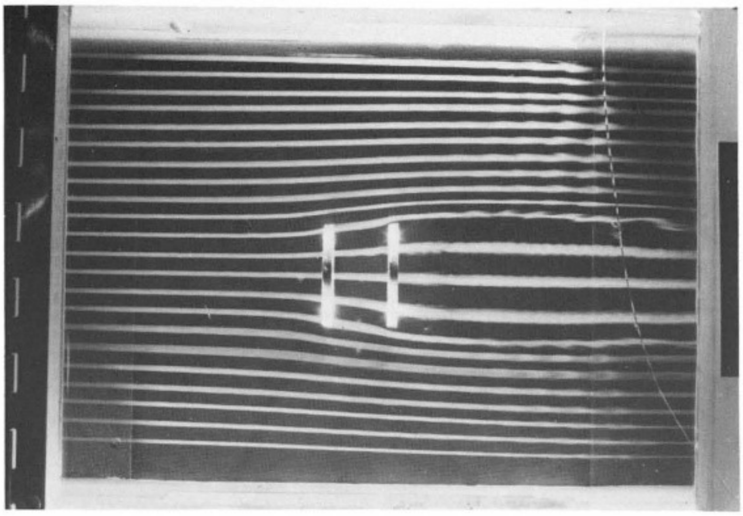

Fig. 2-3. Newman's smoke tunnel test for double-disc spacing/diameter of 0.66 [18].

2.2. LMADT For Confined Flows

In the past, blockage problems were solved with semi-empirical formulae correcting the dimensionless coefficients of the turbines tested in wind tunnels. Glauert [20] developed a model accounting for wind tunnel wall interference by modifying the thrust coefficient of a machine operating with a high axial induction factor. Maskell [21] published a method for bluff bodies in confined flows based on experimental evidence to improve the prediction of the thrust coefficient. Other works aimed to remove the effects of blockage by taking advantage of the actuator disc theory. Barnsley and Wellicome [22] implemented a procedure predicting the thrust coefficient by iterating the ratio of the bypass to core interference factors. Later, Mikkelsen and Sørensen [23] developed a correction based on the wake expansion numerical computation. Finally, Werle [24] corrected blocked wind turbines, illustrating the parametric conditions for the maximum extracted power and contemplating the viscous pressure drop related to the downwind flow mixing.

Although limited experimental validation is present in the literature, these corrections have been used for years to remove the blockage ratio and achieve the performance corresponding to an equivalent unconfined flow. A recent work involving the mentioned methods for wind and water applications was published by Ross and Polagye [25], who demonstrated better results with thrust force correction than power. The authors pointed out that there is no guarantee that these corrections give satisfactory results for an arbitrary test condition.

The development of the actuator disc theory with blockage for hydrokinetics was widely studied from the work of Garrett and Cummins [26] onwards. Notice that the roots of the Garrett and Cummins equation (2.22) are numerically equivalent to Mikkelsen and Sørensen's for wind tunnels. However, the Rigid Lid Actuator Disc Theory (i.e., built with a fixed free surface) demonstrated better results for turbine installation at greater depths. Afterward, Whelan's extension [27] included the Froude number to account for the free surface deformation in shallow water applications. An improvement with two discs was proposed already by Draper and Nishino [28]. Their development helped predict optimal turbine arrangements in tidal channels with centered and staggered configurations, besides the difficulty of extrapolating a realistic flow condition, as stated by Bonar et al. [29].

2.3. Double Actuator Disc Algebraic Development

The purpose of extended LMADT is not just to determine the analytical performance of ideal machines in canals. According to Cacciali et al. [1], the double-disc extension aims to solve numerically a Double Multiple Streamtube code, iterated with the additional inflow correction presented in Chapter 4. Although the extension for cross-flow rotors also applies to tidal applications, this is not investigated further in this work.

This chapter illustrates only the core equations of the Double Multiple Streamtube models presented in Chapter 3 and elaborated for turbine arrays in Chapter 5. This chapter shows the full algebraic development of Free Surface LMADT and Rigid Lid LMADT, unlike the abbreviated treatment depicted in the paper.

2.3.1. Free Surface LMADT

Whelan's model [27] simulates the drag force of a single porous disc spanning over the channel width. The drag simulation agrees with measurements, while the predicted free surface drop is aligned with the prediction of perforated plate tests for blockage ratios up to 0.5, according to Pelz et al. [30]. Whelan's actuator disc theory is extended hereafter to account for an additional porous element representing the downstream blade interaction with the flow. This extension still represents a quasi-1-D model, as it processes only axial flow speeds and axial forces. Geometry and pressure scalar data are related to the Free Surface scheme in Fig. 2-4.

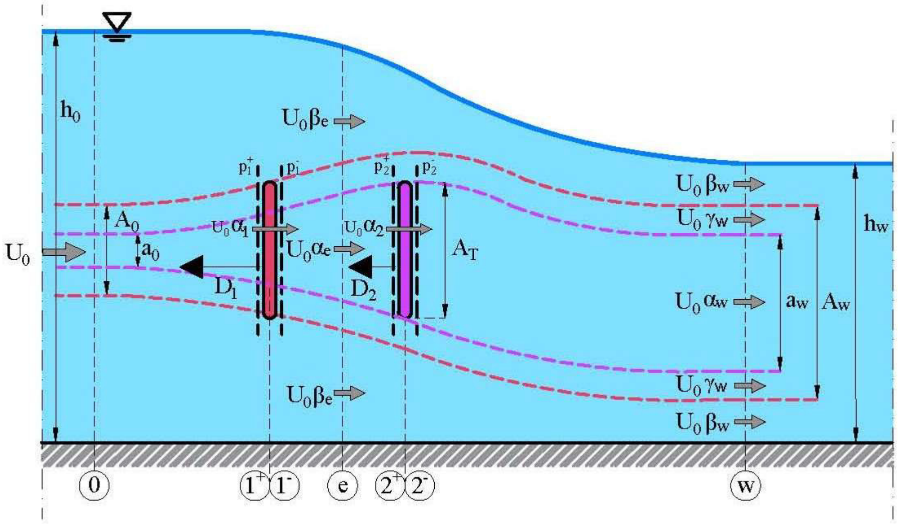

Fig. 2-4. Free Surface scheme for the double-disc LMADT.

Consider a channel flow with negligible wall friction and a series of two porous discs positioned a short distance apart. Upstream of the rotor, inflow depth and flow speed vary according to the axial thrust exerted by the turbine, and a pressure equilibrium is established at the stations {0}, {e}, and {w}, so that depths h_0, h_e, and h_w can be specified in the control volume. Notice that {e} represents the depth achieved by modeling the wake of a single-disc. Since a single-disc must be solved first to solve the double-disc, the station {e} is mandatory for computational purposes, as stated by Draper and Nishino [28]. The momentum conservation over the entire free surface variation {0-w} should account for static and dynamic contributions, implying the streamtube deformation due to gravity.

The static pressure immediately upstream and downstream of each disc can be inferred from the stream filament theory whether constant interference factors are assumed. It is the sine qua non-condition for solving the velocity triangles of a blade when combining momentum and blade element theories. Diversely, a DMS model would become inapplicable.

Moreover, the streamtube deflection of $\Delta h/2$ for a plate deployed above half depth of a channel, as shown by Schmitz et al. [31], cannot be included in solving a DMS model. However, another approach to account for the turbine installation depth is presented. The assumptions for the Actuator Disc Theory account for an infinite number of blades, a non-rotating wake, steady inviscid flow, incompressible fluid homogeneously distributed over the channel cross-sectional area, and pressure equilibrium between each station. A dissipative drag force proportional to the static pressure drop is achieved at each disc.

The sketch indicates A_0 and a_0 for the upstream wake, A_T for the disc/turbine, A_e and a_e for the equilibrium station, A_w, and a_w for the near-wake. The stations are in sequence, and all dimensionless interference factors are scaled to the flow speed U_0, unlike the work of Draper and Nishino [27]. These factors are formulated as the local velocity divided by the upstream flow speed, i.e., $\alpha_1 = U_1/U_0$, $\alpha_2 = U_2/U_0$, $\alpha_e = U_e/U_0$, $\alpha_w = U_w/U_0$, $\gamma_w = U\gamma/U_0$, $\beta_e = U_{be}/U_0$, and $\beta_w = U_{bw}/U_0$ for discs, wakes, annulus flow, and bypass flows, respectively. Blockage ratio and Froude number are defined respective to the station {0} as well, in line with the notation of the interference factors, i.e., $B = A_T/(w{*}h_0)$ and $Fr = U_0/(g{*}h_0)^{½}$.

The distance between the two discs is assumed small enough to prevent flows from mixing, but sufficient to ensure the pressure equalization at station {e}. Therefore, while the bypass and annular flows accelerate from {e} to {w} (from β_e to β_W and from α_e to γ_W), the core flow of the streamtube decelerates (from α_e to α_W). The acceleration of the annular flow implies a contraction between {e} and {w}, consistent with the wake deformation previously indicated, although not visible in the image.

Upstream and downstream static pressure is denoted by p_0 and p_w, respectively, while p_e represents the pressure at the equilibrium between single-disc and double-disc schemes. These correspond to depths h_0, h_e, and h_w in the free surface LMADT. Each drag force D_1 and D_2 (with $D_2 < D_1$) relates to the corresponding interference factors α_1 and α_2. Henceforth, free-surface LMADT model is developed.

a) Upstream disc

The control volumes between stations {0-e} are deduced from Fig. 2-4. Continuity equations (C1.1-C1.2) are written for the core streamtube, while (C1.3) is related to the bypass flow control volume. Bernoulli's equations (B1.1-B1.2) are defined for upstream and downstream, while B1.3 is attained for the bypass flow. The momentum equations (M1.1-M1.2) account for gravity acceleration. Notice that the disc pressure drop Δp_1 in equation (2.1) represents the output of the energy conservation between the upstream {0} and downstream {e} boundaries of the streamtube. Δp_1 is achieved by combining (B1.1), (B1.2), and (B1.3). In turn, the axial drag force (2.2) is determined from (M1.1) and (1). The definition of the drag coefficient (2.3) is straightforward.

Continuity

$$A_0 = A_T\alpha_1 \tag{C1.1}$$

$$A_T\alpha_1 = A_e\alpha_e \tag{C1.2}$$

$$(wh_0 - A_0) = \beta_e(wh_e - A_e) \tag{C1.3}$$

Bernoulli

$$p_0 + \rho\frac{U_0{}^2}{2} = p_1{}^+ + \rho\frac{U_0{}^2\alpha_1{}^2}{2} \tag{B1.1}$$

$$p_1{}^- + \rho\frac{U_0{}^2\alpha_1{}^2}{2} = p_e + \rho\frac{U_0{}^2\alpha_e{}^2}{2} \tag{B1.2}$$

$$p_0 + \rho\frac{U_0{}^2}{2} = p_e + \rho\frac{U_0{}^2\beta_e{}^2}{2} \tag{B1.3}$$

Momentum

$$D_1 = \Delta p_1 A_T \tag{M1.1}$$

$$\rho U_0{}^2A_e(\beta_e{}^2 - \alpha_e{}^2) + \rho U_0{}^2wh_0 - \rho U_0{}^2\beta_e{}^2wh_e + \tfrac{1}{2}\rho gw(h_0{}^2 - h_e{}^2) = D_1 \tag{M1.2}$$

A_0 and A_e (2.4-2.5) are due to the mass conservation at the streamtube control volume. The wake hydrostatic pressure h_e (2.6) is derived from the (B1.3), after substituting h_0 with $U_0{}^2/(g{*}Fr^2)$, attained by reversing the definition of the Froude number. The disc interference factor α_1 as a function of B and Fr in (2.7) is the outcome of continuity at the bypass control volume (C1.3) if A_0, A_e, and h_e are substituted by the right-hand side of (2.4-2.6). Similar definitions were derived by Whelan et al. [27] and Vogel et al. [32].

Introducing the blockage ratio and (2.3-2.7) into the momentum (M1.2), one achieves a quartic polynomial, which unknowns are α_e and β_e. For simplicity, Whelan's equation is implemented instead (2.8). This is a function of the parameters written relative to the upstream station i.e., B, Fr, and implicitly, C_{D1}.

$$\Delta p_1 = \rho \frac{U_0^2}{2}\left({\beta_e}^2 - {\alpha_e}^2\right) \tag{2.1}$$

$$D_1 = \frac{1}{2}\rho A_T {U_0}^2\left({\beta_e}^2 - {\alpha_e}^2\right) \tag{2.2}$$

$$C_{D1} = \left({\beta_e}^2 - {\alpha_e}^2\right) \tag{2.3}$$

$$A_0 = \alpha_1 A_T \tag{2.4}$$

$$A_e = \frac{\alpha_1}{\alpha_e} A_T \tag{2.5}$$

$$h_e = h_0\left[1 - \frac{Fr^2}{2}\left({\beta_e}^2 - 1\right)\right] \tag{2.6}$$

$$\alpha_1 = \frac{\alpha_e\left\{\beta_e\left[1 - \frac{Fr^2}{2}\left({\beta_e}^2 - 1\right)\right] - 1\right\}}{B(\beta_e - \alpha_e)} \tag{2.7}$$

$$Fr^2{\beta_e}^4 + 4\alpha_e Fr^2{\beta_e}^3 + (4B - 4 - 2Fr^2){\beta_e}^2 + (8 - 8\alpha_e - 4Fr^2\alpha_e)\beta_e + (8\alpha_e - 4 + Fr^2 - 4{\alpha_e}^2 B) = 0 \tag{2.8}$$

b) Upstream and downstream discs in tandem

Once the upstream actuator disc is solved, the terms A_0, A_e, α_1, α_e, β_e, and C_{D1} are known. Continuity, Bernoulli, and momentum equations of the entire system are derived. Additional equations are reserved for the annulus flow delimiting the downstream disc (C2.4), and (B2.4), while the bypass flow further accelerates from β_e to β_w. The annular flow also accelerates from α_e to γ_w, thus justifying its slight contraction.

Continuity

$$\alpha_e a_e = \alpha_2 A_T \tag{C2.1}$$

$$\alpha_2 A_T = \alpha_w a_w \tag{C2.2}$$

$$(wh_0 - A_0) = \beta_w(wh_w - A_w) \tag{C2.3}$$

$$\alpha_e(A_e - a_e) = \gamma_w(A_w - a_w) \tag{C2.4}$$

Bernoulli

$$p_e + \rho\frac{{U_0}^2{\alpha_e}^2}{2} = {p_2}^+ + \rho\frac{{U_0}^2{\alpha_2}^2}{2} \tag{B2.1}$$

$${p_2}^- + \rho\frac{{U_0}^2{\alpha_2}^2}{2} = p_w + \rho\frac{{U_0}^2{\alpha_w}^2}{2} \tag{B2.2}$$

$$p_0 + \rho\frac{{U_0}^2}{2} = p_w + \rho\frac{{U_0}^2{\beta_w}^2}{2} \qquad \text{(B2.3)}$$

$$p_e + \rho\frac{{U_0}^2{\alpha_e}^2}{2} = p_w + \rho\frac{{U_0}^2{\gamma_w}^2}{2} \qquad \text{(B2.4)}$$

Momentum

$$D_2 = \Delta p_2 A_T \qquad \text{(M2.1)}$$

$$\rho {U_0}^2 w h_0 - \rho {U_0}^2 {\beta_w}^2 (w h_w - A_w) - \rho {U_0}^2 {\gamma_w}^2 (A_w - a_w) - \rho {U_0}^2 {\alpha_w}^2 a_w + \frac{1}{2}\rho g w\left({h_0}^2 - {h_w}^2\right) = D_1 + D_2 \qquad \text{(M2.2)}$$

The equality of equations (B2.3) and (B2.4) is used to solve for β_w (2.9). Hence, β_w^2 is substituted into (2.10) to obtain the pressure drop at the downstream disc. Coherently to the previous disc analysis, the right-hand side of the pressure drop (2.10) is implemented into the momentum equation (M2.1), yielding the drag force (2.11) and the drag coefficient (2.12). A_w, a_e, and a_w (2.13-2.15) are due to the mass conservation applied to the streamtube control volume. Notice that (2.13) is needed only to define A_w (2.15). Downstream depth h_w in (2.16) is derived as a function of the upstream depth h_0 from Bernoulli's equation (B2.3) if in a specific energy form.

The development of (M2.2) with equations (2.9, 2.14-2.16, and 2.17) gives the final double-disc statement (2.18) in two unknowns, i.e., γ_w and α_w. Once γ_w and α_w are solved with the method proposed in Section 3, β_w is determined from the equation (2.9), and finally, the disc interference factor α_2 is calculated. The polynomial (2.18) is convenient to easily derive the Rigid Lid LMADT, as illustrated in the next section.

$$\beta_w = \sqrt{{\gamma_w}^2 + {\beta_e}^2 - {\alpha_e}^2} \qquad \text{(2.9)}$$

$$\Delta p_2 = \rho\frac{{U_0}^2}{2}\left({\beta_w}^2 - {\beta_e}^2 + {\alpha_e}^2 - {\alpha_w}^2\right) = \rho\frac{{U_0}^2}{2}\left({\gamma_w}^2 - {\alpha_w}^2\right) \qquad \text{(2.10)}$$

$$D_2 = \frac{1}{2}\rho A_T {U_0}^2\left({\gamma_w}^2 - {\alpha_w}^2\right) \qquad \text{(2.11)}$$

$$C_{D2} = \left({\gamma_w}^2 - {\alpha_w}^2\right) \qquad \text{(2.12)}$$

$$a_e = \frac{\alpha_2}{\alpha_e}A_T \qquad \text{(2.13)}$$

$$a_w = \frac{\alpha_2}{\alpha_w}A_T \qquad \text{(2.14)}$$

$$A_w = \frac{A_T}{\gamma_w}\left[\alpha_1 + \frac{\alpha_2(\gamma_w - \alpha_w)}{\alpha_w}\right] \quad (2.15)$$

$$h_w = h_0\left[1 - \frac{Fr^2}{2}\left({\beta_w}^2 - 1\right)\right] \quad (2.16)$$

The terms A_0, A_w, and h_w are replaced into the bypass continuity (C2.3) from equations (C1.1), (2.15), and (2.16), respectively.

$$wh_0 - \alpha_1 A_T = \beta_w w h_0\left[1 - \frac{Fr^2}{2}\left({\beta_w}^2 - 1\right)\right] - \frac{\alpha_1\beta_w}{\gamma_w}A_T - \frac{\alpha_2\beta_w}{\alpha_w\gamma_w}(\gamma_w - \alpha_w)A_T$$

After collecting α_1 at the right-hand side, the blockage ratio appears by dividing the left and right-hand sides by the product $w{*}h_0$, i.e.,

$$\frac{\alpha_2(\gamma_w - \alpha_w)\beta_w}{\alpha_w\gamma_w}B = \beta_w\left[1 - \frac{Fr^2}{2}\left({\beta_w}^2 - 1\right)\right] - 1 - \alpha_1 B\left(\frac{\beta_w}{\gamma_w} - 1\right)$$

Hence, the output of the mass conservation applied at the bypass control volume gives the new disc interference factor α_2 (2.17). Since the downstream disc interference factor can be calculated only after having solved a system built with the final LMADT equation, the local C_{D1}, and equation (2.9), α_2 is allowed to be a function of β_w, γ_w, and α_w.

$$\alpha_2 = \frac{\alpha_w\gamma_w\left\{\beta_w\left[1 - \frac{Fr^2}{2}\left({\beta_w}^2 - 1\right)\right] - 1 - B\frac{\alpha_1}{\gamma_w}(\beta_w - \gamma_w)\right\}}{B(\gamma_w - \alpha_w)\beta_w} \quad (2.17)$$

However, α_2 can be expressed as a function of α_w and γ_w to allow the LMADT derivation. Thus, (2.17) is further manipulated by replacing directly β_w with equation (2.9). Conveniently, C_{D1} is used instead of $({\beta_e}^2 - {\alpha_e}^2)$.

$$\alpha_2 = \frac{\alpha_w\gamma_w\left\{\sqrt{{\gamma_w}^2 + C_{D1}}\left[1 - \frac{Fr^2}{2}\left({\gamma_w}^2 + C_{D1} - 1\right)\right] - 1 - B\frac{\alpha_1}{\gamma_w}\left(\sqrt{{\gamma_w}^2 + C_{D1}} - \gamma_w\right)\right\}}{B(\gamma_w - \alpha_w)\sqrt{{\gamma_w}^2 + C_{D1}}} \quad (*)$$

Combining the momentum conservation (M2.2) with equations (2.14), (2.15), and (2.16), gives:

$$-\rho w h_0 {U_0}^2({\beta_w}^2-1)+\rho w h_0 {U_0}^2\frac{Fr^2}{2}{\beta_w}^2({\beta_w}^2-1)+\rho A_T {U_0}^2\frac{\alpha_1}{\gamma_w}({\beta_w}^2-{\gamma_w}^2)+\rho A_T {U_0}^2\frac{\alpha_2}{\alpha_w\gamma_w}(\gamma_w-\alpha_w)({\beta_w}^2-{\gamma_w}^2)+\rho A_T {U_0}^2\frac{\alpha_2}{\alpha_w}({\gamma_w}^2-{\alpha_w}^2)+\frac{1}{2}\rho w h_0 {U_0}^2\frac{1}{Fr^2}-\frac{1}{2}\rho w h_0 {U_0}^2\frac{1}{Fr^2}\left[1-\frac{Fr^2}{2}({\beta_w}^2-1)\right]^2=D_1+D_2$$

Dividing the left and right-hand sides by the upstream dynamic pressure force ($\frac{1}{2}*\rho*w*h_0*U_0^2$), the sum $B*(C_{D1}+C_{D2})$ is achieved at the right-hand side. Replacing ($A_T/(w*h_0)$) with the blockage ratio B, and collecting the α_2 terms with a slight manipulation, yields:

$$-2({\beta_w}^2-1)+Fr^2{\beta_w}^2({\beta_w}^2-1)+2B\frac{\alpha_1}{\gamma_w}({\beta_w}^2-{\gamma_w}^2)+2B\frac{\alpha_2}{\alpha_w\gamma_w}(\gamma_w-\alpha_w)({\beta_w}^2+\alpha_w\gamma_w)+\frac{1}{Fr^2}-\frac{1}{Fr^2}\left[1+\frac{Fr^4}{4}({\beta_w}^2-1)^2-Fr^2({\beta_w}^2-1)\right]=BC_{D1}+BC_{D2}$$

By substituting C_{D2} with the definition (2.12), thus collecting ($1/Fr^2$) and ordering all terms according to the following order, gives:

$$-({\beta_w}^2-1)+Fr^2{\beta_w}^2({\beta_w}^2-1)-\frac{Fr^2}{4}({\beta_w}^2-1)^2-BC_{D1}-B({\gamma_w}^2-{\alpha_w}^2)+2B\frac{\alpha_1}{\gamma_w}({\beta_w}^2-{\gamma_w}^2)+2B\frac{\alpha_2}{\alpha_w\gamma_w}(\gamma_w-\alpha_w)({\beta_w}^2+\alpha_w\gamma_w)=0$$

Further collecting the terms multiplied by the Froude number,

$$-({\beta_w}^2-1)+Fr^2({\beta_w}^2-1)\left[{\beta_w}^2-\frac{({\beta_w}^2-1)}{4}\right]-BC_{D1}-B({\gamma_w}^2-{\alpha_w}^2)+2B\frac{\alpha_1}{\gamma_w}({\beta_w}^2-{\gamma_w}^2)+2B\frac{\alpha_2}{\alpha_w\gamma_w}(\gamma_w-\alpha_w)({\beta_w}^2+\alpha_w\gamma_w)=0$$

Applying the lowest common denominator to the terms within square brackets and carefully substituting β_w with the equation (2.9) while using C_{D1} instead of $(\beta_e^2-\alpha_e^2)$ for convenience, the following algebraic building blocks are obtained:

- $\frac{Fr^2}{4}\left(\beta_w{}^2-1\right)\left(3\beta_w{}^2+1\right)=\frac{Fr^2}{4}(\gamma_w{}^2+C_{D1}-1)(3\gamma_w{}^2+3C_{D1}+1)$

- $1+B\alpha_w{}^2$

- $\beta_w{}^2-BC_{D1}-\gamma_w{}^2=-(1+B)(\gamma_w{}^2+C_{D1})$

- $2B\frac{\alpha_1}{\gamma_w}\left(\beta_w{}^2-\gamma_w{}^2\right)=2B\frac{\alpha_1}{\gamma_w}C_{D1}$

In the last algebraic component, α_2 is replaced by the equation (*),

- $2B\frac{\alpha_2}{\alpha_w\gamma_w}(\gamma_w-\alpha_w)\left(\beta_w{}^2+\alpha_w\gamma_w\right)=\frac{2(\gamma_w{}^2+C_{D1}+\alpha_w\gamma_w)\left\{\sqrt{\gamma_w{}^2+C_{D1}}\left[1-\frac{Fr^2}{2}(\gamma_w{}^2+C_{D1}-1)\right]-1-B\frac{\alpha_1}{\gamma_w}\left(\sqrt{\gamma_w{}^2+C_{D1}}-\gamma_w\right)\right\}}{\sqrt{\gamma_w{}^2+C_{D1}}}$

These terms are arranged to ensure the construction of an equation with a similar appearance for Free Surface and Rigid Lid models. Therefore, the final double-disc statement (2.18) in two unknowns, i.e., α_w and γ_w, is achieved.

$$\frac{Fr^2}{4}(\gamma_w{}^2+C_{D1}-1)(3\gamma_w{}^2+3C_{D1}+1)+(1+B\alpha_w{}^2)-(1+B)(\gamma_w{}^2+C_{D1})+2B\frac{\alpha_1}{\gamma_w}C_{D1}+\frac{2(\gamma_w{}^2+C_{D1}+\alpha_w\gamma_w)\left\{\sqrt{\gamma_w{}^2+C_{D1}}\left[1-\frac{Fr^2}{2}(\gamma_w{}^2+C_{D1}-1)\right]-1-B\frac{\alpha_1}{\gamma_w}\left(\sqrt{\gamma_w{}^2+C_{D1}}-\gamma_w\right)\right\}}{\sqrt{\gamma_w{}^2+C_{D1}}}=0 \tag{2.18}$$

2.3.2. Rigid lid LMADT

Even though the double-disc Rigid Lid equations are achieved by setting $Fr = 0$ in (2.17) and (2.18) as shown in [1], the complete development is illustrated. It is valid for cross-flow turbines under an almost flat free surface in deep water (as an approximation) or for vertical-axis turbines in water and wind tunnels.

In this model, static pressure p is used instead of hydrostatic pressure. As in the previous model, since a pressure drop is created by the porous disc exerting a drag force and dissipating energy, the static pressure is not recovered downstream ($p_0 < p_w$). The bypass flow is accelerated as the flow passage becomes more constricted by the wake expansion.

All equations of the Free Surface scheme hold, except (C1.3) and (M1.2) for the single-disc and (C2.3) and (M2.2) for the double-disc, substituted by their variant with (v) indicated below. Since water depth does not vary, the dimension w represents an area per unit width or depth. Even though the scheme in Fig. 2-5 shows the channel area per unit depth, it holds for the areal assessments. In addition, equations (6) and (16) lead to the result $h_w = h_0$.

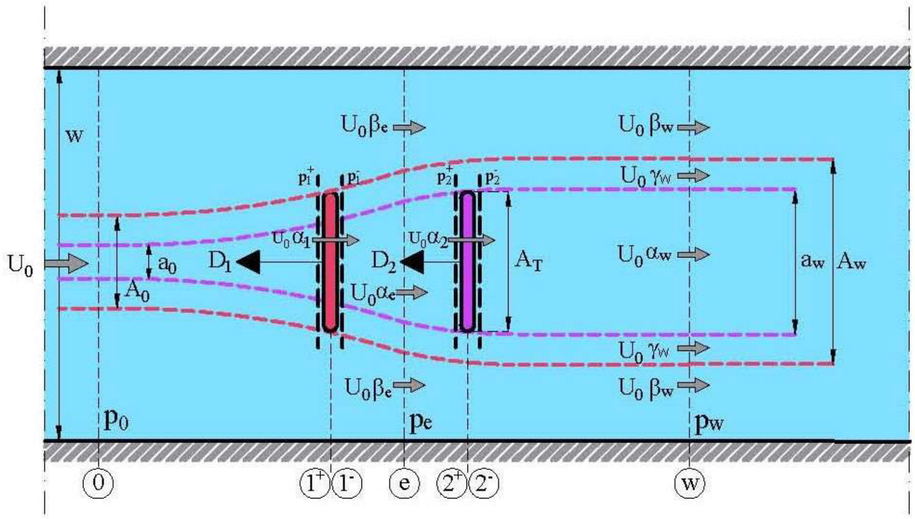

Fig. 2-5. Rigid Lid scheme for the double-disc LMADT.

<u>Continuity</u>

$$(w - A_0) = \beta_e(w - A_e) \quad \text{(C1.3v)}$$

$$(w - A_0) = \beta_w(w - A_w) \quad \text{(C2.3v)}$$

<u>Momentum</u>

$$\rho U_0{}^2 A_e(\beta_e{}^2 - \alpha_e{}^2) - \rho U_0{}^2 w(\beta_e{}^2 - 1) + w(p_0 - p_e) = D_1 \quad \text{(M1.2v)}$$

$$\rho U_0{}^2 A_w(\beta_w{}^2 - \gamma_w{}^2) + \rho U_0{}^2 a_w(\gamma_w{}^2 - \alpha_w{}^2) - \rho U_0{}^2 w(\beta_w{}^2 - 1) + w(p_0 - p_w) = D_1 + D_2 \quad \text{(M2.2v)}$$

---

a) Upstream disc

Since straightforward, the single-disc algebraic development is omitted. Following the previous steps from the bypass continuity equation (C1.3v), the first interference factor is easily derived in equation (2.19). A similar result was achieved by Draper and Nishino [28]. The momentum equation (M1.2v) is developed in the same manner as before, achieving the same quadratic polynomial in (2.20) published by Garrett and Cummins [26].

$$\alpha_1 = \frac{\alpha_e(\beta_e - 1)}{B(\beta_e - \alpha_e)} \tag{2.19}$$

$$\beta_e^{\,2}(1 - B) - 2\beta_e(1 - \alpha_e) + 1 - 2\alpha_e + B\alpha_e^{\,2} = 0 \tag{2.20}$$

b) Upstream and downstream discs in tandem

The terms A_0 and A_w are replaced in the bypass continuity (C2.3v) by the equations (C1.1) and (2.15).

$$w - \alpha_1 A_T = \beta_w w - \frac{\alpha_1 \beta_w}{\gamma_w} A_T - \frac{\alpha_2 \beta_w}{\alpha_w \gamma_w}(\gamma_w - \alpha_w) A_T$$

After collecting α_1 at the right-hand side, the blockage ratio appears by dividing the left and right-hand sides by w, i.e.,

$$\frac{\alpha_2(\gamma_w - \alpha_w)\beta_w}{\alpha_w \gamma_w} B = \beta_w - 1 - \alpha_1 B\left(\frac{\beta_w}{\gamma_w} - 1\right)$$

Therefore, the new disc interference factor α_2 is achieved in equation (2.21) as a function of β_w, γ_w, and α_w, according to the previous algebraic development.

$$\alpha_2 = \frac{\alpha_w \gamma_w \left\{\beta_w - 1 - B\frac{\alpha_1}{\gamma_w}(\beta_w - \gamma_w)\right\}}{B(\gamma_w - \alpha_w)\beta_w} \tag{2.21}$$

The interference factor α_2 is allowed to be a function of α_w and γ_w in (#) for the next LMADT derivation:

$$\alpha_2 = \frac{\alpha_w\gamma_w\left\{\sqrt{\gamma_w{}^2+C_{D1}}-1-B\frac{\alpha_1}{\gamma_w}\left(\sqrt{\gamma_w{}^2+C_{D1}}-\gamma_w\right)\right\}}{B(\gamma_w-\alpha_w)\sqrt{\gamma_w{}^2+C_{D1}}} \qquad (\#)$$

The development of (M2.2v) with equations (2.14), (2.15), and the Bernoulli equation (B2.3) gives:

$$-\rho w U_0{}^2\left(\beta_w{}^2-1\right)+\rho A_T U_0{}^2\frac{\alpha_1}{\gamma_w}\left(\beta_w{}^2-\gamma_w{}^2\right)+\rho A_T U_0{}^2\frac{\alpha_2}{\alpha_w\gamma_w}(\gamma_w-\alpha_w)\left(\beta_w{}^2-\gamma_w{}^2\right)+\rho A_T U_0{}^2\frac{\alpha_2}{\alpha_w}\left(\gamma_w{}^2-\alpha_w{}^2\right)+\frac{1}{2}\rho w U_0{}^2\left(\beta_w{}^2-1\right)=D_1+D_2$$

Reminding that w represents an area per unit depth, dividing the left and right-hand sides by the upstream dynamic pressure ($½*\rho*w*U_0^2$), the sum $B*$ (C_{D1}+C_{D2}) is achieved at the right-hand side. Replacing (A_T/w) with the blockage ratio B, and collecting the α_2 terms with a slight manipulation, yields:

$$-2\left(\beta_w{}^2-1\right)+2B\frac{\alpha_1}{\gamma_w}\left(\beta_w{}^2-\gamma_w{}^2\right)+2B\frac{\alpha_2}{\alpha_w\gamma_w}(\gamma_w-\alpha_w)\left(\beta_w{}^2+\alpha_w\gamma_w\right)+\left(\beta_w{}^2-1\right)=BC_{D1}+BC_{D2}$$

By substituting C_{D2} with the definition (2.12) and ordering all terms,

$$-\left(\beta_w{}^2-1\right)-BC_{D1}-B\left(\gamma_w{}^2-\alpha_w{}^2\right)+2B\frac{\alpha_1}{\gamma_w}\left(\beta_w{}^2-\gamma_w{}^2\right)+2B\frac{\alpha_2}{\alpha_w\gamma_w}(\gamma_w-\alpha_w)\left(\beta_w{}^2+\alpha_w\gamma_w\right)=0$$

By substituting carefully β_w with the equation (2.9) while using C_{D1} instead of (β_e^2-α_e^2) for convenience, the following algebraic building blocks are obtained:

- $1+B\alpha_w{}^2$

- $\beta_w{}^2 - BC_{D1} - \gamma_w{}^2 = -(1+B)(\gamma_w{}^2 + C_{D1})$

- $2B\frac{\alpha_1}{\gamma_w}\left(\beta_w{}^2 - \gamma_w{}^2\right) = 2B\frac{\alpha_1}{\gamma_w}C_{D1}$

In the last algebraic component, α_2 is replaced by the equation (#):

- $2B\frac{\alpha_2}{\alpha_w\gamma_w}(\gamma_w - \alpha_w)\left(\beta_w{}^2 + \alpha_w\gamma_w\right) = \frac{2(\gamma_w{}^2+C_{D1}+\alpha_w\gamma_w)\left\{\sqrt{\gamma_w{}^2+C_{D1}}-1-B\frac{\alpha_1}{\gamma_w}\left(\sqrt{\gamma_w{}^2+C_{D1}}-\gamma_w\right)\right\}}{\sqrt{\gamma_w{}^2+C_{D1}}}$

The Rigid Lid LMADT in equation (2.22) is analogous equation (2.18) and it is a function of two unknowns, i.e., α_w and γ_w,

$$1 + B\alpha_w{}^2 - (1+B)(\gamma_w{}^2 + C_{D1}) + 2B\frac{\alpha_1}{\gamma_w}C_{D1} + \frac{2(\gamma_w{}^2+C_{D1}+\alpha_w\gamma_w)\left[\sqrt{\gamma_w{}^2+C_{D1}}-1-B\frac{\alpha_1}{\gamma_w}\left(\sqrt{\gamma_w{}^2+C_{D1}}-\gamma_w\right)\right]}{\sqrt{\gamma_w{}^2+C_{D1}}} = 0 \qquad (2.22)$$

2.3.3. Boundary conditions

The boundary conditions allow to exclusion of non-physically acceptable solutions. These are illustrated in Tab. 2-1 for upstream and downstream discs. Upstream, the turbine operation implies the acceleration of the bypass flow and the velocity reduction into the wake, such that $\beta_e \geq 1$ and $\alpha_e \leq 1$, with equality occurring whether no power extraction occurs. Solutions for $\beta_e < 1$ are excluded from our interest since energy would be added to the flow instead of being subtracted. In addition, negative solutions of α_e and β_e characterize a flow reversal, so they are disregarded. Since the wake flow is slower than the induced flow at the disc, i.e., $\alpha_e \leq \alpha_1$, the disc interference factor α_1 must be bounded between α_e and 1.

The downstream bypass flow is faster than β_e, and thus $\beta_w \geq \beta_e$ due to additional restriction of the flow passage. Assuming the mathematical relationship between β_w, γ_w, β_e, and α_e in (2.9), the downstream annular flow accelerates such that γ_w is higher than the wake flow exiting the first disc, i.e., $\gamma_w \geq \alpha_e$, thus shrinking slightly the outer streamtube in the downstream half. Notice that the acceleration in the bypass flow β_w from β_e is smoother than the acceleration in the annular flow γ_w from α_e. At the core of the streamtube, the wake deceleration towards α_w is achieved in such a manner that the disc interference factor α_2 is bounded between its minimum speed and maximum, i.e., α_w and α_e. Another boundary condition discarding the supercritical solutions is introduced in the next section.

Tab. 2-1 Boundary conditions for the upstream and downstream interference factors.

Description	Validity	Scheme
α_1	$\alpha_e \leq \alpha_1 \leq 1$	Disc 1
α_e	$0 \leq \alpha_e \leq \alpha_1$	Disc 1
β_e	$\beta_e \geq 1$	Disc 1
α_2	$\alpha_w \leq \alpha_2 \leq \alpha_e$	Discs 1+2
α_w	$0 \leq \alpha_w \leq \alpha_2$	Discs 1+2
γ_w	$\alpha_e \leq \gamma_w \leq \beta_w$	Discs 1+2
β_w	$\beta_w \geq \beta_e$	Discs 1+2

2.4. LMADT Solutions

The 2-D solution space of the ideal C_{D1} and C_{P1} versus the axial induction factor a_1 are depicted from Fig. 2-6 to Fig. 2-13 at increasing blockage ratio B and Froude number Fr. The curves are bounded by the conditions of Tab. 2-1, even though evidence of a feasible performance beyond the Lanchester-Betz limit is demonstrated for the maxima within Rigid Lid and Free Surface solution spaces.

As noticeable, the solutions space for C_{D1} and C_{P1} is visible for the full domain of a_1 [0,1] for all blockage ratios only at Fr = 0. Diversely, as B and Fr increase, the curve may be interrupted due to a lack of feasible solutions. The availability of solutions shrinks even more for $Fr > 0.7$. For higher Fr, plots of C_{D1} and C_{P1} are missing, due to poor outputs.

Moreover, since the drag coefficient always increases for the solutions respecting the boundary conditions, the Glauert correction becomes of doubtful utility. Hence, it is omitted in the LMADT treatment of the Double Multiple Streamtube model, as anticipated in [1].

The tests on single porous plates spanning the test channel width performed by Schmitz and Pelz [31] show that the drag coefficient predicted by the numerically equivalent models of Whelan et. al [27] and Houlsby et al. [33] yield sufficiently accurate outputs. It is enough for experimental validation of the Free Surface LMADT, even though a few considerations related to the turbine depth arise, as discussed in the next section. In addition to the previous boundary conditions, a constraint for checking whether a supercritical condition occurs in the channel flow is formulated. Hence, unfeasible solutions are discarded according to a mathematical statement.

The critical energy in the bypass flow is achieved whether the Froude number at the station w (or e, identically) equals unity, i.e., $U_{w,c} = (g{*}h_{w,c})^{1/2}$, with subscript c indicating the critical condition. Since $U_{w,c} = U_0{*}\beta_{w,c}$, after the normalization of left and right-hand sides by h_0, replacing $U_0/(g{*}h_0)^{1/2}$ with Fr, yields:

$$Fr^2 {\beta_{w,c}}^2 = \frac{h_{w,c}}{h_0}$$

According to equations (2.6) or (2.16), the specific energy conservation between the boundaries of the bypass flow control volume gives:

$$\frac{h_{w,c}}{h_0} = 1 - \frac{Fr^2}{2}\left({\beta_{w,c}}^2 - 1\right)$$

Both statements are combined, achieving the constraint for the bypass flow remaining subcritical in (2.23).

$$\beta_w < \beta_{w,c} = \sqrt{\frac{2+Fr^2}{3Fr^2}} \qquad (2.23)$$

The drag coefficient C_{D1} and the interference factor at disc α_1 appear in the double-disc equations (2.17-2.18) and (2.21-2.22). It implies that the solution of the double-disc polynomial depends on the first disc drag coefficient and disc interference factor. Since we are not yet solving the turbine velocity triangles, the solution space of the downstream disc is determined only by choosing the upstream disc parameters due to its dependency.

For better understanding, the downstream disc is solved from the optimal solutions of the upstream disc at each B and Fr, yielding the following charts. Again, as Fr and B increase, the curves may disappear at a certain point. It is due to the achievement of results invalidating the boundary conditions in Tab. 2-1, upstream or downstream. The choice of modeling each interference factor based on the inflow speed U_0 implies that the domain of the induction factor a_2 starts from values higher than zero so that only part of the domain

[0,1] is enclosed. In double-disc simulations, C_{D2} and C_{P2} curves may be constructed as a function of the equilibrium axial induction factor $a_{2,eq}$. However, the model of this work allows the downstream interference factor to be represented simply as the ratio U_2/U_0, considering that the equilibrium station at the center of the rotor is purely artificial.

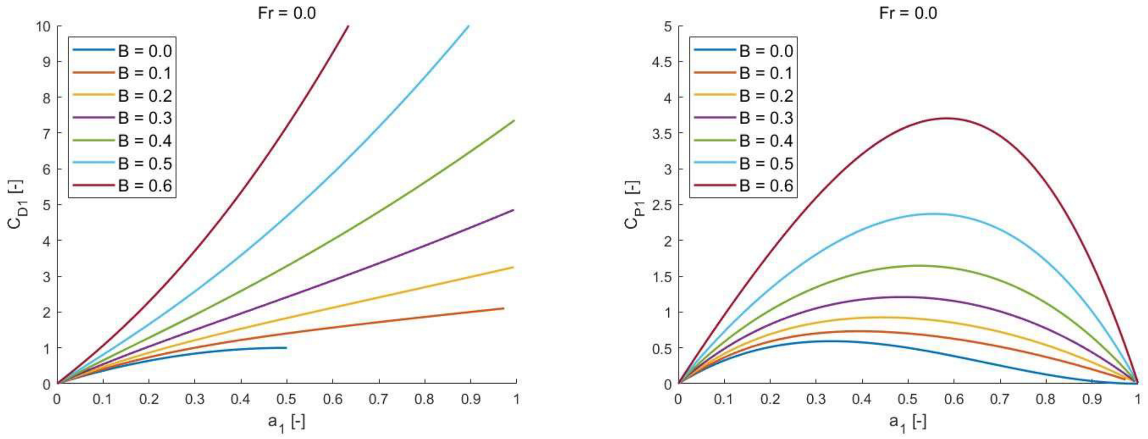

Fig. 2-6. Drag coefficient $\boldsymbol{C_{D1}}$ (**left**) and power coefficient $\boldsymbol{C_{P1}}$ (**right**) in a Rigid-Lid LMADT (***Fr*** = 0) versus the axial induction factor $\boldsymbol{a_1}$ and for ***B*** ranging from zero to 0.6. (Unconfined values obtained from the classical LMADT).

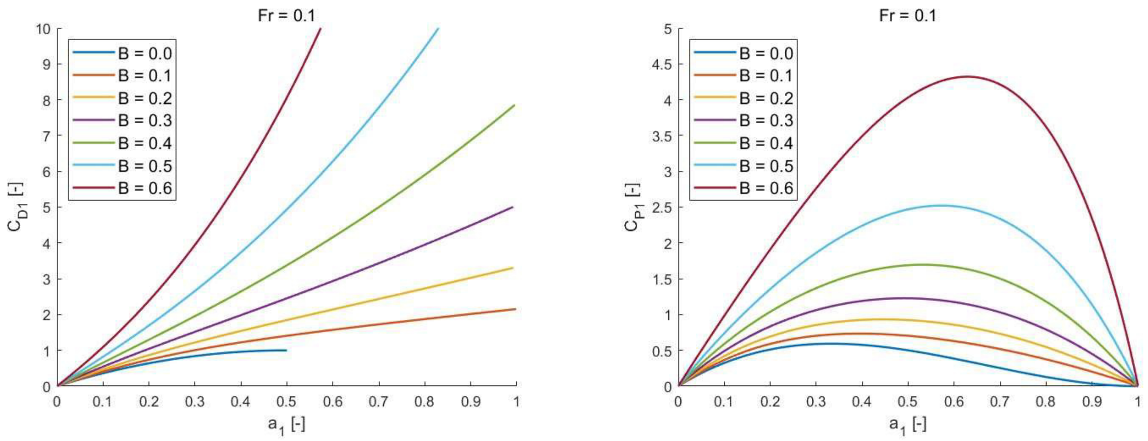

Fig. 2-7. Drag coefficient $\boldsymbol{C_{D1}}$ (**left**) and power coefficient $\boldsymbol{C_{P1}}$ (**right**) in a Rigid-Lid LMADT (***Fr*** = 0.1) versus the axial induction factor $\boldsymbol{a_1}$ and for ***B*** ranging from zero to 0.6. (Unconfined values obtained from the classical LMADT).

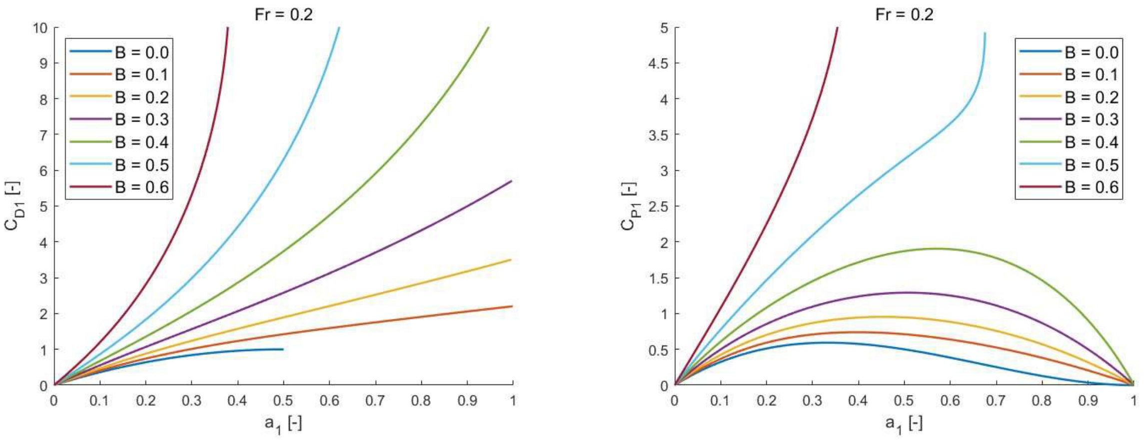

Fig. 2-8. Drag coefficient C_{D1} (**left**) and power coefficient C_{P1} (**right**) in a Rigid-Lid LMADT (***Fr*** = 0.2) versus the axial induction factor a_1 and for ***B*** ranging from zero to 0.6. (Unconfined values obtained from the classical LMADT).

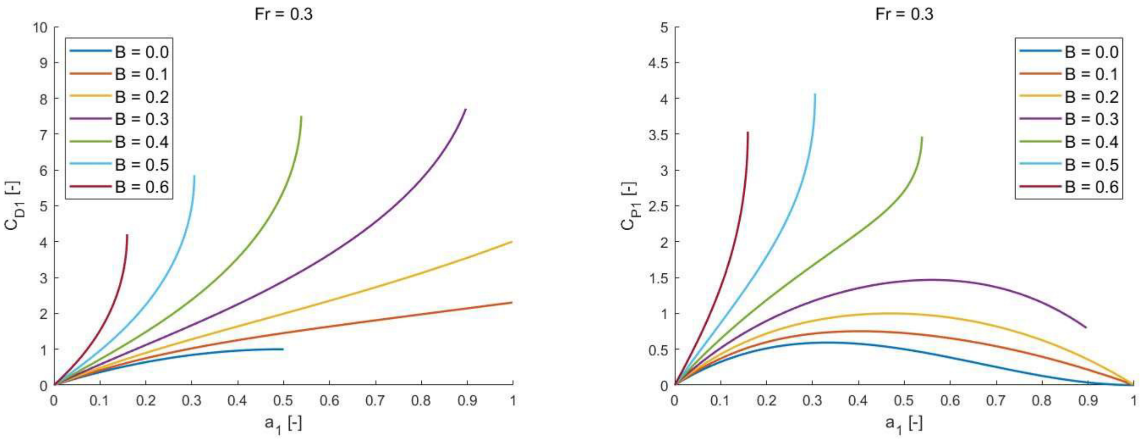

Fig. 2-9. (Left) Drag coefficient C_{D1} (**left**) and power coefficient C_{P1} (**right**) in a Free Surface LMADT (***Fr*** = 0.3) versus the axial induction factor a_1 and for ***B*** ranging from zero to 0.6. (Unconfined values obtained from the classical LMADT).

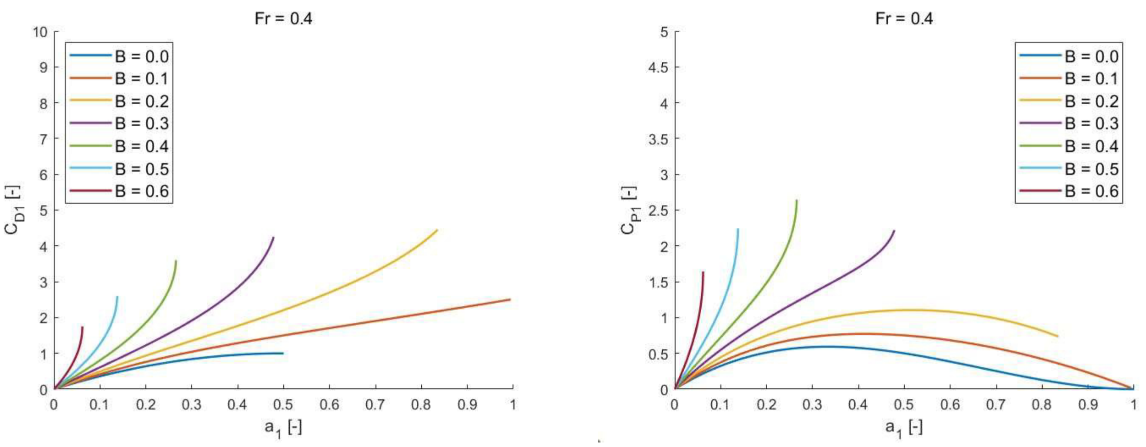

Fig. 2-10. Drag coefficient C_{D1} (**left**) and power coefficient C_{P1} (**right**) in a Free Surface LMADT (***Fr*** = 0.4) versus the axial induction factor a_1 and for ***B*** ranging from zero to 0.6. (Unconfined values obtained from the classical LMADT).

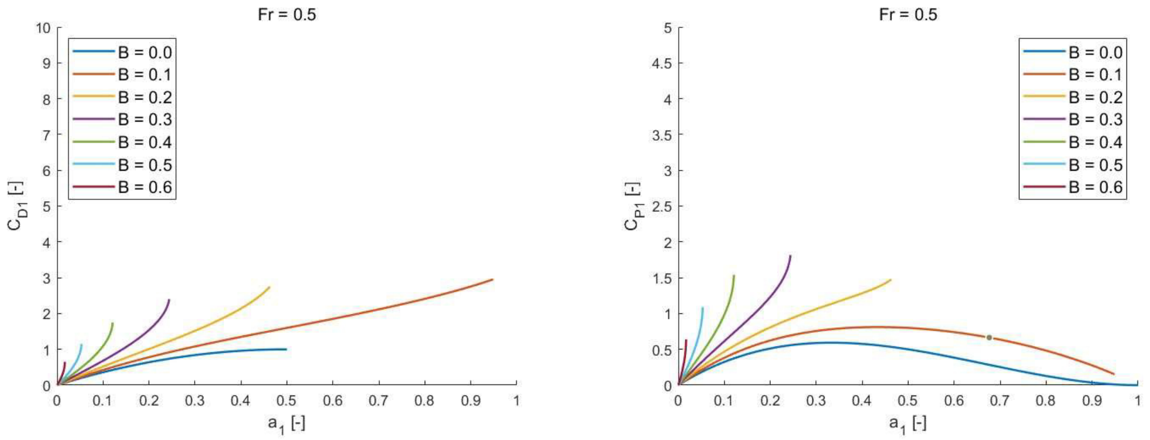

Fig. 2-11. Drag coefficient C_{D1} (**left**) and power coefficient C_{P1} (**right**) in a Free Surface LMADT (Fr = 0.5) versus the axial induction factor a_1 and for B ranging from zero to 0.6. (Unconfined values obtained from the classical LMADT).

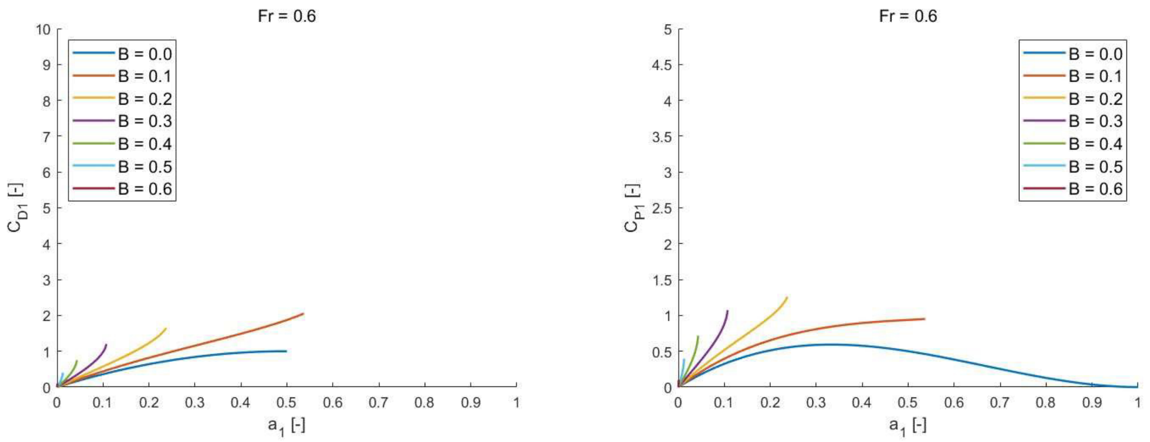

Fig. 2-12. Drag coefficient C_{D1} (**left**) and power coefficient C_{P1} (**right**) in a Free Surface LMADT (Fr = 0.6) versus the axial induction factor a_1 and for B ranging from zero to 0.6. (Unconfined values obtained from the classical LMADT).

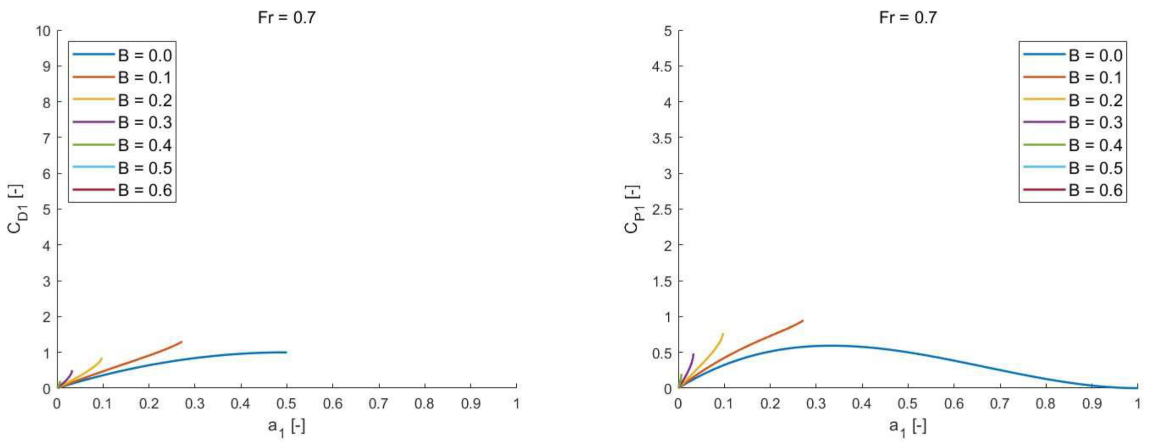

Fig. 2-13. Drag coefficient C_{D1} (**left**) and power coefficient C_{P1} (**right**) in a Free Surface LMADT (Fr = 0.7) versus the axial induction factor a_1 and for B ranging from zero to 0.6. (Unconfined values obtained from the classical LMADT).

The plots of C_{D2} and C_{P2} versus the induction factor a_2 and versus the equilibrium induction factor a_e, i.e., $a_{2,eq} = (1-\alpha_2/\alpha_e)$ are shown in Fig. 2-14 and Fig. 2-15. For simplicity, the curves at higher Fr are not shown but are obtained by solving both discs, as shown previously.

The juxtaposition in Fig. 2-16 of the upstream and downstream drag and power coefficients (C_{D1}, C_{P1}, C_{D2}, C_{P2}, respectively) in turn, achieved from the maxima of the previous solutions, demonstrates that the downstream disc generates curves that are superimposable but very different in magnitude, giving the overall performance a limited increase in power and drag force.

According to Cacciali et al. [1], if B = 0, the freestream double-disc model [34] should be applied instead. Diversely, acceptable outputs are obtained from a small blockage ratio $B \ll 1$ towards $(1-B) \ll 1$. The solution for the maximum power coefficient as a function of the blockage ratio disc was achieved by Garrett and Cummins, i.e., $C_{P1,max} = 16/27*(1-B)^{-2}$, leading to the Lanchester-Betz limit of 16/27 if $B \ll 1$. Since $\beta_e = 1$ in a freestream flow, the Froude condition is demonstrated, i.e., $\alpha_1 = (1+\alpha_e)/2$.

For intermediate blockage ratios, the power coefficient enhances according to the increased momentum exchange in the flow. The swept area may occupy the cross-section entirely such that B = 1. However, the numerical solution with the confined actuator disc theory fails precisely at $B = 0$ and $B = 1$, while Garrett and Cummins [26] justify the asymptotic behavior. For $0 \leq B \leq 1$, the power removed from the flow by the entire system would be $P_{tot} = P_1+P_2$. Since the axial forces D_1 and D_2 are nothing but the product of the drag coefficient to the upstream dynamic pressure force, if P_1+P_2 is written as $U_0*(\alpha_1*D_1+\alpha_2*D_2)$, P_{tot} becomes $\frac{1}{2}\rho*A_T*U_0^3*(\alpha_1*C_{D1}+\alpha_2*C_{D2})$.

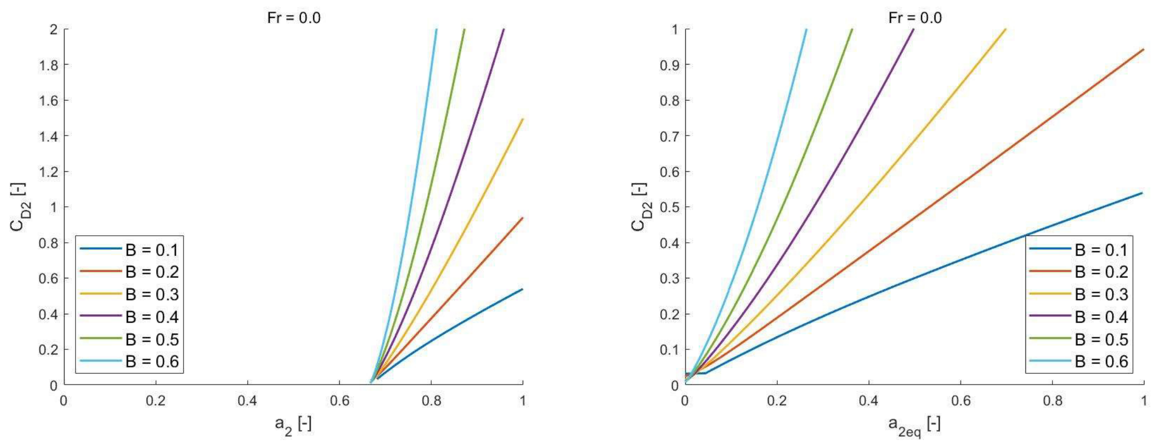

Fig. 2-14. (**Left**) Drag coefficient C_{D2} versus the axial induction factor a_2 and (**right**) drag coefficient C_{D2} versus the equilibrium axial induction factor $a_{2,eq}$ in a Rigid Lid LMADT (***Fr***=0) for ***B*** ranging from zero to 0.6.

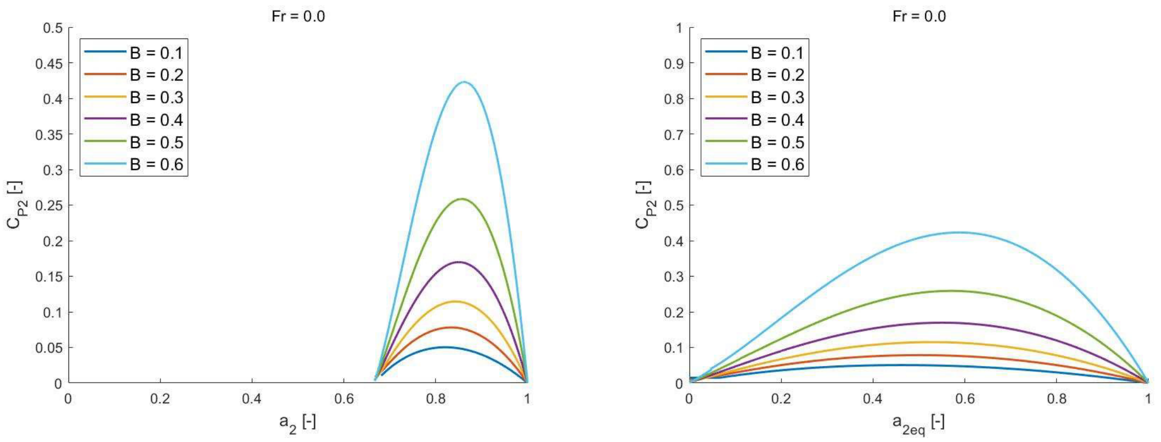

Fig. 2-15. (**Left**) Power coefficient $\boldsymbol{C_{P2}}$ versus the axial induction factor $\boldsymbol{a_2}$ and (**right**) power coefficient $\boldsymbol{C_{P2}}$ versus the equilibrium axial induction factor $\boldsymbol{a_{2,eq}}$ in a Rigid Lid LMADT ($\boldsymbol{Fr}$ = 0) for $\boldsymbol{B}$ ranging from zero to 0.6.

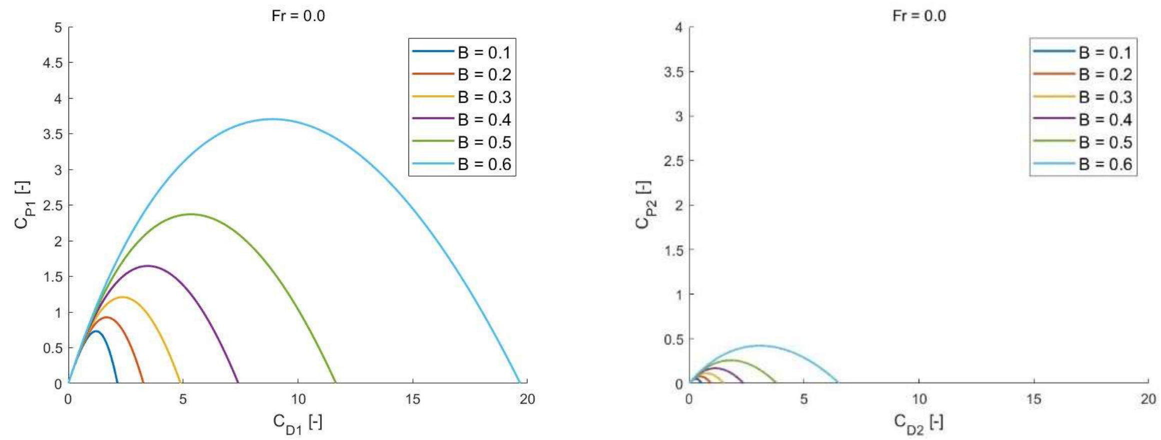

Fig. 2-16. (**Left**) Power coefficient $\boldsymbol{C_{P1}}$ versus the drag coefficient $\boldsymbol{C_{D1}}$ and (**right**) power coefficient $\boldsymbol{C_{P2}}$ versus the drag coefficient $\boldsymbol{C_{D2}}$ in a Rigid Lid LMADT ($\boldsymbol{Fr}$ = 0) for $\boldsymbol{B}$ ranging from zero to 0.6.

The total power P_{tot} to the inflow kinetic power ratio gives the LMADT global performance $C_{P,tot}$ in (2.23), i.e., a function of C_{D1}. Notice that the performance of the second disc depends on the energy made available from the previous disc.

$$C_{P,tot} = \alpha_1\left({\beta_e}^2 - {\alpha_e}^2\right) + \alpha_2({\gamma_w}^2 - {\alpha_w}^2) \tag{2.23}$$

If the drag force exerted by the first disc increases, the global performance $C_{P,tot}$ of the system rises accordingly, while the lower available energy at the downstream disc inevitably reduces the performance C_{P2}. Although a small amount of power is extracted downstream, the second disc allows power to be recovered from the tailwater of the first disc, thus increasing the overall capacity. If the upstream disc does not extract energy (no drag force is exerted), C_{D1} yields zero, while α_1, α_e, and β_e become unitary. By substituting this result into the double-disc Rigid Lid equation (2.20), the single-disc Garrett and Cummins' equation is achieved again in (2.24) with a new Nomenclature. Therefore, the downstream disc would behave like the upstream disc since exerting the same drag force.

$$\gamma_w{}^2(1-B) - 2\gamma_w(1-\alpha_w) + 1 - 2\alpha_w + B\alpha_w{}^2 = 0 \tag{2.24}$$

Newman [18] calculated the performance of a double-disc in a freestream flow, predicting a $C_{P,tot}$ of 16/25, higher than the single-disc Lanchester-Betz limit of 16/27. In Fig. 2-17, it is demonstrated that the asymptotic trend of $C_{P,tot}$ is perfectly aligned with Newman's prediction if the second disc is solved for the C_{D1} solutions corresponding to C_{P1} maxima. Hence, the sum of C_{P1} and C_{P2} maxima yields the global result at a variable blockage ratio.

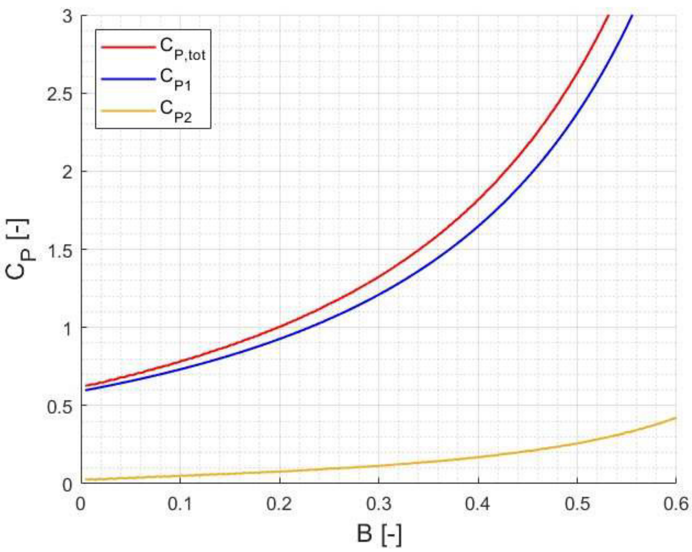

Fig. 2-17. Power coefficient maxima for upstream and downstream discs, C_{P1} (blue line) and C_{P2} (yellow line), respectively, and total power coefficient $C_{P,tot}$ (red line) at a variable blockage ratio B up to 0.6. The blue line tends asymptotically to the Lanchester-Betz limit of 16/27 at $B \approx 0$, whilst the red line tends to Newman's limit of 16/25.

2.5. Rigid Lid and Turbine Depth

A porous plate immersed in a flow at high depths experiences a different drag force than that deployed just below the free surface due to higher axial flow speed near or just below the water still level. The vertical shear over the vertical axis is allowed in unconfined flows, but in confined flows, the flow is averaged when the blockage ratio is introduced. In addition, both independent variables (B and Fr) prevent the possibility of locally including the vertical shear without altering the average value. To include this drop in the drag force, it is perhaps simpler to modify the momentum equations when the submergence depth is increased.

Measurements of the drag force were performed in the facility of DICAM Unitn Hydraulic Laboratory, with plates (h_p 54 mm x w_p 280 mm) built from a porous metallic frame deployed to occupy almost entirely the rectangular channel span (w_c = 305 mm). Depth and Froude numbers were allowed to vary in a subcritical hydraulic regime ($Fr < 1$) by adjusting the downstream drain and thus automatically modifying the blockage ratio.

The visualizations depicted in Fig. 2-18. were achieved by moving the perforated plate from the free surface level to the bottom while keeping a constant discharge. Both images refer to a flow of $Fr < 1$, with a) high free surface drop due to a moderate blockage ratio, assuming the plate positioning in the vicinity of the water level, and b) almost negligible free surface drop due to a lower blockage ratio, with an increased submergence depth.

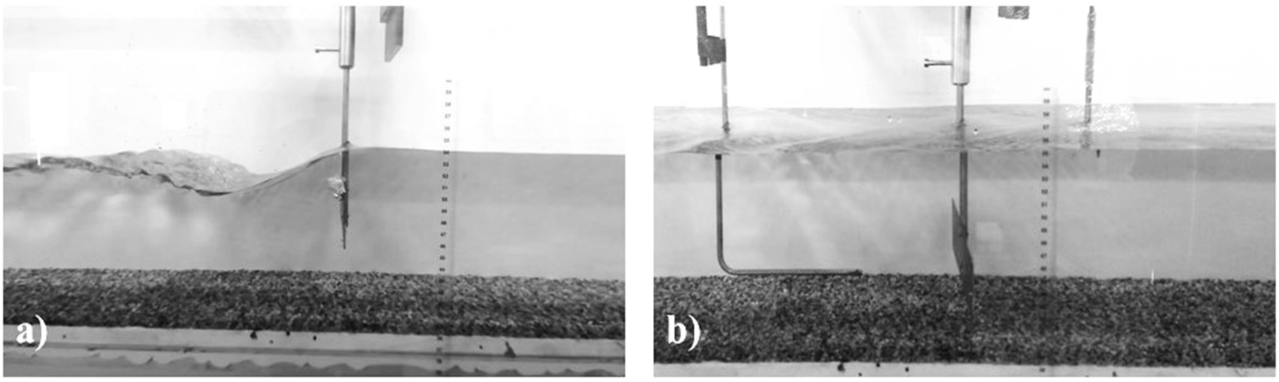

Fig. 2-18. a) Single plate, subcritical flow, consistent free surface variation. **b**) single plate, subcritical flow, negligible free surface variation. Flow direction from right to left.

An almost flat free surface was achieved experimentally, demonstrating that a Rigid Lid-alike condition is allowed by submerging the plate at high depth in a flow of a small Fr. The measurement of the drag force at the shaft revealed that the power dissipated by the second plate is of a smaller magnitude than that originated at the free surface proximity. Indeed, the velocity profile at higher depths drops consistently.

Algebraically, the Rigid Lid condition of hydrokinetic turbines in open channel flows was approximated by Garrett and Cummins [26] by invoking momentum and energy conservation in a pipe flow and assuming a flat-water profile $h_0 \approx h_\infty$.

It led to considering the drag force D proportional to the static pressure drop $\Delta p_{0,\infty}$, i.e., $D = A_\infty{}^*\Delta p_{0,\infty}$. Substituting $\Delta p_{0,\infty} = D/A_0$ into the energy conservation $P_{tot} = A_\infty{}^*U_\infty{}^*\Delta p_{0,\infty}$, yields $P_{tot} = D^*U_\infty$. Although this solution is valid for water and wind tunnels, this does not hold in open channel flows because a hydrostatic pressure gradient is always present when power is converted [35], [30]. The consequence is that the efficiency model proposed by Garrett and Cummins is meaningless for the computation of the power recovered in riverine flows, partly invalidating the models built on that approximation, e.g., EPRI [36], Kartezhnikova and Ravens [37].

As further clarified in Chapter 3, the available power P_{tot} must be proportional to the total head drop ΔH_{tot} developed within the channel length, built as a sum of hydrostatic, kinetic, and geodetic head variations. Hence, in subcritical flows, the Rigid Lid model is used only for approximating the flow at high depth. According to Gauvin-Tremblay and Dumas [38], turbines in different configurations were found almost insensitive to the Froude number, especially at the deepest submergence for $d_h/D_T \geq 2$, where turbines experience almost no local interaction with the free surface.

Therefore, a correction of the momentum theory, including the installation depth, is considered. The deletion of the free surface drop is assumed for $d_h/H_T \geq 2$, being d_h the distance from the water level to the turbine top measured at h_0, and H_T the turbine height of the porous element substituting the turbine diameter D_T. A calibration parameter ξ is defined such that a constant water level is approximated whether $\xi = 1$. Diversely, a complete free surface drop occurs if $\xi = 0$.

In practice, this sub-model allows the Free Surface LMADT to be relaxed according to the turbine depth, while the Froude number is the parameter to be corrected. In the upstream and downstream actuator disc equations (2.7-2.8) and (2.17-2.18), each quadratic term Fr^2 is multiplied by a factor $(1-\xi)$. The expected impact of the Froude number on power extraction and drag force is less significant as the turbine depth increases. The difference $(1-\xi)$ reduces the effect of the Froude number on the flow. ξ is calculated as $d_h/(2H_T)$, such that $0 \leq \xi \leq 1$, based on the investigations of Gauvin-Tremblay and Dumas. Even though a real validation on this calibration parameter is absent, the outputs of this correction are visible directly from the Double Multiple Streamtube simulations shown in the next Chapter. The installation depth d_h is initialized according to the downstream fixed reference and is updated as (Inflow + DMS) iterations proceed.

While exploring the turbine immersion depth, several visualizations of standing waves were achieved at the Hydraulics facility, according to the findings of Myers and Bahaj [39], while approaching the perforated plate to the bottom. Standing waves represent an issue because altering the downstream flow. Apart from their visualization, it is worth mentioning that it can be the consequence of a sub-optimal design resulting in undesirable flow alterations.

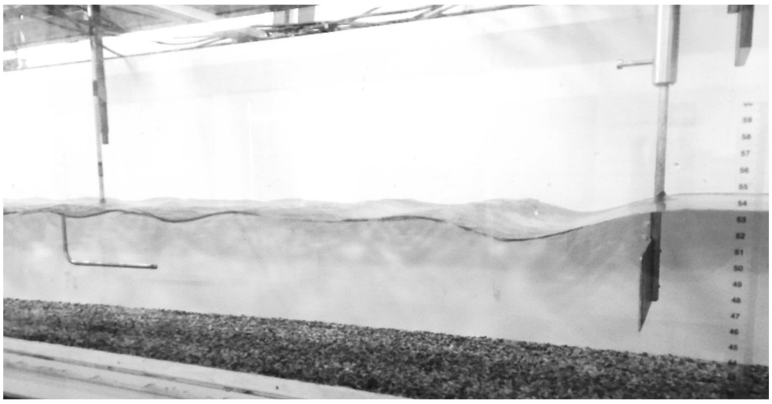

Fig. 2-19. Standing waves generated by moving the plate toward the channel bottom. Flow direction from right to left.

To conclude, the Free Surface actuator holds when the rotor is just immersed in water. The other extreme condition is obtained by removing the effect of the Froude number on the free surface variation and consequent flattening. Therefore, the model becomes dependent only on the blockage ratio, i.e., a full Rigid Lid actuator disc, even though this extreme condition is approximated. Further explanations of this method applied to the Double Multiple Streamtube are given in Chapter 3.

REFERENCES

[1] Cacciali L., Battisti L., Dell'Anna S. Free Surface Double Actuator Disc Theory and Double Multiple Streamtube Model for In-Stream Darrieus Hydrokinetic Turbines. Ocean Engineering **2022**, 260, 112017.

[2] Rankine W.J.M. On the Mechanical Principles of the Action of Propellers. Transactions of the Institute of Naval Architects **1865**, 6, 13-39.

[3] Froude R.E. On the Part Played in Propulsion by Differences of Fluid Pressure. Transactions of the Institute of Naval Architects **1889**, 30, 390-405.

[4] Betz A., Prandtl L. Schraubenpropeller mit Geringstem Energieverlust. Nachrichten der K. Gesellschaft der Wissenschaften zu Göttingen. Math.Phys.Kl. **1919**, 193-217.

[5] Betz A. Das Maximum der Theoretisch Möglichen Ausnutzung des Windes Durch Windmotoren. Zeitschrift für das Gesamte Turbinenwesen **1920**, 26, 307-9.

[6] Van Kuik G.A.M. The Lanchester-Betz-Joukowsky limit. Wind Energy **2007**, 10, 289-291.

[7] Lanchester F.W. A Contribution to the Theory of Propulsion and the Screw Propeller. Transactions of the Institution of Naval Architects **1915**, 57, 98–116.

[8] Joukowsky N.E. Windmill of the NEJ type. Transactions of the Central Institute for Aero-Hydrodynamics of Moscow, 1920. Also published in Joukowsky NE. Collected Papers VI. The Joukowsky Institute for AeroHydrodynamics, Moscow: VI (**1937**) 405–409.

[9] Drzewiecki S. Sur une Methode pour la Determination des Elements Mecaniques des Propulseurs Helicoidaux. Comptes Rendus de L'Académie des Sciences, Paris, (**1892**).

[10] Betz A. Zeitschrift für Flugtechnik und Motorluftfahrt **1920**, 11, 105.

[11] Glauert H. An Aerodynamic Theory of the Airscrew. A.R.C. Reports and Memoranda, 3555 (**1922**).

[12] Glauert H. Aerodynamic theory, vol. 4, chapter Windmills and Fans. W. F. Durand, Springer J., Berlin, Germany, (**1935**).

[13] Hütter U. Beitrag zur Schaffung con Gestaltungsgrundlagen für Windkraftwerke. DissertainTechnische Hoschscule Wien, (**1942**).

[14] Hansen, M. Aerodynamics of Wind Turbines (3rd edition). Routledge (**2015**).

[15] Eggleston D M, Stoddard F. Wind Turbine Engineering Design. United States, **1987**.

[16] Lapin E.E. Theoretical Performance of Vertical-Axis Wind Machines. ASME Paper 75-WA/ENER-1 (**1975**).

[17] Loth J.L., McCoy H. Optimization of Darrieus Turbines with an Upwind and Downwind Momentum Model. Energy **1983**, 7, 313–318.

[18] Newman B.G. Actuator-disc Theory for Vertical-Axis Wind Turbines. Journal of Wind Engineering and Industrial Aerodynamics **1983**, 15, 347-355.

[19] Newman B.G. Multiple Actuator-Disc Theory for Wind Turbines. Journal of Wind Engineering and Industrial Aerodynamics **1986**, 24, 215-225.

[20] Glauert H. Wind Tunnel Interference on Wings, Bodies and Airscrews, Aeronautical Research Committee Reports and Memoranda, 1566 (**1933**).

[21] Maskell E. A Theory of the Blockage Effects on Bluff Bodies and Stalled Wings in a Closed Wind Tunnel. ARC Reports and Memoranda, 3400 (**1963**).

[22] Barnsley M., Wellicome J. Final Report on the 2nd Phase of Development and Testing of a Horizontal Axis Wind Turbine Test Rig for the Investigation of Stall Regulation Aerodynamics. ETSU Agreement E.5A/CON5103/1746, (**1990**).

[23] Mikkelsen R., Sørensen J. Modelling of Wind Tunnel Blockage. Proceedings of the 2002 Global Wind Power Conference and Exhibition, (**2002**).

[24] Werle M. Wind Turbine Wall-Blockage Performance Corrections. Journal of Propulsion and Power **2010**, 26, 1317-132.

[25] Ross H., Polagye B. An Experimental Assessment of Analytical Blockage Corrections for Turbines. Renewable Energy **2020**, 152, 1328-1341.

[26] Garrett C., Cummins P. The Efficiency of a Turbine in a Tidal Channel. Journal of Fluid Mechanics **2007**, 588, 243-251.

[27] Whelan J., Graham J., Peiró J. A Free-Surface and Blockage Correction for Tidal Turbines. Journal of Fluid Mechanics **2008**, 624, 281-291.

[28] Draper S., Nishino T. Centred and Staggered Arrangements of Tidal Turbines. Journal of Fluid Mechanics **2014**, 739, 72-93.

[29] Bonar P.A., Chen L., Schnabl A.M., Venugopal V., Borthwick A.G.L., Adcock T.A.A. On the Arrangement of Tidal Turbines in Rough and Oscillatory Channel Flow. Journal of Fluid Mechanics **2019**, 865, 790-810.

[30] Pelz P.F., Metzler M., Schmitz C., Müller T.M. Upper Limit for Tidal Power with Lateral Bypass. Journal of Fluid Mechanics **2020**, 889, A32.

[31] Schmitz C., Pelz P. Upper Limit for Tidal Turbines. 30th IAHR Symposium on Hydraulic Machinery and Systems. IOP Conf. Series: Earth and Environmental Science, 774, 012127 (**2021**).

[32] Vogel C.R., Houlsby G.T., Willden R.H.J. Effect of Free Surface Deformation on the Extractable Power of a Finite Width Turbine Array. Renewable Energy **2016**, 88, 317-324.

[33] Houlsby G., Draper S., Oldfield M. Application of Linear Momentum Actuator Disc Theory to Open Channel Flow. OUEL 2296/08, (**2008**).

[34] Paraschivoiu I., Delclaux F., Double Multiple Streamtube Model with Recent Improvements. Journal of Energy **1983**, 250–255.

[35] Kirke B. Hydrokinetic and Ultra-Low Head Turbines in Rivers: A Reality Check. Energy for Sustainable Development **2019**, 52, 1-10.

[36] Gunawan B., Neary V.S., Mortensen J., Roberts J.D. Assessing and Testing Hydrokinetic Turbine Performance and Effects on Open Channel Hydrodynamics: an Irrigation Canal Case Study. Albuquerque, USA: U.S Department of Energy (**2017**).

[37] Kartezhnikova, M., Ravens, T.M. Hydraulic Impacts of Hydrokinetic Devices. Renewable Energy **2014**, 66, 425–432.

[38] Gauvin-Tremblay O., Dumas G. Two-way Interaction Between River and Deployed Cross-Flow Hydrokinetic Turbines. Journal of Renewable and Sustainable Energy **2020**, 12,034501.

[39] Myers L., Bahaj J., Wake Studies of a 1/30th Scale Horizontal Axis Marine Current Turbine. Ocean Engineering **2007**, 34, 758-762.

NOMENCLATURE

A	Wider streamtube area *m^2*	α	Core flow interference factor, (U_w/U_0)
A_D	Actuator disc area *m^2*	β	Bypass flow interference factor, (U_b/U_0)
a	Narrower streamtube area *m^2*	γ	Annulus flow interference factor, (U_γ/U_0)
a_1	Upstream axial induction factor, $(1-\alpha_1)$	λ	Tip speed ratio, $(\omega * R_T/U_0)$
a_2	Downstream axial induction factor, $(1-\alpha_2)$	ξ	Depth parameter, $(d_h/(2H_T))$
B	Blockage ratio, $(A_T/(w * h_0))$	ρ	Fluid density *kg/m^3*
C_D	LMADT drag coefficient, $(D/½ * \rho * A_T * U_0^2)$		
C_P	LMADT power coefficient, $(P/½ * \rho * A_T * U_0^3)$	*Subscripts*	
D	Drag force *N*	∞	Undisturbed flow
D_T	Turbine diameter *m*	*0*	Inflow
d_h	Distance from water level to turbine top *m*	*1*	Flow at the upstream disc
Fr	Froude number, $(U_0/(g * h_0)^{½})$	*e*	Flow at the equilibrium
g	Gravity acceleration *m/s^2*	*2*	Flow at the downstream disc
H_T	Turbine height *m*	*w*	Near-wake flow
h_0	Water depth *m*	*tot*	Total
P	Disc power dissipated *W*	*max*	Maximum
p	Static pressure *Pa*	*c*	Critical
T	Axial thrust force *N*		
U	Flow speed *m/s* (see subscripts)	*Suffix*	
U_b	Bypass flow speed *m/s*	+	Immediately upstream flow
U_w	Wake flow speed *m/s*	-	Immediately downstream flow
U_γ	Annulus flow speed *m/s*		
w	Channel width *m*	*Short forms*	
Δh	Depth variation *m*	*DMS*	Double Multiple Streamtube
Δp	Pressure variation *Pa*	*LMADT*	Linear Momentum Actuator Disc Theory

3. DOUBLE MULTIPLE STREAMTUBE FOR IN-STREAM HYDROKINETICS

Chapter adapted to the content of the article:

> *Cacciali L., Battisti L., Dell'Anna S. Free Surface Double Actuator Disc Theory and Double Multiple Streamtube Model for In-Stream Darrieus Hydrokinetic Turbines. Ocean Engineering 2022, 260, 112017. DOI: https://doi.org/10.1016/j.oceaneng.2022.112017.*

The Double Multiple Streamtube illustrated in this chapter solves the extended actuator single-disc equation of Whelan's model with the double-disc LMADT, introduced in Chapter 2 and based on [1]. The 2-D blade element theory is coupled with the extended momentum theory to achieve numerically the axial induction factors of upstream and downstream discs at each azimuthal blade position. The DMS developed can thus predict the performance of rotors deployed in confined waters, even though several sub-models are added to account for different fluid-dynamic losses. The finite length of the blades, the shading due to the rotating shaft, the effect of mechanical struts, flow curvature, and turbine depth represent some corrections implemented for a steady-state prediction. Finally, a streamtube expansion sub-model developed for confined applications is presented in the last section.

3.1. Introduction to Blade Element Momentum Codes

The prediction of rotor power and thrust force of hydrokinetic turbines in confined flows achieved high accuracy with Navier-Stokes solvers, increasingly popular in companies and academic environments. Many recent works based on numerical simulations of cross-flow hydrokinetic turbines currently rely on time-averaged 2-D RANS equations due to the reducing computational effort ensured by fully modeling the turbulence scales. Some examples are reported underneath. Bachant and Wosnik [2] modeled a cross-flow turbine solving with 2-D and 3-D RANS equations and different turbulence models. A turbine loading overprediction was achieved with 2-D simulations compared to experimental data due to the omission of blade effects, struts, and increased blockage. Doan and Obi [3] implemented 2-D RANS equations to investigate a laboratory-scaled rotor and used a blockage correction for validation. By modeling counter-rotating turbines, the authors demonstrated higher power conversion than equally rotating turbines. Kinsey and Dumas [4] assessed numerical blockage corrections for axial-flow and cross-flow turbines and showed that the Rigid Lid Actuator Disc Theory holds for axial-flow and low-solidity cross-flow rotors. The authors demonstrated an underpredicted drag correction factor at high rotor solidity. Consul et al. [5] explored the influence of blockage with 2-D RANS on the hydrodynamic performance of a marine cross-flow turbine operating at a low Froude number, , showing similar outputs from Rigid Lid and Free Surface LMADT when blockage is small. The authors demonstrated that water depth deformation highly depends on the Froude number variation, whereas this effect becomes less sensitive at a reduced Froude number. Shives et al. [6] used an actuator cylinder method with 2-D RANS equations to estimate the performance of a floating H-Darrieus turbine, including a blockage correction to adjust the rotor performance. Concerning drag-driven devices, Shashikumar et al. performed several 2-D and 3-D CFD modeling for rotors operating at a low flow speed. Conventional and tapered Savonius turbines were modeled [7]. The predictions demonstrated that the conventional machine performs slightly better than the tapered rotor. The authors also assumed different blade shapes. The authors also assumed different blade shapes [8], and aspect ratios [9] and included transient simulations at different depth positions [10].

The effective control over the physical process represents one of the most evident advantages of these CFD simulations. However, the computational effort can be demanding and often time-consuming. Fast predictions are often desirable, and this is an advantage for momentum models such as the Blade Element Momentum (BEM). For vertical-axis rotors, the performance prediction often relies on Double Multiple Streamtube models (DMS), which can still play a role as preliminary prediction tools. The following literature about extended actuator disc theories implies that the increase in the power conversion per square meter represents the main advantage induced by the physical blockage of turbines in confined flows. Instead of applying blockage corrections to the outputs of free-stream BEM simulations as performed by Allsop et al. [11], the DMS equations can be directly modified to account for blockage and Froude number as independent variables. In pursuing this goal, Vogel et al. [12] implemented the single-disc Rigid Lid LMADT in their code as a closure for the equations based on Glauert's Blade Element Theory. The authors pointed out that the effect of a constant volume flux on the interaction between rotor tips and bypass flow is uncertain due to the increased velocity of the bypass flow compared to the free-stream flow. Vogel questioned the reliability of Prandtl's tip loss correction in blocked flows. Nevertheless, the code demonstrated the agreement to power and thrust predictions within three percent of equivalent simulations.

A single streamtube model correcting Glauert's model for aircraft propellers [13] was first introduced by Templin [14], but only for the drag coefficient in low-solidity rotors was validated. The improvement of the theory with multiple streamtubes based on the discretization of the flow across the rotor in a series of parallel streamtubes was suggested by Wilson and Lissaman [15], then Strickland [16].

Paraschivoiu [17] and Berg [18] introduced multiple streamtube models based on two actuator discs, with induction factors calculated with a double iteration along each streamtube. Corrections for tip effects and finite aspect ratio were then added later by Paraschivoiu [19], whereas different dynamic stall models were developed.

To our best knowledge, apart from Whelan [20] and Vogel's BEM models [12] dedicated to axial-flow rotors, no code predicts the performance of a cross-flow turbine with confined double-disc equations. Hence, a double-disc extension of Free Surface LMADT is implemented in a DMS procedure as a closure for the 2-D blade element theory.

In VAWT double multiple streamtube models, it is common practice to indicate the upstream station as the known inflow speed. However, this is feasible only if the rotor does not interfere with the upstream flow. Unlike previous DMS models, the upstream {0} and downstream {w] flow stations indicated in Fig. 3-2 do not represent any known flow condition. Since the upstream subcritical current is controlled from downstream, the far-field speed U_∞ is fixed downstream of the mixing region. Thanks to this additional procedure disclosed in Chapter 4, Froude number Fr and blockage ratio B and the DMS are updated numerically up to convergence of the inflow factor, highly improving the reliability of the numerical method.

Different corrections are developed into the DMS to account for flow curvature, shading on the downstream flow due to the rotor shaft, and fluid-dynamic losses due to the struts of the blades. Additional sub-models correcting the installation depth of the machine and a new method for the streamtubes expansion are implemented further. Thus, validation with experimental data is thus executed in Chapter 6.

3.2. Lift and Drag Coefficients

The blade element is investigated to visualize the hydrodynamic forces as depicted in Fig. 3-1 from Paraschivoiu [21]. The lift force per unit length denoted by l represents the component of the reacting force in a perpendicular direction to the relative velocity denoted by W, and the drag force d represents the parallel component. α represents the angle of attack, i.e., the angle at which the blade chord c meets W. Hydrofoils are optimized to maximize the ratio C_l/C_d, with C_l the lift coefficient and C_d the drag coefficient, which equations are indicated in (3.1-3.2). For usual hydrokinetic turbine rotor speeds, C_l and C_d are only functions of the angle of attack and the Reynolds number, in turn, defined as $(\rho{*}W{*}c)/\mu$, with density ρ, dynamic viscosity μ. Notice that ρ and μ are both assumed constant for the hydrokinetic applications.

$$C_l = \frac{l}{\frac{1}{2}\rho W^2 c} \tag{3.1}$$

$$C_d = \frac{d}{\frac{1}{2}\rho W^2 c} \tag{3.2}$$

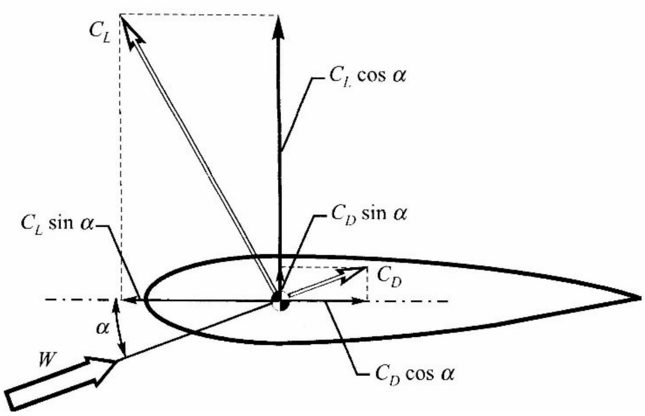

Fig. 3-1. Force coefficients of a blade element hydrofoil from [21].

If the hydrofoil is aligned with the upstream flow (zero α), the drag is the only force acting on the blade element, and the boundary layer remains attached. As the angle of attack α

increases, the pressure gradient rises to allow the streamlines to bend along the profile and lift generates. The dynamic variation of α during the revolution is such that it does not appear instantaneously as a load but has a delay proportional to c/W. The response to the hydrodynamic load depends on whether the boundary layer is attached or partly separated.

3.3. Confined Double Multiple Streamtube Model

The flow in Fig. 3-2 is modeled with a cosine distribution of parallel tubes, azimuthally and vertically discretized. The streamtubes are crossed twice per revolution by a single blade, and this is obtained by two actuators inducing the flow speeds U_1 and U_2, upstream and downstream, respectively. Initially the streamtubes are kept straight, while their expansion is allowed a second phase.

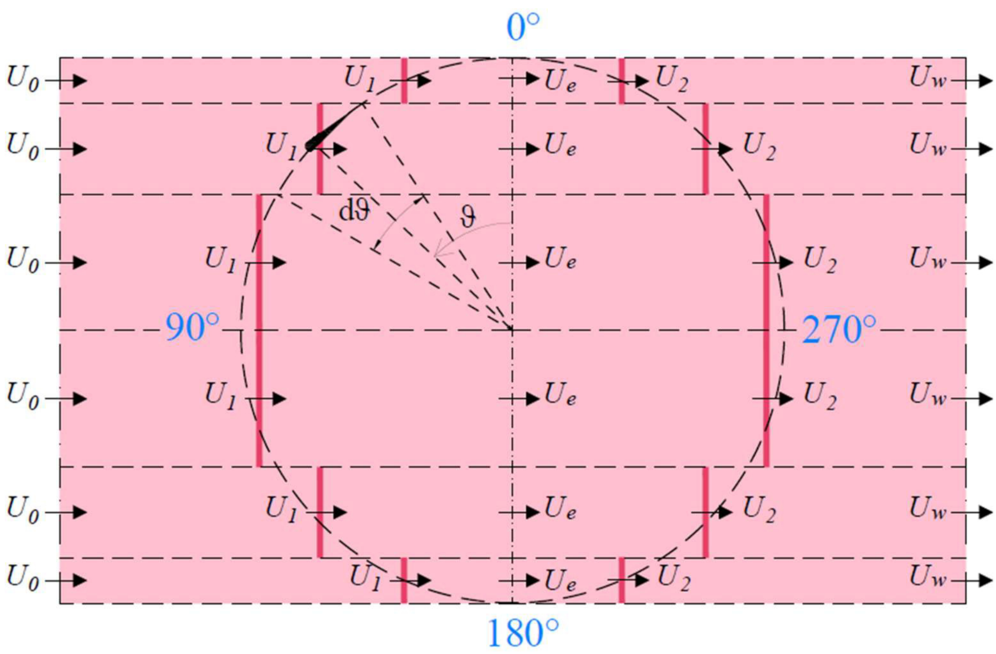

Fig. 3-2. Cosine discretization of multiple streamtubes.

3.3.1. Iterative scheme vs root-finding algorithm

The DMS method implies the iterative scheme depicted in Fig. 3-3, whose focus is reducing the numerical error on the axial induction factor of a single streamtube. Indices i and j refer to iteration and streamtube numbers, respectively. The converged solution of a_1 and C_{D1} is used to solve the downstream momentum equation of the same streamtube.

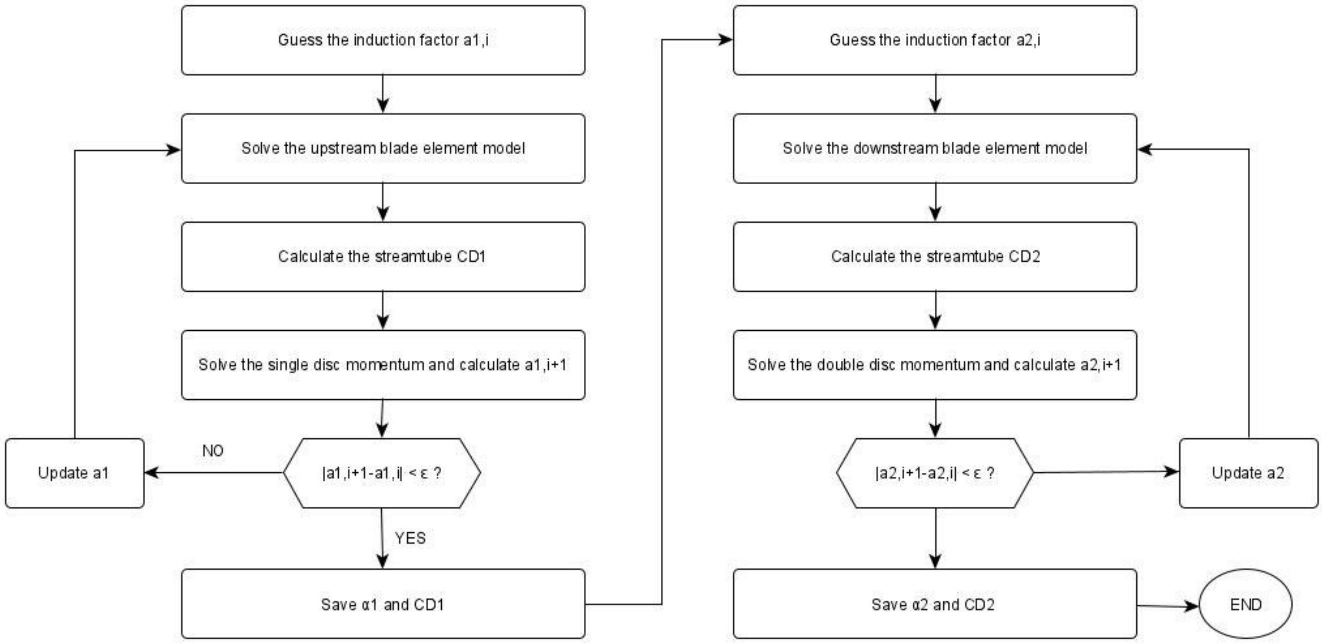

Fig. 3-3. Iterative scheme for a single streamtube of the DMS.

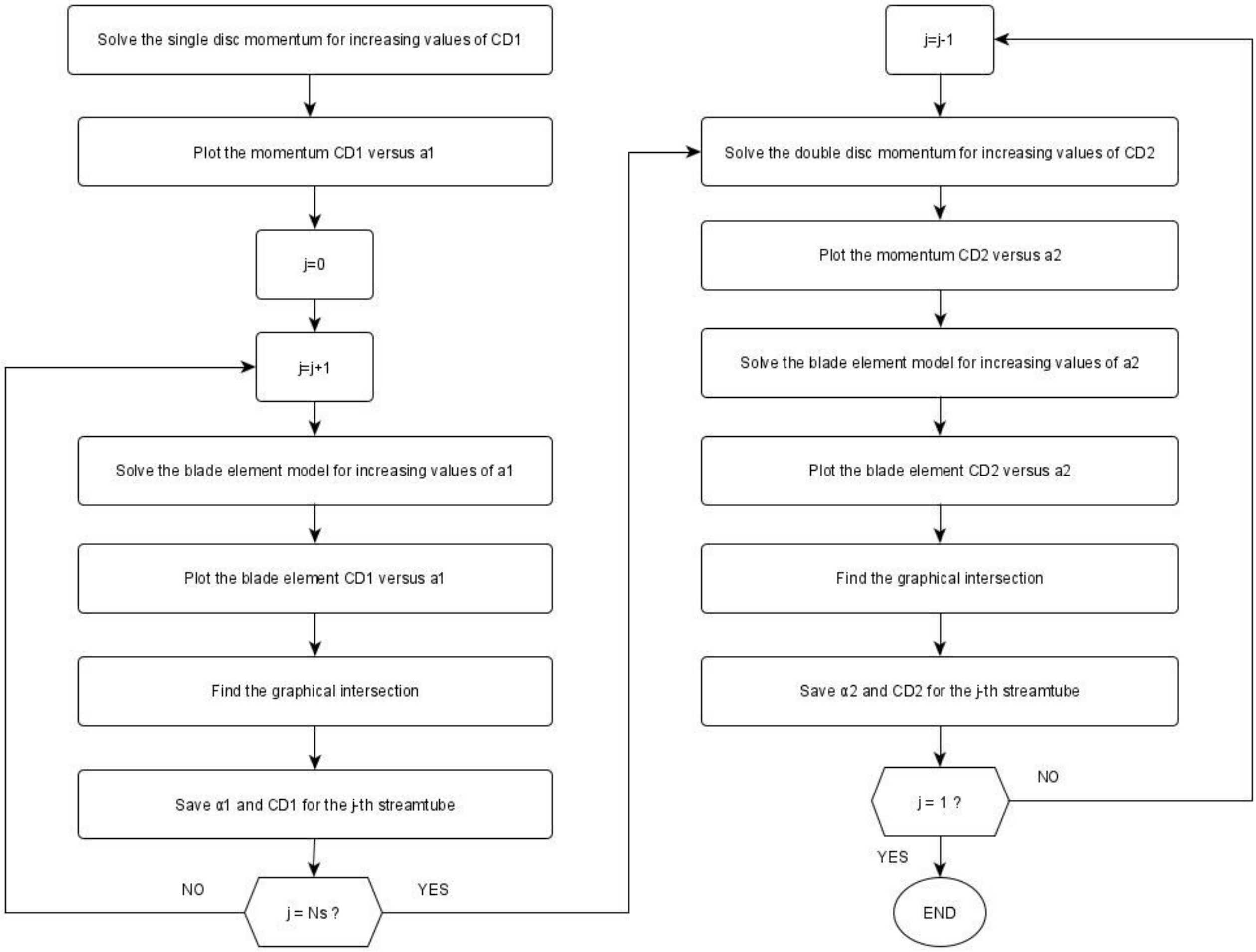

Fig. 3-4. Root-finding algorithm for the DMS.

This tool can be replaced by a root-finding algorithm to be less dependent on the choice of the seed for the induction factor, thus allowing the graphical solution depicted in Fig. 3-4. Previous works [14],[16] show that convergence issues occur in the momentum theory for highly loaded rotors in the blade element code due to inflection points due to the empirical correction.

McIntosh et al. [22] visualized multiple intersections between the momentum and blade element model and solved the equations with a root-finding algorithm for locating crossing points. The numerical solution improves with the graphical solution by increasing the resolution of drag coefficients for the momentum model and induction factors for the blade element model, at the expense of the processing time.

An example is depicted in Fig. 3-5 with the solution at the λ_{opt} found with graphical method for an azimuthal angle of 90°. An equivalent solution is found with the iterative scheme, while a slight divergence is found for angles near 0° and 180°, where notoriously, Blade Element Momentum codes are less accurate.

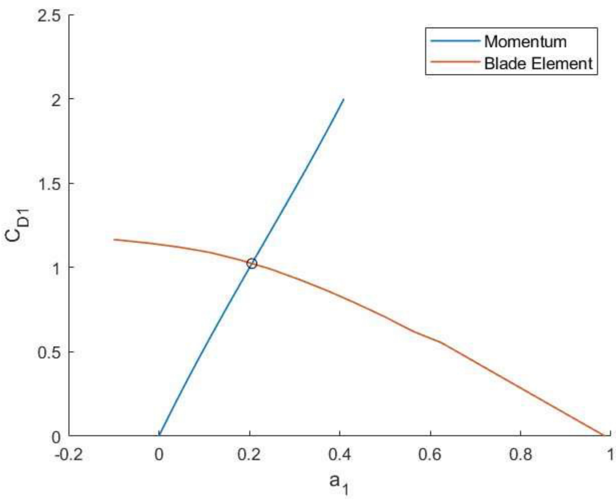

Fig. 3-5. Graphical solution of the root-finding algorithm for the upstream rotor region.

3.3.2. Upstream half of the rotor

According to the Nomenclature, the first interference factor α_1 reduces the flow speed at the first blade pass (3.3). The local relative velocity perceived by the blade W_1 in (3.6) is found by solving the velocity triangle at each azimuthal position as depicted in Fig. 3-6, i.e., by a vector sum up of tangential (3.4) and normal velocities (3.5). ϑ represents the azimuthal displacement, r the local radius, ω the angular velocity, and δ the angle between the blade normal and the equatorial plane, nonzero for curved blades (Fig. 3-7).

$$U_1 = \alpha_1 U_0 \tag{3.3}$$

$$U_t = U_1 \cos\theta + \omega r \tag{3.4}$$

$$U_n = U_1 \sin\theta \cos\delta \tag{3.5}$$

$$W_1 = \sqrt{(U_1 \cos\theta + \omega r)^2 + (U_1 \sin\theta \cos\delta)^2} \tag{3.6}$$

The normalization of the left and right-hand sides of W_1 with U_0 in (3.7) is used later to achieve the time-averaged drag. With non-pitching blades, the angle of attack α (3.8) is given by the normal to tangential velocity ratio.

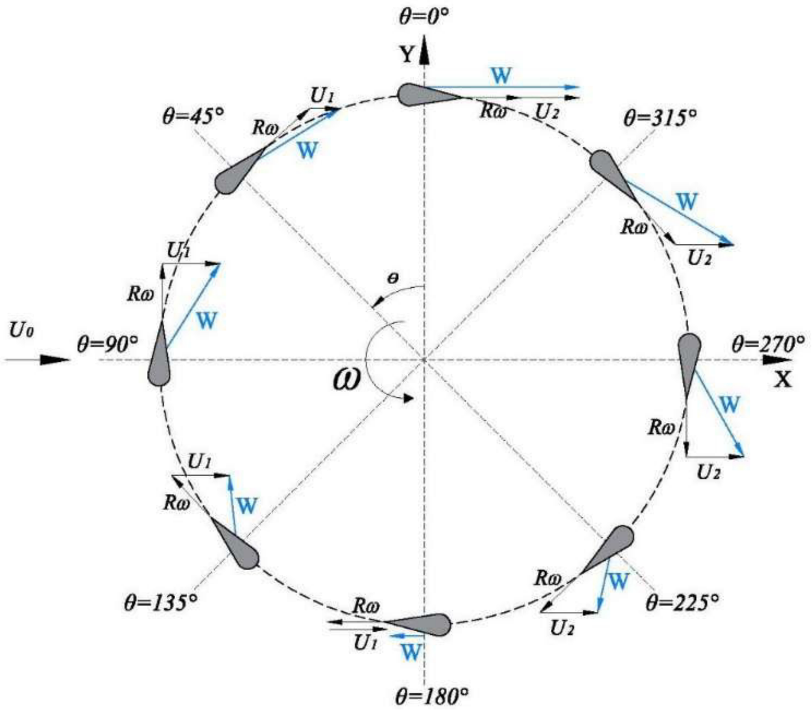

Fig. 3-6. Velocity triangles solved for all azimuthal positions.

$$\frac{W_1}{U_0} = \sqrt{\left(\alpha_1 \cos\vartheta + \frac{\omega r}{U_0}\right)^2 + (\alpha_1 \sin\vartheta \cos\delta)^2} \tag{3.7}$$

$$\alpha = \tan^{-1}\left[\frac{\alpha_1 \sin\theta \cos\delta}{\alpha_1 \cos\theta + \frac{\omega r}{U_0}}\right] \tag{3.8}$$

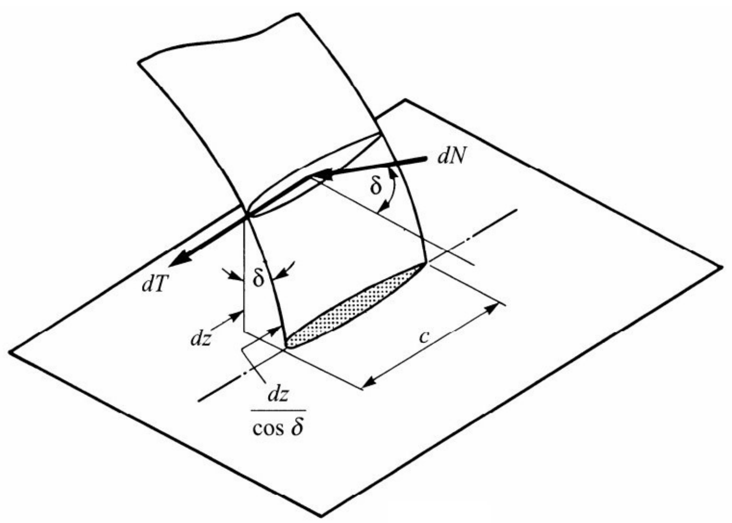

Fig. 3-7. Definition of the angle δ between the blade normal and the equatorial plane. Image from Paraschivoiu [21].

The blade rotation describes pulsating lift and drag forces generating normal and tangential components. The corresponding coefficients C_n and C_t in (3.9) and (3.10) are written in terms of the lift and drag coefficients C_l and C_d at each angle of attack.

$$C_n = C_l \cos(\alpha) + C_d \sin(\alpha) \tag{3.9}$$

$$C_t = C_l \sin(\alpha) - C_d \cos(\alpha) \tag{3.10}$$

Since the angle of attack is positive in the upstream rotor half and negative in the downstream half, these statements are valid for both the upstream and downstream halves. On the hydrofoil reference frame, a blade element with chord c and height dz is subject to a normal force dF_n and a tangential force dF_t, where $\frac{1}{2} \cdot \rho \cdot W^2$ is the relative dynamic pressure. Equations (3.11) and (3.12) are valid at each azimuthal position, with $W = W_1$ upstream and $W = W_2$ downstream.

$$dF_n = C_n \frac{\frac{1}{2}\rho W^2 c}{\cos\delta} dz \tag{3.11}$$

$$dF_t = C_t \frac{\frac{1}{2}\rho W^2 c}{\cos\delta} dz \tag{3.12}$$

According to Templin [14], the instantaneous drag force dD_1 generated on the surface of a single hydrofoil ($c*dz$) in (3.13) can be defined as a function of the azimuthal angle θ. For a single revolution, the time required for a blade crossing a streamtube once is $d\theta/2\pi$. Hence, the time-averaged drag force $D_{1,avg}$ performed by N_b blades is proportional to $(d\theta/2\pi)*N_b$ (3.14). Upstream, the average hydrodynamic drag coefficient of the ith streamtube C_{D1} (3.15.a) is written by normalizing the time-averaged drag to the dynamic drag force ($½*\rho*U_0^2$) on a streamtube of area A, in turn, replaced by $dz*r*d\theta*sin(\theta)$.

The ratio (W_1/U_0) is obtained from the previous equation (3.7). Notice that for an H-Darrieus rotor, whose local radius $r = R_T$, the quantity $N_b*c/(2R_T)$ can be substituted by the rotor solidity σ in the equation (3.15.b). The modulus of $sin(\theta)$ is used to consider the sign of the drag force component when shifting from a normal-tangential reference frame to a channel x-y reference frame.

$$dD_1 = dF_n\, sin\theta\, cos\delta - dF_t\, cos\theta = \frac{1}{2}\rho {W_1}^2 cdz \left(C_n\, sin\theta - C_t \frac{cos\theta}{cos\delta}\right) \tag{3.13}$$

$$D_{1,avg} = \frac{1}{2}\rho {W_1}^2 cdz \left(\frac{d\theta}{2\pi} N_b\right)\left(C_n\, sin\theta - C_t \frac{cos\theta}{cos\delta}\right) \tag{3.14}$$

$$C_{D1} = \frac{D_{1,avg}}{\frac{1}{2}\rho A {U_0}^2} = \left(\frac{N_b c}{2r}\right)\left(\frac{1}{\pi}\right)\left(\frac{W_1}{U_0}\right)^2 \left(C_n \frac{sin\theta}{|sin\theta|} - C_t \frac{cos\theta}{|sin\theta|\, cos\delta}\right) \tag{3.15.a}$$

$$C_{D1} = \frac{D_{1,avg}}{\frac{1}{2}\rho A {U_0}^2} = \left(\frac{\sigma}{\pi}\right)\left(\frac{W_1}{U_0}\right)^2 \left(C_n \frac{sin\theta}{|sin\theta|} - C_t \frac{cos\theta}{|sin\theta|\, cos\delta}\right) \tag{3.15.b}$$

<u>*3.3.3. Downstream half of the rotor*</u>

The second interference factor α_2 implies a further reduction of the flow speed to a value $U_2 < U_e$ in (3.16), from which the relative velocity W_2 (3.17), the ratio W_2/U_0 (3.18), and the angle of attack α (3.19) are attained. Consider that also W_2 is conventionally divided by U_0 and not by U_e, thus simplifying the discussion.

$$U_1 = \alpha_1\, U_0 \tag{3.16}$$

$$W_2 = \sqrt{(U_2\, cos\theta + \omega r)^2 + (U_2\, sin\theta\, cos\delta)^2} \tag{3.17}$$

$$\frac{W_2}{U_0} = \sqrt{\left(\alpha_2 \cos\vartheta + \frac{\omega r}{U_0}\right)^2 + (\alpha_2 \sin\vartheta \cos\delta)^2} \tag{3.18}$$

$$\alpha = tan^{-1}\left[\frac{\alpha_2\, sin\theta\, cos\delta}{\alpha_2\, cos\theta + \frac{\omega r}{U_0}}\right] \tag{3.19}$$

The downstream instantaneous drag force dD_2 in the x-y plane is now dependent on W_2 instead of W_1, and so do the average drag force $D_{2,avg}$ and the streamtube drag coefficient C_{D2}, with different normal and tangential coefficients due to the downstream position. These parameters are listed in equations (3.20-3.22). Notice that the equation (3.22.b) is attained for straight blades.

$$dD_2 = dF_n\, sin\theta\, cos\delta - \; dF_t\, cos\theta = \frac{1}{2}\rho W_2{}^2 cdz\left(C_n\, sin\theta - C_t\frac{cos\theta}{cos\delta}\right) \tag{3.20}$$

$$D_{2,avg} = \frac{1}{2}\rho W_2{}^2 cdz\left(\frac{d\theta}{2\pi}N_b\right)\left(C_n\, sin\theta - C_t\frac{cos\theta}{cos\delta}\right) \tag{3.21}$$

$$C_{D2} = \frac{D_{2,avg}}{\frac{1}{2}\rho A U_0{}^2} = \left(\frac{N_b c}{2r}\right)\left(\frac{1}{\pi}\right)\left(\frac{W_2}{U_0}\right)^2\left(C_n\frac{sin\theta}{|sin\theta|} - C_t\frac{cos\theta}{|sin\theta|\, cos\delta}\right) \tag{3.22.a}$$

$$C_{D2} = \frac{D_{2,avg}}{\frac{1}{2}\rho A U_0{}^2} = \left(\frac{\sigma}{\pi}\right)\left(\frac{W_2}{U_0}\right)^2\left(C_n\frac{sin\theta}{|sin\theta|} - C_t\frac{cos\theta}{|sin\theta|\, cos\delta}\right) \tag{3.22.b}$$

3.3.4. Turbine power

The mechanical power converted is computed from the torque generated from the tangential components of the force on blade elements. The elementary torque dQ (3.23) is the product of the local radius r to the tangential force component dF_t.

$$dQ = C_t\frac{\frac{1}{2}\rho W^2 rc}{cos\delta}dz \tag{3.23}$$

According to Strickland [16], the average rotor torque Q is the integral of all elementary torque contributions over rotor height and a revolution due to N_b blades in equation (3.24), with N_ϑ the number of azimuthal positions and N_z the number of vertical blade segments of length ($dz/cos\delta$). The product of the average torque and the angular velocity $Q{\cdot}\omega$ in (3.25) represents the turbine power.

$$Q = \frac{N_b}{N_\vartheta} \sum_{i=1}^{N_\vartheta} \sum_{j=1}^{N_z} dQ_{i,j} \tag{3.24}$$

$$P = Q\omega \tag{3.25}$$

The known undisturbed flow speed U_∞ does not appear in LMADT equations as these are developed for the volume {0,w}. U_∞ is used only at the end of the DMS procedure to normalize the thrust force T, mechanical torque Q, and the extracted power P, yielding turbine thrust, torque, and power coefficients, i.e., $C_{T,\infty} = T/(½*\rho*A_T*U_\infty^2)$, $C_{Q,\infty} = Q/(½*\rho*A_T*R_T*U_\infty^2)$, and $C_{P,\infty} = P/(½*\rho*A_T*U_\infty^3)$, respectively.

3.4. Model Corrections

The sub-models implemented in this work account for polars database extension, Prandtl's tip loss correction for straight blades, downstream flow correction due to the shading of the shaft, struts interference correction, flow curvature, and turbine depth correction. Lately, also a modified version of the streamtube expansion is introduced. Although Gormont's dynamic stall model adapted by Paraschivoiu [21] and Berg [18] was implemented into the code, since only steady state conditions are assessed in this work, the dynamic stall function is left to the background. The work of the Politecnico di Milano [23] is suggested to account for supplementary polar correction for the dynamic stall, if included.

Conventionally, a DMS streamtube model relies on Glauert's empirical correction [24] for heavily loaded streamtubes. However, this does not hold in a confined flow, where the momentum increases with the induction factor. Therefore, Glauert's correction is not incorporated since questionable whether the blockage is present.

3.4.1. Database extension

The code takes advantage of the method suggested by Battisti et al. [25], correcting the post-stall behavior of the aerodynamic profile. Relating the 3-D behavior of the blade profile in the post-stall to that of a bluff body, the 2-D polars are extended in the post-stall region with the Viterna-Corrigan's method [26], while the experimental database [27] of the hydrofoil and the separated flow curve are linked from the deep-stall angle by an interpolating function.

3.4.2. Finite aspect ratio correction (Lanchester-Prandtl's theory)

According to Abbott [28], an early wind tunnel experiment on wings demonstrated that the rate of change of C_l and C_d with the α is strongly affected by the aspect ratio (*AR*) of the tested model. The slope of the C_l curve is seen to rise progressively with the increase of the wing's *AR*, with a consistent drop in the C_d. Airplane wings of a different *AR* are observed to have the same α at zero lift Fig. 3-8 shows the effect of these findings for the wings of a different aspect ratio. The same phenomenon applies to turbine blades.

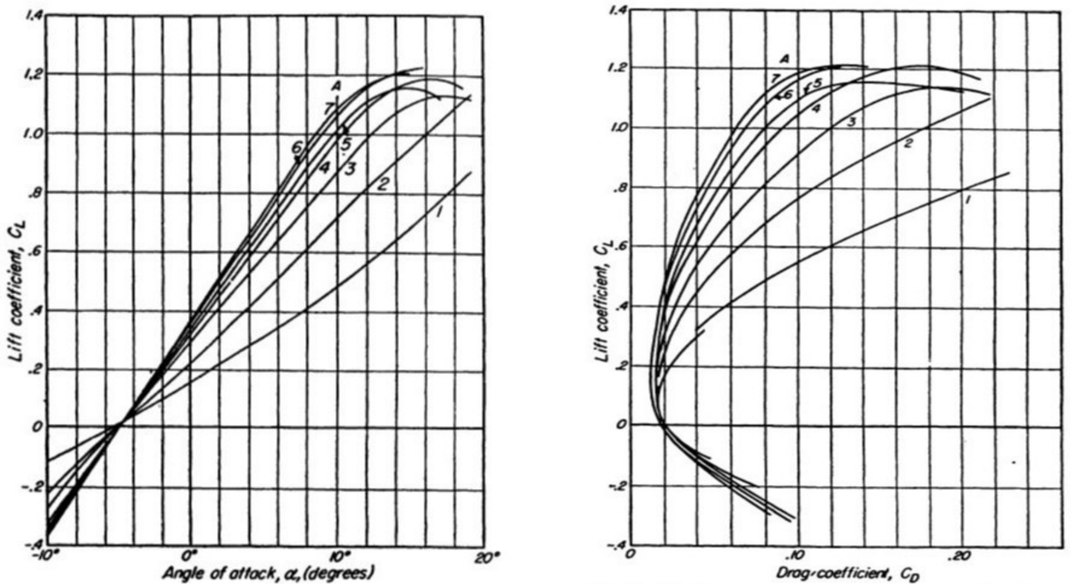

Fig. 3-8. (**Left**) Lift coefficient C_l plotted as a function of the angle of attack α for aspect ratios from 1 to 7. (**Right**) Polar diagrams for seven wings with aspect ratios from 1 to 7. Figures from Abbott [28].

A finite blade length (e.g., the straight blades of an H-Darrieus turbine) induces 3-D effects that modify lift and drag coefficients from their 2-D values. Two phenomena are described. The former is due to streamline deflection that occurs as the flow passes from high pressure to low pressure, altering the angle of attack and the hydrodynamic forces [23]. The latter is due to tip trailing vorticity being the source of the induced drag $C_{d,i}$, and downwash component of the angle of attack, leading to energy losses [29].

A correction for finite blade lengths was developed in the DMS based on Goude's work [29]. However, if the Darrieus turbine is without blade tips, the vortices released from each blade are distributed over the blade length, and the tip-loss correction is not activated, as recommended by Paraschivoiu [21].

The blade aspect ratio (3.26) is the squared blade span to the blade area ratio, reducing the span to the chord ratio for a rectangular blade. With a_0 from (3.27), the 3-D polars $C_{l,3D}$, and $C_{d,3D}$ are determined from the 2-D polars (i.e., relative to a blade of an infinite aspect ratio with all flow components orthogonal to the blade span) based on equations (3.28-3.29). These equations were derived with the assumptions of a constant α, which is accurate only at a low angle of attack where the $C_l = f(\alpha, Re)$ shows a linear trend and the assumption of tip vortices released along a straight line with an elliptical distribution. Hence, as Goude pointed out, this can result in limited accuracy when simulating straight blades.

$$AR = \frac{L}{c} \tag{3.26}$$

$$a_0 = 1.8\pi\left(1 + 0.8\frac{t}{c}\right) \tag{3.27}$$

$$C_{l,3D} = C_{d,2D} + \frac{{C_{l,2D}}^2}{1+\frac{a_0}{\pi AR}} \tag{3.28}$$

$$C_{d,3D} = C_{d,2D} + \frac{{C_{l,3D}}^2}{\pi AR} \tag{3.29}$$

3.4.3. Rotating shaft correction

This correction is implemented by computing a Gaussian velocity deficit distribution of the normal component ΔU_n downstream of the shaft. This sub-model was derived from the velocity distribution behind a cylinder, according to Hinze [30]. The wake of the rotor shaft is produced at the equilibrium velocity U_e, in turn, taken as the characteristic length to define the Reynolds number of a rotating cylinder.

The velocity deficit is calculated at a distance $x = r/D_0$, where r is the local turbine radius and D_0 is the shaft diameter. In an H-Darrieus turbine, it is simply $x = R_T/D_0$, with R_T the maximum rotor radius. Calamote's experiments [31] showed that the wake flow of a rotating cylinder is not so different from that of a fixed cylinder under normal Darrieus rotor operating conditions. Hence, the correction of the wake of a rotating cylinder with the drag coefficients of the fixed cylinder at the operating Re and λ_∞ leads to a small error.

The parameters b = 1.136, c = 0.00765, x_0 = 3.24, x_1 = 0.095 were estimated from the measurements reported in [31], [32], [33], and [34] for a fixed cylinder and $Re = 10^4$ experiencing the drag coefficient C_{D0} = 1.15. The drag is chosen according to Paraschivoiu [21], since for $300 < Re < 3 \cdot 10^5$, the Strouhal number $St = f \cdot D_0/U_e$ of a free-vortex frequency f is constant and equals 0.21. Hence, the velocity variation is replaced by the mean velocity variation $\Delta U_n/2$ acting on the radius of the shaft wake l_w.

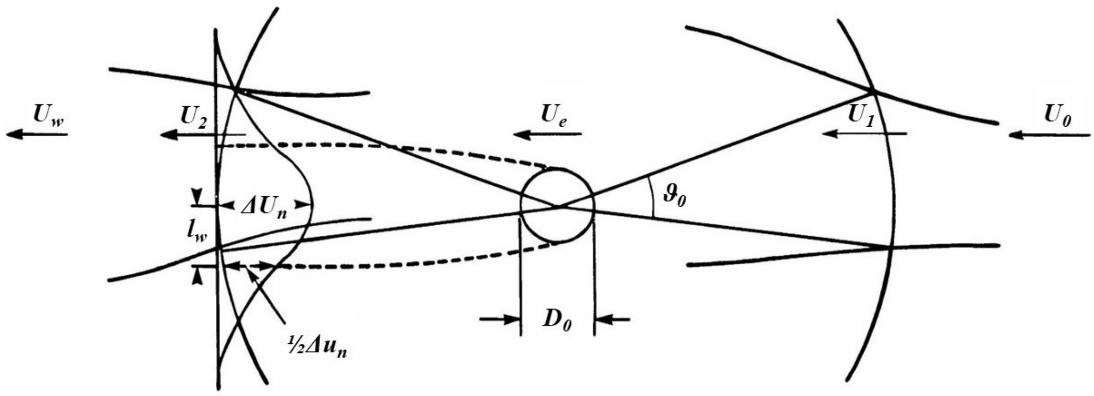

Fig. 3-9. Shaft and Gaussian induced velocity deficit from [21], with modified Nomenclature.

Once determined the lateral distance x at which the velocity deficit ΔU_n occurs, one can derive the equation (3.30) for calculating the approximated radius l_w of the shaft's wake intercepting the downstream velocity distribution illustrated in Fig. 3-9. Hence, from the velocity deficit ΔU_n attained in (3.31), a function tailored for intercept the geometry of the Gaussian velocity distribution yields the updated velocity component U_n according at each azimuthal position. The work of Paraschivoiu [21] is recommended for a more detailed description of the procedure.

$$l_w = \sqrt{D_0 c(x + x_1)} \tag{3.30}$$

$$\frac{\Delta U_n}{U_e} = \sqrt{\frac{bD_0}{x+x_0}} \tag{3.31}$$

3.4.4. Struts correction

The struts correction was introduced by Moran [35] with the overlap of a constant drag coefficient at each radial element. However, as the impact of a fixed drag is high in small Darrieus rotors, the method showed poor results. Goude et al. [36],[37] included the effect of the struts in a DMS model and considered a linear proportionality between the flow speed at the disc and the turbine center in a streamtube. It allowed finding the velocity perceived by each radial element of a strut over the radial length R_s. The present correction is very similar to Goude's implementation even though the reference frame is different, as illustrated in Fig. 3-10. Since the components of radii along the Y-axis, namely $r{*}cos(\theta)$ and $R_s{*}cos(\theta_r)$ are equal, the unknown angle perceived by the radial element θ_r is determined by equation (3.32), with r the radius of the discrete element.

$$\vartheta_r = arccos\left[\left(\frac{r}{R_S}\right) cos(\vartheta)\right] \tag{3.32}$$

The components along the x-axis are instead defined by $r{*}sin(\theta)$ and $R_s{*}sin(\theta_r)$ which ratio gives:

$$\frac{rsin(\vartheta)}{R_S sin(\vartheta_r)} = \frac{rsin(\vartheta)}{R_S sin\left(arccos\left[\left(\frac{r}{R_S}\right)cos(\vartheta)\right]\right)}$$

Since $sin(arccos\ (x)) = \sqrt{1-x^2}$, the ratio yields $\frac{rsin(\vartheta)}{\sqrt{{R_S}^2 - r^2 cos^2(\vartheta)}}$

As the angle perceived by the radial element ϑ_r is determined, the sub-model interpolates the interference factors made available by the DMS at this angle and calculates the local strut flow speed U_{rs} in equation (3.33).

$$U_{rs} = U_e + \frac{(U_1 - U_e) rsin(\vartheta)}{\sqrt{{R_S}^2 - r^2 cos(\vartheta)}} \tag{3.33}$$

Lift and drag coefficients and normal and tangential coefficients are derived after the calculating the relative velocity. Achieved the axial and tangential forces, the definition of parasitic torque and thrust is straightforward.

Rotating the reference frame by 90°, the components of radii along the X-axis, namely $r{*}sin(\theta^1)$ and $R_s{*}sin(\theta_r^1)$ are equal. Since $\theta^1 = (\theta\text{-}\pi/2)$ and $\theta_r^1 = (\theta_r\text{-}\pi/2)$, from trigonometric relations, we achieve that $sin(\theta\text{-}\pi/2) = -cos(\theta)$, and $sin(\theta_r\text{-}\pi/2) = -cos(\theta_r)$, yielding again equation (3.32). Once substituted θ^1 and θ_r^1, the components along the Y-axis are instead represented by $r{*}cos(\theta^1)$ and $R_s{*}cos(\theta_r^1)$. Since $cos(\theta\text{-}\pi/2) = sin(\theta)$, and $cos(\theta_r\text{-}\pi/2) = sin(\theta_r)$, their ratio $r{*}cos(\theta^1)/R_s{*}cos(\theta_r^1)$ yields again $r{*}sin(\theta)/R_s{*}sin(\theta_r)$, from which equation (3.33) is derived once more.

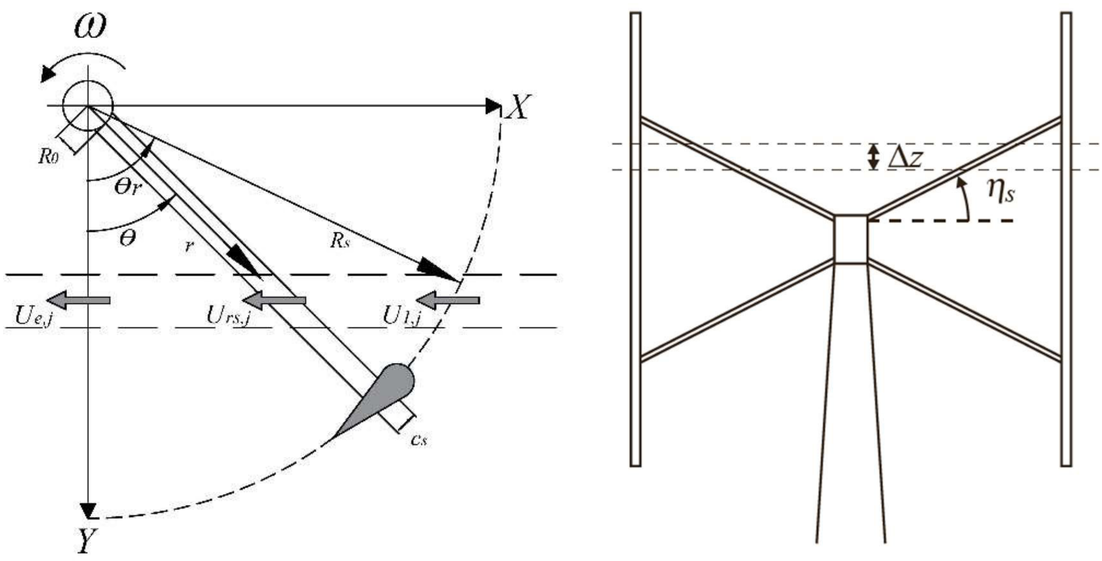

Fig. 3-10. (**Left**) Struts correction based on Goude's model modified according to this reference frame. (**Right**) Definition of the strut angle relative to the horizontal plane from [36].

Downstream, the reference frame is equivalent to that of the first quadrant, with the difference that $\theta^1 = (\theta-\pi)$ and $\theta_r^1 = (\theta_r-\pi)$. The mathematical development gives equations (3.34-3.35). Therefore, the conclusion is that (3.32-3.33) are valid for upstream azimuthal angles, while equations (3.34-3.35) for downstream, respectively. The relative velocity, angle of attack, and axial and tangential forces are based on equations (3.36-3.39), contributing to the local torque and power. According to Goude, equations (3.36-3.38) are different from (3.6), (3.8), and (3.14) due to the definition of the angle η and because of the discretization made in the radial direction.

$$\vartheta_r = arccos\left[\left(\frac{r}{R_s}\right)cos(\vartheta-\pi)\right]+\pi \quad (3.34)$$

$$U_{rs} = U_2 + \frac{(U_e-U_2)rsin(\vartheta-\pi)}{\sqrt{{R_s}^2-r^2\,cos(\vartheta-\pi)}} \quad (3.35)$$

$$W_{rs} = \sqrt{(U_{rs}\,cos\theta+\omega r)^2+(U_{rs}\,sin\theta\,sin\eta)^2} \quad (3.36)$$

$$\alpha_s = tan^{-1}\left[\frac{sin\theta\,sin\eta}{cos\theta+\frac{\omega r}{U_{rs}}}\right] \quad (3.37)$$

$$dD_{rs} = \frac{N_b c\rho {W_{rs}}^2}{4\pi}\,d\vartheta d_{rs}\left(C_n\,sin\theta\,tan\eta - C_t\frac{cos\theta}{cos\eta}\right) \quad (3.38)$$

$$dF_{t,rs} = C_t\frac{1}{2}\rho {W_{rs}}^2 c d_{rs} \quad (3.39)$$

3.4.5. Flow curvature correction

To account for the flow curvature, the equation included in the adaptation of Sharpe [38] and applied by Goude [36] is implemented in this code. The method corrects the normal force coefficient after the variation in the angle of attack. The equation results from a conformal mapping technique about the rotation of a flat plate which is included in the brilliant work of Goude.

As the blade rotates leads to additional curvature effects that slightly modify the effective angle of attack. Considering straight streamtubes, the equation derived from conformal mapping is indicated in (3.40). Notice that ϑ_p represents the blade pitch angle, x_{0r} the normalized blade attachment point offset, W the relative velocity, ω the radian velocity, c the blade chord, and U_D the disc-induced flow speed. Notice that the second term represents the local normal to tangential velocity ratio. As remarked by Goude, this equation is included in Sharpe's adaptation with the assumption that the curvature acts only in the normal direction and that the mounting point is at the center of the blade (x_{0r} = 0) for the simulations presented in Chapter 6. Although implemented, the mounting point is left x_{0r} = 0. With this, the normal force coefficient C_n (3.41) is reduced by the quantity (3.40), assuming the correction factor $a_s = C_{n,0}/\alpha$.

$$\alpha = \vartheta_p + \frac{U_D\, sin\theta\, cos\delta}{U_D\, cos\theta + \omega r} - \frac{\omega x_{0r} c}{W} - \frac{\omega c}{4W} \tag{3.40}$$

$$C_n = C_{n,0} - \frac{a_s \omega c}{4W} \tag{3.41}$$

3.4.6. Turbine depth correction

The quasi-1-D theory does not differentiate between different submergence depths, but momentum equations can be modified slightly according to the method shown in Chapter 2. It leads to a variation in the incidence of extra force due to the free surface variation based on the turbine's vertical placement. The method explained in Chapter 2 is applied directly to the rotor, considered as a single body subject to the effect of the overlying flow, with outputs disclosed in Chapter 6. The method applied to DMS consists of initializing the starting depth d_h from the still water level and thus deriving the depth parameter, which is forwarded to the DMS function. This procedure is iterated for all cycles, interacting with the inflow correction.

3.4.7. Streamtube expansion

This correction extends our previous work based on straight streamtubes [1]. The models from the literature are applicable only partially to the confined DMS model. An assumption in the model of Paraschivoiu [21] is that the velocity direction does not vary, even though the multiple streamtubes are allowed to expand horizontally on a 2-D plane. An implementation issue occurs if the blade does not intercept some tube in the downstream half. Recently, a sub-model predicting an enlargement factor to correct the downstream interference factor calculated without expansion was implemented by Bangga et al. [39].

A change in the flow direction was added in the work of Read and Sharpe [40]. However, a reliable solution for a 2-D and 3-D flow expansion was found by Goude, who determined equations to calculate the dimensionless streamtube width and height at each station. A strength of this method was not only the 3-D spatial development but the ease of the blade azimuthal displacement at the downstream half of the rotor.

The implementation of Paraschivoiu required a change in $\Delta\vartheta$ at each downstream half of the tube, dictating the first streamtube starting from the axis in the flow direction. Goude overcame this issue by allowing the downstream part to be served by independent streamtubes avoiding a change in the azimuthal displacement. Besides this improvement, the downstream interference factor at the equilibrium plane is by interpolation.

The equilibrium interference factor was determined as $\alpha_e = (2\alpha_1\text{-}1)$ in all mentioned methods, implying that their validity does not hold in a confined problem. It adds an issue for the interpolation at the equilibrium station to determine the downstream interference factors. In a 2-D actuator disc, the equilibrium interference factor is defined as $\alpha_e = \alpha_1 * (l_1/l_e)$ so that the previous mathematical statement does not hold.

This work suggests combining Goude and Paraschivoiu's methods, extending the equation for allowing the streamtube expansion to fit the confined Double Multiple Streamtube. The sub-model is set as specified by Goude. Moreover, the equations are determined for both 2-D and 3-D problems, even though the implementation follows the planar development only (2-D), due to clarifying uncertainties of streamtube expansion in the vertical direction straddling the free surface variation, invoking the streamtube contraction visualized in different porous plate tests [41].

The scheme in Fig. 3-11 is achieved from Goude's sub-model with nomenclature adapted to this work. The terms indicated with b represent a streamtube width, and the terms denoted with a represent the dimensionless expansion factors for the upstream half of the rotor, i.e., $a_{y,0}$, $a_{z,0}$, $a_{y,e}$, and $a_{z,e}$. Subscript y refers to the horizontal axis, while subscript z refers to the vertical axis. The expansion factors for the station {0} are given by $a_{y,0} = (1-b_{y,0})$ and $a_{z,0} = (1-b_{z,0})$. For the equilibrium station {e}, these are $a_{y,e} = (b_{y,e}-1)$ and $a_{z,e} = (b_{z,e}-1)$, respectively. The horizontal expansion factors are also defined based on the turbine diameter-to-height ratio in (3.42) and (3.43).

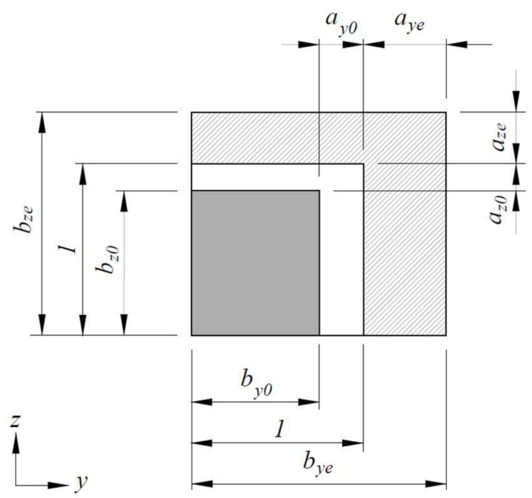

Fig. 3-11. Drawing according to Goude's model [36] of the streamtube cross-section with nomenclature updated for this work. The filled rectangle represents the streamtube at the upstream station {0}, the white rectangle is the upstream disc cross-section {1} normalized to unit length, while the hatched rectangle is the cross-section at the equilibrium station {e}.

$$a_{y,0} = \left(\frac{D_t}{H_t}\right) a_{z,0} \tag{3.42}$$

$$a_{y,e} = \left(\frac{D_t}{H_t}\right) a_{z,e} \tag{3.43}$$

By stating the mass conservation between the streamtube stations, one achieves $A_0 = \alpha_1 {*} A_1$ within {0,1}, and $\alpha_1 {*} A_1 = \alpha_e {*} A_e$ within {1,e}. Since $A_0 = b_{y,0} {*} b_{z,0}$, $A_1 = b_{y,1} {*} b_{z,1} = 1$, and $A_e = b_{y,e} {*} b_{z,e}$, one achieves equations (3.44) and (3.45).

$$b_{z,0} = \frac{\alpha_1}{b_{y,0}} \tag{3.44}$$

$$b_{z,e} = \frac{\alpha_1}{\alpha_e b_{y,e}} \tag{3.45}$$

Replacing $b_{z,0}$ and $b_{z,e}$ (3.44-3.45) into the statements $a_{y,0} = (1-b_{y,0})$ and $a_{z,0} = (1-b_{z,0})$ for the station {0}, and $a_{y,e} = (b_{y,e}-1)$ and $a_{z,e} = (b_{z,e}-1)$ for the station {e}, equations (3.42-3.43) are developed further:

$$1 - b_{y,0} = \left(\frac{D_t}{H_t}\right)\left(1 - \frac{\alpha_1}{b_{y,0}}\right)$$

$$b_{y,e} - 1 = \left(\frac{D_t}{H_t}\right)\left(\frac{\alpha_1}{\alpha_1 b_{y,e}} - 1\right)$$

The horizontal dimensionless widths b_{y0} and b_{ye} are determined by solving the square root of the equations above, yielding (3.46) and (3.47).

$$b_{y,0} = \frac{1}{2} - \frac{D_t}{2H_t} + \sqrt{\left(\frac{D_t}{2H_t} - \frac{1}{2}\right)^2 + \alpha_1 \frac{D_t}{H_t}} \tag{3.46}$$

$$b_{y,e} = \frac{1}{2} - \frac{D_t}{2H_t} + \sqrt{\left(\frac{D_t}{2H_t} - \frac{1}{2}\right)^2 + \frac{\alpha_1}{\alpha_e}\frac{D_t}{H_t}} \tag{3.47}$$

These outputs are significantly different from Goude's, as (3.46-3.47) are derived by treating the interference factor at the equilibrium station as unknown. Reversing the definitions of the expansion factors $b_{z0} = 1-a_{z,0}$, $b_{z,e} = 1+a_{z,e}$, and achieved $a_{z,0}$ and $a_{z,e}$ from equations (3.42-3.43), one determines the vertical dimensionless heights (3.48-3.49).

$$b_{z,0} = 1 - \left(\frac{H_t}{D_t}\right)\left(1 - b_{y,0}\right) \tag{3.48}$$

$$b_{z,e} = 1 - \left(\frac{H_t}{D_t}\right)\left(1 - b_{y,e}\right) \tag{3.49}$$

Once the expansion factors $b_{y,0}$, $b_{y,e}$, $b_{z,0}$ and $b_{z,e}$, are known, the size of the streamtubes is achieved from (3.50-3.53). Horizontal and vertical lengths $\Delta l_{y,1}$ and $\Delta h_{z,1}$ are known from the azimuthal and vertical discretization.

$$\Delta l_{y,0} = b_{y,0}\Delta l_{y,1} \tag{3.50}$$

$$\Delta h_{z,0} = b_{z,0}\Delta h_{z,1} \tag{3.51}$$

$$\Delta l_{y,e} = b_{y,e}\Delta l_{y,1} \tag{3.52}$$

$$\Delta h_{z,e} = b_{z,e}\Delta h_{z,1} \tag{3.53}$$

Hence, the coordinate of each streamline from the centerline is performed by integrating along the horizontal axis (3.54) and the vertical axis (3.55), for any *j*th station and *i*th vertical element. respectively, i.e., $L_j = \Sigma\ \Delta l_{y,j}$ and $H_i = \Sigma\ \Delta h_{z,i}$.

The equations for the downstream disc (3.54-3.55) are slightly different from Goude's equations developed for an unconfined flow. The stations {2} and {w} relate to the second disc and the near-wake, respectively. Once all remaining expansion factors are calculated (3.56-3.57), the previous procedure is repeated, thus finding streamtubes sizes and positions.

$$b_{y,e} = \frac{1}{2} - \frac{D_t}{2H_t} + \sqrt{\left(\frac{D_t}{2H_t} - \frac{1}{2}\right)^2 + \frac{\alpha_2}{\alpha_e}\frac{D_t}{H_t}} \tag{3.54}$$

$$b_{y,w} = \frac{1}{2} - \frac{D_t}{2H_t} + \sqrt{\left(\frac{D_t}{2H_t} - \frac{1}{2}\right)^2 + \frac{\alpha_2}{\alpha_w}\frac{D_t}{H_t}} \tag{3.55}$$

$$b_{z,e} = 1 - \left(\frac{H_t}{D_t}\right)\left(1 - b_{y,e}\right) \tag{3.56}$$

$$b_{z,w} = 1 - \left(\frac{H_t}{D_t}\right)\left(1 - b_{y,w}\right) \tag{3.57}$$

Although the azimuthal positions of the downstream disc are identical to those obtained with straight tubes, the method for the downstream part differs slightly from Paraschivoiu's and Goude's models. According to the actuator disc extension [1], the interference factors α_1 and the drag coefficient C_{D1} are required to calculate α_2 and α_w. Instead of interpolating to yield new equilibrium interference factors α_e (as suggested by Goude) or altering the downstream azimuthal angles (as illustrated by Paraschivoiu), this procedure implies that each streamtube is solved twice. The streamtubes are first solved regularly to define the outputs of the upstream part and to determine a first-attempt value to assign to the downstream half. Thus, an iterative cycle is performed to minimize the error on the width of each streamtube at the equilibrium station. It implies a reshaping the upstream part of the streamtubes as depicted in Fig. 3-12.

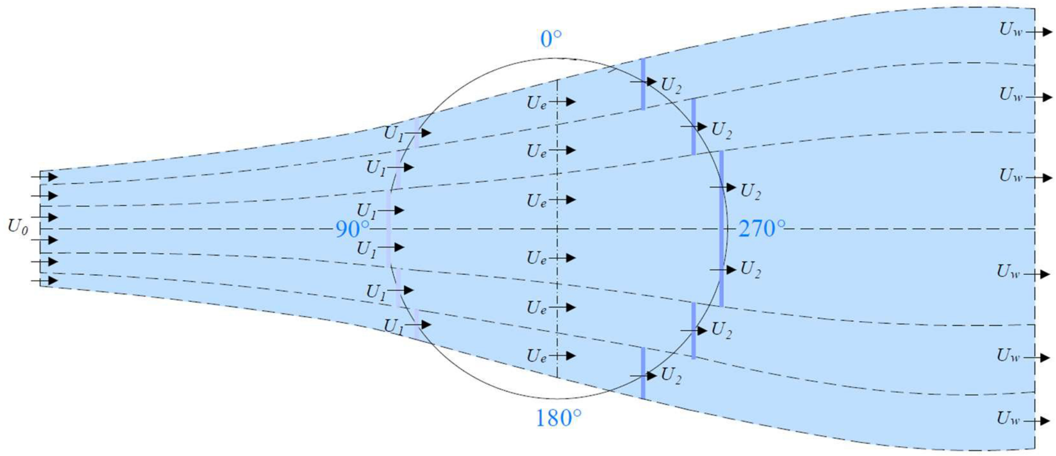

Fig. 3-12. Upstream tubes reshaped to yield corrected equilibrium interference factors α_e, allowing solving the downstream discs at fixed azimuthal positions.

The reshape is necessary to yield the new α_e and solve the downstream disc, whose position remains fixed. Therefore, the outputs of the upstream part are achieved from the first computation, while the outputs of the downstream part are achieved from the iterative method. The final streamtubes do not coincide. However, this sub-model avoids miscalculations for the most lateral streamtubes, as illustrated by Paraschivoiu. This correction is included in the additional assessment of the tested turbine, presented in Chapter 6.

Although not essential, the method allows calculating the size of the accelerated annulus bypassing the second disc to be made explicit. The total flow rate passing through the rotor equals the sum of all upstream tube contributions. It is higher than the flow rate passing through the downstream wake (Fig. 3-13), and thus, the annular distribution represents their difference due to continuity.

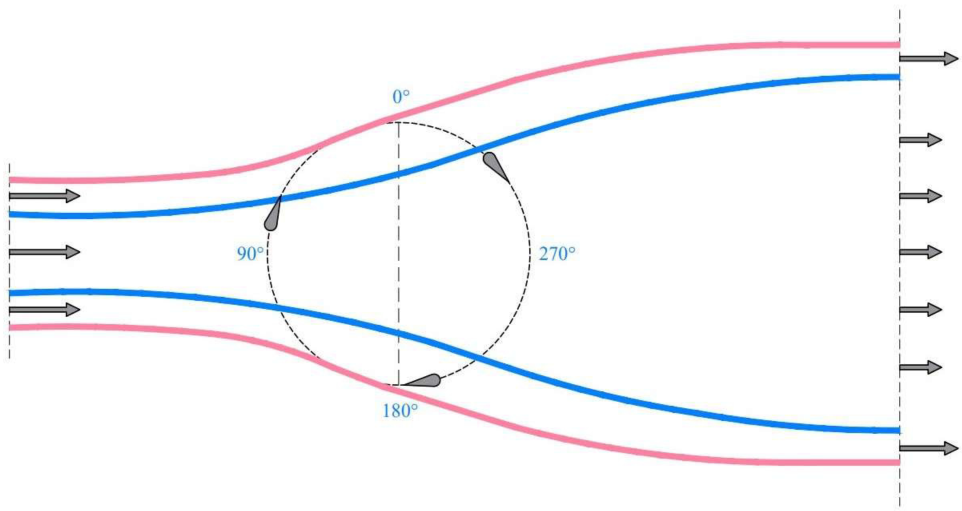

Fig. 3-13. Final result of the streamtube expansion sub-model.

According to the Nomenclature of Chapter 2, denoting with A_e and A_u, the areal extensions of upstream wake and downstream wake at an equilibrium station, and denoting with A_γ and A_W, the areal extensions of annular and downstream wakes, the annular continuity states $(A_e\text{-}A_u)*\alpha_e = (A_\gamma\text{-}A_w)*\gamma_w$. Since $A_e = b_{y,e}*b_{z,e}$, $A_u = b_{y,u}*b_{z,u}$, $A_\gamma = b_{y,\gamma}*b_{z,\gamma}$, and $A_w = b_{y,w}*b_{z,w}$, the annular continuity becomes:

$$\alpha_e\left(b_{y,e}b_{z,e} - b_{y,u}b_{z,u}\right) = \gamma_w\left(b_{y,\gamma}b_{z,\gamma} - b_{y,w}b_{z,w}\right)$$

Since $A_u = \alpha_2/\alpha_e$ and $A_w = \alpha_2/\alpha_w$ due to the downstream wake continuity with turbine area A_T = 1, the vertical expansion factors are achieved in equations (3.58) and (3.59) and substituted into the annular continuity yield equation (3.60).

$$b_{z,u} = \frac{\alpha_2}{b_{yu}\alpha_e} \tag{3.58}$$

$$b_{z.w} = \frac{\alpha_2}{b_{yw}\alpha_w} \tag{3.59}$$

$$\alpha_1 - \alpha_2 = \gamma_w b_{y,\gamma} b_{z,\gamma} - \gamma_w \frac{\alpha_2}{\alpha_w} \tag{3.60}$$

By using the horizontal and vertical expansion factors $a_{y\gamma} = (b_{y\gamma}\text{-}b_{yw})$ and $a_{z\gamma} = (b_{z\gamma}\text{-}b_{zw})$ into the expression $a_{y\gamma} = (D_T/H_T)*a_{z,\gamma}$, yields equation (3.61). Replacing $b_{z,w}$ with equation (3.57), the vertical dimensionless streamtube size $b_{z\gamma}$ is determined in (3.62).

$$\left(b_{y,\gamma} - b_{y,w}\right) = \left(\frac{D_t}{H_t}\right)\left(b_{z,\gamma} - b_{z,w}\right) \tag{3.61}$$

$$b_{z,\gamma} = 1 - \left(\frac{H_t}{D_t}\right)\left(1 - b_{y,\gamma}\right) \tag{3.62}$$

Using (3.64) in the continuity (3.62), one achieves the quadratic equation:

$$b_{y\gamma}{}^2\left(\frac{H_t}{D_t}\right) - b_{y\gamma}\left(\frac{H_t}{D_t} - 1\right) - \psi = 0$$

Notice that ψ represents the dimensionless area of the downstream wake (3.65) and equals equation (2.15), achieved for the algebraic development of the double-disc. Therefore, ψ is calculated since all factors are known, and the quadratic is developed, yielding equation (3.66).

$$\psi = \frac{1}{\gamma_w}\left[\alpha_1 + \frac{\alpha_2}{\alpha_w}\left(\gamma_w - \alpha_w\right)\right] \tag{3.65}$$

$$b_{y,\gamma} = \frac{1}{2} - \frac{D_t}{2H_t} + \sqrt{\left(\frac{D_t}{2H_t} - \frac{1}{2}\right)^2 + \psi\frac{D_t}{H_t}} \tag{3.66}$$

Horizontal and vertical dimensions of the annular element are given by (3.67-3.68).

$$\Delta l_{y,\gamma} = b_{y\gamma}\Delta l_{y,2} \tag{3.67}$$

$$\Delta l_{z\gamma,} = b_{z\gamma}\Delta h_{z,2} \tag{3.68}$$

The annular size is achieved by integrating all discrete components, i.e., $L_\gamma = \Sigma\ \Delta l_{y,\gamma}$ and $H_\gamma = \Sigma\ \Delta h_{z,\gamma}$. The most lateral values of the matrix of γ_w represent the annular interference factors to be included, in case, in the wake development.

REFERENCES

[1] Cacciali L., Battisti L., Dell'Anna S. Free Surface Double Actuator Disc Theory and Double Multiple Streamtube Model for In-Stream Darrieus Hydrokinetic Turbines. Ocean Engineering **2022**, 260, 112017.

[2] Bachant, P., Wosnik, M. Modeling the Near-Wake of a Vertical-axis Cross-Flow Turbine with 2-D and 3-D RANS. Journal of Renewable and Sustainable Energy **2016**, 8, 053311.

[3] Doan Minh N., Obi S. Numerical Study of the Dynamic Stall Effect on a Pair of Cross-Flow Hydrokinetic Turbines and Associated Torque Enhancement Due to Flow Blockage. Journal of Marine Science and Engineering **2021**, 9, 829.

[4] Kinsey T., Dumas G. Impact of Channel Blockage on the Performance of Axial and Cross-Flow Hydrokinetic Turbines. Renewable Energy **2017**, 103, 239-254.

[5] Consul C.A., Willden R.H.J., McIntosh S. Blockage Effects on the Hydrodynamic Performance of a Marine Cross-Flow Turbine. Philosophical Transactions of the Royal Society A **2013**, 371, 0299.

[6] Shives M., Crawford C., Grovue S. A Tuned Actuator Cylinder Approach for Predicting Cross-Flow Turbine Performance with Wake Interaction and Channel Blockage Effects. International Journal of Marine Energy **2017**, 18, 30–56.

[7] Shashikumar C.M., Ramesh Honnasiddaiah, Vijaykumar Hindasageri, Vasudeva Madav. Experimental and Numerical Investigation of Novel V-Shaped Rotor for Hydropower Utilization. Ocean Engineering **2021**, 224, 108689.

[8] Shashikumar C.M., Vijaykumar Hindasageri, Vasudeva Madav. Numerical Investigation of Conventional and Tapered Savonius Hydrokinetic Turbines for Low-Velocity Hydropower Application in an Irrigation Channel. Sustainable Energy Technologies and Assessments **2021**, 43, 100871.

[9] Shashikumar C.M., Vasudeva Madav. Numerical and Experimental Investigation of Modified V-Shaped Turbine Blades for Hydrokinetic Energy Generation. Renewable Energy **2021**, 177, 1170-1197.

[10] Shashikumar C.M., Vijaykumar Hindasageri, Vasudeva Madav. CFD Investigation of Unsteady Three-Dimensional Savonius Hydrokinetic Turbine in Irrigation Channel with Varying Positions for Hydro Power Application. AIP Conference Proceedings 2316 030028 (**2021**).

[11] Allsop S., Peyrard C., Thies P.R., Boulougouris E., Harrison G.P. A Validated BEM Model to Analyse Hydrodynamic Loading on Tidal Stream Turbine Blades. AWTEC Asian Wave and Tidal Energy Conference (**2016**).

[12] Vogel C.R., Willden R.H.J., Houlsby G.T. Blade Element Momentum Theory for a Tidal Turbine. Ocean Engineering **2018**, 169, 215-226.

[13] Glauert H. Wind Tunnel Interference on Wings, Bodies and Airscrews, Aeronautical Research Committee Reports and Memoranda, 1566 (**1933**).

[14] Templin R. Aerodynamic Performance Theory for the NRC Vertical Axis Wind Turbine. LTR-LA-190, NRC lab, Tech. Rep., (**1974**).

[15] Wilson R.E., Lissaman P.B. Applied Aerodynamics of Wind Power Machines, Corvallis, Oregon, p. 117, (**1974**).

[16] Strickland J.H. The Darrieus Turbine, A Performance Prediction Method Using Multiple Stream Tubes, Sandia National Laboratories, Albuquerque, New Mexico, Tech. Rep., (**1975**).

[17] Paraschivoiu I., Delclaux F., Double Multiple Streamtube Model with Recent Improvements. Journal of Energy **1983**, 250–255.

[18] Berg D. An Improved Double-Multiple Streamtube Model for the Darrieus-type Vertical Axis Wind Turbine. 6th B. Wind Energy Conference and Workshop, Minneapolis, (**1983**).

[19] Paraschivoiu I., Desy P., Masson C. Blade-Tip, Finite-Aspect Ratio and Dynamic-Stall Effects on the Darrieus Rotor. AIAA Journal of Propulsion and Power **1988**, 4, 73-80.

[20] Whelan J., J. Graham J., Peiró J. A Free-Surface and Blockage Correction for Tidal Turbines. Journal of Fluid Mechanics **2009**, 624, 281-291.

[21] Paraschivoiu I. Wind Turbine Design. With Emphasis on Darrieus Concept. Presses Internationales Polytechnique, ISBN 978-2-553-00931-0, Canada, (**2009**).

[22] McIntosh S.C., Babinsky H. Convergence Failure and Stall Hysteresis in Actuator-Disk Momentum Models Applied to Vertical Axis Wind Turbines. Journal of Solar Energy Engineering **2009**, 131, 3.

[23] Galetta M. Impact of Dynamic Stall on VAWT Performance: Implementation into a Double Multiple Stream-Tube Tool and Quantification of Model Uncertainty. Politecnico di Milano, Dipartimento di Energia. Master Thesis (**2019**).

[24] Glauert H. Airplane Propellers. Aerodynamic Theory. Springer Berlin Heidelberg, 169-360 (**1935**).

[25] Battisti L., Zanne L., Raciti Castelli M., Bianchini A., Brighenti A. A Generalized Method to Extend Airfoil Polars Over the Full Range of Angles of Attack. Renewable Energy **2020**, 155, 862-875.

[26] Viterna L.A., Corrigan R.D., Fixed Pitch Rotor Performance of Large Horizontal Axis Wind Turbines. Large Horizontal-Axis Wind Turbines. DOE/NASA Workshop on Large Horizontal Axis Wind Turbines, Cleveland, Ohio, 69-85 (**1982**).

[27] Sheldehl R., Klimas P. Aerodynamic Characteristics of Seven Airfoil Sections through 180-Degree Angle of Attack. Sandia National Laboratories: Energy Report (**1981**).

[28] Abbott I.H., Von Doenhoff A.E. Theory of Wing Sections, Section 1.4 (**1959**).

[29] Goude A., Ågren O. Numerical Simulation of a Farm of Vertical Axis Marine Current Turbines. Proceedings of the ASME 2010 29th International Conference on Ocean, Offshore and Arctic Engineering. 29th International Conference on Ocean, Offshore and Arctic Engineering 3. Shanghai, China. 335-344. ASME (**2010**).

[30] Hinze J.O. Turbulence, 2nd ed., McGraw-Hill Series in Mechanical Engineering, New York, Chapter 6, (**1975**).

[31] Calamote J. Cylindres Tourants-Visualizations et Expériences. Institut de Mécanique Statistique de la Turbulence, Marseilles, Frances, COMES Report 81-3198, (**1982**).

[32] Townsend A.A. The Structure of Turbulent Shear Flow. Cambridge University Press (**1976**).

[33] Alexopoulos C.C., Keffer J.F. Extended Measurements of the 2-Dimensional Turbulent Wake. University of Toronto, Department of Mechanical Engineering, Technical Report 6811 (**1968**).

[34] Frauniè P. Contribution a l'Etude des Champs Dynamique et Thermique dans le Sillage de Deux Cylindres de Section Circulaire. Doctoral Thesis, Institut de Mechanique Statistique de la Turbulence, Marseilles, France (**1979**).

[35] Moran W.A. Giromill Wind Tunnel Test and Analysis. Volume 1: Executive summary. Final Report, McDonnell Aircraft Co., Saint Louis, MO., (**1977**).

[36] Goude A. Fluid Mechanics of Vertical Axis Turbines Simulations and Model Development. Thesis Dissertation, Uppsala Universitet, **2012**.

[37] Goude A., Lundin S., Leijon M. A Parameter Study of the Influence of Struts on the Performance of a Vertical-Axis Marine Current Turbine. EWTEC 8th European Wave and Tidal Energy Conference, Uppsala, Sweden, **2009**.

[38] Sharpe D.J. Refinements and Developments of the Multiple Streamtube Theory for the Aerodynamic Performance of Vertical Axis Wind Turbines. In Proceedings of the BWEA Wind Energy Conference, 146–159, (**1984**).

[39] Bangga G., Dessoky A., Lutz T., Krämer E. Improved Double-Multiple-Streamtube Approach for H-Darrieus Vertical Axis Wind Turbine Computations. Energy **2019**, 182, 673-688.

[40] S. Read and D. J. Sharpe. An Extended Multiple Streamtube Theory for Vertical Axis Wind Turbines. 2nd BWEA workshop, Cranfield, UK, 65-72, (**1980**).

[41] Schmitz C., Pelz P. Upper Limit for Tidal Turbines. 30th IAHR Symposium on Hydraulic Machinery and Systems. IOP Conf. Series: Earth and Environmental Science, 774, 012127 (**2021**).

NOMENCLATURE

A	Streamtube area m^2	Re	Reynolds number, ($\rho{*}W{*}c/\mu$)
AR	Blade aspect ratio, (L/c)	R_T	Turbine radius m
A_T	Turbine swept area m^2	R_s	Strut radial length m
a_i	Axial induction factor	r_i	Local radius m
a_0	Correction factor due to blade AR	St	Strouhal number, ($f{*}D_0/U_e$)
a_s	Correction factor for $C_{n,0}$	T	Axial thrust force N
a_y	Horizontal dimensionless expansion factor	t	Blade thickness m
a_z	Vertical dimensionless expansion factor	U	Flow speed m/s (see subscripts)
a_1	Upstream axial induction factor, ($1-\alpha_1$)	U_{rs}	Strut discrete element flow speed m/s
a_2	Downstream axial induction factor, ($1-\alpha_2$)	W	Relative flow speed m/s
B	Blockage ratio, ($A_T/(w{*}h_0)$)	w	Channel width m
b_y	Dimensionless streamtube width	x	Distance of the velocity deficit, (r_i/D_0)
b_z	Dimensionless streamtube height	x_{0r}	Blade mounting point
C_D	LMADT drag coefficient, ($D/½{*}\rho{*}A_T{*}U_0^2$)	y_j	Spanwise streamline coordinate
C_P	LMADT power coefficient, ($P/½\rho{*}A_T{*}U_0^3$)	z_j	Vertical streamline coordinate
$C_{P,\infty}$	Turbine power coefficient, ($P/½{*}\rho{*}A_T{*}U_\infty^3$)	α	Angle of attack, deg
$C_{T,\infty}$	Turbine thrust coefficient, ($T/½{*}\rho{*}A_T{*}U_\infty^3$)	α_i	Disc interference factor
C_d	Hydrofoil drag coefficient, (2-D and 3-D)	Δh	Depth variation m
C_l	Hydrofoil lift coefficient, (2-D and 3-D)	Δl_y	Horizontal streamtube width at the disc
C_n	Hydrofoil normal coefficient	Δh_z	Vertical streamtube height at the disc
C_t	Hydrofoil tangential coefficient	ΔU_n	Normal velocity deficit m/s
c	Blade chord m	δ	Blade normal to equatorial plane angle deg
D	Drag force N	ε	Numerical accuracy
D_0	Shaft diameter m	η	Strut normal to equatorial plane angle deg
D_T	Turbine diameter m	ϑ	Azimuthal displacement deg
d	Drag force per unit length N/m	ϑ_r	Strut element azimuthal displacement deg
dD	Elementary drag force N	λ_∞	Tip speed ratio ($\omega{*}R_T/U_\infty$)
dF_n	Elementary normal force N	μ	Fluid-dynamic viscosity $Pa{*}s$
dF_t	Elementary tangential force N	ξ	Depth parameter, ($d_h/(2H_T)$)
d_h	Distance from water level to turbine top m	ρ	Fluid density kg/m^3
dQ	Elementary torque Nm	ω	Angular velocity rad/s
dz	Discrete vertical element m		
$d\vartheta$	Discrete azimuthal displacement deg	*Subscripts*	
Fr	Froude number, ($U_0/(g{*}h_0)^{½}$)	∞	Undisturbed flow
g	Gravity acceleration m/s^2	0	Inflow
H_T	Turbine height m	1	Flow at the upstream disc
h_0, h_w	Water depth m	e	Flow at the equilibrium
L	Blade length m	2	Flow at the downstream disc
l	Lift force per unit length N/m	w	Near-wake flow
l_w	Shaft wake radius m		
N_b	Number of blades	*Short forms*	
N_z	Number of vertical blade segments	*BEM*	Blade Element Momentum
N_ϑ	Number of blade azimuthal positions	*DMS*	Double Multiple Streamtube
P	Turbine power W	*LMADT*	Linear Momentum Actuator Disc Theory
Q	Mechanical torque Nm	*VAWT*	Vertical-axis wind turbines

4. INFLOW AND BACKWATER ASSESSMENT

Chapter adapted to the content of the article:

> *Cacciali L., Battisti L., Dell'Anna S. Backwater Assessment for the Energy Conversion through Hydrokinetic Turbines in Subcritical Prismatic Canals, Ocean Engineering 2023, 267, 113246. DOI: https://doi.org/10.1016/j.oceaneng.2022.113246.*

Hydrokinetic turbines partially exploit the total head variation created in natural and artificial waterways. In subcritical flows, the sum of the mechanical energy harvested, and the dissipated energy by fluid-dynamic losses and viscous friction, is balanced through the backwater extending far upstream. The latter depends on the turbine operating condition and, thus, on the thrust force generated. Only the downstream momentum is known, while upstream momentum and turbine thrust force are undetermined. To solve this problem, the method illustrated in [1] allows updating the inflow factor for a single turbine, thus achieving a single physical solution. Froude number and blockage ratio are updated at each iteration and used as independent variables for solving the turbine model. According to the actual canal geometry, a specific continuity equation allows inferring the backwater depth from the inflow factor. Hence, this method is integrated with the confined DMS model presented in Chapter 3 to extend the capability of the simulation tool. Experimental data of inflow depth are used to validate this model for single rotors in a subcritical environment.

4.1. The Problem of the Hydraulic Transition

The following experimental and theoretical literature was considered, concerning the hydraulic problem of HK turbines deployed in subcritical flows. Myers and Bahaj [2] tested an axial-flow hydrokinetic turbine in a circulating water channel to investigate the free surface impacts, showing an increase in depth upstream of the rotor, a free surface drop downstream due to the power extraction, and a rise in water depth further downstream due to the wake reaching the free surface. The authors proved that the location of the water depth cusp moves downstream with increased flow speed. Kartezhnikova and Ravens [3] assessed a uniform distribution of turbines on the free surface variation and depth-averaged flow speed by modeling an enhanced bottom roughness, demonstrating that the hydraulic impact agrees with alternative approaches, even though near-field free surface variation cannot be calculated with this technique. Kirke [4] clarified fundamental aspects regarding energy extraction in rivers, emphasizing that hydrokinetic turbines alter the total energy of the flow, accelerating the depth-averaged flow downstream of the rotor. Gauvin-Tremblay and Dumas [5] simulated the interaction of a cross-flow hydrokinetic turbine with the free surface at different submergence depths, remarking that the power extraction is independent of the Froude number as the clearance between the turbine top and still water level increases. In addition, the authors clarified the impossibility of achieving a water depth downstream of the mixing region lower than the uniform value h_∞, due to the perpetual decrease in depth that would be generated if bed friction losses were higher than the channel slope. Yosry et al. [6] tested the performance of a vertical-axis cross-flow rotor in a water channel with a horizontal and inclined bed, with a downstream regulation of the flow and dictating the undisturbed flow condition. For inclined tests, the authors corrected the maximum power with the square of the channel slope, and the optimum tip speed ratio with the fourth root of the channel slope.

The sketch in Fig. 4-1 has much in common with the hydraulic transition of short, localized narrowing of the channel cross-section, with the difference that the flow is not partially blocked by a solid obstacle such as a bridge pier, but rather by a porous device whose rotation reduces the flow speed into the wake. However, the schematic of a hydrokinetic turbine in a gradually varied flow requires additional modeling to calculate the mechanical power extracted and the axial thrust force. Although a cross-flow turbine is depicted in the image, this work also holds for axial-flow turbines.

In subcritical flows, the minimum depth achieved by the flow is greater than the critical value and the energy balance produces a depth h_0 a few diameters upstream of the rotor, which pressure distribution is assumed hydrostatic and streamlines uniformly distributed. Starting from the measured flow {∞}, the free surface is linked to {0} with a behavior depending on turbine shape, vertical positioning, aspect ratio, and rotor speed. Thus, backwater propagates upstream from {0}. Notice that the maximum variation in depth Δh corresponds to that produced by the rotor operating at its highest rotor speed, far away from the point of maximum performance and coinciding with the maximum power released by the flow, including viscous dissipation.

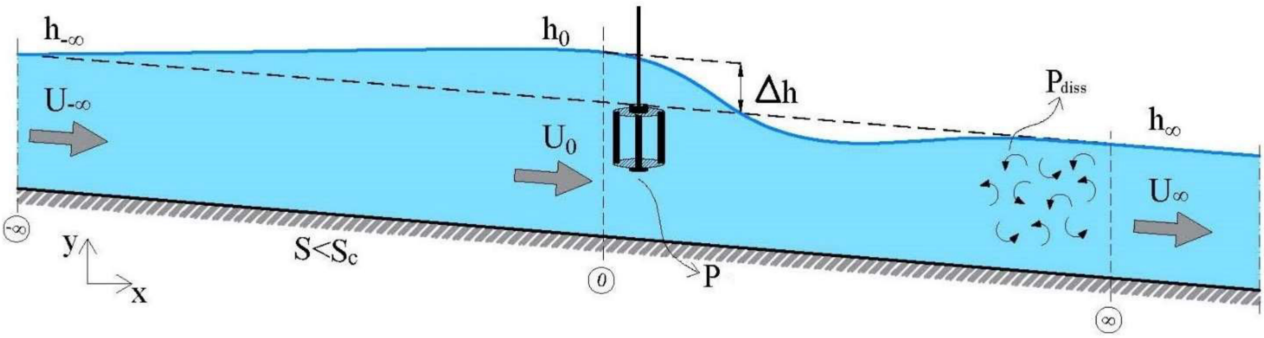

Fig. 4-1. In-Stream hydrokinetic power conversion.

As the turbine wake and bypass flow merge, a turbulent loss is generated, while the conservation of momentum allows the flow to restore its uniform and unperturbed condition over a short distance. In subcritical flows, the upstream flow is regulated from downstream, and this is what occurs experimentally with hydrokinetic devices in [6] and [7], and with porous plates in [8].

Since the power extraction diminishes with the drop in flow speed upstream of the machine, a procedure must be coded to predict in advance the expected inflow, unless it is measured directly from an upstream crossbar.

The method is introduced for the turbine array assessment in artificial canals using momentum predictors adapted for the confined environment. The assessment of HK turbines in open channel flows was performed initially with the extended Linear Momentum Actuator Disc Theory (LMADT), first assuming a fixed free surface by Garrett and Cummins [9], and later incorporating its variation in [10],[11], and [12]. However, validation for riverine flows was absent due to the altered flow propagating upstream, which, introducing bed friction, did not match the inviscid flow assumption. Moreover, the confined LMADT equations depend on upstream independent variables, making its application not feasible if the flow is investigated from downstream. The effort of predicting turbine power and axial thrust with a momentum model is rewarded by integrating the Double Multiple Streamtube (DMS) from [13] with a procedure calculating the upstream flow, as completely disclosed here and just previously mentioned.

An iterative scheme is introduced to scale blockage and Froude number for solving the LMADT between disturbed and undisturbed stations implemented in the DMS model. Within approximation, this procedure allows a steady turbine model to comply with the iterated upstream flow.

This extends the validity of the Actuator Disc Theory to subcritical canals, whether the far-field flow is known from downstream, not previously outlined for these applications. Different prismatic geometries of the transversal area are allowed, thus improving the flexibility of the procedure. The conceptual assessment involving the energy recovery in canals is exposed in Section 4.2, remarking on the feasibility of integrate HK turbines in certain hydropower plants. The method proposed is fully disclosed in Section 4.3 and is validated in Section 4.4.

4.2. CHANNEL ENERGY ASSESSMENT

Linear integral statements of continuity, momentum, and energy conservation are introduced to be enforced to the downstream volume in Fig. 4-1 in the normal direction, with the assumptions of an incompressible fluid, homogeneous, and steady flow in a mild bed slope canal ($S<S_c$). The recovery of the undisturbed depth is allowed by the total head between the boundaries {0} and {∞}, induced by mechanical energy conversion and viscous dissipation.

According to Pelz [14], the energy conservation for this problem can be resumed in the next equation, with ρ the water density, g the gravity acceleration, Q_c the channel discharge, z the geodetic head, h the hydrostatic head, and $U^2/(2g)$ the kinetic head.

$$\rho g Q_c\left(z_0+h_0+\frac{{U_0}^2}{2g}\right)-\rho g Q_c\left(z_\infty+h_\infty+\frac{{U_\infty}^2}{2g}\right)=\rho g Q_c(\Delta H_{tot})=P_{tot}$$

The Coriolis coefficients α_i multiplying the kinetic terms are omitted according to Chanson [15] for the prismatic cross-sections discussed in this work. The surface integral of the work done by the reacting force represents the turbine mechanical power removed from the system and released to the shaft and a turbine model is required to determine the turbine power P. The downstream mixing process leads to a heat exchange from the system to the environment, so the term P_{diss} is derived from the surface integral of the internal energy variation $\rho{*}Q_c{*}(e_0\text{-}e_\infty)$. However, this unknown term is expanded to include the sum of turbine fluid-dynamic losses, the far-wake mixing dissipation, and the losses due to bed friction in the control volume {0,∞}.

Notice that P_{tot} is used instead of the sum P and P_{diss} Solving this equation for the total head in {0}, yields:

$$z_0 + E_0 = z_\infty + E_\infty + \Delta H_{tot} \tag{I}$$

The energy conservation describing the backwater control volume {-∞,0} is represented by equation (II), with h_f the backwater friction head due to the bed shear stress.

$$z_{-\infty} + E_{-\infty} = z_0 + E_0 + h_f \tag{II}$$

Solving (II) for the sum (z_0+E_0) and substituting this result into equation (I), a new definition of the total head is achieved for the control volume between two uniform cross-sections {-∞,∞} in (III). As the undisturbed flow is restored downstream, the upstream specific energy $E_{-\infty}$ equals the downstream E_∞, and the total head variation expected for power extraction and dissipation equals the elevation head variation Δz = ($z_{-\infty}$-z_∞) net of upstream bed friction h_f, meaning that ΔH_{tot} equals the energy recovered by the flow in the backwater. Hence, statement (III) represents the same equation derived by Kartezhnikova and Ravens [3] for a uniform distribution of hydrokinetic devices. However, this equation applies also to a single device in an infinitely long channel, as the uniform flow is regenerated downstream.

$$\Delta H_{tot} = \Delta z - h_f \tag{III}$$

Given the bed slope and channel flow rate, an increase in the total head ΔH_{tot} is compensated by the drop in upstream bed friction so that the turbine is seen like a hydraulic device collecting part of the energy available from the generated disturbance. In terms of momentum, the rise in upstream depth is due to the increasing axial thrust force and rotor speed.

As stated, the highest total head variation does not coincide with the maximum net turbine power. Indeed, at the highest rotor speed, the rotor develops the highest thrust force, and a maximum viscous dissipation arises in the channel flow.

Although on a different scale, the same concept also holds for a generic hydropower system, with ΔH_{plant} the available head variation of the plant, i.e., the elevation head Δz_{plant} net of friction losses $h_{f,plant}$. Some of these plants have ducts and inlet canals conveying a flow rate away from a reservoir to end up in the forebay. By modifying the natural flow path with mild slope riverbeds, these canals allow bed friction losses to diminish and prevent a sudden drop in the head for power extraction, now maximized at the powerhouse in Fig. 4-2.

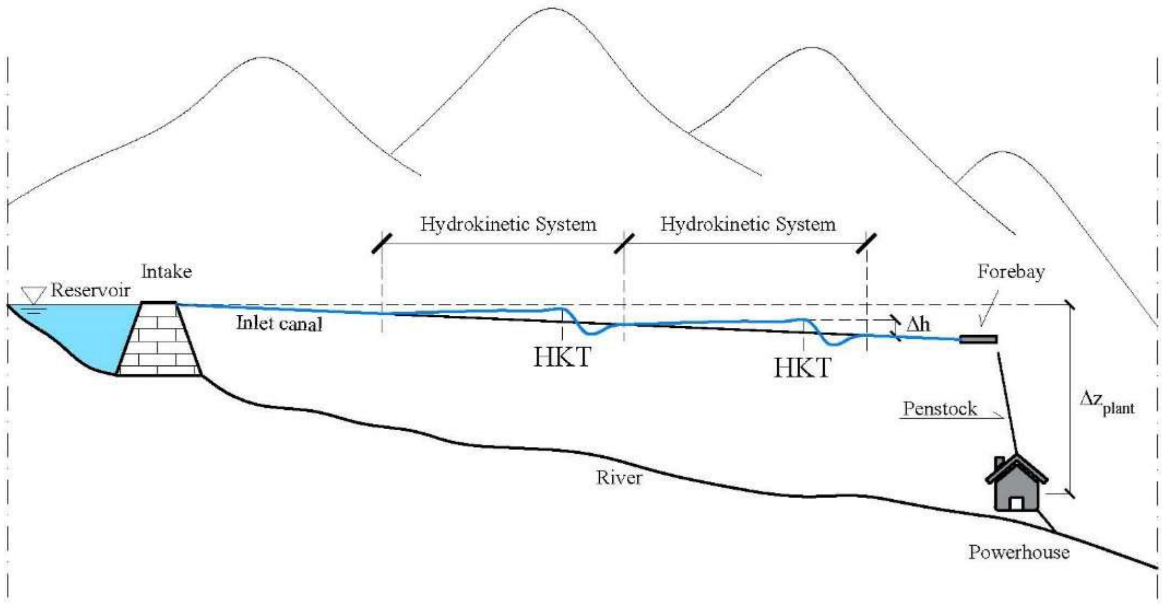

Fig. 4-2. Hydropower derivation incorporating hydrokinetic turbines.

Inlet waterways have subcritical flow regimes, and the flow rate is often regulated through an upstream hydraulic intake. Although the upstream stretch should host a substantial backwater to avoid hydraulic risk, the use of HK devices in inlet canals is generally feasible with no noticeable change in the operation of the hydropower plant.

It demonstrates that hydropower canals can be exploited for hydrokinetics with a design of a combined hydro-hydro plant. Liu and Packey [16] previously discussed the potential benefits and feasibility of integrating existing conventional hydropower stations with HK devices, namely Combined-Cycle Hydropower Systems. The authors highlighted that this technology is under research and development but not yet mature and economically feasible.

It moved our attention from our previous work [7] towards In-Stream HK turbines in inlet hydropower canals, where backwater is somehow bearable upstream to a given limit. These artificial streams have abundant flow rates, and often have wider cross-sections and deep water to allow the installation of several turbines in a single array.

However, greater attention is required to outlet canals (not depicted in the figure), with assessments made on a case-by-case basis. Solutions with HK rotors installed near reaction hydraulic turbines are undesirable. Indeed, Francis, Kaplan, and Bulb turbines operate with a low elevation head, and the backwater due to HK rotors can lead to severe adverse effects on their efficiency.

4.3. ITERATIVE SCHEME FOR MILD SLOPE CANALS

Analytical techniques are widely used to investigate the backwater effect in hydraulic transitions. According to Niebuhr et al. [17], the upstream depth h_0 can be approximated with Yarnell's empirical equation [18] for circular bridge piers. Besides Yarnell's formula, lately calibrated by Charbeneau and Holley [19], different outputs are obtained with the equations of Nagler, Al-Nassri, Rehbock, and Aubuisson. These methods account for static elements immersed in the flow and require empirical parameters of the bridge piers' geometry to be solved. Diversely, our proposal applies directly to the implemented DMS model.

The steady and incompressible momentum conservation is defined according to Kundu et al. [20] for the 1-D flow based on the problem in Fig. 4-3 for a rectangular channel. This sketch represents a hydraulic transition of a mild slope channel with a turbine between {0,∞}.

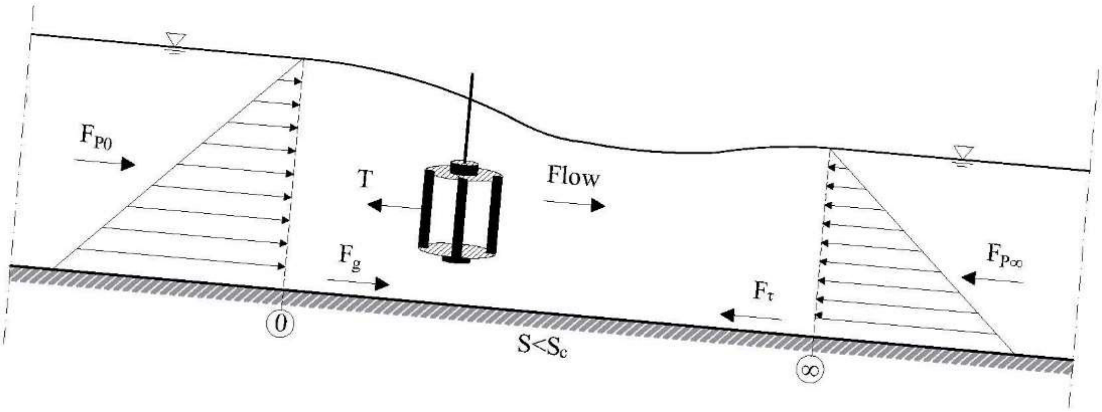

Fig. 4-3. Sketch for the application of the momentum equation.

The hydrostatic pressure forces are indicated in the image with F_{p0} and $F_{p\infty}$. The surface integral of the reacting force per unit area distributed over the turbine is replaced by the thrust force in the normal direction T on the right-hand side. The force due to water weight parallel to the bottom can be included as $F_g = \rho{*}g{*}W{*}S$, with ρ water density, g the gravity acceleration, W denoting the weight of the volume included within the boundaries, and S the bed slope. Notice that momentum corrections factors β_i are treated as the Coriolis coefficients in the energy equation.

An iterative scheme is introduced to scale blockage and Froude number for solving the LMADT between disturbed and undisturbed stations implemented in a DMS model.

$$\rho U_0{}^2 w h_0 - \rho U_\infty{}^2 w h_\infty + \frac{1}{2}\rho g w\left(h_0{}^2 - h_\infty{}^2\right) + \rho g W(S - S_f) = T$$

In most of the transition problems involving bridge piers, F_g is disregarded due to the short channel length involved with a mild slope. Like the weight force component and although the viscosity is crucial in energy conservation, the shear stress force $F_\tau = \rho * g * W * S_f$ plays a limited role over a short and smooth channel length, according to Chanson [15]. Henceforth, the sum of these two contributions is excluded from the rest of the analysis.

A dimensionless statement is derived from the above momentum equation, with blockage, Froude number, and thrust coefficient appearing as independent variables. The equation holds for all channel shapes, but attention must be paid to scaling the Froude number according to the actual geometry, as shown further on.

A linear proportionality between the known far-field speed U_∞ and the unknown flow speed U_0 is assumed in (4.1) by introducing the inflow factor $\phi = U_0/U_\infty$, valid within $0 < \phi \leq 1$. Notice that ϕ must be a positive quantity and non-zero. Recalling the mass conservation, the channel flow area A_0 is written in terms of ϕ in (4.2). The transversal area of a rectangular flow passage is $w_\infty * h_\infty$, and the equation (4.2) further drops into the proportionality of water depths (4.3).

The far-field Froude number Fr_∞ (4.4), blockage ratio B_∞ (4.5), and thrust coefficient $C_{T,\infty}$ (4.6) refers to the station {∞}, while the upstream Froude number Fr and blockage ratio B must be scaled to account for the variation of the inflow due to the actual thrust force.

$$U_0 = U_\infty \phi \tag{4.1}$$

$$A_0 = \frac{A_\infty}{\phi} \tag{4.2}$$

$$h_0 = \frac{h_\infty}{\phi} \tag{4.3}$$

$$Fr_\infty = \frac{U_\infty}{\sqrt{g h_\infty}} \tag{4.4}$$

$$B_\infty = \frac{A_T}{A_\infty} \tag{4.5}$$

$$C_{T,\infty} = \frac{T}{\frac{1}{2}\rho A_T {U_\infty}^2} \tag{4.6}$$

Using (4.1-4.6) in the momentum equation and dividing the left and right-hand sides by ($\frac{1}{2} * \rho * A_\infty * U_\infty^2 \neq 0$), the unknown ϕ and the variables Fr_∞, B_∞, and $C_{T\infty}$ appear. The dimensionless equation (4.7) represents a third-degree polynomial to be solved for ϕ, as previously shown in [13]. The thrust coefficient $C_{T,\infty}$ varies at each iteration while Fr_∞ and B_∞ remain constant.

$$2{Fr_\infty}^2\phi^3 - \left(C_{T,\infty} B_\infty {Fr_\infty}^2 + 2{Fr_\infty}^2 + 1\right)\phi^2 + 1 = 0 \tag{4.7}$$

A single feasible solution is achieved within the domain $0< \phi \leq 1$ for subcritical flows. The polynomial holds for ϕ, Fr_∞, and $B_\infty \neq 0$, but $C_{T,\infty}$ can be zero, leading to the physically acceptable solution $\phi = 1$ (no flow disturbance).

The cubic polynomial yields the numerical solutions in Fig. 4-4 for increasing values of $C_{T\infty}$. In all charts, the drop in ϕ is immediately evident at high B_∞ given the Fr_∞, while the drop in ϕ is not noticeable at high Fr_∞ and mild B_∞, irrespective of $C_{T,\infty}$. The thrust force depends on the turbine operating point, and is an output of this problem. The higher the thrust force, the larger the reduction in ϕ is observed. It is even more evident when the turbine is installed at the free surface proximity, with B_∞ the factor most influencing momentum conservation.

The far-field Fr_∞ is calculated after measurements of the undisturbed flow field. After the turbine installation, altered depth h_0 and water speed U_0 appear from the undisturbed values h_∞ and U_∞. However, h_0 and U_0 are unknown, and a hydrodynamic turbine model calculating the thrust force is required to close the system.

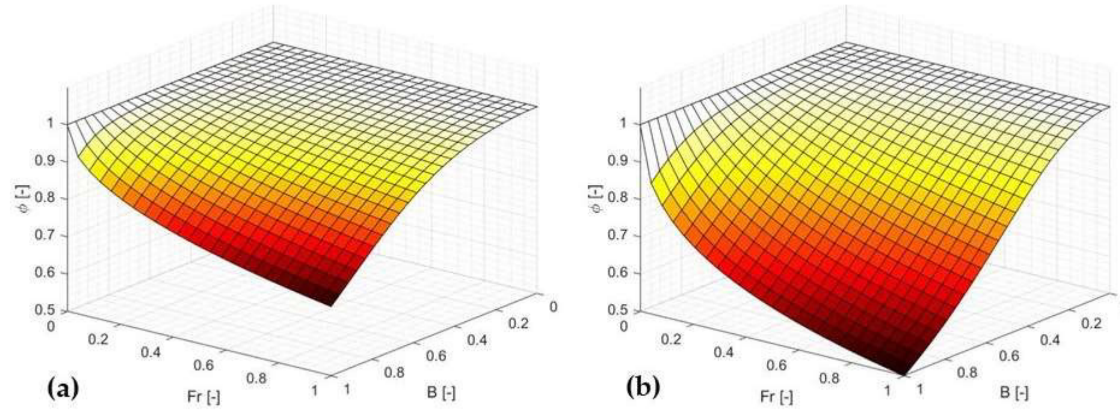

Fig. 4-4. Solutions for ϕ in the domain (0,1] visualized for $\phi > 0.5$ vs Froude number ***Fr*** and blockage ratio ***B*** at a prescribed $C_{T,\infty}$ of (**a**) 0.5 and (**b**) 2.0.

Therefore, a Double Multiple Streamtube is integrated with the Actuator Disc Theories suggested by Whelan et al. [10] and Cacciali et al. [13] for single-disc and double-disc theories, respectively.

The control volume for the turbine model is bounded in Fig. 4-5. Notice that the independent variables Fr and B in the DMS code refer to the station {0}. The turbine thrust force divided by the far-field flow dynamic pressure force gives the turbine thrust coefficient, as indicated in equation (4.6). It is the output of the DMS model depicted in the flowchart in Fig. 4-6.

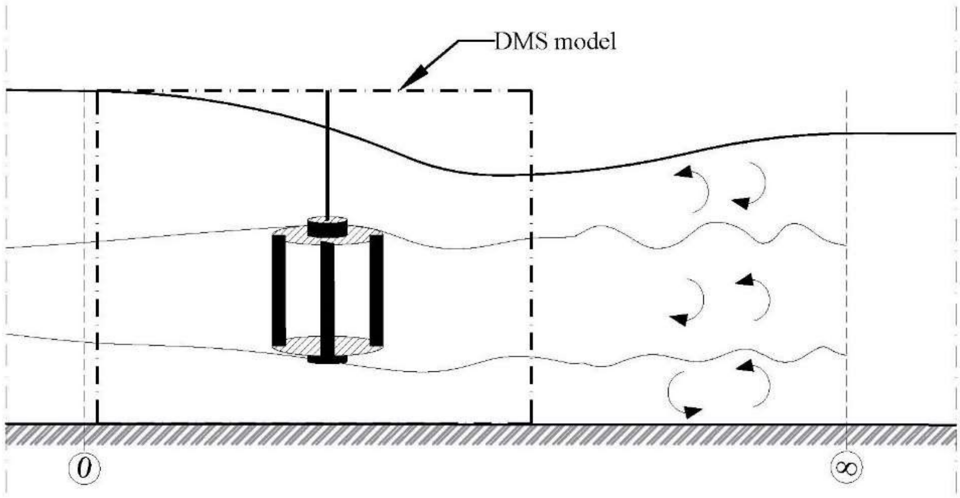

Fig. 4-5. Control volume of the confined DMS model.

For the first iteration, ϕ = 1 and $Fr = Fr_\infty$, $B = B_\infty$. Then, the inflow Froude number and blockage (Fr, B) are scaled so that the $C_{T,\infty}$ is updated by the DMS model so the cubic polynomial (4.7) is solved for ϕ. Inflow Froude number Fr and blockage ratio B diminish from the far-field value, while the inflow factor ϕ drops from unity.

The blockage ratio B scales linearly with the far-field blockage ratio B_∞ (4.8). It is achieved immediately by substituting A_0 from the mass conservation (4.2) into $B = A_T/A_0$, and equalizing the turbine areas, i.e., $A_T = (B*A_\infty)/\phi$ and $A_T = B_\infty*A_\infty$.

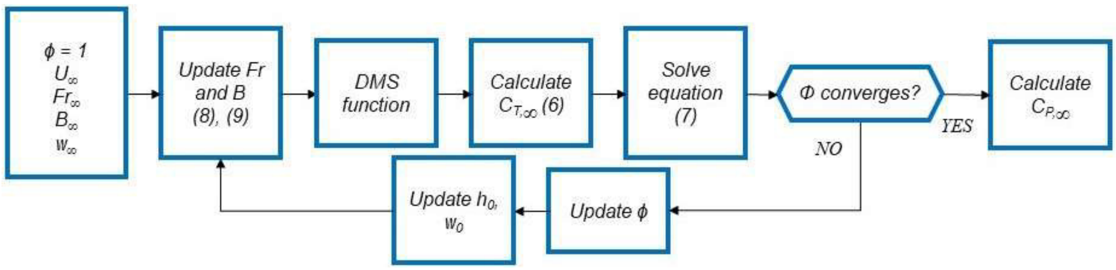

Fig. 4-6. Flowchart to solve the hydraulic transition.

The Froude number scaling function requires further attention as it must be valid for all canal shapes. Therefore, the mathematical statement (4.9) is achieved by replacing U_0 with equation (4.1) and A_0 with equation (4.2) in $U_0 = Fr*(g*A_0/w_0)^{1/2}$, and equalizing the speed U_∞ appearing on the left-hand side with the far-field flow speed definition $U_\infty = Fr_\infty*(g*A_\infty/w_\infty)^{1/2}$.

$$B = \phi B_\infty \tag{4.8}$$

$$Fr = \phi^{3/2}\left(\frac{w_0}{w_\infty}\right)^{1/2} Fr_\infty \tag{4.9}$$

In rectangular canals, the Fr is independent of the free surface width, but for different prismatic canals, the width w_0 is unknown at this stage. This issue is solved by stating a continuity equation for the specific cross-sectional shape to avoid miscalculations. From statement (4.2), the area of the canal is written as a function of the parameters in Fig. 4-7. The development of the mass conservation for triangular and trapezoidal shapes yields the equations in Tab. 4-1.

The free surface width is introduced as a function of water depth [21]. Once solved the continuity for h_0 and calculated the free surface width w_0, the inflow Froude number is finally scaled according to the equation (4.9).

Notice that "double-trapezoidal" refers to a trapezoidal canal with an additional trapezoidal bottom, whose angular coefficient m_t and bottom width b_t relate to the top trapezoid, and the height y_b and the area A_b refer to the bottom section, as assumed submerged.

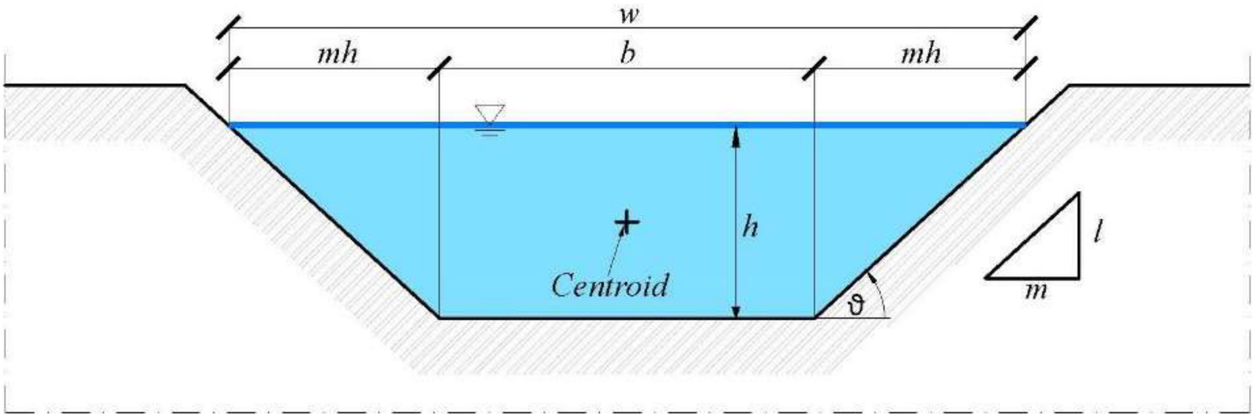

Fig. 4-7. Parameters of a non-rectangular canal.

Albeit the complexity recovering the uniform flow pattern after the near-wake expansion, the wake expands over the whole water column entraining the outer flow [22], which mixes with the turbine flow rate Q_T. This mixing induces an internal energy variation in the far-wake due to the triggered viscous dissipation. The bed elevation contribution (z_0-z_∞) is included in the total head variation ΔH_{tot}, and empirical data are needed to compute the flow speed variation in the wake for calculating the wake recovery length [23],[24].

Since the turbine power conversion is trailed by viscous and bed friction restoring the far-field flow, only part of the available mechanical power can be exploited by the turbine. The downstream losses are estimated by equation (4.10), since derived from (I). Notice that P is known at this point, as it represents the output of the turbine model.

Tab. 4-1 Continuity equations and free surface width relationships for different prismatic canals.

Shape	Continuity equation	Width
Rectangular	$h_0 = h_\infty/\phi$	$w_0 = b$
Triangular	$h_0 = h_\infty/\sqrt{\phi}$	$w_0 = 2mh_0$
Trapezoidal	$m(\phi h_0{}^2 - h_\infty{}^2) + b(\phi h_0 - h_\infty) = 0$	$w_0 = 2mh_0 + b$
Double-trapez.	$m_t(\phi h_0{}^2 - h_\infty{}^2) - (2y_b m_t - b_t)(\phi h_0 - h_\infty) + (\phi - 1)[y_b(y_b m_t - b_t) + A_b] = 0$	$w_0 = 2m(h_0 - y_b) + b_t$

$$P_{diss} = \rho g Q_c \Delta H_{tot} - P \tag{4.10}$$

According to Pelz [14], hydraulic efficiency η represents a measure of the dissipation attributable to viscous friction and should include bed friction, internal energy variation due to mixing, and rotor fluid-dynamic losses. Since all these terms are included in P_{diss}, the hydraulic efficiency η represents the ratio of turbine power and total power indicated in equation (4.11).

$$\eta = \frac{P}{P_{tot}} \tag{4.11}$$

The backwater recovery length can be further calculated with a step or integral method to estimate the longitudinal spacing between the turbines or turbine arrays, avoiding the effects of hydraulic superposition due to multiple elements in series. It directly contributes to estimate the capacity available in a channel flow that minimizes the environmental impact of the backwater. For equally-spaced turbine arrays, the method is illustrated in Chapter 5.

4.4. Results and Discussion

Chapter 1 shows the tests performed on a Darrieus hydrokinetic turbine of a 0.5 m diameter into a narrow canal with acquisitions of rotor speed, axial thrust force, and mechanical torque at 2 kHz. Depth was measured simultaneously upstream of the rotor with an accuracy of ± 0.005 m. All measurements were averaged in time at each rotor speed. A top view of the operating turbine is shown in Fig. 4-8.

Fig. 4-8. Top-view of the canal during high-speed turbine operation.

With a Matlab function tailored to the investigated channel, local Froude numbers are calculated based on the hydraulic depth, i.e., the ratio of the cross-sectional area to the maximum width occupied by the free surface. The simulation is performed with the DMS code developed to investigate the performance of the hydrokinetic turbine in blocked flows. The simulation is performed with the DMS code developed to investigate the performance of the hydrokinetic turbine in blocked flows. The iterative procedure is set up according to the scheme in Fig. 4-6, whilst the continuity of a double-trapezoidal canal from Tab. 4-1 was solved to update the inflow Froude number Fr.

Preliminary results show the differences between corrected and far-field parameters. Experimental data are shown in Fig. 4-9 with a plus marker while numerical data are shown by a dotted line. The dashed line corresponds to the constant Fr_∞ and B_∞ relative to the far-field flow. As the tip speed ratio increases, Froude number and blockage vary over a limited range.

The tip speed ratio denoted by λ_∞ is the ratio of the turbine tangential speed U_{tan} to the undisturbed flow speed U_∞. The root mean square deviation (RMSD) of the prediction to the experimental data gives 2e-3 for the Fr and 9e-3 for B. The drop in Fr is substantial after the deployment of the turbine.

An increase in axial force measured at the shaft for an increased rotor speed corresponds to a higher hydrostatic head in front of the rotor. Similarly, the increasing tip speed ratio translates into a reduction in the Froude number. The trend of experimental Fr aligns with the prediction, demonstrating the validity of the proposed mathematical statement. The decrease in the Froude number is consistent with the reduction in blockage. An increasing depth upstream of the turbine determines a drop in the swept area to the channel cross-section area ratio. It is illustrated in Fig. 4-9, where the upstream blockage ratio diminishes, as λ_∞ increases from left to right. The linearly scaling the blockages is also validated within tolerance.

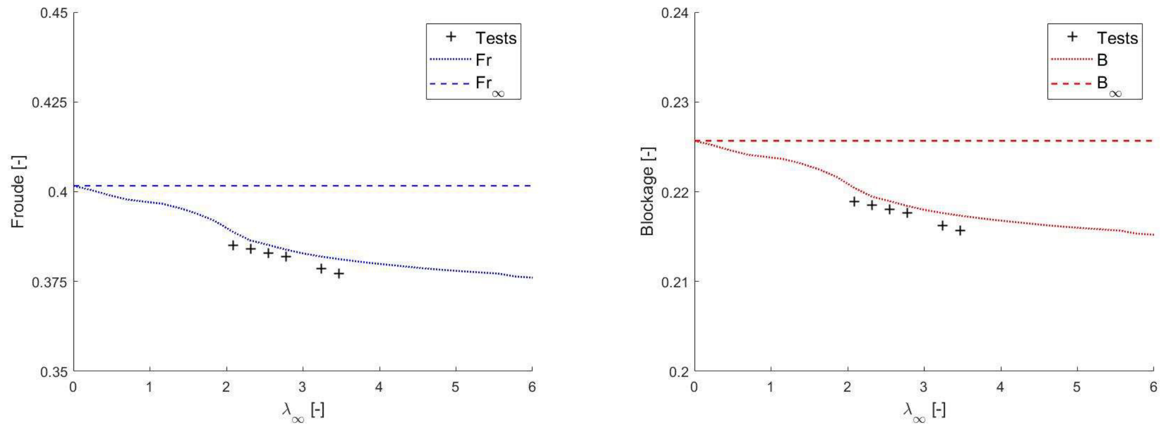

Fig. 4-9. (**Left**) Upstream Froude number $\boldsymbol{Fr}$ vs tip speed ratio $\boldsymbol{\lambda_\infty}$ with $\boldsymbol{Fr_\infty}$. (**Right**) Upstream blockage ratio $\boldsymbol{B}$ vs tip speed ratio $\boldsymbol{\lambda_\infty}$ with $\boldsymbol{B_\infty}$.

The variation of the total energy head to the hydrostatic head in the hydraulic transition is disclosed in Fig. 4-10. The test condition upstream of the rotor is represented by a blue square marker for the total head, and a blue triangle for the kinetic head. The downstream flow is characterized by grey markers instead.

According to Kirke [4], the turbine energy conversion accelerates the mean flow after being decelerated upstream, and the total energy decays from its maxima in {0} to the far-field value in {∞}. The contributions to the total head are thus given by the sum of the variation in the hydrostatic head (+), kinetic head (-), and elevation head (+) between {0,∞}.

The flow passing through the turbine Q_T reduces its speed and pressure, thus transferring mechanical energy to the shaft. The total head is maximum upstream of the rotor, and the head loss in this operative condition is proportional to the variation of the total energy (H_0-H_∞). The point of minimum depth achieved by the current is not indicated in the chart because the non-uniformity of the flow.

Moreover, the transition of a channel narrowing or the flow passage through bridge piers approximates a similar hydraulic problem. Indeed, the difference in momentum between the flow at a minimum depth M_w and the undisturbed flow M_∞ yields zero if gravity and friction force components are disregarded between these neighboring cross-sections.

Notice that the transition of a channel narrowing or the flow passage through bridge piers approximates a similar phenomenon. Indeed, the difference in momentum between the flow at a minimum depth M_w and the undisturbed flow M_∞ yields zero if gravity and friction force components are disregarded between these neighboring cross-sections.

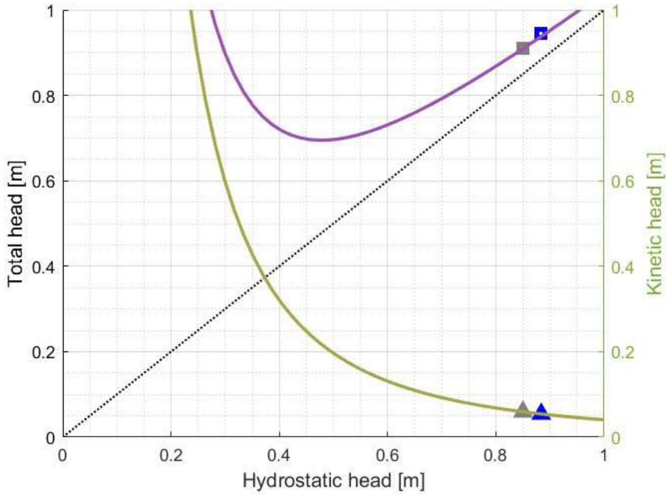

Fig. 4-10. Total head ***H*** (squares) and kinetic head ***k*** (triangles) vs hydrostatic head ***h***. Undisturbed flow {∞} markers and inflow {0} markers are depicted in grey and blue, respectively.

A dotted line (corrected prediction) and a dashed line (no correction) show the numerical improvements in thrust coefficient $C_{T,\infty}$ and power coefficient $C_{P,\infty}$ vs the tip speed ratio λ_∞, thus anticipating some outputs from Chapter 6 in Fig. 4-11. Although a slight deviation in the $C_{T,\infty}$ is depicted at low λ due to dynamic stall, the prediction consistently improves for average rotor speeds. The root mean square deviation for $C_{T,\infty}$ and $C_{P,\infty}$ over the six operative points and additional observations are reported in [7].

Although estimated and not further discussed in this work, the hydraulic efficiency peaks approximately at 39.0%, with a slight contribution of the difference in bed elevation to ΔH_{tot} due to the short canal length identified.

Hydraulic efficiency introduces the capability of the rotor to exploit part of the available power, but its estimate adds complexity to the experimental activity. Indeed, uncertainty in the assessment of the total energy due to a questionable placement of upstream and downstream stations can arise, in addition to testing inaccuracies inducing an error propagation in averaging the far-field U_∞ and inflow U_0.

Ambitious tests and time-consuming simulations are required at each rotor speed and in several downstream crossbars to test the decay in shear stress towards the undisturbed flow. However, the power coefficient is a parameter readily available after the measurement and definition of U_∞. In rivers and canals, $C_{P,\infty}$ is a measure of the amount of energy converted into mechanical energy and indicates the apparent performance of the turbine-channel system, including the booster effect of blockage. This variation in Nomenclature is convenient for comparing plants built on different canals, as the far-field flow at the undisturbed cross-section {∞} is not altered by backwater effects as it is in {0}.

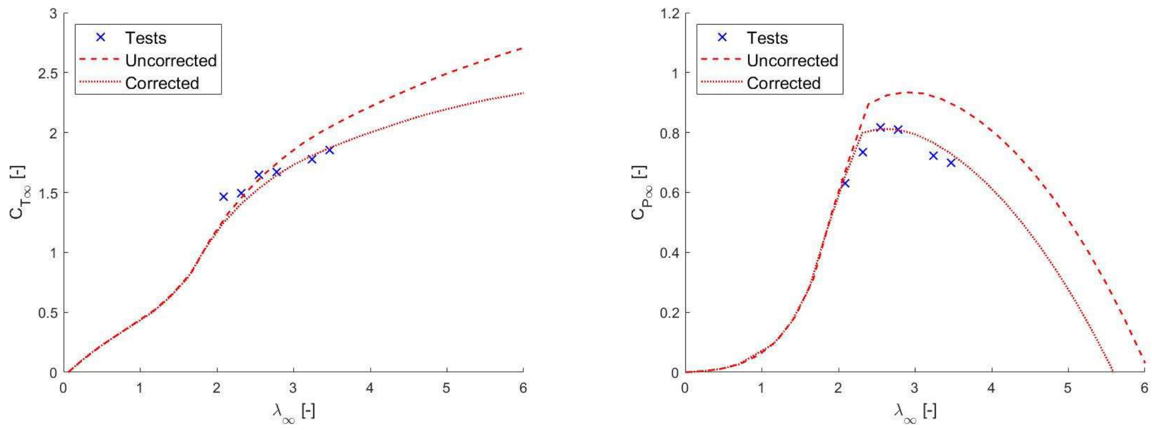

Fig. 4-11. (**Left**) Thrust coefficient $C_{T,\infty}$ vs tip speed ratio λ_∞. (**Right**) Power coefficient $C_{P,\infty}$ vs tip speed ratio λ_∞.

References

[1] Cacciali L., Battisti L., Dell'Anna S. Backwater Assessment for the Energy Conversion Through Hydrokinetic Turbines in Subcritical Prismatic Canals. Ocean Engineering **2023**, 267, 113246.

[2] Myers L., Bahaj J., Wake Studies of a 1/30th Scale Horizontal Axis Marine Current Turbine. Ocean Engineering **2007**, 34, 758-762.

[3] Kartezhnikova M., Ravens T.M. Hydraulic Impacts of Hydrokinetic Devices. Renewable Energy **2014**, 66, 425-432.

[4] Kirke B. Hydrokinetic and Ultra-Low Head Turbines in Rivers: A Reality Check. Energy for Sustainable Development **2019**, 52, 1-10.

[5] Gauvin-Tremblay O., Dumas G. Two-way Interaction between River and Deployed Cross-Flow Hydrokinetic Turbines. Journal of Renewable and Sustainable Energy **2020**, 12, 034501.

[6] Yosry A.G., Jimenez A.F., E.A. Alvarez, E.B. Marigorta. Design and Characterization of a Vertical-axis Micro Tidal Turbine for Low-Velocity Scenarios. Energy Conversion and Management **2021**, 237, 114144.

[7] Cacciali L., Battisti L., Dell'Anna S., Soraperra G. Case Study of a Cross-Flow Hydrokinetic Turbine in a Narrow Prismatic Canal. Ocean Engineering **2021**, 234, 109281.

[8] Schmitz C., Pelz P.F. Upper Limit for Tidal Turbines. 30th IAHR Symposium on Hydraulic Machinery and Systems, IOP Conf. Series: Earth and Environmental Science 774, 012127, 2021.

[9] Garrett C., Cummins P. The Efficiency of a Turbine in a Tidal Channel. Journal of Fluid Mechanics **2007**, 588, 243-251.

[10] Whelan J., J. Graham J., Peiró J. A Free-Surface and Blockage Correction for Tidal Turbines. Journal of Fluid Mechanics **2009**, 624, 281-291.

[11] Houlsby G.T., Draper S, Oldfield M.L.G. Application of Linear Momentum Actuator Disc Theory to Open Channel Flow. Technical Report 2296 (2008), Oxford University Engineering Laboratory, UK.

[12] Polagye B. Hydrodynamic Effects of Kinetic Power Extraction by In-Stream Tidal Turbines. Thesis dissertation, University of Washington (2009).

[13] Cacciali L., Battisti L., Dell'Anna S. Free Surface Double Actuator Disc Theory and Double Multiple Streamtube Model for In-Stream Darrieus Hydrokinetic Turbines. Ocean Engineering **2022**, 260, 112017.

[14] Pelz P.F. Upper Limit for Hydropower in an Open-Channel Flow. Journal of Hydraulic Engineering **2011**, 137, Issue 11.

[15] Chanson H. The Hydraulics of Open Channel Flow: An Introduction; Butterworth-Heinemann, Oxford, UK, 2nd Edition (2004), ISBN 9780750659789.

[16] Liu Y., Packey D.J. Combined-Cycle Hydropower Systems - The Potential of Applying Hydrokinetic Turbines in the Tailwaters of Existing Conventional Hydropower Stations. Renewable Energy **2014**, 66, 228-231.

[17] Niebuhr C.M., Hill C., Van Dijk M., Smith L. Development of a Hydrokinetic Turbine Backwater Prediction Model for Inland Flow through Validated CFD Models. Processes **2022**, 10, 1310.

[18] Yarnell, D. Bridge Piers as Channel Obstructions; United States Department of Agriculture: Washington, DC, USA, (1934).

[19] Charbeneau R.J., Holly E.R. Backwater Effects of Bridge Piers in Subcritical Flow. Center of Transportation Research, University of Texas, Project Summery Report 1805-S, (2001).

[20] Kundu P.K., Cohen, I. M., Dowling D.R. Fluid Mechanics, Fifth Edition (2011), ISBN 9780123821010.

[21] Henderson F. M. Open Channel Flow, MacMillan Company, (1966) New York.

[22] Müller S., Muhawenimana V., Wilson C., Ouro P. Experimental Investigation of the Wake Characteristics Behind Twin Vertical Axis Turbines. Energy Conversion and Management **2021**, 247, 114768.

[23] Araya D, Colonius T., Dabiri J.O. Transition to Bluff-Body Dynamics in the Wake of Vertical-Axis Wind Turbines. Journal of Fluid Mechanics **2017**, 813, 346_381.

[24] Ouro P., Runge S., Luo Q., Stoesser T. Three-Dimensionality of the Wake recovery Behind a Vertical Axis Turbine, Renewable Energy **2019**, 133, 1066-1077.

Nomenclature

A_0, A_∞	Canal cross-sectional area m^2	y_b	Height of bottom shape m, (Fig. 4-7)
A_b	Area of the bottom geometry m^2, (Fig. 4-7)	z	Elevation head m
A_T	Turbine swept area m^2	ΔE	Specific energy variation m
B, B_∞	Blockage ratio, (A_T/A)	ΔH_{tot}	Available total head variation m
b	Canal bottom width m, (Fig. 4-7)	Δh	Hydrostatic head drop m
C_P, $C_{P,\infty}$	Power coefficient, $P/(½{*}\varrho{*}A_T{*}U^3)$)	Δk	Kinetic head drop m
C_T, $C_{T,\infty}$	Thrust coefficient, $T/(½{*}\varrho{*}A_T{*}U^2)$)	Δz	Elevation head drop m
E	Specific energy m	ϕ	Inflow factor, (U_0/U_∞)
Fr, Fr_∞	Froude number	η	Hydraulic efficiency, (P/P_{tot})
g	Gravity acceleration m/s^2	λ_∞	Tip speed ratio, (U_{tan}/U_∞)
H	Total Head m	ρ	Fluid density kg/m^3
h_0, h_∞	Hydrostatic head m, (Fig. 4-7)		
h_f	Bed friction head m	*Subscripts*	
M	Channel Momentum m^2	$-\infty$	Far-upstream undisturbed flow
m	cot(ϑ) *deg*, (Fig. 4-7)	∞	Downstream undisturbed flow
P	Turbine power, W	0	Inflow
P_{diss}	Dissipated power, W	t	Top geometry, (Fig. 4-7)
P_{tot}	Total power W	b	Bottom geometry, (Fig. 4-7)
Q_c	Channel flow rate m^3/s	w	Near-wake flow
Q_T	Turbine flow rate m^3/s		
S	Bed slope m/m	*Short forms*	
S_f	Friction slope m/m	*DMS*	Double Multiple Streamtube
T	Axial thrust force N	*HK*	Hydrokinetic
U_0, U_∞	Mean flow speed m/s	*LMADT*	Actuator Disc Theory
U_{tan}	Tangential rotor speed m/s	*RMSD*	Root mean square deviation
w_0, w_∞	Free surface width m, (Fig. 4-7)		

5. Multi-Array Design for Hydrokinetic Turbines in Hydropower Canals

Chapter based on the content of the article:

> *Cacciali L., Battisti L., Dell'Anna S. Multi-Array Design for Hydrokinetic Turbines in Hydropower Canals. Energies 2023, 16(5), 2279. DOI: https://doi.org/10.3390/en16052279.*

The attractiveness of hydropower canals for hydrokinetic power exploitation is based on the availability of continuously flowing water and sufficiently large wetted areas for accommodating rotors of different geometry and size. The design of hydrokinetic plants in these waterways involves the choice of the array layout, rotor geometry, turbine spacing, and array spacing and accounts for the control of the resultant backwater to avoid upstream flooding hazards. Several works in the literature have shown that array power optimization is feasible with small array spacings, disregarding the limitation in the power output induced by backwater upstream. In this study, a 1-D channel model, the Double Multiple Streamtube, and wake sub-models are integrated to predict an array layout that maximizes the array power. Single and multi-array schemes are developed according to the iterative method illustrated in Chapter 4. However, multiple rotors generating the array blockage complicate the assessment, implying running the DMS code for all turbines with inflow data updated iteratively at each rotor speed.

5.1. Introduction to Multi-Array Modeling

The full description of the multi-array model is included in the recent work published in [1]. The idea of integrating existing hydropower plants with hydrokinetic turbines was suggested by Liu and Packey [2] for the development of Combined-Cycle Hydropower Systems, for which the objective was to harvest additional energy from the tailwater in currents leaving dams. The energy recovery in hydropower canals was then discussed by Cacciali et al. [3] to attempt the installation of cross-flow HK devices in inlet hydropower canals connecting basins with a subcritical flow, with lateral embankments that conveniently accommodate structural works. This application is suitable in some parts of northern Italy, i.e., a mountainous area with several hydroelectric plants built more than hundred years ago. An example of hydro-hydro application is illustrated in Fig. 5-1 concerning the rotors being tested by HE Powergreen S.r.l. [4] in the Biffis canal, i.e., a waterway used to supply the hydropower plant in Bussolengo (VR), Italy.

The deployment of multiple arrays represents a trade-off between power optimization and environmental control. Indeed, besides the energy harvested, an adverse effect is posed by the backwater generated from the operating turbines, thus implying the requirement for automated depth measurement. It forces the designer to strictly design the array with a limitation on the backwater induced by the plant. On the other hand, the basin operator cannot allow flooding hazards to occur due to faulty design.

The most relevant works intended for canals and fluvial applications are presented in the following material: part of these references are based to array power optimization in tidal flows, including assessments of turbine spacing and array spacing.

Fig. 5-1. An array of aligned vertical-axis cross-flow hydrokinetic turbines deployed in a regular canal. Image from HE Powergreen S.r.l. [4].

Turbine arrays were investigated by Gauvin-Tremblay and Dumas [5] in aligned and staggered configurations; the investigation showed that the local blockage and turbine–wake interaction affect the performance of an array, which, in turn, dominates the downstream row. The wake deflection originating from the upstream vertical-axis turbines highlighted a negative impact on the staggered configuration. The authors clarified that an aligned layout with an inward rotation of the rotors is desirable. Their work demonstrated no advantages in terms of power extraction for the aligned configuration over a staggered layout in a wide channel, but higher power output was shown by the aligned configuration in a narrower environment. Gauvin-Tremblay and Dumas also observed higher mean power extraction per turbine by increasing the longitudinal spacing between the turbine arrays; however, they also affirmed that the larger the lateral spacing, the higher the total power. Almost all these results were confirmed by the model presented in our work, except for those regarding lateral spacing, as will be clarified later.

Gonzalez-Gorbeña et al. [6] assessed turbine arrays with a surrogate-based method for regular and irregular channels. Both uniform and non-uniform flow scenarios were investigated. Inline and staggered arrays were investigated, leading to the determination of capacity factors and profitability. Polynomial and radial basis-surrogate methods were used to fit an objective function based on two variables: the lateral and the longitudinal spacings. This method is promising, although the downstream flow does not affect the upstream flow, wherein horizontal rotors were simplified as actuator discs.

Okulov et al. [7] tested longitudinally aligned horizontal axis hydrokinetic turbines with particle image velocimetry to measure the flow properties upstream and downstream of the devices including up to four elements, highlighting the interference of the turbine wake on the downstream turbine, which was deployed closer. The authors remarked on a continuous drop in turbine performance due to the upstream wake reducing the inflow speed with higher turbulence. Unlike Okulov, we clarify that optimal rotor placement in a narrow canal or riverbed should enable the rotor's detachment from reduced longitudinal spacings due to turbulent phenomena. It was clarified through the on-site experience of H.E. Powergreen S.r.l. [4], which demonstrated evident backwater phenomena due to the variation in rotor speed and lateral spacing.

Septyaningrum et al. [8] investigated co-rotating and counter-rotating turbines by analysing turbulence intensity in the interaction zone, thereby demonstrating that flow superposition is not the only reason for flow acceleration, as an additional influence is contributed by a closer spacing between the turbines, which confers a jet-type flow effect for the bypass flow. The authors proved that a faster velocity superposition and lower turbulence intensity are achieved with inward counter-rotating rotors. Although not discussing the backwater phenomenon, the authors indicated that the performance of downstream turbines in a multi-array layout would be sub-optimal if operating in the wake of upstream turbines.

Riglin et al. [9] simulated different array layouts with a CFD solver based on RANS equations mimicking a hydro-farm. A substantial drop in power was observed from the upstream to downstream units, showing that the operation of a turbine in the wake of the upstream turbines significantly reduces the energy available downstream.

Vennell et al. [10] reviewed the main parameters affecting the large turbine arrays in tidal flows, highlighting that the enhanced drag due to power extraction reduces the mean flow speed as the flow approaches the rotors. Moreover, the authors specified that optimally tuned turbines in large arrays perform differently from tuned isolated turbines. Some of the effects of a large array discussed by Vennell can be applied to on-land subcritical canals, e.g., in efforts to boost a turbine's output by adjusting its relative position within the turbine array. In this work, this effect is obtained by modifying the spacing between the turbines. Vennell indicated that higher capacity is obtained by adding supplementary turbines to an array, but the behavior of the power curve differs among wide and narrow channels.

A high contribution to array-based analytical models can be attributed to Nishino, Willden, and Draper, even though the confined actuator disc theory was extended in its free surface double-disc version in our previous work [11], which was subsequently updated with a method accounting for the backwater in subcritical flows [3]. Although staggered turbine layouts have been assessed about tidal flows [12]-[14], their actual application in hydropower canals is questionable, as closely spaced rows would cause an increase in turbulent effects and hydrostatic depth, which is only tolerable to a small extent, and which will be explained further later. With aligned rotors, the hydraulic transition to be solved at each turbine array resembles the solution introduced by Cacciali et al. [3]. Once the equilibrium in hydrostatic pressure is reached upstream of each turbine array, the computation of the average flow speed in the cross-section is iteratively feasible.

Nishino and Willden [12],[13] described the flow disturbance due to multiple turbines involving a large portion of the channel. The flow proximity was ideally assessed on a large scale with actuator discs due to power extraction in a tidal environment showing that the turbine-scale wake expansion occurs faster than the expansion around the turbine array. Draper and Nishino [14] developed a model for centered and staggered actuator discs and concluded that two rows should have a small spacing only if staggered; otherwise, centered arrangements should be kept as far apart as possible, which agrees with our findings. Subsequently, a theoretical model accounting for both the turbine and array scales was introduced by Vogel et al. [15] for a finite-width array of tidal turbines. However, these analytical approaches are controversial if applied to narrow canals of an arbitrary cross-sectional geometry when a subcritical flow is subject to downstream control.

Since undisturbed subcritical flow occurs downstream of any hydraulic resistance [16], a reference flow speed U_∞ is designated for performance and axial force computations. Alternatively, the inflow speed U_0 instead of U_∞ at the denominator would complicate the assessment as multiple and contemporary flow speed measurements and data processing would be required at each cross-section. The turbine thrust coefficient and the power coefficient are defined once more as $C_{T,\infty} = T/(½*\rho*A_T*U_\infty^2)$ and $C_{P,\infty} = P/(½*\rho*A_T*U_\infty^3)$, with ρ denoting the water density, T denoting the turbine thrust force, P the mechanical power, A_T the rotor swept area, and U_∞ the far-field flow speed. The array thrust coefficient is defined by $C_{TA,\infty} = T_{A,i}/(½*\rho*A_A*U_\infty^2)$ and the power coefficient by $C_{PA,\infty} = P_{A,i}/(½*\rho*A_A*U_\infty^3)$. $T_{A,i}$ and $P_{A,i}$ represent the thrust force and power developed at the ith array, and A_A denoting the array's transversal area. Since U_∞ is constant in a steady flow and is determined before any assessment, it is preferable to relate the dimensionless coefficients to the undisturbed flow [3].

The hydraulic transition due to the turbine array entails free surface deformation in canals, waterways, and rivers with a cross-section almost entirely occupied by cross-flow or axial-flow hydrokinetic turbines. In a previous study, Myers and Bahaj illustrated the free surface effects achieved experimentally in water channels at various speeds [17]. Moreover, the variation in the clearance between the top of the turbine and the still water level can also create undesirable phenomena, as clarified further on.

The potential for hydrokinetic energy exploitation has been determined in several works [18]-[22], with many estimating the total head variation in a section of the channel without introducing a turbine model. These assessments offer the advantage of simplicity and allow for direct access to data when designing hydrokinetic systems. However, a rigorous estimation of this potential that accounts for the free surface development in the investigated canal stretch has not yet been provided. Due to the complexity and computational cost of the numerical works conducted with CFD simulations on turbine arrays, estimates of the available capacity in a simple, quick, and effective manner are rare. In addition, analytical models only provide macroscopic picture of the energy extraction in water flows that do not differentiate each turbine in the array [5]. Analytical models concerning ideal actuator discs draw interesting conclusions regarding the layouts of turbine arrays, even though neglecting aspects of turbine operation and turbine–wake interaction. This fact prompted us to consider designing a model that overcomes the limitations of the actuator discs, i.e., including the fluid-dynamic losses of each turbine and avoiding the excessive computational costs necessitated by CFD models.

Therefore, a tool that quantitatively estimates the exploitable resources in a canal to pre-size the hydrokinetic plant was developed, which incorporated the complete prediction of the free surface variation induced by the rotors from a uniform station (downstream) to the exhaustion of the backwater (far upstream). Moreover, different prismatic channel geometries can be considered, thus adding flexibility to the simulation. The integrated use of a DMS model for vertical-axis turbines [11] with a hydraulic model for solving the hydraulic transition for single rotors [3], the computation of the level of backwater generation [23], and a simplified investigation of the recovery length downstream of the array from the research in [24],[25] enable the rapid prediction of the available and exploitable capacity.

This tool predicts the array power from real rotors and overcomes the limitation of approximating ideal rotors with actuator discs. The fluid flow distant from each turbine is simplified as a 1-D channel flow based on a subcritical hydraulic regime, i.e., respecting the physics of open channel flows. However, based on momentum models, this code does not allow for the direction of rotation of the rotors to be distinguished, nor does it allow for the mutual influence of the wakes. The development of turbine wakes is executed by exploiting regressions, simplifying the modeling process because power dissipation is treated quantitatively. The method requires that the wakes from an upstream array do not affect the fluid-dynamics of the downstream array. Indeed, on an industrial scale, the array problem should be treated over a consistent longitudinal stretch. Unlike some of the cited works, the deployment of rotating elements in the wake of other rotors for systems designed over long, longitudinal stretches seems illogical. For design purposes, it is crucial ensuring sufficient longitudinal spacing to recover, albeit partially, the velocity and depth of the flow. With the help of tests performed at the Unitn Hydraulics Laboratory on plates immersed in a water channel, theoretical insights on the asymptotic trend of the maximum backwater from array to array are discussed.

The proposed method is introduced in a single-array and multi-array scheme presented in Sections 5.2 and 5.3, respectively. Section 5.2.1 includes the definitions of turbine and array blockage ratios, whereas Section 5.2.2 shows an optimization scheme to build the power curve of a single turbine and select the best performance at the optimum tip speed ratio. This procedure is repeated for all turbines in the array. When the turbine's thrust and power are determined, the total thrust force of the array relaxes the inflow blockage and Froude number. Once converged, the code updates each rotor's power and thrust force and maximizes the performance of each turbine at a certain rotor speed, determining the array power. If required, the environmental boundary condition is activated to limit the backwater to a prescribed depth variation (Section 2.1.3). Sections 5.2.4, 5.2.5, and 5.2.6 treat the approximation of the near-wake, transition-wake, and far-wake past the turbines. Hence, Section 5.2.7 shows the methods for estimating the reduction in the backwater upstream according to energy or momentum principles.

The results discussed later in Chapter 6.2 focus on sensitivity analysis (Section 6.2.1), array design (Section 6.2.2), and simulations of large plants (Section 6.2.3). First, a sensitivity analysis is performed concerning turbine spacing and then regarding array spacing for a plant built with four arrays and four turbines per array. The simulations dedicated to the array design in Section 6.2.2 show the best prediction within a selected number of cases based on a constant blockage ratio and a fixed level of rotor solidity, thereby allowing a reduction in the number of variables. A limitation in the backwater would alter the outputs of the simulation. It would direct the design toward less-expensive and lower-power solutions. Section 6.2.3 shows the expected free surface variation from a simulation performed for a plant of many arrays.

5.2. Single Array Scheme

In this study, a canal of a double-trapezoid cross-section was investigated to perform simulations with the multi-array optimizer, which initially employed undisturbed flow data (U_∞, h_∞, and Fr_∞). A Manning's coefficient n of 0.031 at a certain cross-section was calibrated with a design flow rate Q_c of 124 m^3/s, depth h_∞ = 6.52 m, and local bed slope S of 3.84$*$10^{-4}, along with a determination of the bulk flow speed U_∞ (1.439 m/s) and Froude number Fr_∞ (0.223). Geometric details of the cross-section depicted in Fig. 5-2 were retrieved from Malini [26]. Technical data were drawn from local sources with authorization and are not disclosed in this work. The Froude number is calculated as $Fr_\infty = U_\infty*(g*A_\infty/w_\infty)^{-1/2}$, with U_∞ denoting the mean far-field flow speed, A_∞ representing the transversal wetted area, w_∞ denoting the free surface width, and g denoting gravity acceleration.

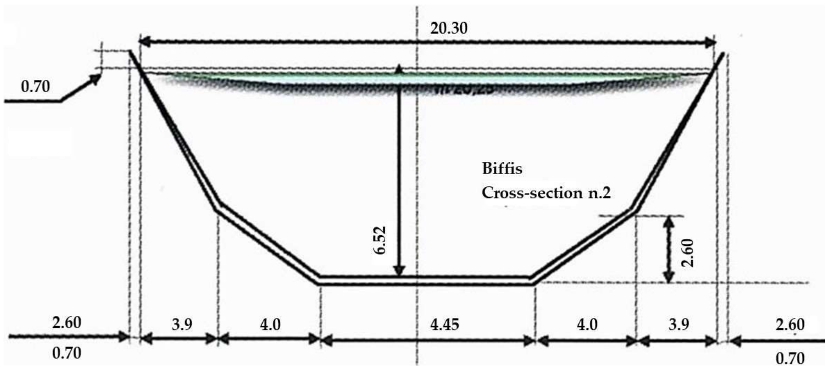

Fig. 5-2. Cross-section of interest in the Biffis canal from Malini [26], which was modified according to the design specifications of this work.

Generally, acoustic Doppler velocimetry (ADV) and subsequent data processing at different times allow for flow speed to be averaged spatially and over time. If data are scarce, entropy methods [27] offer a reliable alternative in achieving of the mean flow speed in ungauged streams. Indeed, investigations [28],[29] have demonstrated that the entropy parameter does not depend on energy or friction slope S_f. This justifies why the mean value of the entropy parameter at gauged sites remains approximately constant regardless of the discharge. The far-field blockage generated by a turbine array $B_{A,\infty}$ is given by the sum of the turbine's area to wetted area ratios (5.1).

$$B_{A,\infty} = \frac{N_T A_T}{A_\infty} \tag{5.1}$$

Considering a single-turbine array with multiple rotors aligned orthogonally to the direction of the flow, all flow passages are modeled as independent tubes (Fig. 5-3) sharing equal flow conditions upstream {0} and downstream {∞}, similar to the model depicted in [12].

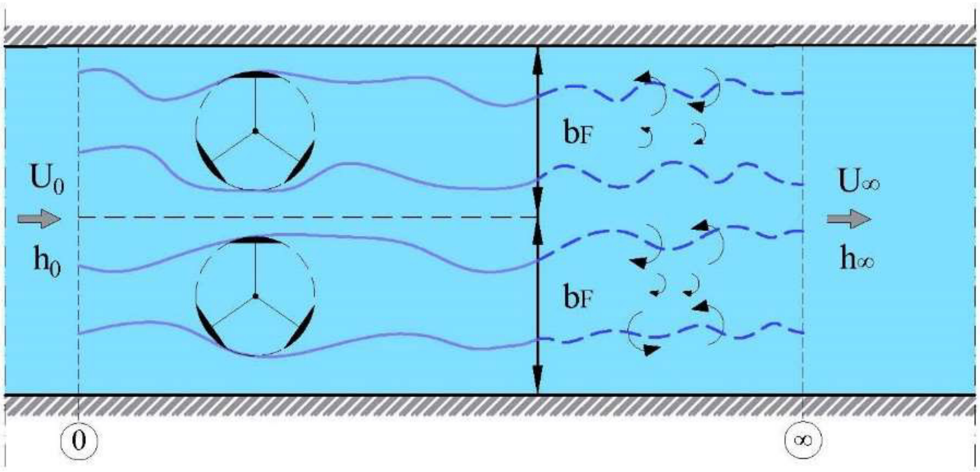

Fig. 5-3. Control volume of an array of aligned HK turbines in a channel flow.

Each turbine wake is shaped by its flow passage, which, in turn, bounded by the adjacent tubes and canal walls. The hydrostatic velocity profile is dictated for all streamtubes to allow the DMS code to be applied. The wetted area in {0} is divided into flow passages from the canal wall to half of the horizontal spacing turbine d_T or from a centreline to another centreline, as further depicted in Fig. 5-4. According to Vogel et al. [15], the turbine blockage is given by equation (5.2), with $A_{F,j}$ denoting the flow passage associated with the jth turbine, from left to right, and $A_{T,j}$ denoting the turbine swept area.

$$B_{T(j)} = \frac{A_T}{A_{F(j)}} \tag{5.2}$$

An array-scale blockage is built considering different flow passages based on the canal cross-section geometry, which is unlike Vogel's method for tidal turbines. Since a constant $B_{T,j}$ is present only in wide (and rectangular) channels or when two turbines are symmetrically distributed over the cross-section, the $B_{T,j}$ varies in trapezoidal channels with large arrays.

If the array consists of two rotors dividing the wetted area A_0 symmetrically, DMS simulations would predict the same outputs. Otherwise, different $B_{T,j}$ would lead to an uneven distribution of thrust and power outputs for the turbines. Fig. 5-4 shows examples of the subdivision in flow passages, in which higher blockage assigned centrally, and lower blockage is assigned laterally. The inflow speed is assumed uniform upstream of the station {ith}. In a wide navigable waterway, the array can be positioned on a side, resulting in an asymmetrical distribution of streamtubes. This case is not discussed further for brevity.

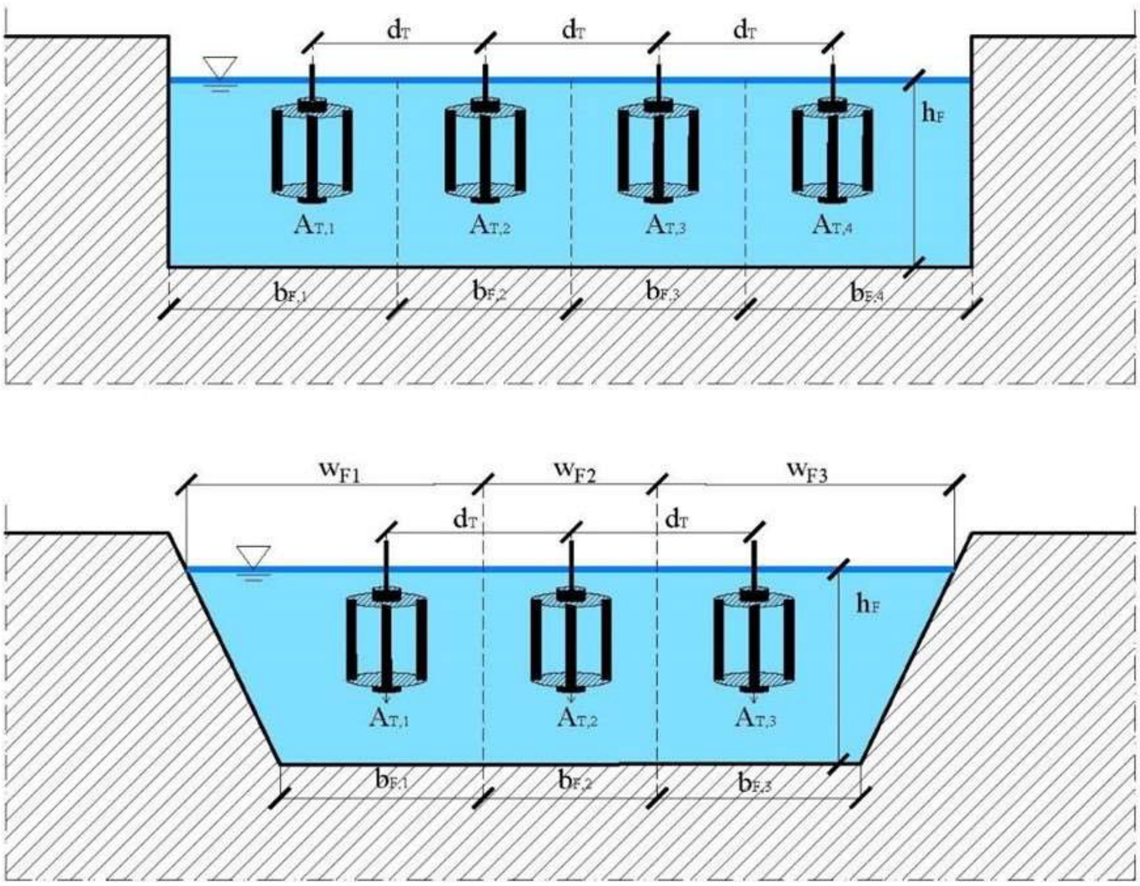

Fig. 5-4. Flow passages determined for multiple HK turbines.

5.2.1. Iterative scheme for a single array

The procedure valid for the entire turbine fence is henceforth derived, while the scheme for a single rotor is explained in [3]. The inflow factor $\phi = U_0/U_{ref}$ is defined in a domain $0 < \phi \leq 1$, while the ith array blockage ratio (5.3) and Froude number (5.4) are scaled from Fr_{ref} and $B_{A,ref}$ to iteratively solve the hydraulic transition. Notably, for the first array from downstream $U_{ref} = U_\infty$, $Fr_{ref} = Fr_\infty$, and $B_{A,ref} = B_{A,\infty}$, but for the others, the downstream flow is represented by a reference station, indicated as "*ref*".

The array thrust coefficient $C_{TA,ref}$, i.e., the ratio of the resultant thrust force generated over the entire structure to the reference dynamic pressure force (5.5), is used to solve the momentum conservation between upstream and downstream stations {0, *ref*} whose equation is given in (5.6).

$$B_A = \phi B_{A,ref} \tag{5.3}$$

$$Fr = \phi^{3/2}\left(\frac{w_0}{w_{ref}}\right)^{1/2} Fr_{ref} \tag{5.4}$$

$$C_{TA,ref} = \frac{T_A}{\frac{1}{2}\rho U_{ref}{}^2 N_T A_T} \tag{5.5}$$

$$2Fr_{ref}{}^2\phi^3 - \left(C_{TA,ref}B_{A,ref}Fr_{ref}{}^2 + 2Fr_{ref}{}^2 + 1\right)\phi^2 + 1 = 0 \tag{5.6}$$

The resultant force is the sum of the individual forces, i.e., $T_A = \sum T_j$. Notice that the array area $N_T{*}A_T$ appears at the denominator in (5.5). Hence, the cubic polynomial (5.6) must be solved numerically for ϕ once that $C_{TA,ref}$, $B_{A,ref,}$ and Fr_{ref} are known. This mathematical statement holds for a single turbine and multiple turbines as well, but in this case, array blockage and the resultant axial force are used instead.

The DMS model [11] is applied repeatedly for each turbine so that $C_{TA,ref}$ is achieved after the summation of all thrust forces. The updated solution of (5.6) yields the new U_{ref}, $B_{A,ref}$, and Fr_{ref}. According to the canal shape, a continuity equation is solved to achieve w_0 and thus Fr, as illustrated in Table 1 of [3]. The cycle iterates to convergence of the inflow factor ϕ. To assess the flow speed variation from the most upstream array to downstream, a global inflow factor ϕ_g is also defined as U_0/U_∞.

5.2.2. Power optimization scheme

The need for an environmental check may be imposed by the channel manager of by specific regulations requiring the operator to minimize the increase in hydrostatic level upstream the whole plant. Therefore, an additional flag is introduced, which, if activated, reduces the rotor speed from the point of maximum performance. Refer to the environmental control section for further explanation. A wide range of rotor speeds Ω (rpm) is selected and indexed with k from 1 to N_Ω, and for each prescribed Ω, the previous iterative method is executed. The array blockage ratio is then calculated based on the upstream cross-section, and the single-turbine blockage ratio $B_{T,j}$ is determined through a function based on the geometrical separation of the flow passages from the inflow cross-section of depth h_0 and area A_0, while N_T represents the number of turbines within the array. The function is recalled at each inflow factor iteration, as the change in the cross-section area A_0 and depth h_0 are both functions of ϕ.

Since the inflow Froude number Fr and blockage ratios $B_{T,j}$ are known, the Double Multiple Streamtube function is executed for all turbines, thus determining the turbine thrust force T, power P, and minimum depth h_w, which are used as illustrated in the flowchart of the multi-array scheme in Section 5.3. Thus, array thrust force T_A and power P_A are calculated by integrating all the contributions within the array, thereby yielding the thrust coefficient $C_{TA,ref}$ from (5.5). The inflow factor ϕ is updated by solving Equation (5.6). The process is repeated until ϕ converges for a single rotor speed Ω, and then for all rotor speeds. Finally, the array power is optimized, and a single rotor speed $\lambda_{\infty,opt}$ is achieved after each rotor performance maximization (Fig. 5-5).

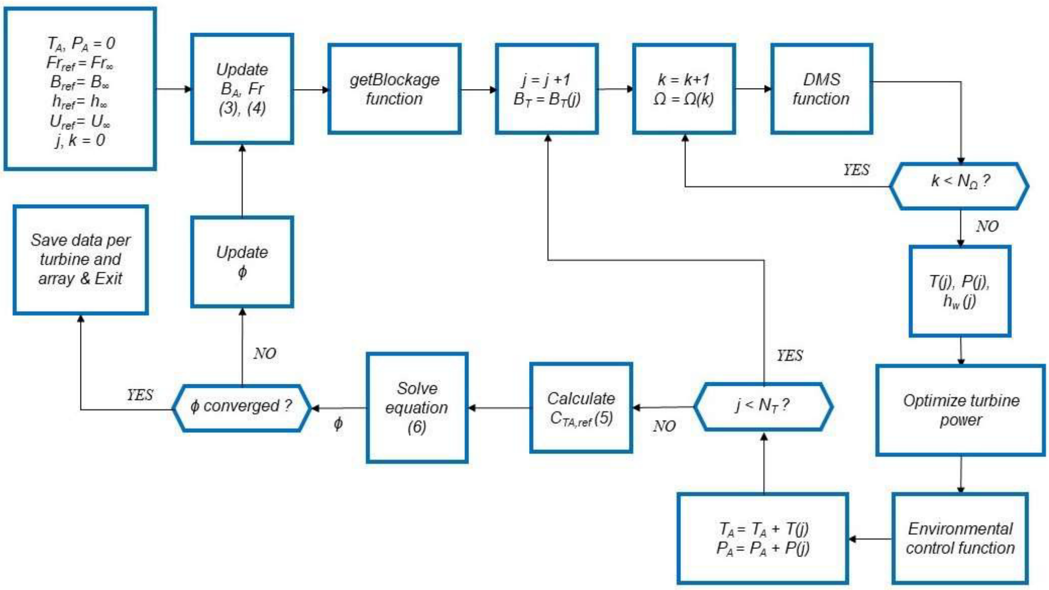

Fig. 5-5. Flowchart of the power optimization scheme for a single array.

The lateral spacing d_T between the turbines influences the performance through the locally generated blockage. Hence, once activated, the environmental control function is recalled before achieving the array thrust T_A and power P_A. Further notes on coded optimization schemes are available in [1].

5.2.3. Environmental constraint

Environmental control for overbank risk can be an excellent aid to avoid significant hydraulic issues due to excessive backwater. If activated, the previous scheme is carried out once for all arrays. Thus, if one of the inflow depths is higher than the recommended value, i.e., $\Delta h_{i,\infty} > \Delta h_{lim}$, a rotor speed modifier is introduced in the code. By default, it corresponds to a reduction of 1 rpm as a first step. However, it can be modified by the user. It is applied first to the most downstream array so that the code re-executes the computations for all turbine arrays with the same rotor speed modifier. The code verifies the environmental constraint once more at the end of the procedure. If the result is negative, the code implements a new step for speed reduction, inducing a drop in the rotor performance to respect the constraint.

5.2.4. Wake transition

The implemented methods predict the length of the far-wake distribution, with or without pre-setting. Moreover, the free surface variation in the near-wake downstream of the turbine is approximated to visualize the local effect of each rotor on the flow. The flow past the turbine shows a non-uniform distribution, which is not representative of the free surface throughout the channel cross-section.

Araya et al. [24] investigated the relation between dynamic solidity σ_D and the transition to bluff body dynamics in a vertical-axis rotor to determine the wake recovery length. Assuming the ratio of time scales (t_v/t_{conv}), i.e., the percentage of convection time required by the blades to close the gaps in between them during rotation, and the geometric factor (R_T/c), with R_T denoting the turbine radius and c denoting the blade chord, the dynamic solidity is formulated in Equation (5.7).

$$\sigma_D = 1 - \frac{R_T}{c}\frac{t_v}{t_{conv}} = 1 - \frac{1}{2\pi\sigma_A\lambda} \tag{5.7}$$

σ_A represents the rotor solidity defined by Araya (i.e., $N_b{*}c/(2\pi{*}R_T)$), while λ is the tip speed ratio ($\omega{*}R_T/U_0$). Although both definitions are valid, σ_A differs from the rotor solidity, i.e., $\sigma = N_b{*}c/(2R_T)$. The time scale t_v represents the time required by the operating turbine to close the gaps between the blades $t_v = l/(N_b{*}U_0{*}\lambda)$ while the convective time scale denoted by t_{conv} is the time required for a free stream particle to travel the distance $l = 2\pi{*}R_T{*}(1-\sigma_A)$, i.e., $t_{conv} = l/U_0$, with l denoting the sum of the gaps in the circumference of the turbine rotor. If $\lambda >> 1$, the turbine's wake mimics that of a full cylinder with $\sigma_D \approx 1$, but if $\lambda > 1/(2\pi{*}\sigma_A)$, the dynamic solidity σ_D increases monotonically with λ or σ_A. If $\lambda = 0$, the degree of interaction of the incident flow with the blades is unknown as it depends on the orientation of the rotor, and σ_D is indeterminate; otherwise, if $\lambda < 1/(2\pi{*}\sigma_A)$, the dynamic solidity is negative $\sigma_D < 0$ with a loss of physical meaning.

Based on the spectrum of the Strouhal number St vs. the downstream length (d_t/D_T), Araya et al. demonstrated the existence of a streamwise point where blade vortices decay to the point where they no longer account for the most energetic fluctuations in the flow so that bluff body oscillations start to dominate the wake dynamics. The far wake exhibited low-frequency oscillations typical of bluff bodies near $St = 0.26$, consistent with HAWT wake studies, e.g., those conducted by Chamorro et al. [30] and Okulov et al. [31].

As a result, Equation (5.8) revealed a linear correlation with σ_D and the location of downstream transition X_t where a shear-layer instability occurs, thus achieving the near-wake length in turbine diameters D_T. The correlation results from a linear regression of the wake transitions and dynamic solidities in different vertical-axis turbines. An increasing σ_D gives weaker shed vortices, with a faster transition into the wake.

$$d_t = D_T(4.78 - 4.93\sigma_D) \tag{5.8}$$

5.2.5. Wake recovery

A power law correlating dynamic solidity σ_D and the absolute minimum velocity was determined by Araya et al. [24], indicating that an increasing σ_D yields a faster rate or recovery of the velocity deficit into the wake, i.e., the higher the solidity, the greater the initial velocity deficit. The velocity recovery profiles of vertical-axis rotors were aligned to that of a solid cylinder according to the predictions of Schlichting [32] and Iungo and Porté-Agel [33] for turbulent free-shear flows and horizontal-axis wind turbine wakes. Since the maximum Reynolds stress occurs on the spanwise plane, the turbine aspect ratio AR is ascertained to play a significant role in the wake distribution. Indeed, an increasing aspect ratio produces more significant spanwise fluctuations in the wake recovery. The downstream recovery of the wake velocity deficit is expressed by the power law illustrated by Ouro et al. [25], which can be reversed into Equation (5.9) to determine the far-wake length d_f. U_w represents the known streamwise velocity in the near wake, i.e., ($U_w = \alpha_{w^*}U_0$), and a and b denote the power law coefficient and exponent according to Araya [24] for the rotor of a given aspect ratio. From the velocity deficit ΔU, one determines the local flow speed along the centerline $U_\# = \Delta U + U_0$. The length d_f is found by substituting $U_\#$ with the undisturbed flow speed U_∞; thus, a reduction in velocity yields $\Delta U = U_\infty - U_0$.

$$d_f = D_T \left[\frac{\frac{\Delta U}{U_0} + U_w}{a} \right]^{1/b} \tag{5.9}$$

5.2.6. Including inflow and wake regions

The free surface variation over and past a turbine array is modeled to visualize the downstream phenomena. The depth upstream of the single-array h_0 was determined via the previous iterative procedure, while the depth h_∞ is known. In the inflow region, streamlines are sensitive to the rotor induction, which spans from {0} to the turbine inlet. Its length is assumed by default ($d_0/D_T = 5.0$), whereas the Standard [34] indicates ($d_0/D_T = 2.5$), according to the modeling of wind turbine inflow [35].

With 2-D modeling, Adamski [36] introduced blockage to include the bottom of a channel for an unbounded rotor. Plots of the dynamic pressure demonstrated that the wake persists further downstream for turbines at the free surface proximity, and the turbine wake expands more uniformly for deeper installation. The minimum wake velocity at 20 D_T downstream diminished for a rotor placement next to the free surface. Adamski demonstrated the enhancement of free surface fluctuations with turbine placement near the free surface, with stationary waves generated downstream of the rotor with amplitude decaying in space.

The near-wake region past the turbine is characterized by shed vortices creating a shear layer isolating the low-momentum region of the core flow from the high-velocity region outside of the wake. The transition point represents the streamwise coordinate where bluff body oscillations start dominating the wake dynamics. In the near-wake region, blade vortices decay until they no longer account for high energy fluctuations. According to Ouro et al. [25] and Müller et al. [37], the near-wake region is exhausted within two turbine diameters past the turbine ($d_w/D_T \leq 2$), as drawn approximately with a dashed line in Fig. 5-6.

Fig. 5-6. Near-wake distribution of four cross-flow turbines from [4].

Within the transition region ($2 \leq d_w/D_T \leq 5$), the wake starts to vertically and laterally expand with a higher turbulent flow entrainment that increases the turbulent fluxes and intensity, and momentum starts to recover faster [25]. In the far-wake region, the core momentum is recovered according to turbine dynamic solidity and aspect ratio such that Reynolds stresses decay to their minimum at ($d_f/D_T = 14$) and ($d_f/D_T = 10$), respectively. A near-wake length is determined according to Araya's procedure once dynamic solidity σ_D (5.7) is known.

Therefore, the inflow length d_0 is added to the lengths of the near-wake region dw, transition region dt, and far-wake region d_f. According to the research of Müller et al. [37], the transition wake length can be approximated as $d_t/D_T = 3.0$. The above procedure is valid for the very-downstream array, while the assessment of other turbine arrays is described in Section (5.3). For more details on the local free surface deformation on each rotor, see [1].

<u>*5.2.7. Backwater region*</u>

Since channel geometry, Manning's coefficient n, bed slope S, and inflow depth h_0, are known, a direct step method is developed from h_0 to determine the backwater distribution of the gradually-varied flow. This can be performed based on the energy or momentum principle, according to Henderson [23]. At each step, the former reduces the water depth slightly from the previous value of a discrete dy, so that the new wetted area A, the hydraulic radius R_h and mean flow speed U are calculated. Since the Chezy coefficient C is given by the ratio ($R_h^{1/6}/n$) and the local friction slope S_f is inversely proportional to the square of C according to Manning's formula, S_f is derived from (5.10). Once the mean values $S_{J,avg,}$ and Fr_{avg} are determined from two steps, the discrete longitudinal specific energy variation $(dE/dx)_{avg}$ is derived from the 1-D Saint-Venant equation (5.11). The amount $(dE/dx)_{avg}$ divided by dE (5.12) yields the distance dx, and the coordinates x and h are collected from the inflow depth h_0 to the far-field h_∞.

$$S_f = \frac{U^2 n^2}{{R_h}^{4/3}} \tag{5.10}$$

$$\frac{dE}{dx} = S - S_{f,avg} \tag{5.11}$$

$$dE = dy(1 - {Fr_{avg}}^2) \tag{5.12}$$

The second method is based on the local momentum (5.13), with $\overline{Ay}$ denoting the moment of area of the cross-section, and $\overline{y}$ denoting the depth from the surface to the section centroid, according to Henderson [23]. The average shear stress over a step τ_{avg} is calculated as a function of the friction slope from (5.14), and the longitudinal steps dx are found by averaging the discrete momentum variation dM to the mean step longitudinal area, as shown in (5.15), with p denoting the wetted perimeter.

$$M = \overline{Ay} + \frac{{Q_c}^2}{gA} \tag{5.13}$$

$$\tau_{avg} = \rho g R_h S_{f,avg} \tag{5.14}$$

$$dx = \frac{dM}{AS - \frac{p\tau_{avg}}{\rho g}} \tag{5.15}$$

5.3. Multi-Array Scheme

The macroscopic functional scheme is illustrated in Fig. 5-7. After the setup of the parameters for the first array, the optimization tool (Fig. 5-5) performs cycles to calculate the optimum rotor speed maximizing the array power for each row from 1 to N_A, with or without the environmental control. The wake recovery length dW is determined, and the first array is placed at the longitudinal coordinate $X_A(1) = X_{ref} + dW$, thus establishing the initial downstream coordinate X_{ref}. In our case, $X_{ref} = 0$, while dW yields the distance from the determined zero to the first array's installation. The second array is placed at a distance d_A from the former. Hence, depths and flow speeds are determined for the channel at each discrete step up to recovery.

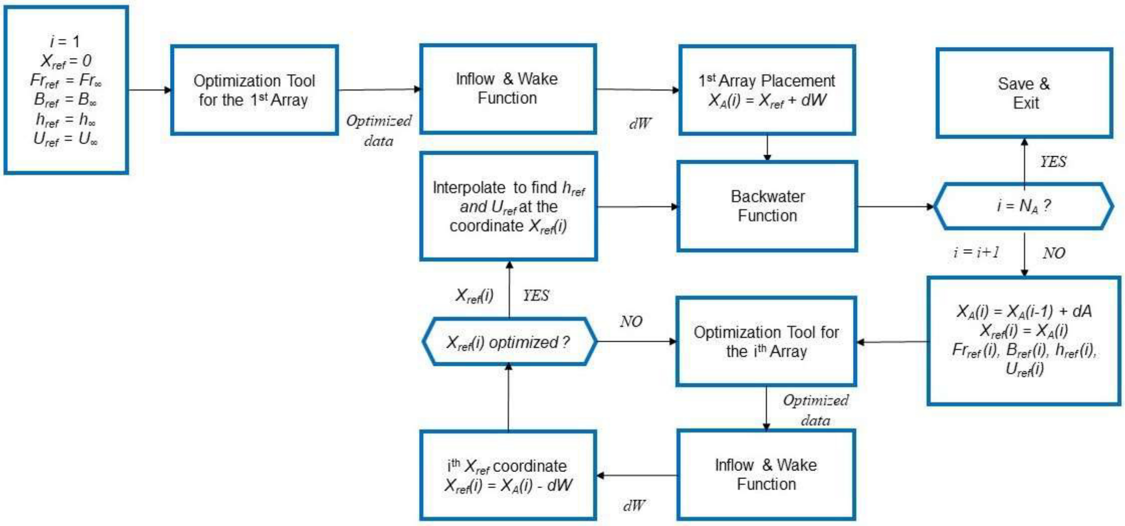

Fig. 5-7. Flowchart for solving DMS applied to an array of HK turbines.

If the new array's position anticipates the depletion of the previous backwater, an interpolation at the new $X_{ref}(2)$ yields the reference parameters, i.e., Fr_{ref}, B_{ref}, U_{ref}, and h_{ref}. After setting $X_{ref}(i) = X_A(i)$, the code iterates the optimization tool and the wake function to allow finding a first estimate of X_{ref} at convergence. However, the wake must develop such that $X_{ref}(i) = X_A(i) - dW$. This implies that X_{ref} for the second array is achieved at a gradually varied station immersed in the backwater. At the reference position, the depth from the still water level to the top of the turbines is again determined, allowing the free surface LMADT equations of the turbine model to account for the actual installation depth, which is updated further during the array's iteration.

If the new array position is set beyond the decay of the backwater upstream, so equal power is extracted from the two arrays due to identical fluid-dynamic conditions [3]. Notice that the channel is idealized as an equally distributed geometry towards infinity, with constant bed slope and roughness, and no other hydraulic transitions or obstacles. As a result, equal free surface variation and axial thrust force are expected. However, depending on the slope and Manning's roughness coefficient, this is likely to occur with extreme spacings between the arrays.

5.4. OPTIMUM DESIGN SOLUTION

The power of the plant consists of the sum of the power contributions from all arrays. In turn, the array power consists of the sum of the power outputs from all the turbines.

$$P = \sum_{i=1}^{N_A} P_{A,i} = \sum_{i=1}^{N_A}\sum_{j=1}^{N_T} P_{T,i,j} = \sum_{i=1}^{N_A}\sum_{j=1}^{N_T} \frac{1}{2}\rho A_{T,i,j} {U_\infty}^3 C_{P,\infty,i,j}$$

Considering turbines with equal geometry and size for all arrays, and replacing the summation of the power coefficients with a function F, P can be written as:

$$P = \frac{1}{2}\rho A_T {U_\infty}^3 \sum_{i=1}^{N_A}\sum_{j=1}^{N_T} C_{P,\infty,i,j} = \frac{1}{2}\rho A_T {U_\infty}^3 F$$

Therefore, the optimization consists of finding the power coefficients that maximize the objective function P, with conditions of backwater limitation Δh applied, thus maximizing the investment's net present value (or minimizing the Levelized Cost of Energy $LCoE$). $LCoE$ is used to assess and compare different methods of energy production and consists of the ratio of the net present value of the total costs to the Net Present Value of the electrical energy produced over a plant's lifetime. The design solution that maximizes F with all the constraints is given by:

$$P_{max} = \left[\frac{1}{2}\rho A_T {U_\infty}^3 * \max(F)\,, \min(\Delta h)\,, \min\,(LCoE)\right]$$

The minimization of sound emission and structural loads to limit the impact of structural works on canal embankments, etc..., represent other possible conditions to be assessed in future to find the optimum design solution.

REFERENCES

[1] Cacciali L., Battisti L., Dell'Anna S. Multi-Array Design for Hydrokinetic Turbines in Hydropower Canals. Energies **2023**, 16(5), 2279.

[2] Liu Y., Packey D.J. Combined-Cycle Hydropower Systems - The Potential of Applying Hydrokinetic Turbines in the Tailwaters of Existing Conventional Hydropower Stations. Renewable Energy **2014**, 66, 228-231.

[3] Cacciali L., Battisti L., Dell'Anna S. Backwater Assessment for the Energy Conversion Through Hydrokinetic Turbines in Subcritical Prismatic Canals. Ocean Engineering **2023**, 267, 113246.

[4] Available online: https://www.he-powergreen.it/ (accessed on 15 December 2022).

[5] Gauvin-Tremblay O., Dumas G. Hydrokinetic Turbine Array Analysis and Optimization Integrating Blockage Effects and Turbine-Wake Interactions. Renewable Energy **2022**, 181, 851-869.

[6] Gonzalez-Gorbeña, E.; Qassim, R.Y.; Rosman, P.C.C. Optimisation of Hydrokinetic Turbine Array Layouts via Surrogate Modelling. Renewable Energy **2016**, 93, 45–57.

[7] Okulov, V.L.; Naumov, I.V.; Kabardin, I.K.; Litvinov, I.V.; Markovich, D.M.; Mikkelsen, R.F.; Sørensen, J.N.; Alekseenko, S.V.; Wood, D.H. Experiments on Line Arrays of Horizontal-Axis Hydroturbines. Renewable Energy **2021**, 163, 15–21.

[8] Septyaningrum, E.; Hantoro, H.; Utama, I.K.A.P.; Prananda, J.; Nugroho, G.; Mahmashani, H.; Satwika, N.A. Performance Analysis of Multi-Row Vertical Axis Hydrokinetic Turbine-Straight Blade Cascaded (VAHT-SBC) Turbines Array. Journal of Mechanical Engineering and Sciences **2019**, 13, 5665–5688.

[9] Riglin J., Daskiran C., Jonas J., Schleicher W.C., Oztekin A. Hydrokinetic Turbine Array Characteristics for River Applications and Spatially Restricted Flows. Renewable Energy **2016**, 97, 274-283.

[10] Vennell R., Draper S., Funke S. Designing Large Arrays of Tidal Turbines: a Synthesis and Review. Renewable & Sustainable Energy Reviews **2015**, 41, 454-472.

[11] Cacciali L., Battisti L., Dell'Anna S. Free Surface Double Actuator Disc Theory and Double Multiple Streamtube Model for In-Stream Darrieus Hydrokinetic Turbines. Ocean Engineering **2022**, 260, 112017.

[12] Nishino T., R.H.J. Willden. The Efficiency of an Array of Tidal Turbines Partially Blocking a Wide Channel. Journal of Fluid Mechanics **2012**, 708, 596-606.

[13] Nishino T., R.H.J. Willden. Two-scale Dynamics of Flow Past a Partial Cross-Stream Array of Tidal Turbines. Journal of Fluid Mechanics **2013**, 730, 220-244.

[14] Draper S., Nishino T. Centred and Staggered Arrangements of Tidal Turbines. J. Fluid Mech. **2014**, 739, 72-93.

[15] Vogel C.R., Houlsby G.T., Willden R.H.J. Effect of Free Surface Deformation on the Extractable Power of a Finite Width Turbine Array. Renewable Energy **2016**, 88, 317-324.

[16] Gauvin-Tremblay O., Dumas G. Two-way Interaction Between River and Deployed Cross-Flow Hydrokinetic Turbines. Journal of Renewable & Sustainable Energy **2020**, 12, 034501.

[17] Myers L., Bahaj J., Wake Studies of a 1/30th Scale Horizontal Axis Marine Current Turbine. Ocean Engineering **2007**, 34, 758-762.

[18] Filizola N., Melo E., Armijos E., McGlynn J. Preliminary Analysis of Potential for River Hydrokinetic Energy Technologies in the Amazon River. IDB Technical Note (Energy Division), IDB-TN-891, (**2015**).

[19] Jacobson J.P., Assessment and Mapping of the Riverine Hydrokinetic Resource in the Continental United States (No. 1026880), Electric Power Research Institute (EPRI), (**2012**).

[20] Ridgill M., Neill S.P., Lewis M.J., Robins P.E., Patil S.D. Global Riverine Theoretical Hydrokinetic Resource Assessment. Renewable Energy **2021**, 174, 654-665.

[21] D'Auteuil S., Birjandi A., Bibeau E., Jordan S., Soviak J., Friesen D. Riverine Hydrokinetic Resource Assessment Using Low Cost Winter Imagery. Renewable & Sustainable Energy Reviews **2019**, 105, 293-300.

[22] Botto A., Claps P., Ganora D., Laio F. Regional-Scale Assessment of Energy Potential from Hydrokinetic Turbines used in Irrigation Channels. SEEP2010 Conference Proceedings, June 29th – July 2nd, Bari, Italy, (**2010**).

[23] Henderson F. M. Open Channel Flow, MacMillan Company, (1966) New York.

[24] Araya D, Colonius T., Dabiri J.O. Transition to Bluff-Body Dynamics in the Wake of Vertical-Axis Wind Turbines. Journal of Fluid Mechanics **2017**, 813, 346_381.

[25] Ouro P., Runge S., Luo Q., Stoesser T. Three-Dimensionality of the Wake recovery Behind a Vertical Axis Turbine, Renewable Energy **2019**, 133, 1066-1077.

[26] Malini C. Il Canale Biffis. Serie Acque e Bonifiche, Sometti Editore, ISBN 8874956762, **2017**.

[27] Chiu, C.L. Entropy and Probability Concepts in Hydraulics. Journal Hydraulic Engineering **1987**, 113, 583–599.

[28] Moramarco T., Singh V.P. Formulation of the Entropy Parameter Based on Hydraulic and Geometric Characteristics of River Cross Sections. Journal of Hydrologic Engineering **2010**, 15(10).

[29] Farina G., Alvisi S., Franchini M., Moramarco T. Three Methods for Estimating the Entropy Parameter M Based on a Decreasing Number of Velocity Measurements in a River Cross-section, Entropy **2014**, 16, 2512–252.

[30] Chamorro L.P., Hill C., Morton S., Ellis C., Arndt R.E.A., Sotiropoulos F. On the Interaction Between a Turbulent Open Channel Flow and an Axial-Flow Turbine. Journal of Fluid Mechanics **2013**, 716, 658–670.

[31] Okulov V.L., Naumov I.V., Mikkelsen R.F., Kabardin I.K., Sørensen J.N. A Regular Strouhal Number for Large-Scale Instability in the Far Wake of a Rotor. Journal of Fluid Mechanics **2014**, 747, 369–380.

[32] Schlichting H. Boundary Layer Theory, 4th edition. McGraw-Hill (1**960**).

[33] Iungo G.V., Porté-Agel F. Volumetric Lidar Scanning of Wind Turbine Wakes Under Convective and Neutral Atmospheric Stability Regimes. Journal of Atmospheric and Oceanic Technology **2014**, 31, 2035–2048.

[34] International Standard IEC. IEC 61400-12. Power Performance Measurements of Electricity Producing Wind Turbines. International Electrotechnical Commission, Geneva (**2005**).

[35] Meyer Forsting A.R. Modelling Wind Turbine Inflow: The Induction Zone. Ph.D Thesis. Department of Wind Energy Aerodynamic design, DTU (2017).

[36] Adamski S.J. Numerical Modeling of the Effects of a Free Surface on the Operating Characteristics of Marine Hydrokinetic Turbines. MSc Thesis, University of Washington (**2013**).

[37] Müller S., Muhawenimana V., Wilson C., Ouro P. Experimental Investigation of the Wake Characteristics Behind Twin Vertical Axis Turbines. Energy Conversion and Management **2021**, 247, 114768.

NOMENCLATURE

A_0, A_∞	Canal cross-section area m^2	R_h	Hydraulic radius m
A_A	Turbine array area, ($N_T{*}A_T$) m^2	R_T	Turbine radius m
A_F	Turbine flow-passage area m^2	S	Bed slope
A_T	Turbine swept area m^2	S_f	Friction slope
AR	Turbine aspect ratio	T	Axial thrust force N
$\overline{Ay}$	Moment area m^2	T_A	Array axial thrust force N
B_A, $B_{A,\infty}$	Array blockage ratio, ($N_T{*}A_T/A$)	U_0, U_∞	Mean flow speed m/s
B_T	Turbine blockage ratio, (A_T/A_F)	w_0, w_∞	Free surface width m
C_P, $C_{P,\infty}$	Turbine power coefficient, ($P/(½{*}\varrho{*}A{*}U^3)$)	X	Axial coordinate from the origin m
$C_{PA,\infty}$	Array power coefficient, ($P_A/(½{*}\varrho{*}A_A{*}U^3)$)	ΔH	Total head variation m
C_T, $C_{T,\infty}$	Turbine thrust coefficient, ($T/(½{*}\varrho{*}A{*}U^2)$)	Δh	Free surface variation m
$C_{TA,\infty}$	Array thrust coefficient, ($T_A/(½{*}\varrho{*}A_A{*}U^2)$)	$\Delta(h_i - h_{i-1})$	Deviation in water depth, m
c	Blade chord m	Δh_{lim}	Environmental constraint m
D_h	Hydraulic depth	ΔU	Flow speed variation m/s
D_0	Shaft diameter m	Ω	Rotor speed rpm
D_T	Turbine diameter m	α_w	Near-wake interference factor, (U_w/U_0)
d	Wake length m (See subscripts)	λ, λ_∞	Tip speed ratio
d_A	Array spacing m	ρ	Fluid density kg/m^3
d_T	Turbine spacing m	σ	Rotor solidity, ($N_b{*}c/(2R_T)$)
dE	Specific energy variation m	σ_A	Rotor solidity from [24], ($N_b{*}c/(2{*}\pi{*}R_T)$)
dW	Total wake length m	σ_D	Dynamic solidity, ($1-1/(2\pi{*}\sigma_A{*}\lambda)$)
dx	Discrete longitudinal step m	ϕ	Inflow factor, (U_0/U_{ref})
dy	Discrete variation in water depth m	ϕ_g	Global inflow factor, (U_0/U_∞)
Fr, Fr_∞	Froude number, ($U/(g{*}D_h)^{½}$)	ω	Angular velocity rad/s
g	Gravity acceleration m/s^2		
H_T	Turbine height m	*Subscripts*	
h_0, h_∞	Water depth m	f	Far-wake
M	Channel momentum m^2	opt	Optimum
N_A	Number of arrays	ref	Reference
N_b	Number of blades	t	Transition-wake
N_T	Number of turbines	w	Near-wake
N_Ω	Number of selected rotor speeds		
n	Manning's coefficient $m^{-1/3}s$	*Short forms*	
P	Turbine power W	*DMS*	Double Multiple Streamtube
P_A	Array power W	*HK*	Hydrokinetic
Q_c	Channel flow rate m^3/s	*LMADT*	Linear Momentum Actuator Disc Theory

6. RESULTS AND DISCUSSION

Section 6.1 adapted to the article:

Cacciali L., Battisti L., Dell'Anna S. Free Surface Double Actuator Disc Theory and Double Multiple Streamtube Model for In-Stream Darrieus Hydrokinetic Turbines. Ocean Engineering 2022, 260, 112017. DOI: https://doi.org/10.1016/j.oceaneng.2022.112017.

Section 6.2 based on the article:

Cacciali L., Battisti L., Dell'Anna S. Multi-Array Design for Hydrokinetic Turbines in Hydropower Canals. Energies 2023, 16(5), 2279. DOI: https://doi.org/10.3390/en16052279.

The prediction of thrust and power coefficients is illustrated with sensitivity on all the main parameters influencing the model corrections, including the streamtube expansion introduced in Chapter 3. The vertical discretization is accomplished, first, with a single blade element and later, including the small blade element characterizing the blade curvature, improving the accuracy. Hence, the azimuthal discretization is investigated by varying the number of the streamtubes. Although many sub-models are required to include secondary flow effects and additional fluid-dynamic losses, the simulation performed on the Darrieus rotor tested in Chapter 1 shows promising results. Predictions of different multi-array layouts allow drawing remarks on turbine and array spacings, documented with the outputs of a sensitivity analysis. An array power output is optimized by increasing the turbine aspect ratio and the number of machines. With depth control, a drop in the turbine performance is achieved with a decrease in the expected backwater. Finally, flow visualizations with porous plates at different spacings confirm the validity of the hydraulic assessment integrated with the previous rotor model and the asymptotic behavior of the deviation in the inflow depth.

6.1. Single Turbine Assessment

The first simulations are carried out on the turbine data from Chapter 1 [1], i.e., a Darrieus rotor consisting of three straight blades built with NACA0021 profiles deployed in the narrow waterway in Fig. 6-1. The solution of the DMS was described in Chapter 4 based on [2], with the additional iterative inflow correction [3] illustrated in Chapter 3.

Fig. 6-1. Three-bladed Darrieus hydrokinetic turbine in [1].

The high solidity represents a limiting factor for the performance due to the intense interaction between the blades, as well as the optimum operation occurring at a low tip speed ratio, but, on the other hand, the shape of the blades was engineered to allow a tip-loss reduction, maintaining high performance. The tip speed ratio is here defined based on the undisturbed flow speed, i.e., $\lambda_\infty = \omega{\cdot}R_T/U_\infty$.

Next are illustrated the single blade outputs. Further, a sensitivity analysis on the sub-models is carried out for the simulated $C_{T,\infty}$ and $C_{P,\infty}$ to the tip speed ratio λ_∞ over six operating conditions, excluding the last experimental point from [1] at which the turbine operates at the runaway speed. Notice that the Lanchester-Prandtl's correction is not activated due to the absence of blade tips on this rotor.

This work relies on the polar database built at Reynolds numbers between 0 and 10^7. Fig. 6-2 shows the database extension for C_l and C_d to the post-stall region for this profile, attained with Viterna-Corrigan's method, as mentioned in the previous section.

6.1.1. Blade outputs

Hereafter, the single-blade outputs are shown over a complete revolution. In Fig. 6-3 the axial induction factor is depicted versus the azimuthal blade position ϑ. he plot of induction factors is preferred to the plot of interference factors for better visualization. The maximum induction factor is achieved at 90° and 270° where the blade is orthogonal to the flow and the drag force is higher. As the shaft correction is activated, the downstream induction slightly drops at the cusp due to the shaft's interference with the wake.

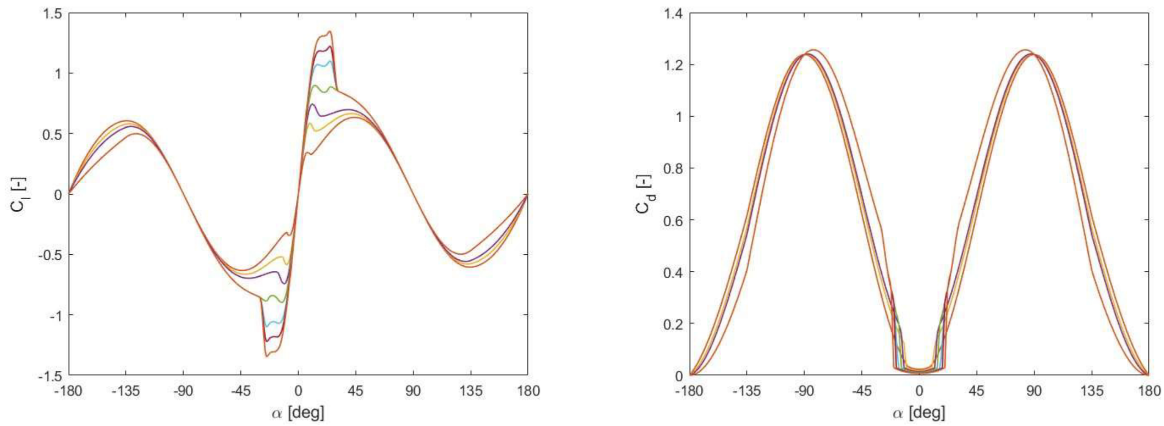

Fig. 6-2. Extension of the database lift coefficient C_l (**left**) and drag coefficient C_d (**right**) database for the hydrofoil NACA0021 from low to high Reynolds number.

The induction factor increases with the tip speed ratio demonstrating a drop in the flow rate processed by the machine, suggested by a low porosity of the discs. The higher induction factor for $\vartheta > 180°$ is consistent with a lower turbine power downstream, in line with the theory presented in Chapter 2. Velocity triangles are solved at each rotor speed, and the peaks in the axial induction factor coincide with higher angles of attack (α), as inferred from Fig. 6-3. However, a low tip speed ratio implies that C_l and C_d approach the deep stall angle , i.e., a sudden drop in lift and steep rise in the drag-reducing the blade performance, thus denoting high α. The optimum tip speed ratio λ_∞ is achieved when the average mechanical torque is maximized over a revolution, i.e., at the rotor speed of 110.21 rpm. Although the deep stall is identified numerically only at the first operative point, the dynamic stall hysteresis must be assessed with a specific unsteady routine, out of the purpose of this work.

The predicted Reynolds numbers at the investigated rotor speeds range between 0.72e5 and 2.75e5, including all operative points, in line with experimental data [1]. The graph in Fig. 6-4 shows the ratio Re/Re_{max} versus the azimuthal angle. As the λ_∞ increases, the tangential speed dominates in velocity triangles, leading to a low variation in the Reynolds number. At low λ_∞, the Reynolds number variation corresponds to higher turbine power loss.

The variation in the blade's power coefficient $C_{P,\infty}$, calculated respective to the far-field flow U_∞, is shown in Fig. 6-4 versus the azimuthal angle. According to the double actuator disc extension, the power coefficient drops as the flow passes upstream and downstream. The shaft correction slightly reduces the cusp of the downstream curve, further decreasing the power conversion.

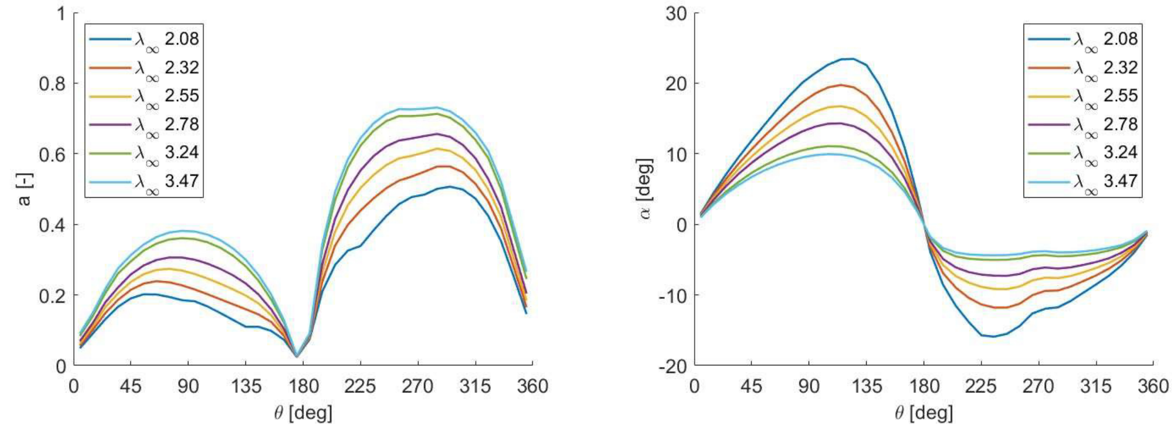

Fig. 6-3. (**Left**) Axial induction factor $\boldsymbol{a}$ vs azimuthal position ϑ for a single blade. (**Right**) Axial Angle of attack $\boldsymbol{\alpha}$ vs azimuthal position ϑ for a single blade.

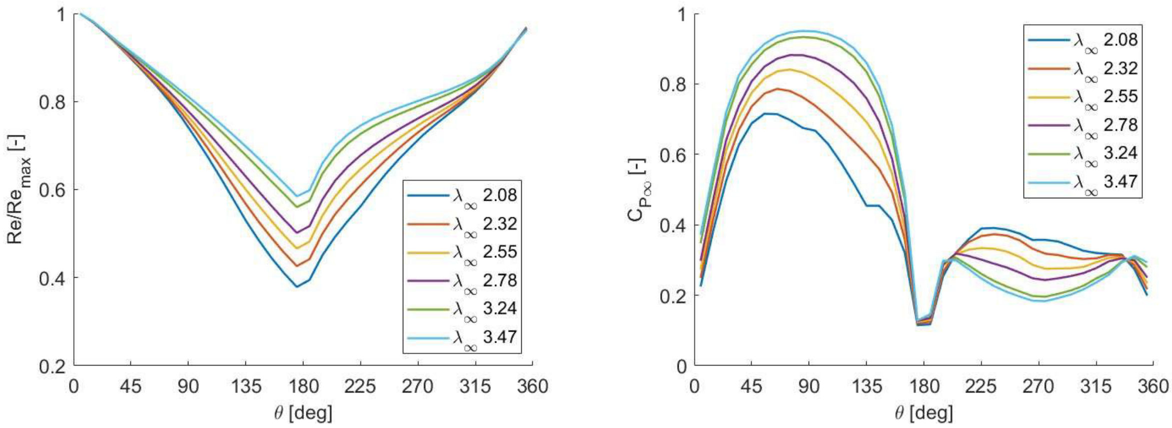

Fig. 6-4. (**Left**) Normalized Reynolds number $\boldsymbol{Re/Re_{max}}$ vs azimuthal position ϑ for a single blade. (**Right**) Power coefficient $\boldsymbol{C_{P,\infty}}$ vs azimuthal position ϑ for a single blade.

6.1.2. Sensitivity analysis

Based on each sub-model implemented, the turbine outputs are visualized from Fig. 6-5 to Fig. 6-9, while each sub-model correction is activated and deactivated. The sensitivity analysis is performed by calculating the root mean square deviation (RMSD) of predictions to experimental data, with outputs depicted in Tab. 6-1. The results of the inflow assessment are shown in Fig. 6-5. The unperturbed flow speed U_∞ varies according to its absolute error, thus modifying the canal flow rate. The method effectively increases the accuracy of the prediction, with higher improvement in the power coefficient $C_{P,\infty}$. The corrected curves are just slightly dependent on the variation in the speed U_∞ and due to a low change in the far-field Froude number Fr_∞ between low and high flow rates. A wider variation in Fr_∞ would yield a more noticeable displacement of the mean curve. A large overestimation in $C_{T,\infty}$ and

$C_{P,\infty}$ is shown if the inflow correction is switched off. This implies that U_∞ cannot be used as inflow speed, showing the effectiveness of this iterative procedure.

Shaft, mechanical struts, and curvature corrections are all compared to the best-simulated curve achieved from the previous inflow correction, whose far-field speed is $U_\infty = 1.078$ m/s.

Fig. 6-6 is achieved by activating and deactivating the shading due to the rotating shaft on the downstream blade interactions. Its effect is visible on all azimuthal charts of Fig. 6-3 and Fig. 6-4. The fitting of $C_{T,\infty}$ and $C_{P,\infty}$ slightly improves, and both coefficients are reasonably reduced compared to their trend without shaft shading. This correction is in line with the overall results of other DMS models. Notice that the thrust coefficient slightly improves towards the best curve if this correction is switched off, as illustrated in Tab. 6-1. However, this does not hold for the $C_{P,\infty}$. Another sub-model concerns struts generating fluid-dynamic losses. The hydrokinetic turbine investigated has no struts but has blades extending horizontally to the shaft. The DMS does not consider top and bottom horizontal blade elements. However, two mechanical struts per blade of a fixed chord are modeled. The actual horizontal section is discretized into ten elements, and the simulation generates the curves in Fig. 6-7. The variation of the thrust coefficient due to this sub-model is small enough to be disregarded. On the other hand, the power coefficient is strongly affected by fluid-dynamic losses, thus making the correction highly effective for this rotor.

The effect of flow curvature in Fig. 6-8 is almost negligible in this case, possibly due to the zeroing of the component arising from the mounting point ($x_{0r} = 1/4$), as depicted in Goude's work. Although an improvement in the $C_{P,\infty}$ is obtained without this correction, as better shown in Tab. 6-1, this is not true for the $C_{T,\infty}$. For evaluating the best curves in all figures, this sub-model was activated. The installation depth sub-model is evaluated in Fig. 6-9. As h_0 is determined at each tip speed ratio, the factor ξ for test conditions is initially calculated with $d_h = 0.1$ m from downstream and updated iteratively. The generated curve is compared with the outputs of a complete Free Surface ($\xi = 0$) and Rigid Lid ($\xi = 1$) cases. As illustrated in Chapter 4, the outputs of Tab. 6-1 are based on a single vertical discrete element, which simplifies the rotor geometry. Apart from the mild effects of the flow curvature correction and rotating shaft correction, other sub-models consistently improve thrust and power coefficient. The sub-model improves the prediction by including the turbine depth directly in the momentum equation. Additional simulations on different rotors are needed to assess the general validity of this sub-model. The sub-model shows the struts fluid-dynamic losses, and its implementation is articulate. However, the geometry of the mechanical struts simplified, but no better method for profiled struts is available. Other sub-models applicable to flat plates are those of Moran [4], further illustrated by Paraschivoiu [5] and Bianchini et al. [6].

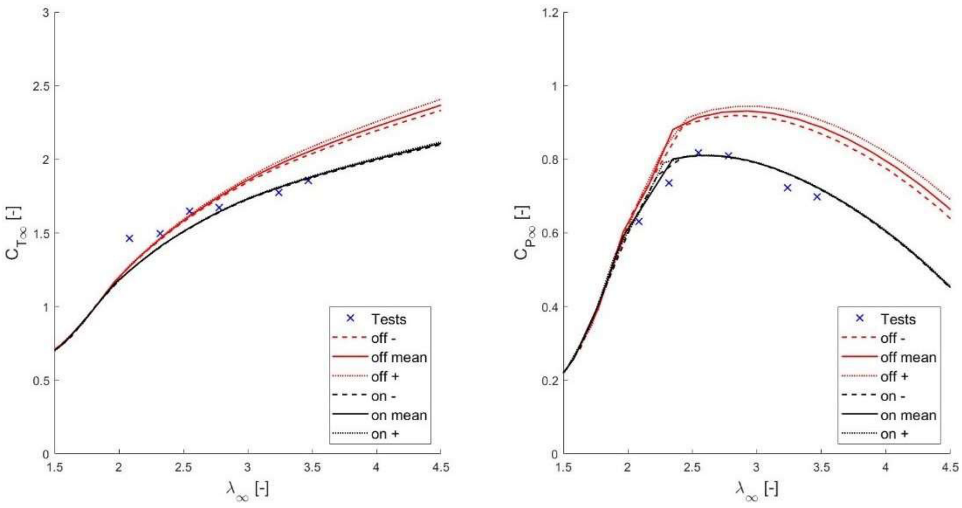

Fig. 6-5. Inflow correction: Thrust coefficient $C_{T,\infty}$ and power coefficient $C_{P,\infty}$ vs tip speed ratio λ_∞.

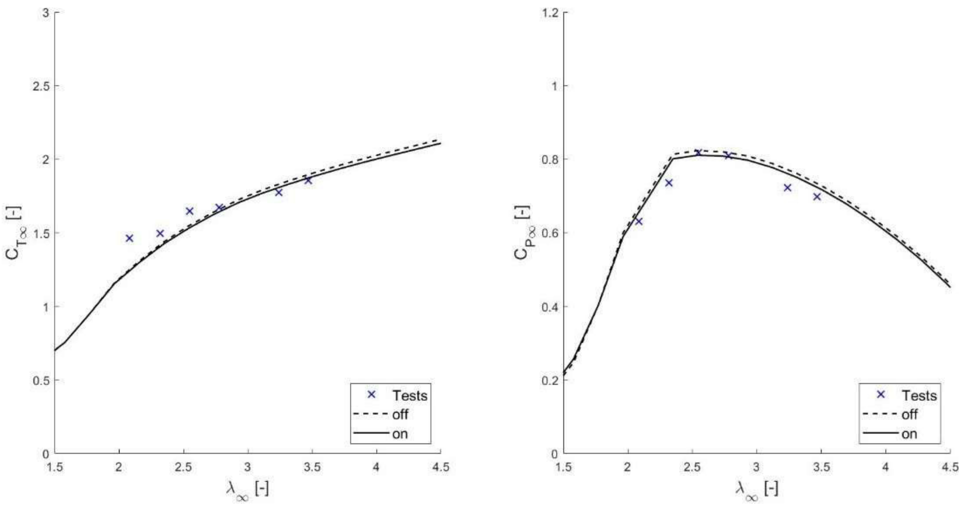

Fig. 6-6. Rotating shaft correction: Thrust coefficient $C_{T,\infty}$ and power coefficient $C_{P,\infty}$ vs tip speed ratio λ_∞.

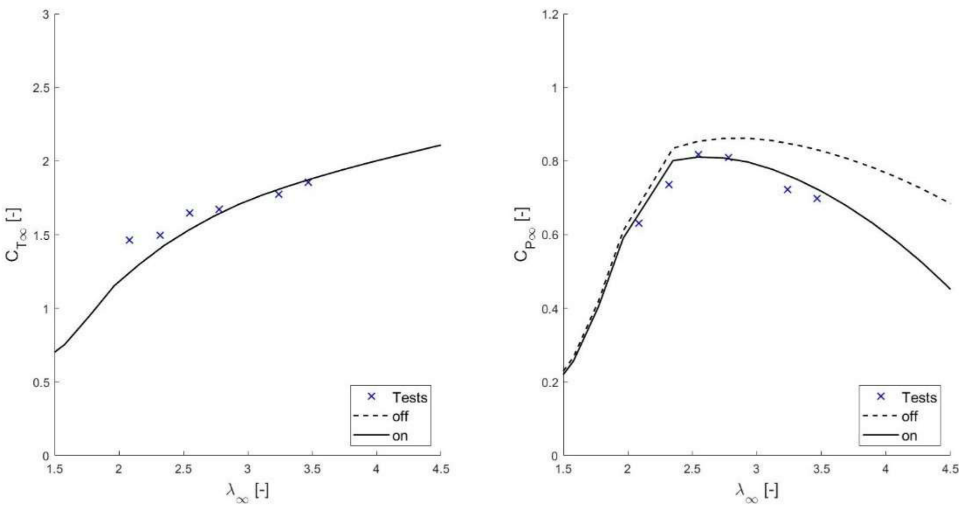

Fig. 6-7. Struts correction: Thrust coefficient $C_{T,\infty}$ and power coefficient $C_{P,\infty}$ vs tip speed ratio λ_∞.

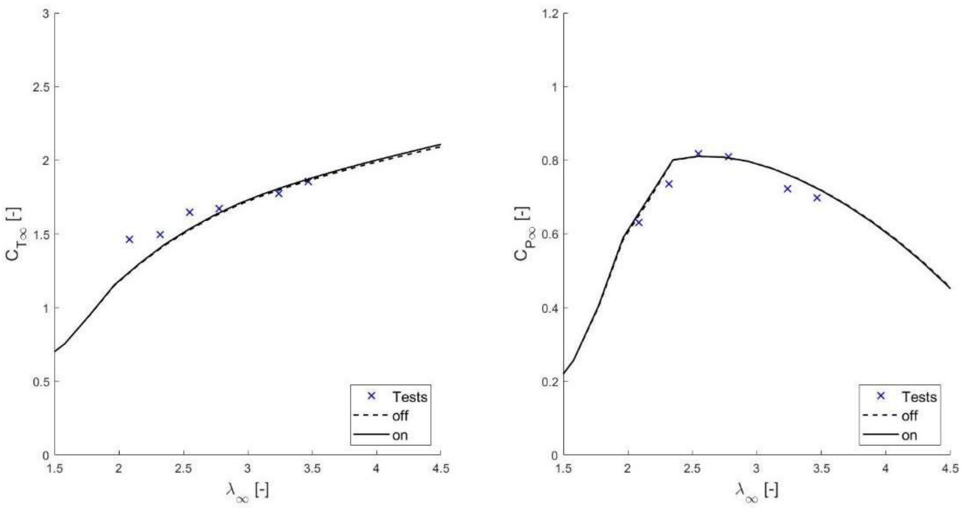

Fig. 6-8. Flow curvature correction: Thrust coefficient $C_{T,\infty}$ and power coefficient $C_{P,\infty}$ vs tip speed ratio λ_∞.

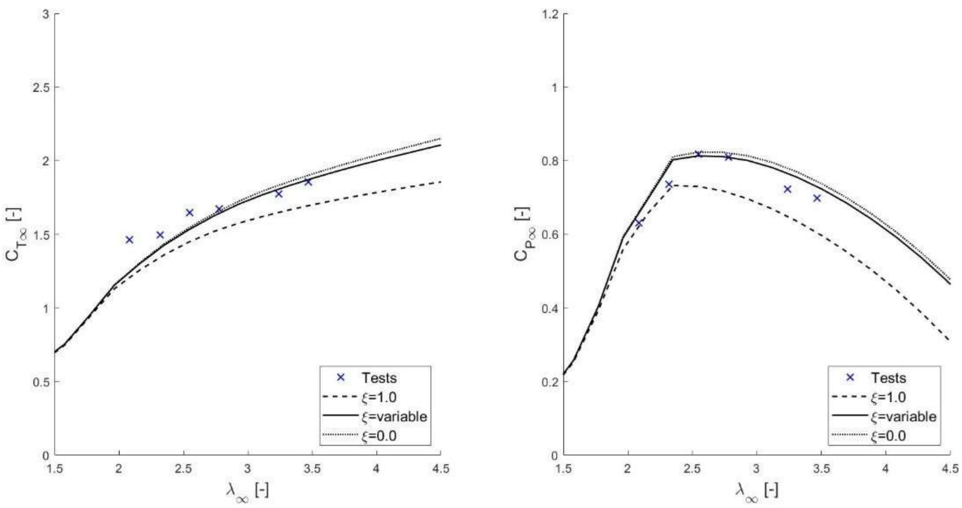

Fig. 6-9. Depth correction: Thrust coefficient $C_{T,\infty}$ and power coefficient $C_{P,\infty}$ vs tip speed ratio λ_∞.

Tab. 6-1. Sensitivity analysis including (1-5) sub-models.

Description	RMSD ($C_{T,\infty}$)	RMSD ($C_{P,\infty}$)
Best curves (all corrections included)	0.108	0.033
Inflow correction (off)	0.140	0.140
Shaft correction (off)	0.103	0.028
Struts correction (off)	0.108	0.090
Flow curvature (off)	0.111	0.033
Installation depth correction ($\xi = 0$)	0.106	0.044
Installation depth correction ($\xi = 1$)	0.177	0.073

Since the downstream hydraulic information is transferred upstream in riverine flows, isolated Blade Element Momentum models inadequately describe the physical phenomenon. However, it is possible to make intelligent use of the DMS with the additional iteration of the inflow factor, showing better predictions of $C_{T,\infty}$ and $C_{P,\infty}$ than those achieved by the DMS alone (Chapter 4).

Including top and bottom curvature of the blades modeled as diagonal pieces (Fig. 6-10), the turbine model further improves. The angle δ is of ± 45°. Again, the horizontal part of the blade is considered like a mechanical strut inducing fluid-dynamic losses because horizontal blade elements cannot be modeled as blades in the model. Hence, the turbine is modeled with two straight vertical elements and two diagonal elements.

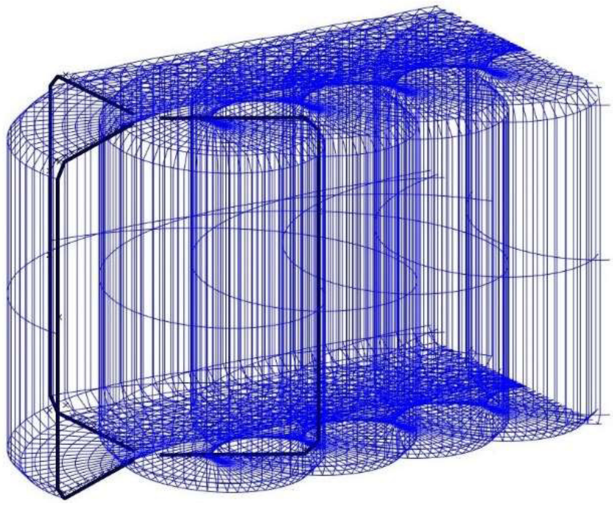

Fig. 6-10. 3-D drawing of the rotow (from a lifting line development).

The new prediction includes all model corrections but excludes the streamtube expansion. In this case, the sensitivity of the azimuthal discretization is tested. Improvement is demonstrated by decreasing $\Delta\vartheta$, with 72, 36, 18, and 6 streamtubes, thus achieving 2.5°, 5.0°, 10°, and 30°, respectively. Although all predictions are satisfactory (Fig. 6-11 and Tab. 6-2), poorer visual matching is shown by the solution for $\Delta\vartheta$ = 30°. Since the outputs do not change consistently within the other cases, a choice of $\Delta\vartheta$ = 5° seems fair enough to solve the problem for this small turbine. The changes in the RMSD within the presented simulations are barely significant. Although worsening, the outputs of this simulation are more physically based.

Tab. 6-2. New sensitivity analysis of vertical and azimuthal discretization including (1-5) sub-models.

Description	RMSD ($C_{T,\infty}$)	RMSD ($C_{P,\infty}$)
Azimuthal discretization (dϑ=2.5°)	0.112	0.045
Azimuthal discretization (dϑ=5.0°)	0.112	0.045
Azimuthal discretization (dϑ=10.0°)	0.111	0.045
Azimuthal discretization (dϑ=30.0°)	0.114	0.048

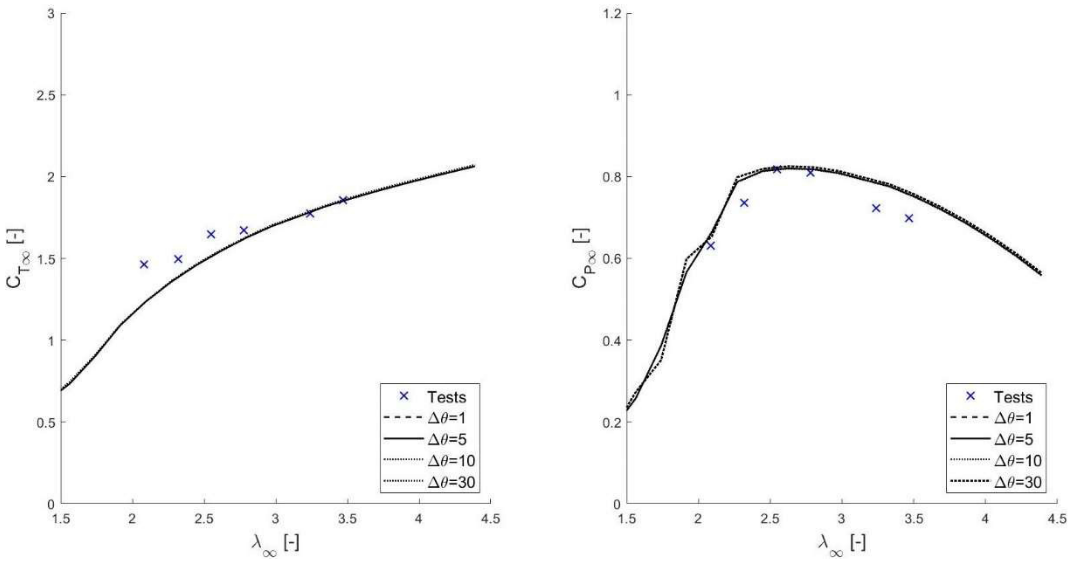

Fig. 6-11. Azimuthal discretization: Thrust coefficient $C_{T,\infty}$ and power coefficient $C_{P,\infty}$ vs tip speed ratio λ_∞.

Finally, the turbine performance is predicted with the streamtube expansion correction described in Chapter 3. Although the effect of the expansion has a limited impact considered the rotor size, the RMSD of $C_{T,\infty}$ and $C_{P,\infty}$ improves with respect to the solution based on straight streamtubes (the vertical near-wake expansion is ignored, even though determined algebraically).

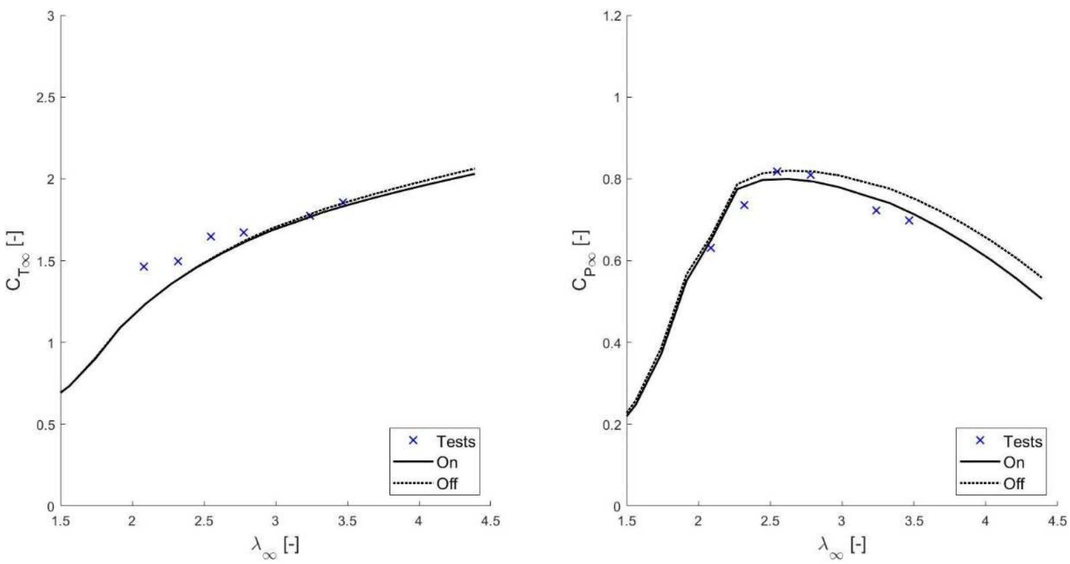

Fig. 6-12. Flow expansion correction: Thrust coefficient $C_{T,\infty}$ and power coefficient $C_{P,\infty}$ vs tip speed ratio λ_∞.

The vertical near-wake expansion is ignored, even though determined algebraically. According to Schmitz and Pelz [7], the free surface variation induces a local contraction of the streamtube due to the turbine head drop, partially limiting the vertical expansion of the near-wake. A contraction of the annular streamtube was effectively modeled considering the acceleration induced bypassing the second disc, with interference factors from α_e to γ_w.

A more thorough investigation of rotors of larger diameters is appropriate to provide a further evaluation concerning the wake development over the free surface drop. The corrected results in Tab. 6-3 and Fig. 6-12 are assumed as the most reliable prediction in this work. The power coefficient improves past the optimum up to high tip speed ratios.

Tab. 6-3. Sensitivity analysis of the streamtube expansion correction.

Description	RMSD ($C_{T,\infty}$)	RMSD ($C_{P,\infty}$)
Streamtube expansion correction (on)	0.104	0.029
Streamtube expansion correction (off)	0.112	0.045

In the azimuthal charts of Fig. 6-13, the improvement of the streamtubes expansion is noticeable only downstream for the axial induction factor and power coefficient. It is due to the method which leaves unchanged the induction factors at the first disc. The variation in the thrust force, angle of attack and Reynold's number is not identifiable, and is not shown. The axial induction factor rises to nearly 180° and 360°, indicating the effectiveness of the correction.

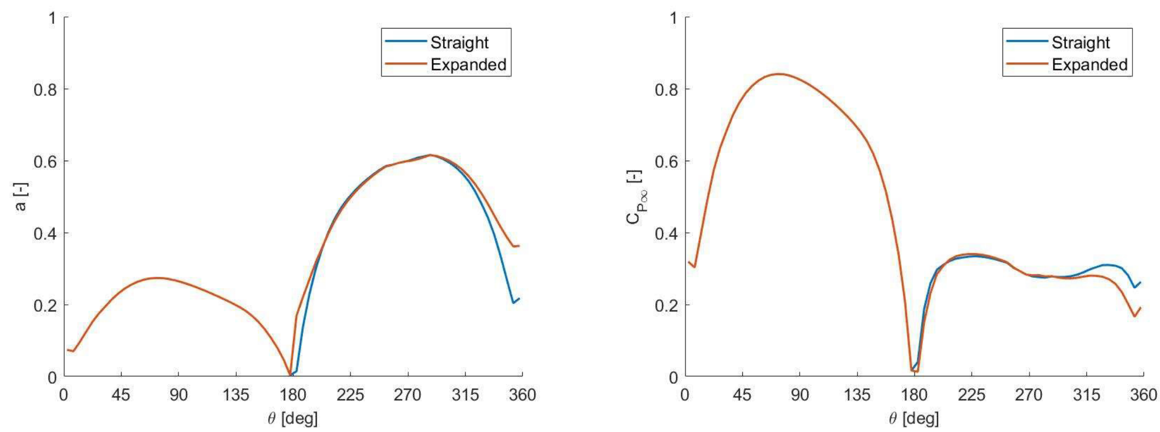

Fig. 6-13. (**Left**) Difference between straight and expanded streamtubes on the axial induction factor ***a***. (**Right**) Difference in power coefficient $C_{P,\infty}$ vs the azimuthal position ϑ for a single blade at a λ_∞ of 2.55.

The wake generated with straight and expanded streamtubes is depicted further with the downstream velocity contours for the turbine at the optimum tip speed ratio in Fig. 6-14. A more extensive wake is observed in the image on the right, but the deviation is minimal. Notice that the annular flow is neglected in this image. The channel is narrow, and the blockage generated is substantial. Therefore, the expanded wake does not deviate much from the straight-tube solution is plausible, given the contraction determined by lateral flow due to continuity.

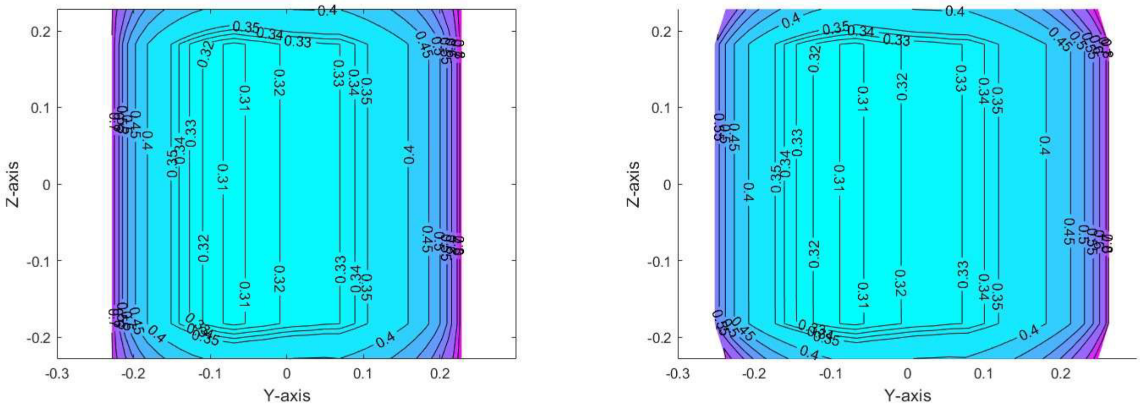

Fig. 6-14. (**Left**) Velocity contours generated far downstream with straight streamtubes. (**Right**) Velocity contours generated far downstream with expanded streamtubes.

The prediction at the optimality is assessed for the vertical straight element and the diagonal element approximating the blade's curvature. Since this turbine has a closed-ring shape and the horizontal blade elements are attached to the shaft from the top and the bottom, Prandtl's tip loss correction is not applied. The induction factor of the diagonal blade element drops due to the lower interference with the flow. Although the angle of attack of the straight blade element increases up to 16.75° upstream (Fig. 6-15), it never stalls and is less likely for the thin segment.

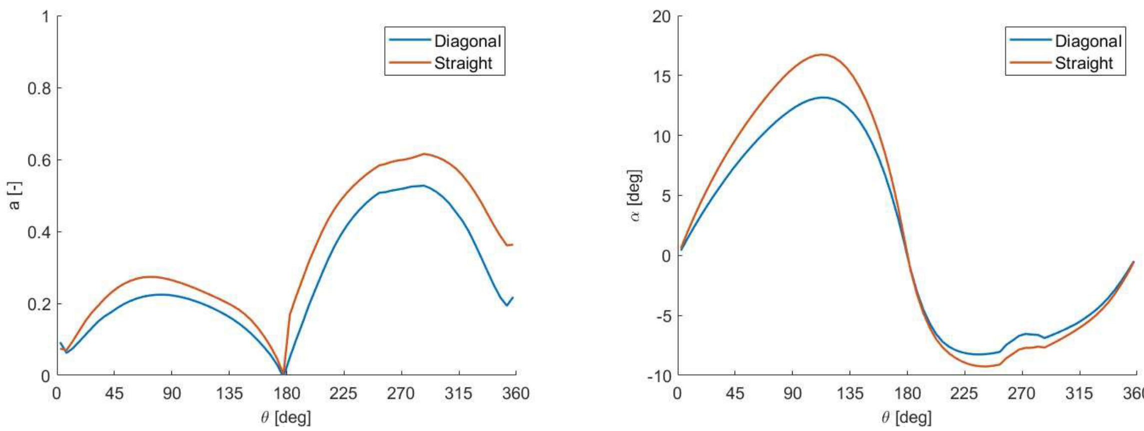

Fig. 6-15. (**Left**) Axial induction factor $\boldsymbol{a}$ vs azimuthal position ϑ for a single blade. (**Right**) The angle of attack $\boldsymbol{\alpha}$ vs azimuthal position ϑ for a single blade.

This turbine shape certainly reduces hydrodynamic losses, but the behavior of straight elements and curvature differ as their shape implies a different λ_∞, i.e., 2.55 for the vertical element and 2.34 for the blade top. The normal force coefficient C_n per unit height is similar between both elements, and the tangential force coefficient C_t is more consistent upstream, according to the trend of the angle of attack (Fig. 6-16). Finally, the difference in $C_{T,\infty}$ and $C_{P,\infty}$ between top and core blade elements is depicted in Fig. 6-17.

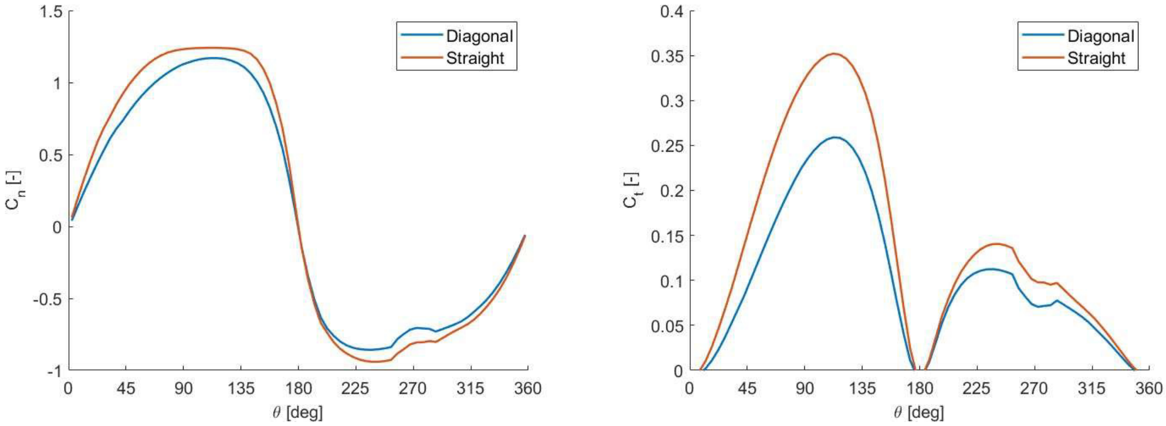

Fig. 6-16. (**Left**) Normal force coefficient C_n vs azimuthal position ϑ for a single blade. (**Right**) Tangential force coefficient C_t vs azimuthal position ϑ for a single blade.

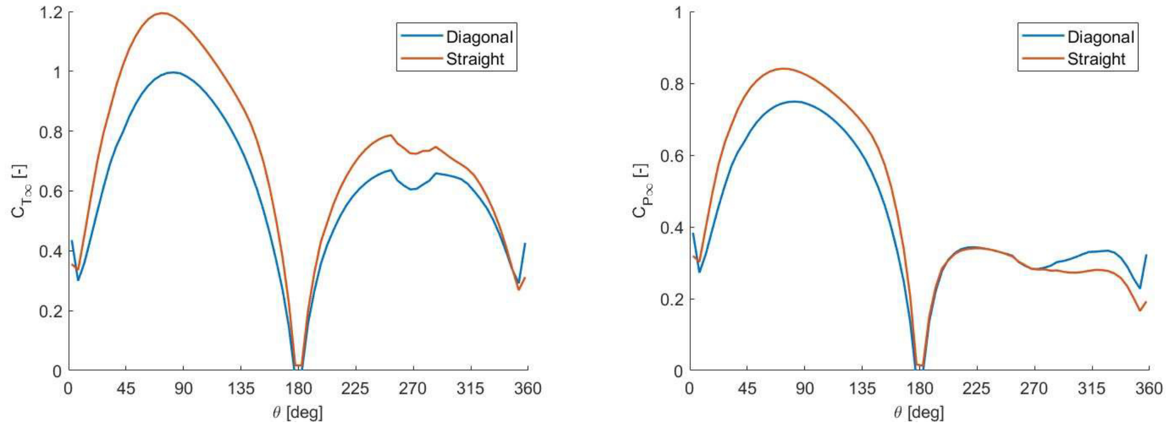

Fig. 6-17. (**Left**) Thrust coefficient $C_{T,\infty}$ vs azimuthal position ϑ for a single blade. (**Right**) Power coefficient $C_{P,\infty}$ vs azimuthal position ϑ for a single blade.

6.2. TURBINE ARRAYS ASSESSMENT

The momentum methods disclosed in Chapter 5 are tested to investigate the effect of turbine spacing and array spacing on axial forces and power, observing that the increase in thrust is reasonably proportional to the rise in backwater depth. The results illustrated in this section are identical to those depicted in the recent work [8].

The momentum method is tested to investigate the effect of turbine spacing and array spacing on axial forces and power, which indicates an increase in thrust reasonably proportional to the rise in backwater depth. The predictions are carried out based on the concession discharge of the hydropower canal depicted in Fig. 5-2, which was subject to ongoing hydrokinetic turbine testing.

An optimization procedure was conducted on few design cases based on different array features. Array blockage and turbine solidity are kept constant to assess the most suitable design solutions, and the turbine aspect ratio varies between alternatives after fixing array blockage ratio. A final computation is performed based on the research shown in [8] to predict the distribution of the free surface variation and maximum power output for a large plant incorporating many arrays.

6.2.1. Sensitivity analysis

Predictions of the array thrust force and power are collected vs. the global inflow factor ϕ_g, defined as U_i/U_∞, with the subscript (i) related to the actual array, starting from downstream. The same three-bladed geometry of the prototype [1] is used for the simulations. Lower solidity and a higher aspect ratio are chosen to reduce fatigue and torque ripple, as suggested in Chapter 1. In this work, solidity is defined as the chord-to-diameter ratio multiplied by the number of blades, i.e., $\sigma = N_b{*}c/(2R_T)$.

For the first assessment, a rotor size ($D_T{*}H_T$) of 2.0 × 3.0 m is selected, with a shaft diameter D_0 of 0.18 m, solidity $\sigma = 0.36$, and aspect ratio (AR) of 1.5. The blade profile is an asymmetric DU06W200, which is less prone to dynamic stall at low tip speed ratios, with a chord length c of 0.24 m. Since the computational time increases with the number of arrays, faster simulation is facilitated with an azimuthal displacement of 15 deg, whilst the starting turbine depth is 0.2 m from the still water level.

The streamtube expansion is not activated to limit the computational cost of the simulation. For the same reason, no environmental constraint is activated for the initial predictions. The sensitivity of array thrust, and power based on turbine spacing d_T and array spacing d_A are investigated in the following sections.

a) Turbine spacing (d_T)

The array thrust coefficient $C_{TA,\infty}$ vs. global inflow factor ϕ_g for a plant of four arrays is shown on the left side of Fig. 6-18 according to different turbine spacings d_T (different color). Each marker represents the array $C_{TA,\infty}$ from the most upstream array (left side) to downstream (right side).

Spacings of 2.5 m, 3.0 m, and 3.5 m between each rotor vertical-axis (corresponding to 1¼, 1½, and 1¾ equivalent lengths based on turbine diameters D_T) are chosen and the array spacing d_A is set to 50 m. The lower turbine spacing of 2.5 m guarantees a safety margin of 0.5 m between the blades of neighboring turbines, while the higher spacing of 3.5 m represents the limit for four turbines (2.0 × 3.0 m in size) about the available wetted area and the selected clearance between the turbine top and the still water level of the undisturbed flow. On the right side of Fig. 6-18, the array power coefficient $C_{PA,\infty}$ is investigated. $C_{TA,\infty}$ and $C_{PA,\infty}$ are calculated as $T_{A,i}/(½{*}\rho{*}A_A{*}U_\infty{}^2)$ and $P_{A,i}/(½{*}\rho{*}A_A{*}U_\infty{}^3)$, respectively.

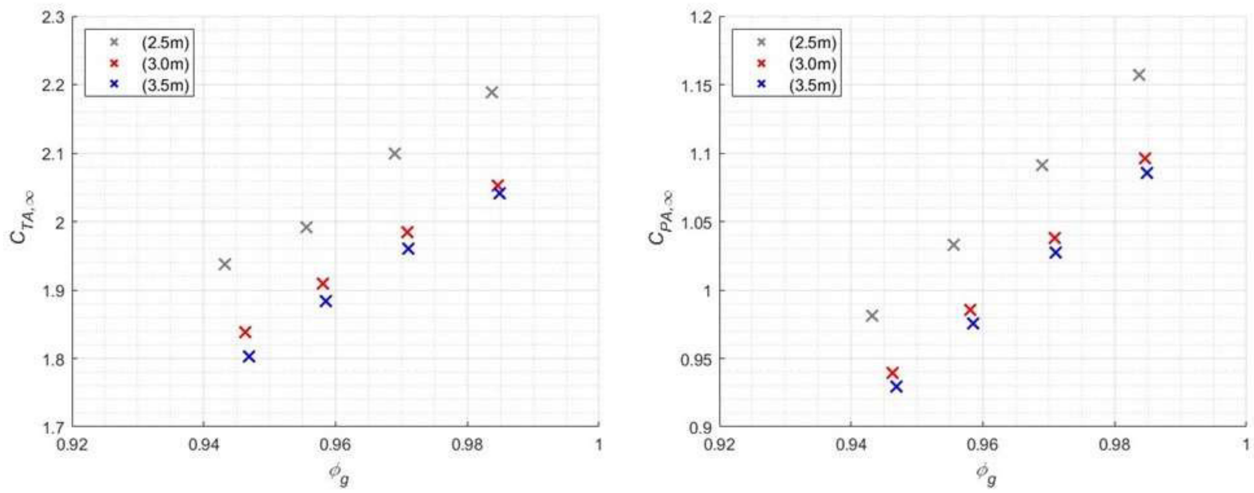

Fig. 6-18. (**Left**) Effect of the turbine spacing d_T on the array thrust coefficient $C_{TA,\infty}$ vs. global inflow factor ϕ_g for a plant of four arrays. (**Right**) Effect of the turbine spacing d_T on the array power coefficient $C_{PA,\infty}$ vs. global inflow factor ϕ_g for a plant of four arrays. The three predictions are depicted from downstream to upstream with the same color from right to left.

Array thrust and power drop as the turbine spacing d_T increases; however, for a single simulation of four arrays and proceeding upstream (from right to left), the array power decreases linearly. The first step in d_T of 0.5 m (from 2.5 to 3.0 m) implies the highest drop in $C_{TA,\infty}$ and $C_{PA,\infty}$, while a second step induces a lower reduction. Since the turbine spacing d_T defines each flow passage and the turbine blockage ratio $B_{T,j}$, the higher the d_T the smaller the blockage for the core turbines, which is expected to convert more power in the array. Therefore, reducing thrust force and power are expected as d_T increases.

The maximum thrust and power are achieved by the very-downstream array depicted on the right. At each hydraulic transition, mechanical power and total thrust force drop with the reduction in the inflow factor ϕ_g. Linearity is demonstrated for the variations in the power with a very high correlation ($R^2 > 0.99$) in all simulations. Moreover, linearity holds only for a small plant. As better illustrated in Section 6.2.3, if the scale of the plant is larger, the behavior is no longer linear.

b) Array spacing (d_A)

When d_T is fixed, thrust and power sensitivity vs. global inflow factor ϕ_g is tested by varying the array spacing d_A from 50 m to 500 m, as illustrated in Fig. 6-19. Since the rotor size and turbine spacing d_T do not change in these predictions, the first array downstream shares the same outputs regardless of d_A. Array thrust and power output rise slightly from a turbine array to another as d_A increases because the backwater reduces progressively with distance, thus determining a higher recovery of the water velocity.

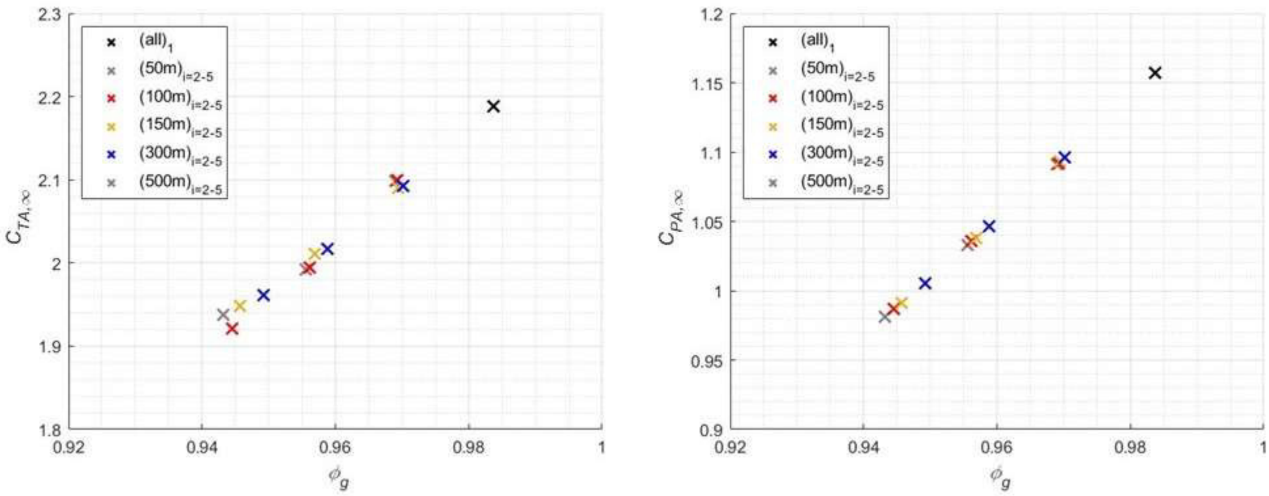

Fig. 6-19. (**Left**) Effect of the array spacing d_A on the array thrust coefficient $C_{TA,\infty}$ vs. global inflow factor ϕ_g for a plant of four arrays. (**Right**) Effect of the array spacing d_A on the array power coefficient $C_{PA,\infty}$ vs. global inflow factor ϕ_g for a plant of four arrays. The most downstream array is indicated with a black marker. The series of arrays from downstream to upstream are depicted with the same color from right to left.

Hence, a high amount of energy is harnessed at the farthest array if d_A is high. This concept extends to an ideal condition. If the spacing between two arrays exceeds the recovery length of the backwater, the power converted from both is the same. It proves the physical consistency of the model. Hence, from the perspective of pure energy conversion, the best choice would be to ensure their placement far apart, thus affording as much energy as possible and reducing part of the risk of upstream flooding.

Again, $C_{TA,\infty}$ and $C_{PA,\infty}$ reduce progressively at the upstream arrays, suggesting that the upstream rotors are optimum at a lower rotor speed than the downstream rotors speed. In the image, the $C_{PA,\infty}$ from the same plant is linearly distributed over a straight line regardless of array spacing and number. Hence, linearity is demonstrated again with $R^2 > 0.99$ for a small plant. However, the deviation in $C_{TA,\infty}$ and $C_{PA,\infty}$ at the second array between all feasible d_A is not high, and it becomes more consistent from the third array onward.

6.2.2. Array design

The previous sensitivity analysis demonstrates the improvement in the array power output with a reduced turbine spacing, even though higher axial forces and depths are afforded. Another finding is that highly spaced arrays harness more energy than closer arrays. However, the choice of the array spacing is based on the available length of the channel stretch and the expected investment, and this implies knowledge of the number of arrays. A cash flow analysis will be carried on in future to achieve the most convenient design solution.

In the ideal scenario considered herein, 1 km of the canal is dedicated to simulations with four turbine arrays, with the target of maintaining a swept area of 24 m^2, thus generating a constant blockage ratio ($B_{A,\infty}$) of 0.279 based on Equation (1). Turbines are scaled according to Tab. 6-4, assuming a fixed turbine solidity, thus excluding the dependency of $C_{P,\infty}$ on σ. However, the turbine spacing d_T has no constraints due to the different turbine sizes within a limited canal cross-section. Hence, although $B_{A,\infty}$ and σ are constant, this does not hold for d_T, whose variations slightly affect hydrodynamic forces. Notice that the turbine spacing d_T is chosen to be as small as possible to increase the turbine blockage and maximize array power extraction. Again, a minimum breadth of 0.5 m is left as a safety margin for all predictions.

By fixing the height of the turbines to 3.0 m and maintaining a level of solidity of σ = 0.36, the diameter is determined from the ratio A_T/H_T. Moreover, the chord is scaled according to the above definition of σ, yielding c = 0.24 R_T. The investigation is performed with arrays consisting of two larger turbines with an AR of 0.75, three turbines with an AR of 1.125, and four smaller turbines with an AR of 1.5. The longitudinal spacing is fixed, i.e., d_A = 250 m. The array power coefficients $C_{PA,\infty}$, and the free surface variation $\Delta h_{i,\infty}$ distributed over the arrays for each turbine aspect ratio, are outlined in Fig. 6-20.

Tab. 6-4. Cases investigated with respect to array design. Nomenclature: N_A number of arrays, N_T number of turbines per array, d_A array spacing, d_T turbine spacing, A_T turbine swept area, AR turbine aspect ratio, D_T turbine diameter, H_T turbine height, and c blade chord.

Case	N_A	N_T	d_A	d_T	A_T	AR	D_T	H_T	c
[#]	[#]	[#]	[m]	[m]	[m^2]	[-]	[m]	[m]	[m]
a	4	2	250	4.5	12	0.75	4	3	0.48
b	4	3	250	3.167	8	1.125	2.667	3	0.32
c	4	4	250	2.5	6	1.5	2	3	0.24

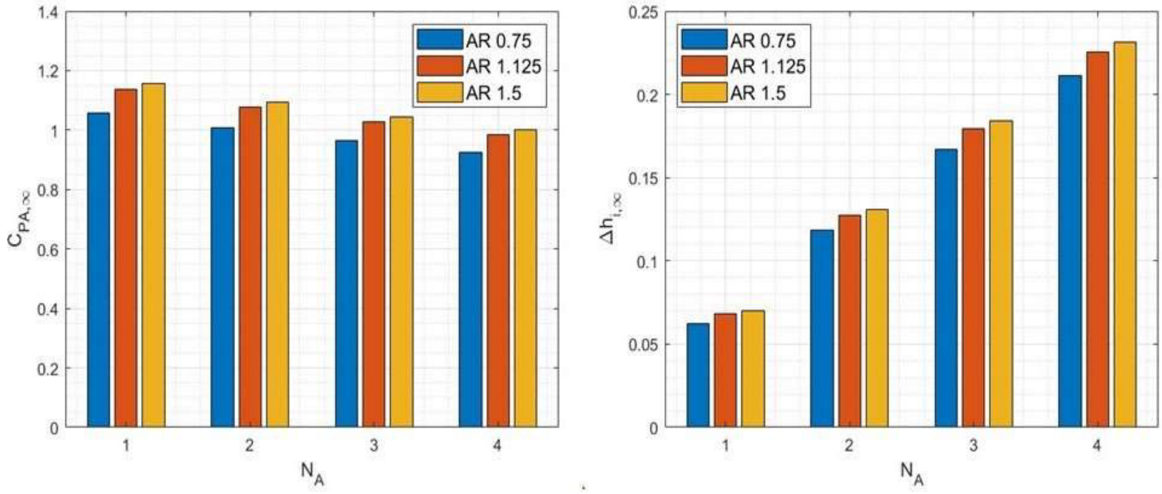

Fig. 6-20. (**Left**) Array power coefficient $C_{PA,\infty}$ vs. number of arrays N_A. (**Right**) Free surface variation $\Delta h_{i,\infty}$ vs. number of arrays N_A. Different color indicate the various simulations (blue markers indicate 2-turbine arrays with AR = 0.75, red markers indicate 3-turbine arrays with AR = 1.125, and yellow markers indicate 4-turbine arrays with AR = 1.5).

Although $C_{PA,\infty}$ does not vary noticeably between cases (*b*) and (*c*), the highest array performance is achieved by a row of four closely spaced turbines with an AR = 1.5 but poor result is determined for a row of two high-diameter turbines (AR = 0.75). According to the results of previous section, the array power output decreases from the most downstream array toward the upstream direction. The limitation of higher power conversion is represented by the increased free surface variation $\Delta h_{i,\infty}$ determined with respect to the undisturbed flow depth, i.e., $(h_i - h_\infty)$.

The outputs of the optimum solution of this assessment are shown in Fig. 6-21 for the most downstream array. The schemes on the left column represent the local free surface distribution generated by each turbine over its predicted longitudinal extension. The direction of the flow is from right (inflow) to left (flowing past the area of turbulent dissipation). Since the turbines deployed at the center of the canal convert more power, they generate higher free surface variation, while a mild variation occurs for the lateral turbines. The flow past the array (on the left) represents the undisturbed flow achieved downstream of the hydrokinetic plant. The central and right schemes represent the thrust coefficient $C_{T,\infty}$ and power coefficient $C_{P,\infty}$ curves, respectively, vs. the tip speed ratio λ_∞. Although not illustrated, the depth in the canal increases from the first to the last array, and the curves of $C_{T,\infty}$ and $C_{P,\infty}$ slightly drop from downstream to upstream. The inflow speed of the turbine arrays placed furthest upstream decreases, implying a reduction in the performance of the upstream rotors. Notice that lateral rotors harness the same energy, and the same occurs to core rotors. It is a drawback of the momentum model, incapable of catching differences between inward or outward rotation directions.

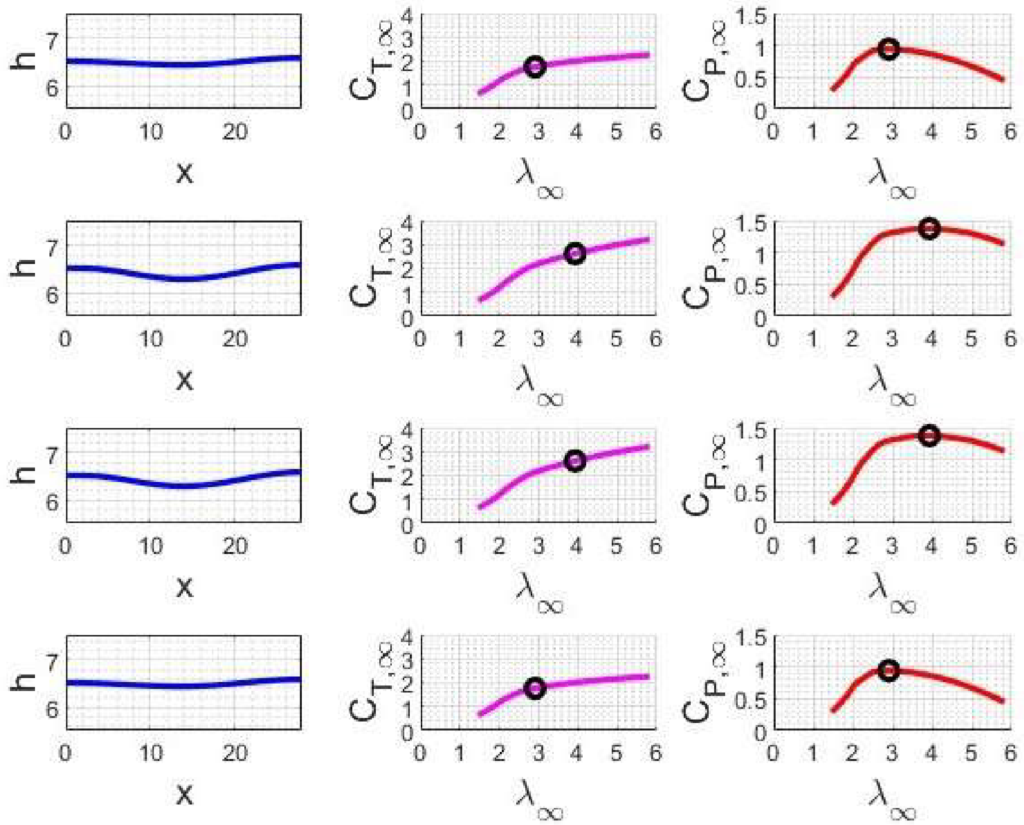

Fig. 6-21. Downstream turbine array of four turbines of an AR = 1.5 operating at $\lambda_{\infty,opt}$. The left column indicates the local free surface deformation in space for each turbine with flow directed from right to left. The central and last columns represent turbine thrust coefficient $C_{T,\infty}$ and power coefficient $C_{P,\infty}$, respectively, for each turbine of the array.

By activating the environmental constraint limiting the backwater to a value of Δh_{lim} a decreasing array power would is achieved. A maximum water depth is imposed from a regulation of the channel manager. If Δh_{lim} is smaller than the expected hydrostatic head variation generated by a given turbine array operating at maximum power, a sub-optimal response, induced by the rotor speed limitation, would be achieved. It would mean a lower power output from the turbines drawn for higher mechanical power, thus limiting the choice of the best array design solution between lower-capacity plants.

<u>*6.2.3. Large plants*</u>

The images in Fig. 6-22 illustrate two perforated plates at a constant spacing and fixed elevation from the channel bed executed at the DICAM Facility (see Chapter 2). Notice that the flow direction is from right to left. Considering the limited channel length of the facility, other plates were allowed to be "added" upstream of the last plate only by repeating the test with a new regulation of the downstream flow through the drain. The previous backwater was recreated downstream for a new experiment, for which there were no changes in the spacing between the plates. Depths measurements were performed at precise spacings from the upstream plate to allow for reliable matching with the new regulated depths.

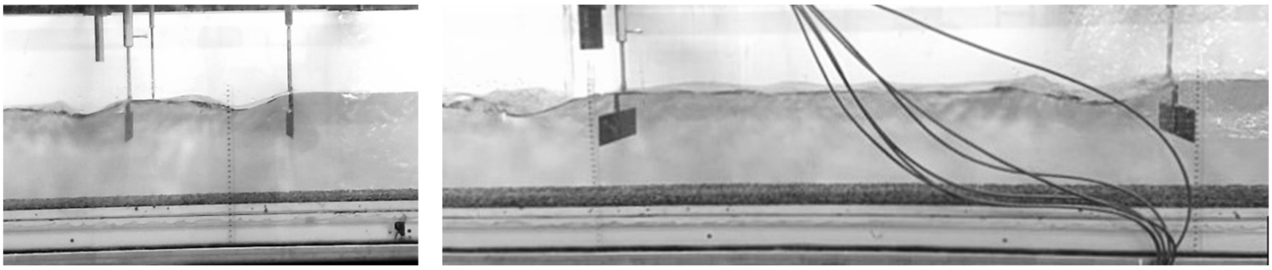

Fig. 6-22. (**Left**) Discharge $\boldsymbol{Q_c}$ = 32.3 l/s, spacing between the plates $\boldsymbol{d}$ = 0.316 m, height from the bottom $\boldsymbol{y_z}$ = 0.115 m, upstream depth $\boldsymbol{h_0}$ = 0.20 m, upstream flow speed $\boldsymbol{U_0}$ = 0.530 m/s, and measured thrust force over the first plate $\boldsymbol{T}$ = 7.51 N. (**Right**) Discharge $\boldsymbol{Q_c}$ = 35.7 l/s, spacing between the plates $\boldsymbol{d}$ = 1.0 m, height from the bottom $\boldsymbol{y_z}$ = 0.101 m, upstream depth h_0 = 0.201 m, upstream flow speed $\boldsymbol{U_0}$ = 0.583 m/s, and measured thrust force over the first plate $\boldsymbol{T}$ = 5.54 N.

Since the turbines are expected to operate at maximum performance, the resultant backwater depth is not severe as that generated at higher rotor speeds. The highest turbine thrust force occurs at a rotor speed at which almost no mechanical power is collected at the shaft, and the maximum energy is dissipated in the channel. To render a test more consistent with real turbines, the porosity of the plates should be adjusted progressively upstream to approximate the regulation of the optimum turbine tip speed ratio $\lambda_{\infty,opt}$.

According to the measurements of drag forces and depth of each plate, an asymptotic deviation in the inflow depth was speculated for high number of arrays of optimized turbines. This phenomenon occurs if one approximates the channel as an ideal water body free of obstacles, whose geometric cross-section is distributed over the investigated channel stretch and with a constant depth of the plate, measured from the channel bottom. Hence, the steady distribution of depth, flow speed, thrust, and power is predicted over a certain distance to improve the modeling of combined hydroelectric–hydrokinetic systems.

Fig. 6-23 shows the expected reduction in the water depth variation at the *i*th array, even though bed slope and precise free surface deformation are neglected in the image. As mentioned, the turbine elevation from the canal bed z_d is fixed, with the submergence depth increasing with each supplementary array. In contrast, if the turbine depth is maintained constant at the free surface proximity, more consistent backwater develops upstream. Therefore, a progressive drop in the flow speed upstream is inevitable unless the new row is placed after the backwater exhaustion, even when many kilometers away.

A single-turbine test was performed to visualize this phenomenon and reduce the inaccuracy resulting from the numerical procedure. For this purpose, a prediction is made wherein a series of equal turbines of the type shown in [1] are positioned with an array spacing of 10 m in the canal illustrated in the same work. The water depth increases after each hydraulic transition, and the total head variation ΔH_i reduces the mechanical power availability. The array (or turbine) power output P_A scales linearly for a small number of arrays (≤5); then, it is approximated by a quadratic polynomial to about 20–25 turbine arrays (which is still reasonable for large plants). High number of turbine arrays imply that a logarithmic curve fits the estimates, with $R^2 > 0.99$.

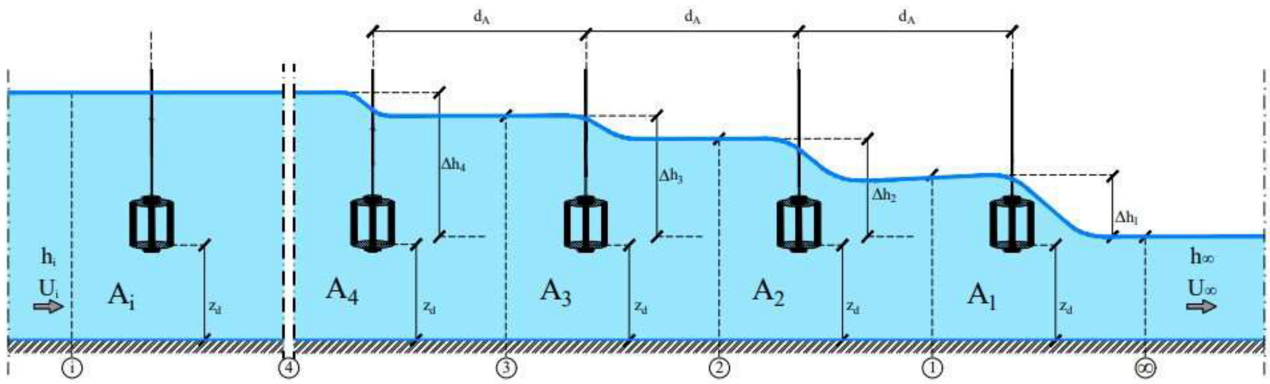

Fig. 6-23. The asymptotic trend of water depth variation Δh caused by increasing the number of arrays or turbines. Although not appreciable, backwater depth decreases upstream from each hydraulic transition. (Image is not to scale.)

For the case investigated, the deviation in the inflow depth $\Delta(h_i - h_{i-1})$ is approximated with a power law $y = a \times x^b$, in which x denotes the number of arrays, the coefficient $a > 0$, and the exponent $b < 0$. Ideally, $\Delta(h_i - h_{i-1})$ would drop to zero asymptotically, suggesting almost identical inflow depth and conditions for power conversion far upstream in a plant of many arrays. However, the approximation is valid as the deviation in water depth $\Delta(h_i - h_{i-1})$ approaches the numerical accuracy of the model (i.e., 1 mm) in Fig. 6-24. The curve of $\Delta(h_i - h_{i-1})$ implies that the hydrostatic head is expected to achieve an asymptotic value after a certain number of arrays within the imposed physical tolerance. Moreover, a slight drop in depth between the two turbine arrays is still present due to the backwater. This trend is generalized for any array layout of aligned turbines. Therefore, the imposed physical tolerance to the model determines the length scale to ascertain the asymptotic deviation $\Delta(h_i - h_{i-1})$. If a tolerance of 5 mm is selected (which is more consistent with the typical sensitivity level of many probes), asymptotic behavior is reached after about 15 arrays (in this example).

Thus, the expected far-field condition in a large plant of aligned rotors resembles Fig. 6-23, even though this distribution is valid for ideal canals. The assumptions of an infinitely long channel with a homogeneous, unobstructed geometry and stationary flow do not realistically represent the characteristics of large plants. Indeed, a transient variation in the flow rate would imply that the discharge cannot be assumed constant over the entire stretch of a channel simultaneously. Turbulence, local head losses, and finite lengths of artificial canals further complicate the flow.

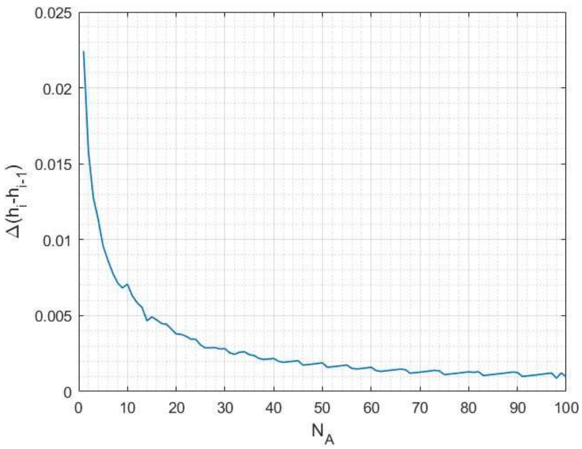

Fig. 6-24. Deviation in inflow depth $\Delta(h_i - h_{i-1})$ vs. the number of arrays N_A.

A similar problem was illustrated by Karteznikova and Ravens [9] for a homogeneous distribution of closely spaced turbines in a regular channel. The authors modeled an almost flat free surface far upstream, speculating that a uniform flow with a change in the canal Manning's roughness coefficient is achieved, with turbine power derived according to Garrett and Cummins' equation [10].

REFERENCES

[1] Cacciali L., Battisti L., Dell'Anna S., Soraperra G. Case Study of a Cross-Flow Hydrokinetic Turbine in a Narrow Prismatic Canal. Ocean Engineering **2021**, 234, 109281.

[2] Cacciali L., Battisti L., Dell'Anna S. Free Surface Double Actuator Disc Theory and Double Multiple Streamtube Model for In-Stream Darrieus Hydrokinetic Turbines. Ocean Engineering **2022**, 260, 112017.

[3] Cacciali L., Battisti L., Dell'Anna S. Backwater Assessment for the Energy Conversion through Hydrokinetic Turbines in Subcritical Prismatic Canals, Ocean Engineering **2023**, 267, 113246.

[4] Moran W.A. Giromill Wind Tunnel Test and Analysis. Volume 1: Executive summary. Final Report, McDonnell Aircraft Co., Saint Louis, MO., **1977**.

[5] Paraschivoiu I. Wind Turbine Design. With Emphasis on Darrieus Concept. Presses Internationales Polytechnique, ISBN 978-2-553-00931-0, Canada, **2009**.

[6] Bianchini A., Ferrari L., Magnani S. Start-Up Behavior of a Three-Bladed H-Darrieus VAWT: Experimental and Numerical Analysis. Proceedings of the ASME Turbo Expo, 1, **2011**.

[7] Schmitz C., Pelz P. Upper Limit for Tidal Turbines. 30th IAHR Symposium on Hydraulic Machinery and Systems. IOP Conf. Series: Earth and Environmental Science **2021**, 774, 012127.

[8] Cacciali L., Battisti L., Dell'Anna S. Multi-Array Design for Hydrokinetic Turbines in Hydropower Canals. Energies **2023**, 16(5), 2279.

[9] Kartezhnikova M., Ravens T.M. Hydraulic Impacts of Hydrokinetic Devices. Renewable Energy **2014**, 66, 425-432.

[10] Garrett C., Cummins P. The Efficiency of a Turbine in a Tidal Channel. Journal of Fluid Mechanics **2007**, 588, 243-251.

NOMENCLATURE

A_A	Turbine array area m^2	Re	Reynolds number, $(\rho * W * c/\mu)$
AR	Turbine aspect ratio	U_0, U_∞	Mean flow speed m/s
a_1, a_2	Axial induction factor, $(1-U_i/U_0)$, $_{i=1,2}$	W	Relative flow speed m/s
B_A, $B_{A,\infty}$	Array blockage ratio, $(N_T * A_T/A)$	x_{0r}	Blade mounting point
B_T	Turbine blockage ratio, (A_T/A_F)	α	Angle of attack, *deg*
C_P, $C_{P,\infty}$	Turbine power coefficient $P/(½ * \rho * A_T * U^3))$	ΔH_i	Total head variation m
C_T, $C_{T,\infty}$	Turbine thrust coefficient $(T/(½ * \rho * A_T * U^2))$	$\Delta h_{i,\infty}$	Free surface variation m
C_d	Hydrofoil drag coefficient, (2-D and 3-D)	$\Delta(h_i - h_{i-1})$	Deviation in water depth, m
C_l	Hydrofoil lift coefficient, (2-D and 3-D)	Δh_{lim}	Environmental constraint m
C_n	Hydrofoil normal coefficient	ϑ	Azimuthal displacement *deg*
C_t	Hydrofoil tangential coefficient	λ, λ_∞	Tip speed ratio $(\omega * R_T/U)$
c	Blade chord m	μ	Fluid-dynamic viscosity $Pa*s$
D_h	Hydraulic depth m	ξ	Depth parameter $(d_h/(2H_T))$
D_0	Shaft diameter m	ρ	Fluid density kg/m^3
D_T	Turbine diameter m	σ	Rotor solidity $(N_b * c/(2R_T))$
d_A	Array spacing m	ϕ_g	Global inflow factor (U_0/U_∞)
d_T	Turbine spacing m	ω	Angular velocity rad/s
Fr, Fr_∞	Froude number, $(U/(g * D_h)^{½})$		
H_T	Turbine height m	*Subscripts*	
h_0, h_∞	Water depth m	*max*	Maximum
N_A	Number of arrays	*opt*	Optimum
N_b	Number of blades	*ref*	Reference
N_T	Number of turbines		
P_A	Array power W	*Short forms*	
Q_c	Channel flow rate m^3/s	*DMS*	Double Multiple Streamtube
R_T	Turbine radius m	*LMADT*	Linear Momentum Actuator Disc Theory
T_A	Array thrust force N	*RMSD*	Root Mean Square Deviation

7. CONCLUSION

Chapter based on the following articles:

Cacciali L., Battisti L., Dell'Anna S., Soraperra G. Case Study of a Cross-Flow Hydrokinetic Turbine in a Narrow Prismatic Canal. Ocean Engineering 2021, 234, 109281. DOI: https://doi.org/10.1016/j.oceaneng.2021.109281.

Cacciali L., Battisti L., Dell'Anna S. Free Surface Double Actuator Disc Theory and Double Multiple Streamtube Model for In-Stream Darrieus Hydrokinetic Turbines. Ocean Engineering 2022, 260, 112017. DOI: https://doi.org/10.1016/j.oceaneng.2022.112017.

Cacciali L., Battisti L., Dell'Anna S. Backwater Assessment for the Energy Conversion through Hydrokinetic Turbines in Subcritical Prismatic Canals, Ocean Engineering 2023, 267, 113246. DOI: https://doi.org/10.1016/j.oceaneng.2022.113246.

Cacciali L., Battisti L., Dell'Anna S. Multi-Array Design for Hydrokinetic Turbines in Hydropower Canals. Energies 2023, 16(5), 2279. DOI: https://doi.org/10.3390/en16052279.

7.1. On the Experimental Activity

The tests illustrated in Chapter 1 show the rotor interference on the flow in a narrow canal. No significant change in flow rate or depth was observed before the placement of the turbine, allowing the estimate of the mean flow speed from averaged measurements. The main findings may be of help for future experiments to be conducted on larger channels and with various turbine arrays.

During the operation, the expected backwater phenomenon was observed and measured from the rotor station towards the first crossbar, showing no overbank flow. The conclusion is that the measurement of the undisturbed flow speed cannot be executed in the vicinity of the turbine. Several turbine diameters are required downstream to reduce the turbulent dissipation and recover a quasi-undisturbed flow. Measurements before the rotor immersion are even more advisable.

Unsteady phenomena affected the measurements due to the hydraulic disturbance produced after each rotor speed change. Therefore, effective thrust force and mechanical torque were ascertained only at the hydraulic equilibrium after the transients. The highest power coefficient was achieved at a low tip speed ratio, surpassing the Lanchester-Betz limit due to a consistent blockage ratio. However, the limit does not hot hold for a confined environment.

Torque oscillations, shaft vibrations, and varying bending moments on the support structure were observed due to a pulsating lift force on the blades, confirming that these phenomena are common in cross-flow rotors. However, the tests demonstrated excessive torque ripple and vibrations at the optimality. A drop in these effects was evident only at higher rotor speed, thus suggesting improvements in the rotor design. Hence, a reduction in the rotor solidity was recommended, for reducing vibration and increasing the lifetime of the structural elements, currently subjected to high mechanical fatigue. Then, an increased turbine aspect ratio was recommended for further decreasing the torque ripple, even though limiting mechanical power.

7.2. On The Confined Actuator Disc Theory

The unconfined Actuator Disc Theory has a long tradition in universities, and its use devoted to wind power is standard in the literature. However, the stand-alone use of the free-surface extension has also been repeatedly called upon for shallow-water applications, with various positive practical implications, but often related to ideal machines.

Although different authors approximated the power conversion in open channel flows with the Rigid Lid extension, numerically equivalent to Mikkelsen and Sørensen method for wind tunnels, the over-simplification of a flat free surface is not plausible. Whelan's improvement introduced the hydrostatic pressure gradient, which partly solved the issue by incorporating the Froude number as an independent variable.

However, experimental and numerical tests demonstrated that the Froude number is progressively less effective on the turbine performance as turbine depth increases. At depths of approximately twice the turbine height, the turbine operation is equivalent to that of a ducted rotor. In this case, a negligible Froude number can be eventually tolerated and approximated. Diversely, since degrading with depth, the effect of the Froude number has a lower impact on axial load and performance than the blockage ratio.

A question may arise for the reader. Since the Actuator Disc Theory relies on the inviscid flow assumption, how can we use this simple model to describe a complex phenomenon of the power dissipated from a porous element in a subcritical current? The answer may not be satisfactory, but it is elegant. The simple momentum theory allows modeling the phenomenon only if the left and right boundaries of the channel control volume are identified with two cross-sections at which pressure equilibrium is stated. Since a free surface variation occurs over the porous element, the momentum conservation is applicable only between the inflow station and a station of a minimum depth, implying different pressure gradients. It diversifies the free surface LMADT from the traditional unconfined LMADT for which the static pressure drop occurs only across the disc. According to Pelz et al. (2020), the gradients behind the turbine are too large, and the distribution of pressure and velocity is unknown. However, the error committed to fixing an induced flow speed upstream and downstream of the disc in a streamtube is small, as confirmed experimentally with porous plates. In addition, a short channel length between these cross-sections implies that bed friction and a mild bed slope can be assumed negligible. Since the geometry of the expanding streamtube contains the near-wake flow and excludes the transition to the far-wake, the release of shed vortices does not allow the outer flow entrapment, which would induce mixing viscous dissipation. The conclusion is that the inviscid Actuator Disc Theory approximates the phenomenon only if stated between the boundaries of the free surface variation. Implementing the Double Multiple Streamtube model illustrated in Chapter 3, the hydrofoil introduces lift and drag forces, both functions of the angle of attack and the chord Reynolds number, thus implicitly introducing viscosity. The implication is that the turbine model includes fluid-dynamic losses. Hence, the flow around the turbine is no longer inviscid, regardless of the momentum theory.

One may think that the undisturbed flow far upstream represents the inflow condition to set for this problem. However, backwater involves bed friction, disregarded in the LMADT treatment. Hence, the hydrokinetic problem in the riverine environment is solved with a turbine model and a more general channel momentum equation, including the altered inflow and the undisturbed flow downstream. To conclude, this work allows the compliance between the confined LMADT with the physics of a subcritical flow, improved even further with the double-disc extension, consistent with the visualizations performed with perforated plates from the Hydraulics Facility of the University of Trento.

7.3. ON THE DOUBLE MULTIPLE STREAMTUBE FOR SUBCRITICAL FLOWS

Based on the preliminary outputs illustrated in Chapter 6 for the hydrokinetic prototype, accurate prediction of performance and axial loads are drawn from the confined Double Multiple Streamtube model, which effectively and elegantly involves momentum methods.

Different sub-models correcting for wake shading caused by the rotating shaft, parasitic torque due to blade struts, and curvature of the flow were coded to improve the model reliability. A sub-model relaxing the free surface variation is devised to account for the actual turbine depth. A consistent reduction in the free surface drop variation over the rotor is predicted as the turbine is immersed at higher depths.

Moreover, since the turbine interferes with the unknown upstream flow speed, the inflow Froude number and blockage ratio are updated before operating the DMS. Diversely, the improper use of the U_∞ as inflow speed would lead to an overestimation of the thrust coefficient and power coefficient.

By means of a sensitivity analysis, the best prediction of performance and thrust force is found by activating the sub-models altogether. Although additional simulations are required to test other cross-flow hydrokinetic turbines, the Double Multiple Streamtube is validated with sufficient accuracy for a three-bladed turbine, according to the available data. The implementation of a modified streamtube expansion correction improves the prediction even further.

The iterative scheme solving the hydraulic transition of an HK rotor in Chapter 4 predicts the expected upstream depth and inflow factor from the known undisturbed flow. A channel momentum equation and the confined Double Multiple Streamtube model are processed iteratively in an integrated manner to solve the turbine model with consistent upstream parameters. At convergence, the backwater depth is determined from the updated inflow factor. The outputs of this method satisfactorily agree with the measurements of the upstream flow illustrated in Chapter 1. Backwater extends upstream, allowing the flow to recover the head variation through a drop in the upstream bed friction. As shown in the energy chart of the canal, the total head is maximum at the inflow cross-section, indicating that the increase in hydrostatic head yields the highest contribution to total head variation in mild slope canals.

7.4. ON THE MULTI-ARRAY DESIGN TOOL

The presented multi-array tool yields a valuable assessment of turbine arrays along mild slope hydropower canals and can be used to estimate a reliable power output with systematic modeling of each hydraulic transition.

The exploitable capacity in a channel flow is estimated with turbines operating at maximum performance and considering canals and rotors' geometry, turbine spacing, and array spacing. In addition, by incorporating a backwater assessment, the code provides visualizations of a 1-D free surface distribution showing the backwater propagating from each successive array from a downstream cross-section. Finally, by integrating a Double Multiple Streamtube model operating in a confined environment with a variable Froude number and blockage ratio, the tool overcomes the limitations of the analytical modeling with actuator discs. Indeed, the model accounts for the turbine's fluid-dynamic losses, turbulent mixing loss, and channel friction losses to calculate upstream free surface propagation. The simulation outputs based on the cases investigated show the following results:

- A sensitivity analysis demonstrated that closely spaced turbines in aligned arrays convert more power than widely spaced turbines. Indeed, an increase in turbine spacing shrinks the size of each flow passage and enhances the level of turbine blockage. As confirmed by the simulations, higher turbine blockage is achieved by the rotors deployed at the center of the row, which notably harness more energy.
- If the hydrokinetic plant design involves a canal stretch of a given length, the sensitivity analysis shows that closely spaced arrays perform inadequately in subcritical flows. Wide array spacing allows for the partial recovery of higher flow conditions for the new turbine array, thus implying higher power output.
- Assuming a scheduled number of rows with an equal number of turbines of a given solidity, different array layouts for the investigated canal cross-section demonstrate that four small turbines of a high aspect ratio are more beneficial than three medium-sized turbines or two large turbines of a small aspect ratio. While constraining the maximum expected free surface variation in the plant, a sub-optimal response induced by the rotor speed limitation is achieved by the same turbine array, foreseen for higher capacity.
- For a small plant (number of arrays ≤5), a row's maximum power output drops linearly with the number of turbine arrays. For a reasonable number of rows in a large plant, this measure is approximated by a quadratic polynomial.
- The deviation in the inflow depth asymptotically tends to be zero for a consistent multi-array plant in ideal canals, suggesting almost identical inflow depth and conditions for power conversion far upstream in a plant of many rows, with a recurrent reduction in depth within each array spacing due to backwater.

With this tool, an assessment of the capacity enabled by multiple turbine arrays is performed. Future developments will be focused on temporal analysis of flow rates via duration curves developed for each channel for which temporal data are known. Therefore, the tool will be timed to calculate new performance curves for the turbines and estimate the annual energy production (AEP) and the capacity factor (CF).

This thesis proposes equations extending the Free Surface Actuator Disc Theory to yield drag forces and interference factors from a series of two porous discs in open channel flows. The new model includes blockage ratio and Froude number as independent variables, which are inferred in advance to yield a single solution in the prescribed domain. The theoretical extension is integrated with the Blade Element Theory in a Double Multiple Streamtube model (DMS) to predict axial loads and the performance of confined Darrieus turbines. The turbine thrust force influences the flow approaching the rotor. Hence, a momentum method is applied to solve the hydraulic transition in the channel, achieving the unknown inflow factor from the undisturbed flow imposed downstream. The upstream blockage ratio and Froude number are thus updated iteratively to adapt the DMS to subcritical applications. The DMS is corrected further to account for the energy losses due to mechanical struts and turbine shaft, flow curvature, turbine depth, and streamtube expansion. Sub-models from the literature are partly corrected to comply with the extended actuator disc model. The turbine model is validated with experimental data of a high-solidity cross-flow hydrokinetic turbine that was previously tested in a canal at increasing rotor speeds. Turbine arrays are investigated by integrating the previous turbine model with wake sub-models to predict the plant layout maximizing the array power. An assessment of multi-row plants shows that the array power improves with closely spaced turbines. In addition, highly spaced arrays allow a partial recovery of the available power to be exploited upstream by a new turbine array. The highest array power is predicted by simulations on different array layouts considering constant array blockage ratio and rotor solidity. Finally, assuming a long ideal channel, the deviation in the inflow depth is speculated to become asymptotic after many arrays, implying almost identical power conversion upstream.